Rapid and robust microstructural imaging with diffusion MRI

Xinyu Ye

St Edmund Hall

University of Oxford

A thesis submitted for the degree of

Doctor of Philosophy

Michaelmas 2025

Acknowledgements

The past three years as a DPhil student have been a wonderful time for me. This thesis and the works it contains, would not have been possible without the unwavering support and love of my fabulous supervisors,collaborators, friends, and family.

First and foremost, I would like to express my deepest gratitude to my amazing supervisors Professors Wenchuan Wu and Karla Miller, who have provided me with invaluable support and guidance throughout my DPhil studies. It's my pleasure to explore the beauty of neuroimaging with you. Wenchuan, you are not only a supervisor but also a close friend who shares both scientific and life experience with me. Karla, your deep insights in the MRI field, passion for the research and continuous encouragement has made my DPhil a great journey full of inspiration and excitement.

I am sincerely grateful to everyone in the FMRIB physics group. FMRIB is not only a place where we exchange valuable ideas and thoughts on scientific projects during meetings and discussions, but also a friendly place where we share fun stories in daily life and help each other solve problems. Special thanks to my fellow students and friends Ziyu Li, Zhiyu Zheng, Silei Zhu, Qijia Shen, James Kent, Minhao Hu, Hao Li, Ben Keedwell, Hugh Simmons, James Bacon, Jason Lyu and others. You have illuminated my DPhil journey. I'd also like to thank people in the FMRIB analysis group for their support. Huge thanks to Jesper Andersson, Hossein Rafipoor and Michiel Cottaar for their valuable suggestions on diffusion data analysis.

I also want to thank my Master supervisor Prof. Hua Guo for guiding me how to start conducting systematic scientific research and how to develop the career. Special thanks to Prof. Xiaoping Wu and Prof. Fan Lam who have inspired me a lot with their unwavering eagerness to advance technical progress. Thanks my collaborators Dr. Amy Howard, Prof. Natalie Voets and Izabelle Lovgren for their support in the multi-TE dMRI project. Huge thanks to Dr. Yiming Dong at Leiden and Hongwei Li at Fudan, whose passion for MRI truly impressed me. Massive thanks to 504B comrades, Jiyu Chen, Xiaoyu Guo, Shixuan Su, Zhenxi Ou, Shun Yi, Lirui Wang, the Guo lab members and all friends for the companionship and encouragement.

I am also very grateful for the generous funding given by Clarendon Scholarships which supports my DPhil study and Karla for the financial support I received for the last term of my study.

Last but not least, I'd like to say thank you to my family, my grandparents Zhaogui Ye, Dexiu Chen, Guangfa Li, Guozhen Yang and my parents Qing Ye and Yan Li who have provided me with unconditioned love and support throughout my lifetime. You have always been the castle and shield for me when the winds howl and the rains fall. A special thank you to my partner Anni Wang. Because of you, I know—from the depths of the Pacific, to the edge of the Galaxy—that I will never walk alone.

Like constellations too bright for a single sky, my gratitude to all, beyond the reach of pen and ink, resonates with each heartbeat. *Hanc marginis exiguitas non caperet* (This margin is too small to contain it).

Abstract

Diffusion magnetic resonance imaging (dMRI) provides an non-invasive way to detect tissue microstructure information by probing the Brownian motion of water molecules and estimating the diffusion properties using signal analysis models. dMRI is broadly used in neuro disease detection and basic neuroscience studies. The most widely used dMRI acquisition technique is a two-dimensional (2D) single-shot echo planar imaging sequence due to its rapid acquisition speed. Recently, many advanced diffusion analysis models have been proposed which offer more specific estimates of tissue biophysical properties from acquired dMRI signals compared to simpler models like diffusion tensor imaging (DTI). However, these analysis models require acquisition of large numbers of diffusion volumes, which increases the dMRI scan time significantly and hinders their wider in vivo applications. Many efforts have been made to develop acquisition and reconstruction methods for fast dMRI scans, yet the trade-off between scan time, spatial resolution and model specificity still remains as a major challenge for dMRI studies.

The works in this thesis aim to develop acquisition and reconstruction methods that allow for rapid and robust brain microstructural imaging with dMRI. Firstly, a joint k-q reconstruction method based on Gaussian process is developed for accelerating multi-shell dMRI acquisition. Secondly, a computationally efficient eddy current and motion robust joint k-q reconstruction method is developed to increase the robustness of the joint reconstruction methods when the subjects may be uncooperative during scans. Thirdly, we extend the previous methods to accelerate diffusion-relaxometry imaging for microstructural imaging with higher specificity by using a k-q-TE joint acquisition and reconstruction method. The methods developed in this thesis seek to reduce the dMRI scan time while preserve the image quality and analysis accuracy, which offers potential to enable advanced microstructural imaging within clinically feasible time.

Contents

List of Figures

List of Tables

1 Introduction

Contents

1.1 Motivation

Diffusion-weighted magnetic resonance imaging (dMRI) probes the motion of water molecules using diffusion-sensitising gradients of different strengths along different directions, allowing non-invasive detection of tissue structures at the microscopic scale, which provides valuable information for studying basic neuroscience and disease[1, 2].

To infer tissue microstructure with dMRI, we need signal models to link dMRI signals and the underlying tissue microstructure, and a number of diffusion volumes with different diffusion encoding directions and weightings (b values) to provide specific information regarding microstructural features, such as fibre orientation, cell density and cell size. For example, diffusion tensor imaging (DTI) is a relatively simple model, which uses dMRI signals from different diffusion directions to fit a tensor[3, 4]. DTI assumes Gaussian distribution of water displacement and models a single fibre population in one voxel. Only a small number of diffusion directions

and a single b value are required to fit the DTI model. However, DTI cannot capture non-Gaussian diffusion in biological tissues due to e.g. restriction and cannot resolve complicated fibre architecture such as crossing.

To address the limitations of DTI, many advanced diffusion analysis models have been proposed in the past two decades, which provide higher specificity about tissue microstructure than conventional DTI[5–9] by acquiring a larger number of dMRI volumes with multiple b shells and many directions to disentangle complex microstructure within one voxel. However, this acquisition requirement incurs higher scan time burden, which hinders their wider applications in human scans.

2D Single-shot Echo-planar imaging (EPI) is widely used in dMRI acquisition due to its fast acquisition speed and robustness against motion. However, although EPI has high acquisition efficiency during the signal readout period, the scan time in dMRI is dominated by the long diffusion encoding. Therefore, dMRI sequences are generally inefficient. Besides, conventional 2D EPI acquires image slices in a sequential order, so the acquisition time for each volume is proportional to the number of slices. To achieve high resolution scans with a large brain coverage requires a large number of slices and thus increases scan repetition time (TR) for each volume. Therefore, for human scans, conventional 2D single-shot EPI is not efficient enough to acquire the amount of data needed for advanced diffusion models.

In the meantime, the intrinsic signal-to-noise ratio(SNR) of dMRI is very low, as diffusion gradients used to generate diffusion weighting cause strong signal decays, especially when higher b values (i.e., stronger diffusion weighting) are acquired. Besides, high spatial resolution acquisition, which provides more detailed anatomy information, can further exacerbates the SNR problem, due to the reduced voxel size and increased echo times (TE) caused by the long readout train.

Various acquisition and reconstruction methods have been developed to accelerate dMRI scans [10]. Conventional parallel imaging methods like SENSE and GRAPPA[11, 12] have been used to accelerate the 2D EPI acquisition by shortening the readout length. But the most effective approach to date is Simultaneous multislice (SMS) imaging [13–15] , which acquires multiple slices at the same

time, reducing the acquisition time of each diffusion direction and increasing SNR efficiency by shortening the TR. To reduce image distortion and blurring, in-plane undersampling can be combined with SMS accelerations, but the reconstruction can become ill-conditioned as in-plane and SMS rely on the same coil information for spatial encoding, making it difficult for high acceleration. Additionally, the low SNR of dMRI further limits the achievable acceleration factor compared to other modalities such as functional MRI [16, 17]. Regularized reconstruction methods have been employed to mitigate these limitations[18, 19], yet these techniques are still not efficient enough for in vivo application of microstructural models like neurite orientation dispersion and density imaging (NODDI) [7] and diffusion spectrum magnetic resonance imaging (DSI) [20], which require a large number of dMRI volumes for robust model fitting.

Recently, joint k-q reconstruction methods have been proposed to further accelerate dMRI by leveraging the information redundancy between q space points (samples in the diffusion space) and jointly reconstructing k space data from different diffusion directions to allow for a higher acceleration factor. Compressed sensing and other domain transformation methods were used to exploit the property of q space data as priors[21–27]. These methods have demonstrated the capability to achieve higher acceleration factors compared to reconstruction methods that process each dMRI image individually. While it's very promising for achieving rapid microstructural imaging with diffusion MRI, current methods still face major challenges:

Firstly, current methods use specific diffusion models or assumptions to represent the signal in reconstruction, which may introduce bias when fitting the results with different diffusion analysis models. Besides, most of the current methods focus on leveraging information redundancy between diffusion directions in a single b shell, which is not optimal for multi-shell acquisitions which are commonly used in neuroscience research involving multiple b values. Thus, a relatively model-independent joint k-q reconstruction method that can exploit both angular and cross-shell relations needs to be developed.

Another major challenge for joint k-q reconstruction is the misalignment between the acquired dMRI data from different diffusion directions or b values, caused by eddy-current distortion and subject motion, which can lead to errors in reconstruction if not corrected. Joint motion estimation and reconstruction methods have been developed [28, 29] which aim at correcting for the motion-induced artifacts during image reconstruction, yet directly applying these methods to joint k-q reconstruction imposes high computational burdens, which would hinder its application in practice. Additionally, none of the current joint k-q reconstruction methods have considered eddy current induced distortions that vary cross diffusion directions and b values. Thus, a computationally efficient eddy current and motion robust joint k-q reconstruction method needs to be developed to improve the robustness of the reconstruction.

Finally, recent years have seen a surge of research on multi-dimensional MRI and one promising direction is combined diffusion-relaxometry MRI which acquires data with different diffusion- and relaxometry- weightings in a multi-dimensional space. Commonly used dMRI models probe brain tissue microstructure properties by dividing signals into different compartments. These models make strong assumptions about certain tissue parameters (e.g., homogeneous T2 values across tissue compartments and fixed diffusivities) for robust model fitting. However, such assumptions would lead to bias and not represent the actual biophysical property of tissue[30, 31]. By using combined diffusion-relaxometry MRI, parameters that were previously fixed can now be estimated from the higher-dimensional data, which reduces bias in the fitting, enabling better separation of tissue compartments and more accurate interpretation of microstructure information[32, 33]. However, a key challenge in applying such methods in human scanning is the even longer scan time associated with the acquisition of additional data along the relaxometry encoding dimension on top of the diffusion encoding dimension. Current reconstruction methods mainly deal with dMRI or relaxometry data separately without leveraging shared information in multiple dimensions jointly. These methods are suboptimal and have limitations when the data have low SNRs (e.g. at high TEs or high

b values). Thus, more effective acceleration methods for combined diffusion-relaxometry acquisition are needed.

1.2 Thesis outline

To address the challenges above, this thesis describes the development of robust acquisition and reconstruction methods for improving the scan efficiency and imaging quality of microstructural imaging with diffusion MRI. The structure of this thesis is as follows:

Chapter 2 introduces the background of research projects, including the basic concept of MRI physics, image formation and fast MRI. The second part of the chapter covers the concept of dMRI and conventional acquisition and reconstruction methods for dMRI.

Chapter 3 is the first research chapter which extends Diffusion Acceleration with Gaussian process Estimated Reconstruction (DAGER) method, previously developed by our group for single-shell dMRI acceleration, to multi-shell condition by introducing joint multi-shell reconstruction and correcting for Rician noise distribution when fitting Gaussian Processes models. Simulated and in-vivo results demonstrate that the proposed method can significantly improve the image quality of reconstructed dMRI data with high acceleration factors, enabling advanced multi-shell diffusion analysis within a much shorter scan time.

Chapter 4 is the second research chapter which incorporates eddy current and motion correction into the joint k-q reconstruction framework to make the method more robust to the misalignments between diffusion volumes in practical scans. A computationally efficient optimisation algorithm is also proposed to reduce the memory burden for the joint misalignment correction and image reconstruction. Simulated and in-vivo results demonstrate that this method enables higher acceleration factor with improved image quality and model fitting accuracy for dMRI data acquisition in less cooperative subjects.

Chapter 5 is the third research chapter which extends the previous robust multi-shell dMRI reconstruction method to combined diffusion-relaxometry imaging

using multi-TE dMRI as an example. To better utilize the shared information across both q space and different TEs, a joint k-q-TE reconstruction based on Gaussian process modelling is proposed to improve diffusion-relaxometry imaging quality at high acceleration factors. An in vivo acquisition protocol is designed and the method is tested on both healthy volunteers and Traumatic brain injury (TBI) patients. The results show robust microstructural fitting results within much shorter scan time.

Chapter 6 concludes the research work in this thesis and discusses potential future research directions.

2 Background

Contents

2.1 MRI physics

This section introduces the basic concept of MRI based on the content of standard MRI textbooks[34–37].

2.1.1 MR Signal

MRI emerges from nuclear magnetic resonance (NMR), during which the nuclei within an external magnetic field absorb and re-emit radio frequency (RF) energy.

A nucleus with an odd atomic number and/or odd neutron number possess an angular momentum $\vec{J}$, called spin. In classical description, since the proton carries

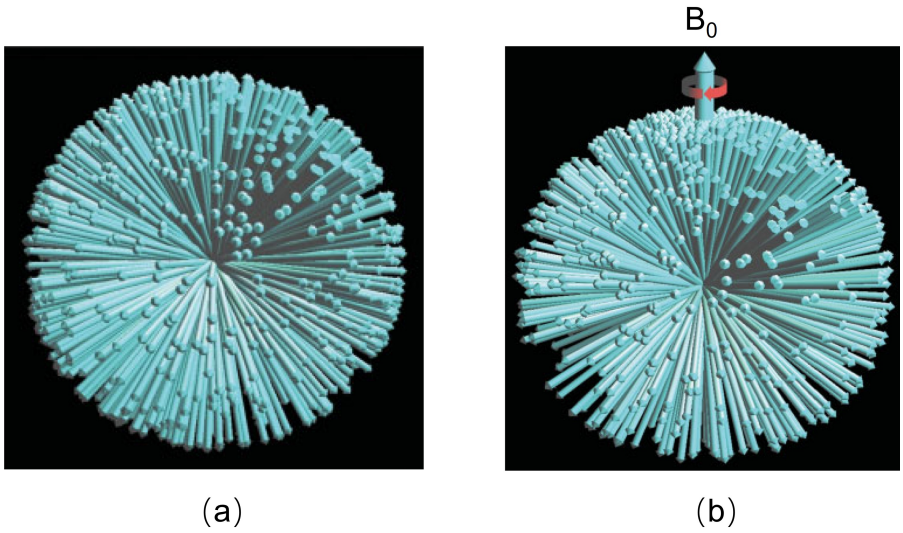

Figure 2.1: Effects of Magnetization. (a)In thermal equilibrium magnetic moment vectors have random directions. (b) In the presence of an external field, the magnetic moment vectors slightly align with the field. The figure is reproduced from [38].

a positive electric charge, this angular momentum leads to a circulating electric current, thus generating an associated magnetic moment $\vec{\mu}$. The relation between the angular momentum and magnetic moment is derived as:

$$\vec{\mu} = \gamma \vec{J} \tag{2.1}$$

where γ represents the gyromagnetic ratio of the nucleus (e.g., $\gamma = 2.675 \times 10^8$ rad/s/T for ^1H and $\gamma = 7.075 \times 10^7$ rad/s/T for ^{23}Na).

Magnetization

Without an external magnetic field, at thermal equilibrium, the directions of $\vec{\mu}$ are random due to random thermal motions. Thus no net magnetic magnetization $\vec{M}$ (i.e. vector sum of $\vec{\mu}$ from all protons) can be observed as shown in Figure 2.1(a) [38].

When exposed to an external magnetic field B_0, the spins have a slight tendency to be aligned with the direction of the external field as shown in Figure 2.1(b) [38]. A net magnetization $\vec{M}$ is then generated. In the presence of B_0, any magnetic moment vector μ takes two possible positions: parallel and anti-parallel with different energy states.

Considering the Boltzmann relationship, the spin population difference between two spin states can be expressed as:

$$\frac{N_{\uparrow}}{N_{\downarrow}} = \exp\left(\frac{\Delta E}{KT_s}\right) \tag{2.2}$$

where $N_{\uparrow}$ is the number of parallel spins, $N_{\downarrow}$ is the number of anti-parallel spins, K is the Boltzmann constant, T_s is the absolute temperature and ΔE is the energy difference between two spin states expressed as:

$$\Delta E = \gamma \hbar B_0 \tag{2.3}$$

where $\hbar$ represents the Planck constant divided by 2π. Given that ΔE is much smaller than KT_S, the spin population difference can be approximated as:

$$N_{\uparrow} - N_{\downarrow} \approx N_s \frac{\gamma \hbar B_0}{2KT_s} \tag{2.4}$$

where N_s is the total number of spins. Although the fraction of the difference in the spin population compared to the total spin number is small, it can still generate an observable net magnetization $\vec{M}$ if N_s is large.

Precession

In the classical framework, $\vec{\mu}$ is a magnetic moment vector and the rate of the angular momentum change equals the torque from the external field B_0 (applied in the z-direction of laboratory frame, $\vec{k}$ is the unit vector along z-axis):

$$\frac{d\vec{J}}{dt} = \vec{\mu} \times B_0 \vec{k} \tag{2.5}$$

Since $\vec{\mu} = \gamma \vec{J}$, the following equation can be derived:

$$\frac{d\vec{\mu}}{dt} = \gamma \vec{\mu} \times B_0 \vec{k} \tag{2.6}$$

The net magnetization $\vec{M}$ is the sum of all magnetic moment vectors, thus

$$\frac{d\vec{M}}{dt} = \gamma \vec{M} \times B_0 \vec{k} \tag{2.7}$$

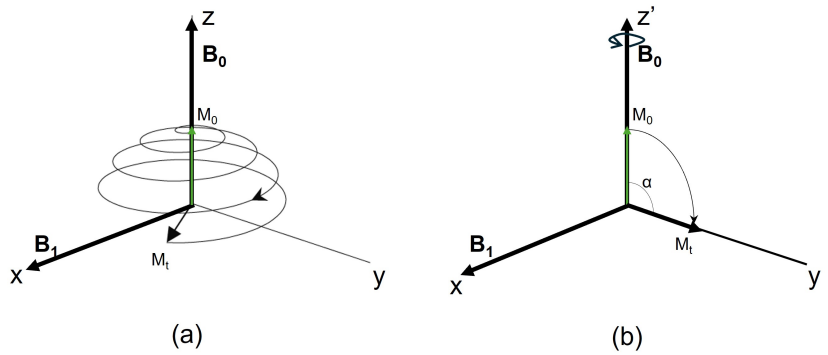

Figure 2.2: Movement after Excitation. (a)In the laboratory frame, M rotates about both z-axis (B_0) and x-axis (B_1), from the inital position M_0 to timepoint t position M_t. (b) In the rotation frame, M rotates only about x-axis (B_1), leading to a flip angle α from z-axis

The solution to Eq.2.7 is

$$\begin{cases} M_{xy}(t) = M_{xy}(0)e^{-i\gamma B_0 t} \\ M_z(t) = M_z(0) \end{cases} \tag{2.8}$$

where $M_{xy}(0)$ and $M_z(0)$ are initial values. Eq.2.8 describes a precession motion around the z-axis at a fixed frequency:

$$\omega_0 = \gamma B_0 \tag{2.9}$$

which is called Larmor frequency.

Excitation

To detect the MRI signal, the magnetization vector $\vec{M}$ needs to be changed away from the direction of the external field B_0 (usually along z-axis) to produce a temporally changing magnetic flux which can be detected by the receiver coils of the MRI scanner using Faraday's law. The step is called excitation.

Excitation is achieved by applying another external radio-frequency (RF) magnetic field B_1 which oscillates in the transverse plane (x-y plane) . To satisfy the resonance condition, the B_1 field is tuned to the Larmor frequency. B_1 is usually called RF pulses.

In the classical picture, B_1 field applies a torque on $\vec{M}$, forcing it to tilt away from the equilibrium direction along z-axis to rotate about the B_1 field direction.

Figure 2.2(a) shows the effects of B_1 field applied along x-axis in the laboratory frame. Apart from rotating about B_0 field direction (z-axis), $\vec{M}$ also rotates about B_1 field direction (x-axis), thus rotating away from z-axis. To better illustrate this effect, a rotating frame is defined whose transverse plane rotates about z-axis at the same frequency as Larmor frequency as shown in Figure 2.2(b). In the rotating frame, precession about B_0 disappears while the flipping about B_1 remains. The angle of rotation away from z-axis is called flip angle α, which can be calculated based on the RF field strength and duration (τ):

$$\alpha = \int_0^\tau \gamma B_1(t)dt \tag{2.10}$$

Relaxation

After excitation by an RF pulse, the excited spins release the energy they absorbed during excitation and the perturbed $\vec{M}$ has a tendency to return to its equilibrium state M_0 along z-axis. This process consists of two parts, the recovery of longitudinal magnetization M_z, called T_1 relaxation and the destruction of transverse magnetization M_{xy} called T_2 relaxation.

T_1 relaxation

During T_1 relaxation, the spins transfer energy to its surroundings (lattice), thus it's also called spin-lattice relaxation. During this process, the longitudinal magnetization M_z gradually returns to its equilibrium value M_0. The speed of this exponential recovery process is determined by a constant value T_1:

$$M_z(t) = M_z^0\left(1 - e^{-t/T_1}\right) + M_z(0_+)e^{-t/T_1} \tag{2.11}$$

here T_1 is the time needed for M_z to grow from 0% to 63% M_0 after a 90 degree RF pulse (Figure 2.3(a)), $M_z(t)$ is the magnetization along z-axis at time t, $M_z(0_+)$ is the magnetization along z-axis after the RF excitation.

Since the MR signal is proportional to the M_z, to allow time for T_1 relaxation, a time interval know as TR (repetition time) is applied between successive excitations. A longer TR enables better T_1 recovery, thus producing stronger MR signals though the scan time is increased.

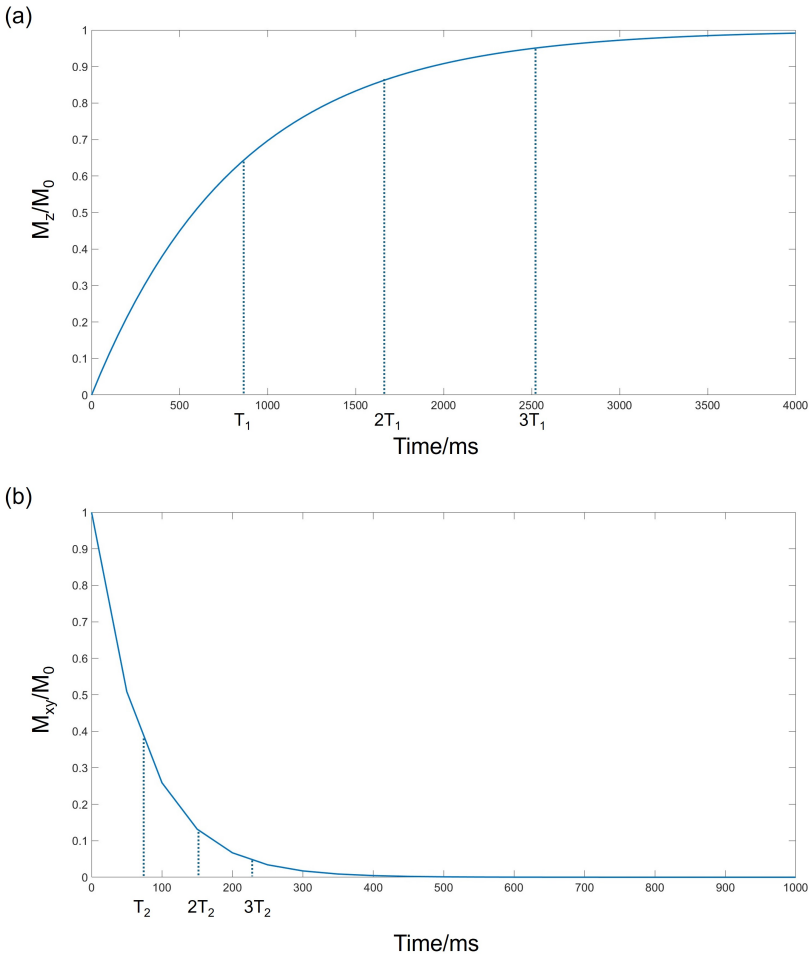

Figure 2.3: T_1 and T_2 Relaxation. (a)T_1 relaxation. Longitudinal magnetisation M_z gradually recovers to M_0. T_1 is set as 838 ms [39] as a typical value for white matter tissue at 3T. (b)T_2 relaxation. Transverse magnetisation M_{xy} gradually decays to 0. T_2 is set as 74 ms [39] as a typical value for white matter tissue at 3T.

T_2 and T_2^* relaxation

During T_2 relaxation, the spins lose phase coherence (also called dephasing) due to the variable precessing frequency caused by molecular interactions, leading to decay of transverse magnetization M_{xy}. Thus it's also called spin-spin relaxation. During this process, the transverse magnetization M_{xy} gradually decays and the speed of this exponential decay process is determined by another constant value T_2:

$$M_{xy}(t) = M_{xy}(0^+)e^{-t/T_2} \tag{2.12}$$

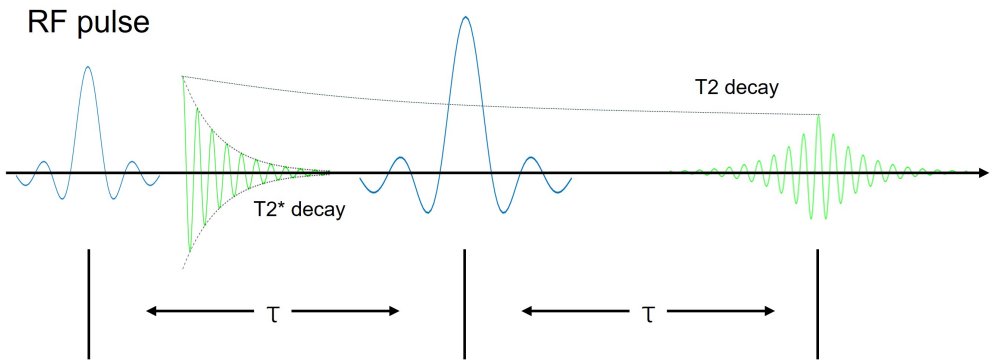

Figure 2.4: Illustration of a spin echo formation. After applying a 90° excitation RF pulse, the spins exhibit T_2* decay due to dephasing caused by spin-spin interaction and local field inhomogeneity. By applying a a 180° refocusing RF pulse, the spins become refocused and form a spin echo at timepoint 2τ.

here T_2 is the time needed for M_{xy} to decay from 100% to 37% M_0 after a 90 degree RF pulse (Figure 2.3(b)), $M_{xy}(t)$ is the magnetization in transverse plane at time t, $M_{xy}(0_+)$ is the magnetization in transverse plane immediately after an RF excitation. Apart from spin-spin interaction, magnetic field inhomogeneity caused by B_0 inhomogeneity, susceptibility-induced local field inhomogeneity and applied gradient magnetic field (covered in next section) also leads to spin dephasing, which causes more rapid $M_{xy}(t)$ decay. This process is referred to as T_2^* decay and the relation between T_2 and T_2^* is described as:

$$\frac{1}{T_2^*} = \frac{1}{T_2} + \frac{1}{T_2'} \tag{2.13}$$

where T_2' represents the signal decay caused by field inhomogeneity. In order to mitigate the signal loss caused by T_2', as shown in Figure 2.4, following the 90° excitation RF pulse, a 180° refocusing RF pulse can be applied to reverse the spin dephasing due to the field inhomogeneity, causing the spins to rephase and the signal to grow gradually and reaches the maximum value at the time point 2τ. This process is referred to as forming a 'spin echo' and the time point 2τ is called echo time (TE).

Bloch equation

The above discussed effects on the net magnetization $\vec{M}$ can be described using the Bloch equation which illustrates the behaviour of $\vec{M}$ under external magnetic

fields while considering relaxation effects:

$$\frac{d\vec{M}}{dt} = (\vec{M} \times \gamma \mathbf{B}) - \frac{M_x\hat{i} + M_y\hat{j}}{T_2} + \frac{(M_0 - M_z)\hat{k}}{T_1} \tag{2.14}$$

here $\mathbf{B}$ is the total magnetic field including the main field B_0, RF field B_1 and gradient field (see next section), $\hat{i}$,$\hat{j}$,$\hat{k}$ are the unit vectors along x,y and z-axis respectively.

2.1.2 Image formation

Gradient field

With B_0 field and B_1 field, MRI signals can be generated from the object. With a receiver coil system, the detected MR signal at a time point t can be derived as an integral from all spatial locations after demodulation (which removes the carrier frequency of the signal $e^{-i\omega_0(r)t}$):

$$S(t) = \int \rho(r) e^{-i\triangle\omega(r)t}\, dr \tag{2.15}$$

here $\rho(r)$ is the proton density at spatial location r, $\triangle\omega(r)$ is the inhomogeneous field at location r. Since the signals detected is the sum of all signals from the entire imaging field of view, it's not possible to differentiate the signals from different spatial origins directly. To tackle this challenge, MRI scanners use gradient coils which generate gradient magnetic fields to achieve spatial localization of MRI signals. The gradient coils typically produce three magnetic fields that vary along orthogonal axes. The produced field has the same direction aligned with B_0 but different magnitudes varying linearly along x,y and z axes, respectively. The effective field strength at a certain spatial location is:

$$\mathbf{B} = \mathbf{B_0} + (\mathbf{G}\cdot\mathbf{r})\hat{k} \tag{2.16}$$

where $\mathbf{G} = [G_x, G_y, G_z]$ represents gradient strength along x,y,z directions and $\mathbf{r}$ is the position in 3D spatial coordinate. Due to the existence of the gradient field, spins at different spatial locations experience different local field strengths, thus leading to different Larmor frequencies:

$$\omega(r) = \omega_0 + \gamma(\mathbf{G}\cdot\mathbf{r}) \tag{2.17}$$

which produces a linear mapping between spatial location **r** and the resonance frequency $\omega(r)$. Thus, it's possible to use Fourier transform described in later section to form images from MRI signals.

Slice Selection

Slice-selective excitation is an important way for spatial localisation in MRI, which only excites MR signals from one slice or slab of the entire imaging volume.

Slice selection is achieved by concurrently applying a gradient magnetic field with an RF pulse. Specifically, a linear gradient field is turned on to make the spin resonance frequency varying at different locations. At the same time, an RF pulse tuned to a specific frequency is applied, which will excite the spins precessing at the matched resonance frequency, thus, achieving spatially selective excitation. This gradient field is called slice-selection gradient. In order to select an axial slice, the slice section direction is chosen along the z-axis, and the required slice selection gradient can be described as $\mathbf{G_{ss}} = [0, 0, G_z]$, which creates a linear mapping between slice position along z-axis and the resonance frequency.

To design a selective RF pulse,the Fourier transform method can be used. Given the condition of small flip angle excitation, the RF pulse shape and the spatial selection profile (desired frequency function) $p(f)$ have a Fourier transform relation:

$$B_1(t) \propto \int_{-\infty}^{\infty} p(f) e^{-i2\pi ft}\, df \tag{2.18}$$

thus it's possible to design the RF pulse shape given the desired spatial selection function.

The Fourier method assumes linear performance of spin systems during excitation which doesn't hold true in practice. Besides, the Fourier transform approach builds on the small-flip-angle assumption. For more accurate RF pulse design, Bloch equation approach can be employed which solves numerical equations to design the RF pulse. However, due to its simplicity, the Fourier transform method is commonly used in practice and the accuracy is still acceptable for flip angles up to 90°. The following part describes how to use this method to achieve a target profile when using small flip angle excitation as shown in Figure 2.5.

Assuming a slice of width $\triangle z$ centred at $z = z_0$ needs to be excited, the spatial selection function can be expressed as the following boxcar function:

$$p_s(z) = \Pi\left(\frac{z - z_0}{\Delta z}\right) \tag{2.19}$$

In the presence of the slice selection gradient $\mathbf{G_{ss}} = [0, 0, G_z]$ mentioned above, the resonance frequency at location z is:

$$\omega_z = \omega_0 + \gamma G z \tag{2.20}$$

and the frequency in Hz is ($\bar{\gamma} = \gamma/2\pi$):

$$f_z = f_0 + \bar{\gamma} G_z z \tag{2.21}$$

thus, the desired frequency function is:

$$p_s(f) = \Pi\left(\frac{f - fc}{\Delta f}\right) \tag{2.22}$$

where

$$fc = f_0 + \bar{\gamma} G_z z_0 \tag{2.23}$$

$$\Delta f = \bar{\gamma} G_z \Delta z \tag{2.24}$$

Considering the Fourier transform relation between the RF pulse shape and the desired frequency function, the RF pulse shape needs to be designed as the Fourier transform of the boxcar (rectangular) function, which can be derived as:

$$B_1(t) \propto \Delta f sinc(\pi \Delta f t) e^{-i2\pi f_c t} \tag{2.25}$$

merging the previous equations, the RF excitation frequency is:

$$\omega_{rf} = \omega_0 + \gamma G_z z_0 \tag{2.26}$$

and the RF pulse envelop is a sinc function:

$$B_1^e(t) = A sinc(\pi \Delta f t) \tag{2.27}$$

here A is a constant related to the flip angle.

With slice selection, we can localize signals from a 2D slice, but we still cannot distinguish signals from different in-plane locations within the slice. To address this limitation, frequency and phase encodings were introduced.

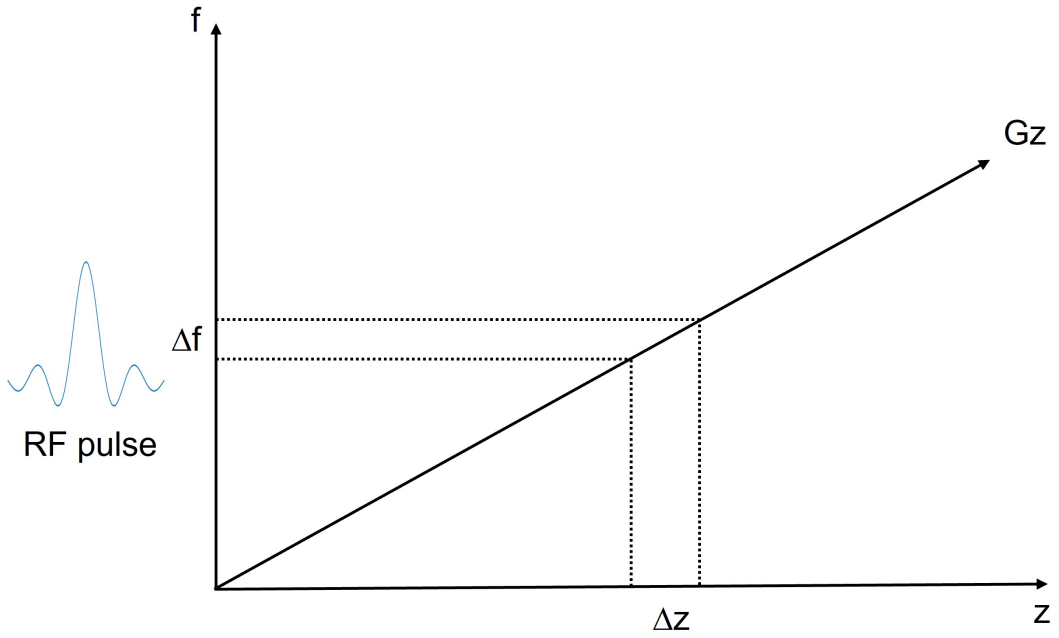

Figure 2.5: Illustration of slice selection. The slice-selection gradient G_z leads linearly changing resonance frequency along the slice direction. A frequency selective RF pulse only excites spins in certain frequency range Δf, thus selectively exciting signals from a slice with thickness Δz.

Frequency encoding

Frequency encoding encodes the MR signal based on its oscillation frequency which is dependent on its spatial origin. Similar to the idea of slice-selection gradient, a linear gradient field G_x, which is called frequency encoding gradient, adds different local fields to the main B_0 field along x-axis, and the Larmor frequency at location x is:

$$\omega_x = \omega_0 + \gamma G_x x \tag{2.28}$$

And the received signal $S(t)$ within the excited region after demodulation is:

$$S(t) = \int \rho(x) e^{-i\gamma G_x x t}\, dx \tag{2.29}$$

Since the frequency of signal is linearly related with its spatial location, a Fourier transform can be applied to separate signals from different spatial positions along the frequency encoding direction. The frequency encoding gradient is turned on during the readout. However, frequency encoding alone cannot resolve the spatial information along the perpendicular directions.

Phase encoding

To solve multi-dimensional spatial localization, the concept of phase encoding was introduced. Instead of applying a gradient field during excitation or readout, a phase encoding gradient G_y is turned on for a short interval T_{pe} then turned off. During this interval, signals at different spatial locations along the phase encoding dimension accumulate different phase. After the gradient is turned off, an initial phase angle is generated:

$$\phi(y) = -\gamma G_y y T_{pe} \tag{2.30}$$

which is linearly related to the signal location y. And the received signal $S(t)$ within the excited region with both phase encoding and frequency encoding after demodulation is:

$$S(t) = \int \rho(x,y) e^{-i\gamma G_y y T_{pe}} e^{-i\gamma G_x x t}\, dydx \tag{2.31}$$

Apart from frequency encoding along x, the signals are now also phase encoded in the phase encoding dimension (magnetizations at different spatial locations have different phase), which can be used to separate signals from different voxels along y dimension. For 2D Cartesian acquisition, phase encoding gradients are turned on for a short time after excitation and before readout gradient over multiple signal readouts through acquisition.

k space

Considering both frequency encoding and phase encoding, the received signal $S(t)$ after demodulation can be expressed as:

$$S(t) = \int \rho(r) e^{-i\gamma r \cdot \int G(\tau) d\tau}\, dr \tag{2.32}$$

where $\mathbf{G} = [G_x, G_y, G_z]$ describes the amplitude of gradients along three axes defining

$$k(t) = \frac{\gamma}{2\pi} \int G(\tau) d\tau \tag{2.33}$$

the following equation can be derived:

$$S(t) = \int \rho(r) e^{-i2\pi r \cdot k(t)}\, dr \tag{2.34}$$

which reveals the Fourier transform relation between formulated MR signals (named, k space data) and proton density spatial maps. Thus, with a Fourier transform of the acquired k space data, MRI images can be reconstructed. Due to the Fourier transform property, as a transform pair, many imaging properties are related to how k space is sampled. For example, considering the Nyquist sampling theorem, the data sampling rate in k space must be high enough to reconstruct the image without aliasing. The imaging field of view (FOV) is related to the k space sampling gap as $FOV = \frac{1}{\Delta k}$. Signals coming from outside the FOV will cause aliasing artifacts. The image resolution is determined by the coverage of k space $\frac{1}{k_{max}}$ with k_{max} being the maximum coverage of k space along the corresponding dimension. So a larger k space coverage is associated with a higher spatial resolution.

By changing the gradient waveform design, k space data can be sampled with different trajectories. Figure 2.6 shows several common k space trajectories used in MRI. Figure 2.6 (a) shows a simple 2D Cartesian acquisition. By applying phase encoding gradients with different amplitude and/or duration, followed by a readout gradient, the k space data are acquired line by line along the phase encoding direction. Acquiring one single line per repetition time requires long scan times. An accelerated version of 2D Cartesian acquisition is Echo planar Imaging (EPI), as shown in Figure 2.6 (b). By alternating the polarity of readout acquisition between adjacent phase encoding lines and adding blips (phase encoding gradients) along phase encoding dimension, EPI acquires multiple phase encoding lines within one repetition time, thus significantly reducing scan time. Non-Cartesian trajectories can also be used to collect k space data. Figure 2.6 (c) shows spiral acquisition which starts from the centre of k space and rotates outward toward the edge of k space. Spiral acquisition enables very short TEs and higher SNR compared to Cartesian acquisition. However, artifacts in non-Cartesian imaging are more complicated compared to Cartesian imaging and are more difficult to correct (like blurring

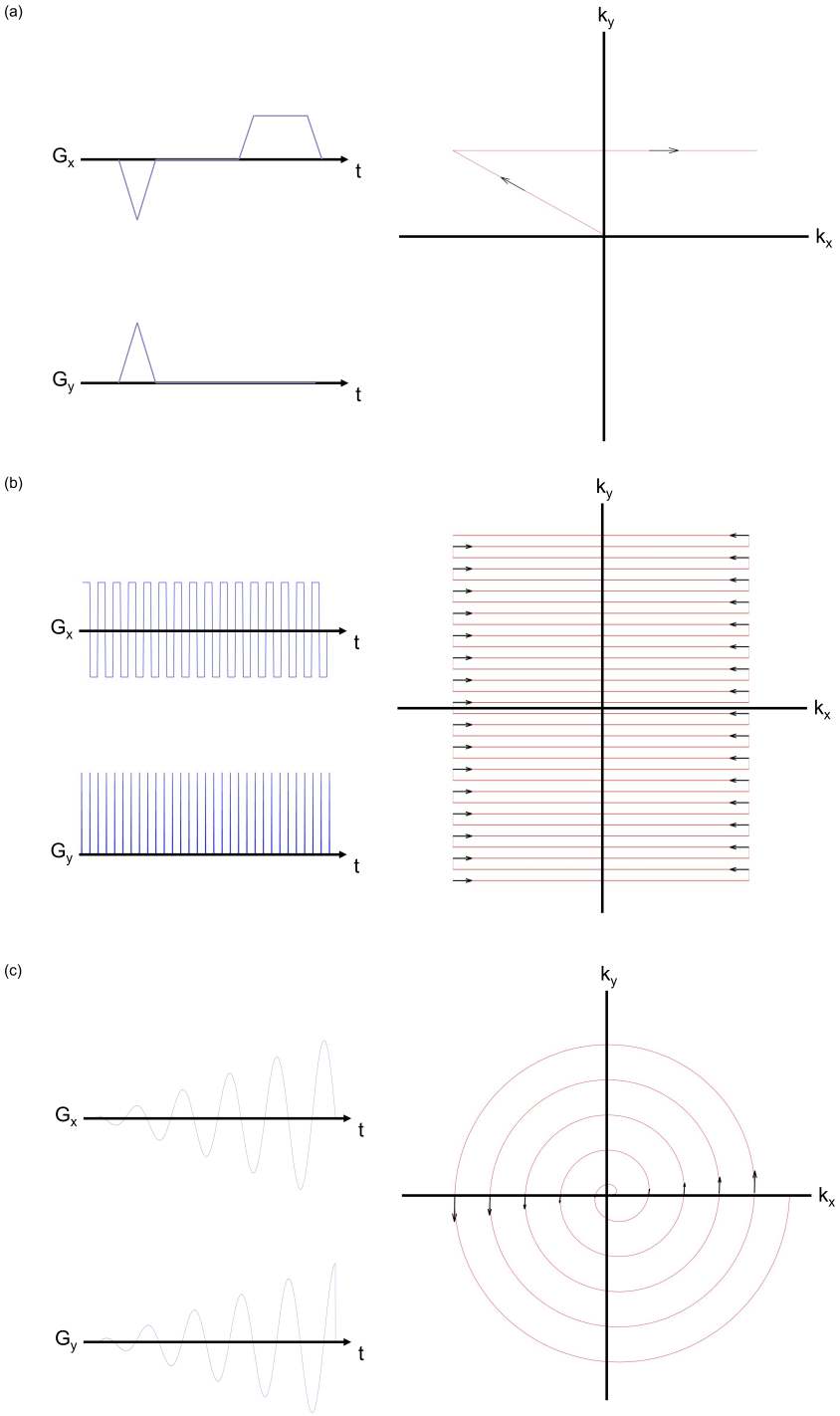

Figure 2.6: Illustration of common k space trajectories and corresponding gradient waveforms. (a) 2D cartesian acquisition. (b) Echo planar Imaging (EPI) acquisition. (c) Spiral acquisition.

artifacts in spiral imaging due to B_0 field inhomogeneity). To date, Cartesian acquisitions are commonly used in practice for MRI scans. But due to its intrinsic benefits, including high scan efficiency and robustness against motion, non-Cartesian imaging techniques have unique advantages in areas like cardiac imaging.

2.1.3 Parallel Imaging

MRI acquisition is much slower compared to other imaging techniques, such as CT and ultrasound, since multiple excitations are needed to form an image, and a time interval between adjacent excitations is needed to allow for signal recovery. As discussed above, to avoid aliasing, the sampling gap in k space Δk is determined by the image FOV and the k space coverage is determined by the spatial resolution. A 'fully sampled' dataset is one that meets both sampling-gap and resolution criteria.

To accelerate MRI scans, modern MRI systems are equipped with multiple receiver coils which enables 'parallel imaging'. During data acquisition, the gap between adjacent sampling positions in k space is increased while the maximum k space coverage remains unchanged. In this way, some k space data are skipped so the scan time is reduced, while the image resolution is preserved. The fraction of the acquired data compared to the fully sampled data is called reduction factor R.

However, the increased k space sampling gap leads to reduced FOV, causing aliasing artifacts. With parallel imaging, missing data points are estimated during image reconstruction based on the spatial sensitivity encoding information provided by the multiple coils, which can resolve aliasing artifacts. The most commonly used parallel imaging reconstruction techniques include Sensitivity Encoding (SENSE) and Generalized Autocalibrating Partially Parallel Acquisitions (GRAPPA)[11, 12]. The following section will give a brief introduction of them.

SENSE

SENSE is an image space based parallel imaging technique, which separates the aliased signals in the reduced FOV image to create a full-FOV image using coil sensitivity information.

Assuming a 2 fold acceleration in k space, in the reconstructed images, 2 voxels are collapsed together into one voxel due to the reduced FOV caused by skipping k space lines as shown in Figure 2.7(a).

Different receiver coils have different spatial sensitivity information. In the reduced FOV image acquired from a single coil, the signal at each voxel is the sum of voxel intensities from different positions weighted by the correspondingly local coil sensitivities as shown in Figure 2.7(b).

A linear relation between the target unaliased image vector $\mathbf{x_p}$ and the acquired aliased data $\mathbf{y_p}$ obtained by direct Fourier transform at a pixel location p can be expressed as:

$$\mathbf{y_p} = S_p \mathbf{x_p} \tag{2.35}$$

where $\mathbf{y_p}$ is a vector of size $N_c \times 1$ representing the data from N_c coils, $\mathbf{x_p}$ is a vector of size $N_R \times 1$ representing the original R voxels collapsed into one voxel, S_p represents the sensitivity map ($N_c \times R$) at the corresponding R voxels locations. SENSE reconstruction obtains the unfolded image by solving the following optimisation problem:

$$\mathbf{x_p} = \arg\min_{\mathbf{x_p}} \|S_p \mathbf{x_p} - \mathbf{y_p}\|_2^2 \tag{2.36}$$

which can be solved using least square minimisation as: $\mathbf{x_p} = (S_p^H S_p)^{-1} S_p^H \mathbf{y_p}$, where H is the conjugate operator. Considering the receiver noise correlation matrix Φ between coils, the reconstruction can be formulated as:

$$\mathbf{x_p} = (S_p^H \Phi^{-1} S_p)^{-1} S_p^H \Phi^{-1} \mathbf{y_p} \tag{2.37}$$

Gradient-based optimisation methods can also be utilized to solve the SENSE reconstruction if the pseudo inverse is computationally expensive (e.g., in non-Cartesian reconstruction). Although parallel imaging accelerates MRI acquisition, the SNR of the reconstructed images is reduced compared to the images derived from the fully sampled datasets. This SNR loss comes from two sources. First, fewer k space samples are acquired so the SNR is reduced by the factor $\sqrt{R}$. Second,

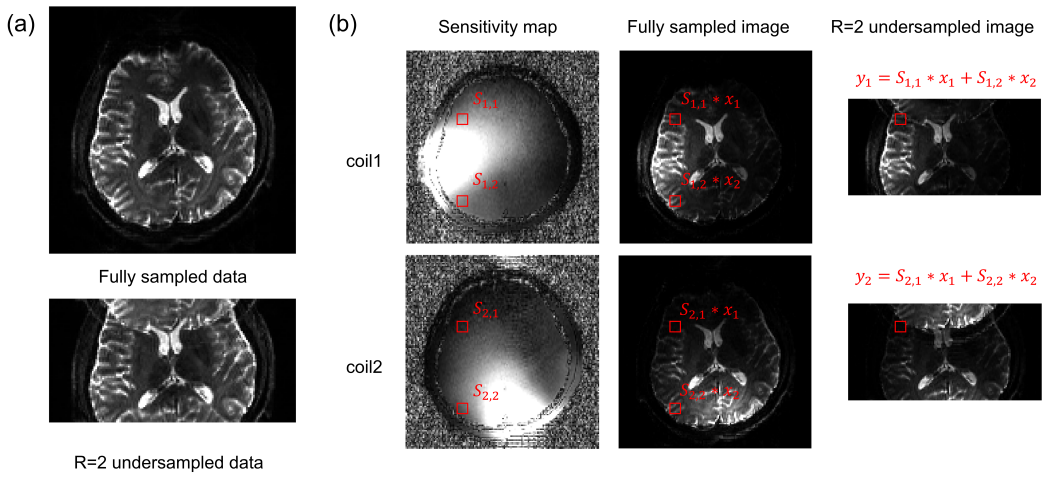

Figure 2.7: Illustration of SENSE reconstruction.(a) Coil combined images are shown.Fully sampled data produce full FOV images while R=2 undersampled data produce reduced FOV images with 2 fold aliasing. (b)Illustration of R=2 SENSE reconstruction. Each voxel is weighted by the local sensitivity map in the image of each coil. The voxels in the R=2 aliased image is a linear combination of signals from different spatial locations weighted by coil sensitivity.

sensitivity profiles from different coils are not independent due to coil geometry. As a result, solving the inverse reconstruction problem for unfolding the image can be ill-conditioned, leading to amplified noise. The SNR ratio between fully sampled and reconstructed undersampled image can be calculated as:

$$\frac{SNR_{full}}{SNR_{under}} = \sqrt{R}\sqrt{(S^H\Phi^{-1}S^H)^{-1}_{p,p}(S^H\Phi^{-1}S^H)_{p,p}} \tag{2.38}$$

where Φ is the noise covariance matrix.

The term $\sqrt{(S^H\Phi^{-1}S^H)^{-1}_{p,p}(S^H\Phi^{-1}S^H)_{p,p}}$ represents the noise amplification in the reconstruction, which is related to the coil geometry, thus it's called local geometry factor g (g-factor). A higher g-factor leads to stronger noise amplification in the reconstruction. If the columns of S are more correlated (i.e., high correlation between sensitivity maps of different coils), the reconstruction inverse problem becomes more ill-posed, and leads to a larger g-factor; If the columns of S are less correlated (e.g., uncorrelated sensitivity maps between coils), the inverse problem becomes better conditioned, and leads to a smaller g-factor.

The g-factor can be reduced by better coil array design. Besides, it can also be reduced by optimising the undersampling patterns, such that sensitivity of aliased voxels are less correlated. One very successful example is CAIPI sampling (controlled aliasing in parallel imaging results in higher acceleration)[40], where different slices that collapse together during acquisition are shifted inplane, creating more different coil sensitivity information between the aliased voxels.

To reconstruct images using SENSE, coil sensitivity maps need to be measured beforehand[41] . The 'sum-of-squares' method divides the image from single coil by the image combined from the coil array to get the coil-specific sensitivity maps. This method is simple yet vulnerable to noise. Walsh et al. proposed using an adaptive matched filter to suppress background noise in the maps [42]. Wavelet based denoising methods have also been proposed [43, 44]. ESPIRIT [45] method is a widely used method to improve the accuracy of coil sensitivity estimation by generating sensitivity map using eigenvalue decomposition from fully sampled calibration data.

To further improve the reconstruction performance, methods have been proposed to explore properties like sparsity and low rankness in the signals and use the prior information as a regulariser in the SENSE reconstruction. For example, in compressed sensing reconstruction [46]:

$$\mathbf{u} = \arg\min_{\mathbf{u}} \|\mathrm{DFS}\mathbf{u} - \mathbf{y}\|_2^2 + \|f(\mathbf{u})\|_1 \tag{2.39}$$

here D is the undersampling operator, F is the Fourier transform, f transform the data into a domain (e.g., wavelet) where data is sparse. By changing the regulariser term, it's also possible to incorporate different types of prior information to improve parallel imaging reconstruction.

GRAPPA

Another widely used parallel imaging technique is called GRAPPA. Unlike SENSE, GRAPPA directly fills in the missing k space data of each coil prior to the image combination.

Assuming linear dependence relationships exist between k space samples from different receiver coils within local k space neighbourhoods, GRAPPA method

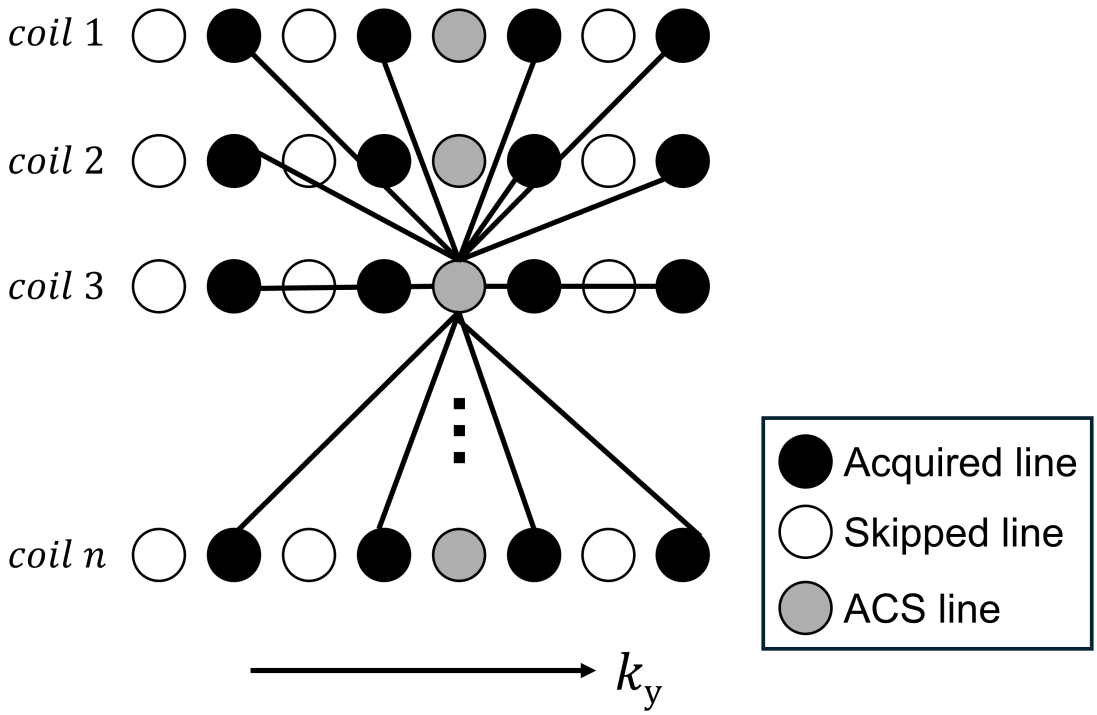

Figure 2.8: Illustration of GRAPPA reconstruction. One missing k space data line of each coil is estimated from a weighted linear combination of data from multiple acquired lines of all coils. The weights are trained based on fully sampled ACS data at k space center

uses data from multiple lines from all coils to fit one missing line in a single coil (as shown in Figure 2.8):

$$S_j(r) = \sum_{l=1}^{L} w(r, j, l)(R_r S_l) \tag{2.40}$$

where $S_j(r)$ is the k space data in coil j at a location r, L is the total coil number, $w(r, j, l)$ refers to the kernel weights for linear combination of acquired data between coil j and l, R_r refers to the selection operator for acquired data in the neighbourhood of location r . The GRAPPA kernel weights are trained based on fully sampled k space center lines, which is also called auto-calibration signal (ACS).

GRAPPA directly fills in missing k space lines by training a kernel for k space interpolation, thus it's not straightforward to add image prior like sparsity or low rank into the original GRAPPA framework. SPIRIT [47] has been proposed to extend GRAPPA as a constrained optimization problem to enable more general and flexible reconstruction.

k space based parallel imaging techniques like GRAPPA avoid direct estimation of sensitivity maps which may improve the reconstruction quality when the sensitivity map estimation is challenging. g-factor maps can also be derived for GRAPPA reconstructions [48].

2.2 Diffusion MRI

Diffusion is a process describing the random walk of molecules in the medium. Diffusion MRI technique probes this movement of water molecules to detect tissue microstructure information. This section gives a brief introduction on basic diffusion MRI principles along with acquisition and reconstruction methods for diffusion MRI.

2.2.1 Diffusion MRI principle

Diffusion in biological tissues

Molecular diffusion is caused by Brownian motion also known as thermal motion, which is the random motion of particles suspended in a medium[49]. The behaviour of the unrestricted diffusion is described by the following equation proposed by Albert Einstein[50]:

$$r_{rms} = \sqrt{2DT} \tag{2.41}$$

where r_{rms} is the root-mean-squared displacement, D is the diffusion coefficient and T is the diffusion time. In biological tissues, diffusion of water molecules is affected by the tissue microstructure including macromolecules, cell membrane and other cellular structures. By measuring the water diffusion property of tissues, complex microstructure properties can be detected, providing valuable information for basic and clinical neuroscience research[51].

Diffusion MRI signal

Diffusion of water molecules leads to dephasing effects in the presence of local field inhomogeneities, which causes extra decay in MRI signals as discovered by Hahn[52].

Carr and Purcell later proposed a direct measurement method of diffusion effects using a spin echo sequence[53]. In that experiment, a constant magnetic field gradient G was turned on during the spin echo sequence, creating a linearly changing magnetic field for different spatial positions. For a spin at location x, assuming it stays at the current position for time τ', a phase shift is generated as:

$$\phi = -\gamma(B_0 + Gx)\tau' \tag{2.42}$$

If the spin does not move, an opposite phase shift, $-\phi$ will be generated due to the refocusing pulse. At the spin echo time, the net phase shift of the spin is related to the spin motion history. So for static spins, the total phase shift is zero. However, if the spin moves to another position due to diffusion, a different phase shift will be generated, leading to de-phasing effects at the echo time. Using this method, the acquired MR spin echo signals are sensitive to the diffusion process of water molecules, allowing for the measurement of diffusion properties. Torrey also proposed a mathematical formulation of diffusion in MRI by adding a diffusion term into the Bloch equation[54]. The most commonly used dMRI preparation sequence is proposed by Stejskal and Tanner in 1965 as shown in Figure 2.9, which is called pulsed gradient spin echo (PGSE)[55]. Instead of using constant gradients, a pair of identical diffusion encoding gradients, each lasting a time duration of δ with a time gap Δ, are applied. The first gradient is applied between the excitation pulse and the refocusing pulses while the other is applied between the refocusing pulse and the spin echo. The first diffusion gradient induces a phase change: $\phi_1 = -\gamma\delta G x_1$ for a spin at position x_1. During the second diffusion gradient, if the spin moves to position x_2, the phase change is $\phi_2 = -\gamma\delta G x_2$. The 180° refocusing pulse reverses the first phase, so the net phase change is $\phi_2 - \phi_1 = -\gamma\delta G(x_2 - x_1)$. This random dephasing effect of spins in water molecules leads to extra signal attenuation, and the following equation can be derived assuming free Gaussian diffusion:

$$\frac{S_b}{S_0} = e^{-bD} = e^{-(\gamma\delta G)^2 D(\Delta - \frac{\delta}{3})} \tag{2.43}$$

where S_b is the diffusion weighted signal,S_0 is the non-diffusion weighted signal, b is called b value which represents the level of the induced sensitivity on diffusion from

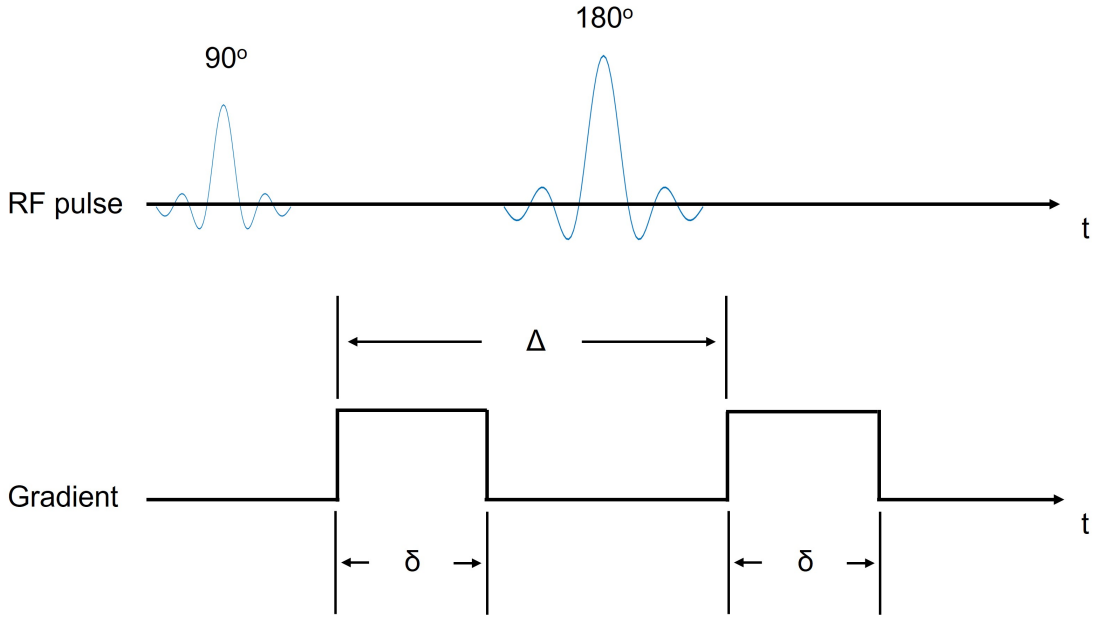

Figure 2.9: Illustration of PGSE sequence. A pair of diffusion encoding gradients of duration δ are applied. The first gradient is applied between the excitation pulse and the refocusing pulse while the other one applied between the refocusing pulse and the spin echo. The time gap between two diffusion gradients is Δ.

diffusion encoding gradients, and D is the diffusion coefficient which represents diffusivity. G can be applied along different directions to detect the diffusivity along that orientation.

Diffusion MRI measurement

With diffusion MRI, it's possible to probe tissue microstructure information by measuring diffusion property. The diffusion coefficient D can be estimated from two dMRI measurements using different b values. For example, a non-diffusion weighted image S_0 (b=0) and a diffusion weighted image S_b (b>0) can be acquired to calculate D:

$$D = \frac{1}{b} ln \frac{S_0}{S_b} \tag{2.44}$$

Since tissue diffusivity is influenced by complicated microstructure properties and other processes such as exchange and magnetization transfer, the calculated D

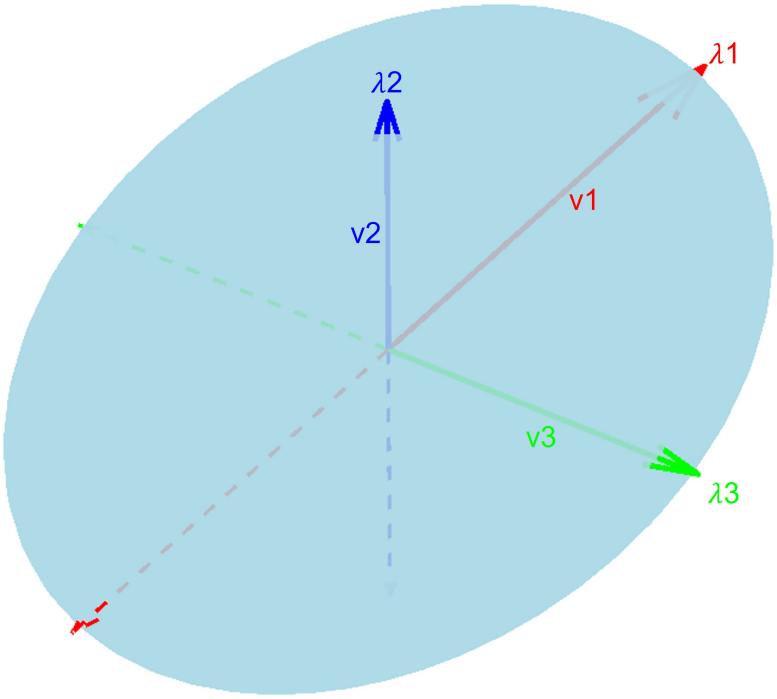

Figure 2.10: Illustration of a DTI tensor. The tensor can be viewed as an ellipsoid determined by the tensor eigenvectors (v_1, v_2, v_3) and eigenvalues $(\lambda_1, \lambda_2, \lambda_3)$.

is called apparent diffusion coefficient (ADC).

The single scalar ADC value only describes the mean isotropic diffusion in media. In practice, the water diffusion varies in different directions due to the complicated geometry of tissue structures, leading to anisotropic diffusion. To describe the directional difference of diffusion, diffusion tensor imaging (DTI) technique [56] was proposed by mapping the diffusivity at each voxel as a tensor characterised as a 3×3 matrix:

$$\mathbf{D} = \begin{bmatrix} D_{xx} & D_{xy} & D_{xz} \\ D_{yx} & D_{yy} & D_{yz} \\ D_{zx} & D_{zy} & D_{zz} \end{bmatrix} \tag{2.45}$$

The diagonal values represent the variance along x,y and z-axis while the off-diagonal values denote the covariances which are symmetric. The tensor can be viewed as an ellipsoid whose shape is determined by the tensor eigenvectors (v_1, v_2, v_3) and eigenvalues $(\lambda_1, \lambda_2, \lambda_3)$ as shown in Figure 2.10.

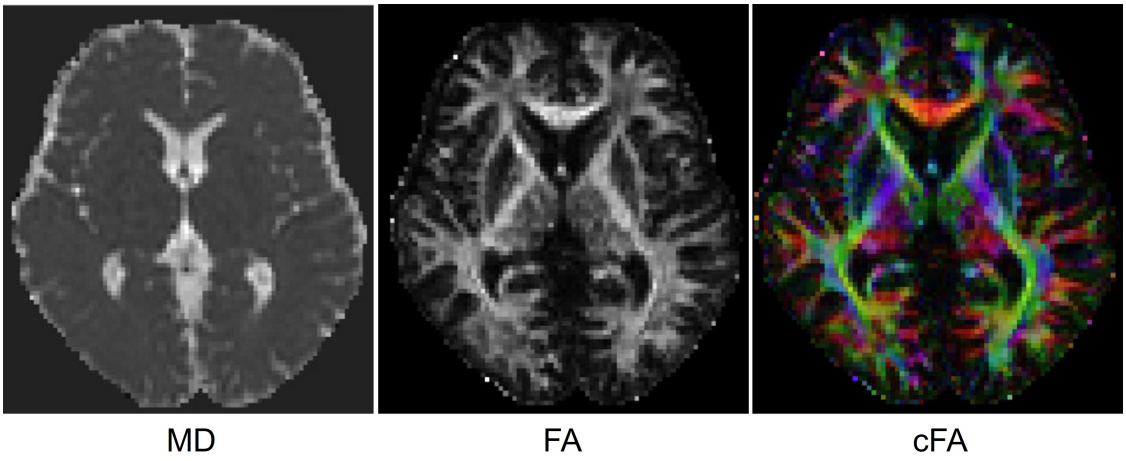

Figure 2.11: Diffusion metrics derived from DTI. Representative MD, FA and colored FA maps are shown.

With DTI model, the diffusion weighted signal can be described as:

$$S_b = S_0 e^{-b[Gx,Gy,Gz]\begin{bmatrix} D_{xx} & D_{xy} & D_{xz} \\ D_{yx} & D_{yy} & D_{yz} \\ D_{zx} & D_{zy} & D_{zz} \end{bmatrix}[Gx,Gy,Gz]'} \tag{2.46}$$

where $[Gx, Gy, Gz]$ is the directional vector for the diffusion encoding gradient.

To fit the DTI model. at least six diffusion weighted images with non-coplanar, noncollinear diffusion encoding directions (b>0) and a non-diffusion weighted image need to be acquired.

After fitting the diffusion tensor, a number of diffusion metrics can be derived. Mean diffusivity (MD), which evaluates the average diffusivity, is an important biomarker (e.g., for stroke) [57]. It can be derived as $MD = \frac{1}{3}\sum_{i=1}^{3}\lambda_i$. Fractional anisotropy (FA), which evaluates the anisotropy of water diffusion, reflects fibre integrity. It can be derived as $FA = \sqrt{1.5}\frac{\sqrt{\sum_{i=1}^{3}(\lambda_i - \lambda_{\text{avg}})^2}}{\sqrt{\sum_{i=1}^{3}\lambda_i^2}}$. FA is sensitive to some pathological conditions such as frontotemporal dementia [58] and inflammatory diseases[59]. Another important metric is V_1, which is the direction of the eigenvector associated with the largest eigenvalue. A principal diffusion direction (PDD) can be defined with V_1 and used for white-matter fiber tractography. Representative MD, FA and colored FA (FA-weighted vector-component in color presentation) maps are shown in Figure 2.11.

DTI is widely used in many applications, yet it has some limitations. DTI model assumes Gaussian diffusion and a single fibre population in one voxel. Thus, it cannot capture non-Gaussian diffusion in biological tissues due, e.g., to restriction. Besides, multiple tissue compartments comprising distinct structures may exist in one voxel, which cannot be differentiated with DTI. To improve the specificity for microstructure information, advanced diffusion modellings like Diffusion Kurtosis Imaging (DKI) [8]have been proposed to reflect the complexity of tissue microstructure by considering non-Gaussian diffusion in the signal model. DKI provides diffusion metrics like mean Kurtosis (MK) which is calculated as the average of the kurtosis along all directions, and a higher MK value represents higher microstructural complexity.

Multi-compartment dMRI models based on certain biophysical assumptions have also been developed. These models assume that the tissue microstructure consists of several compartments and use different parameters to represent specific microstructure features. Models like Standard Model of Diffusion [60], neurite orientation dispersion and density imaging (NODDI) [7]and Soma and Neurite Density MRI (SANDI) [61]have been proposed which provide more detailed microstructure parameters as potential biomarkers for disease detection.

NODDI is one of the most widely used biophysical models for mapping tissue microstructure. NODDI splits the tissue into three compartments: intra-cellular, extra-cellular, and cerebrospinal fluid (CSF), each showing unique diffusion behavior as shown in Figure 2.12. The signal model can be expressed as:

$$A = (1 - f_{\text{iso}})(f_{\text{intra}} A_{\text{intra}} + (1 - f_{\text{intra}}) A_{\text{ec}}) + f_{\text{iso}} A_{\text{iso}} \tag{2.47}$$

where A refers to the full normalized signal, A_{intra} is the normalized intra-cellular signal, A_{ec} is the normalized extra-cellular signal, A_{iso} is the normalized CSF signal, f_{iso} is the fraction for CSF and f_{intra} is the fraction for intra-cellular compartment.

Intra-cellular compartment refers to the space restricted by the membrane of neurites, and is modeled as a set of sticks with highly restricted diffusion perpendicular to neurites and unhindered diffusion $d_{\parallel}$ along them. The sticks

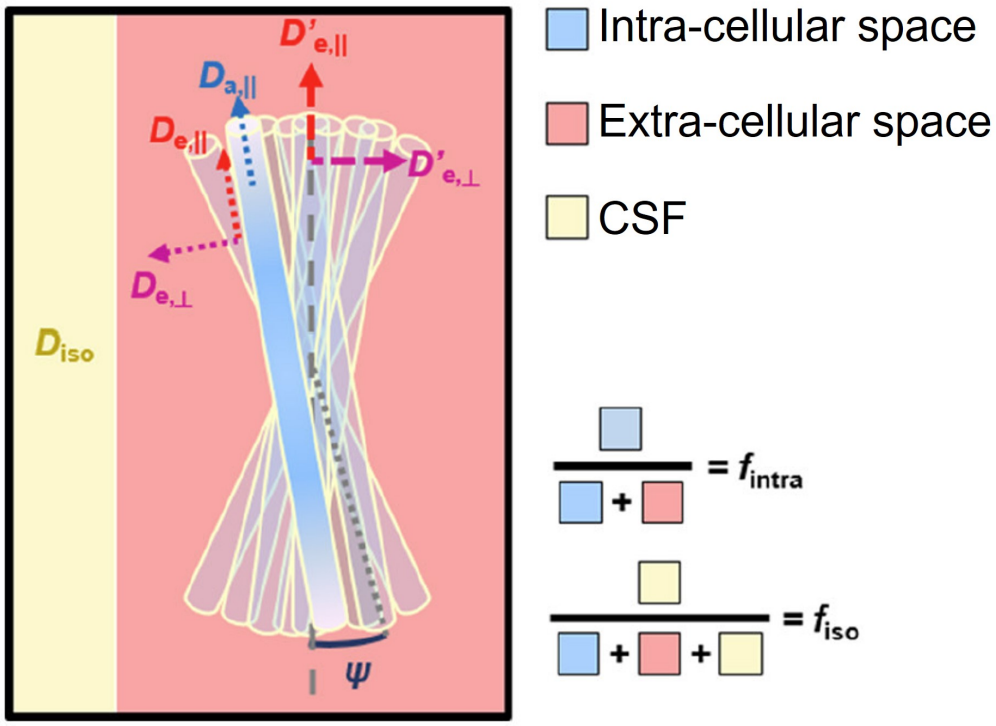

Figure 2.12: Illustration of multi-compartment model like NODDI. The tissues are split into three three compartments: intra-cellular, extra-cellular, and cerebrospinal fluid (CSF), each with different diffusion properties. The figure is reproduced from[9].

have different orientations and the orientation distribution represents the coherence of the structures. Extra-cellular compartment refers to the space around the neurites, consisting of glial cells and cell bodies in gray matter. The nurites hinder the diffusion of water molecules in the external-cellular space but not restricting it, thus anisotropic Gaussian diffusion characterised by parallel diffusivity $d'_{\parallel}$ and perpendicular diffusivity $d'_{\perp}$ is used to model this compartment. The CSF compartment refers to the space with cerebrospinal fluid. Isotropic Gaussian diffusion d_{iso} is used to model it.

Since the multi-compartment models have many parameters and are prone to degeneracy, certain assumptions are usually made with some parameters fixed in the model fitting. For example, NODDI sets the intrinsic free diffusivity $d_{\parallel}$ and isotropic diffusivity d_{iso} to fixed values, and assumes extra-cellular diffusivity $d'_{\parallel}$ and $d'_{\perp}$ are dependent on intra-cellular parameters. In this way, NODDI provides three parameters on tissue microstructure features: f_{intra} which represents the density

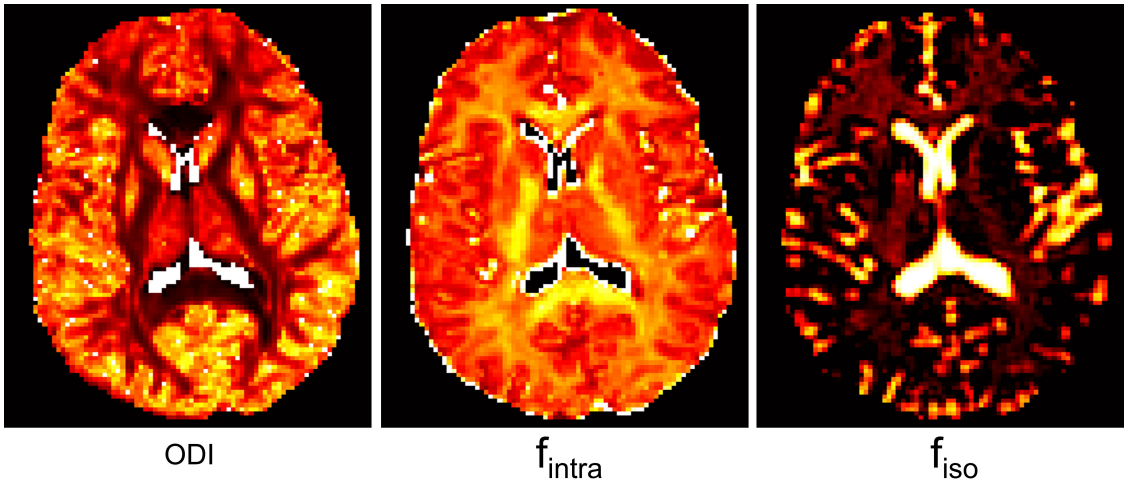

Figure 2.13: Parameter maps derived from NODDI based on the dataset from NODDI Matlab toolbox website http://mig.cs.ucl.ac.uk/index.php?n=Tutorial.NODDImatlab. Representative f_{intra}, f_{iso} and ODI maps are shown.

of axons or dendrites; f_{iso} which refers to the extent of CSF contamination and orientation dispersion index (ODI), which is calculated based on the orientation distribution of the intra-cellular sticks and estimates the orientation coherence of neurites. Representative f_{intra}, f_{iso} and ODI maps are shown in Figure 2.13.

2.2.2 Acquisition and Reconstruction methods for diffusion MRI

2D single-shot EPI (ssh-EPI) is widely used for diffusion MRI acquisition due to its rapid scan time. However, since ssh-EPI acquires 2D plane in one excitation, the echo spacing between adjacent phase encoding lines is long, leading to low bandwidth along phase encoding dimension. Thus, the susceptibility-induced field inhomogeneity causes severe distortion artifacts. Besides, the images suffer from T_2 blurring artifacts due to the long readout, limiting the achievable resolution. Parallel imaging techniques can alleviate this problem by skipping phase encoding lines during acquisition, thus reducing the effective echo spacing between adjacent phase encoding lines, increasing the bandwidth and reducing the artifacts. However, the achievable in-place acceleration factor is limited due to the intrinsic low SNR of dMRI.

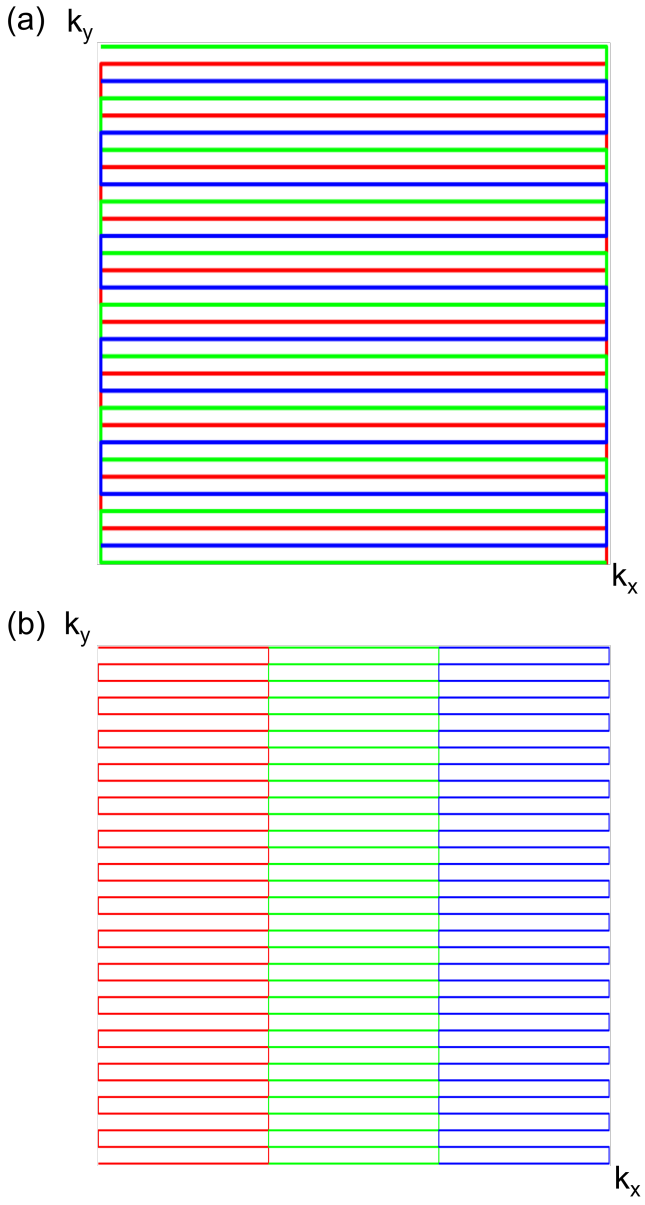

Figure 2.14: Illustration of multi-shot EPI sequence.(a)Interleaved EPI. k space are segmented into three shots along phase encoding dimension.(b)Readout segmented EPI. k space are segmented into three shots along readout encoding dimension.

To overcome the drawbacks of ssh-EPI, multi-shot EPI techniques which separate k space into multiple segments acquired during several acquisitions along phase encoding dimension (interleaved EPI) [62] or readout dimension (readout segmented EPI) [63, 64] as shown in Figure 2.14. In this way, the effective bandwidth of phase encoding dimension is higher and readout is shorter, thus relieving the distortion and blurring artifacts. However, physiological motion like cardiac pulsation leads to phase variations between different k space segments. If directly combining multi-shot data, it will lead to image artifacts. One way to solve this problem is acquiring a navigator which shares similar phase variations with the image echo and then using the phase information for the correction of imaging data. The navigator is commonly a low resolution image acquired using an extra echo [65, 66]or extracted during the imaging acquisition [67–69]. Recently, reconstruction methods like multiplexed sensitivity-encoding (MUSE)[70] and Multi-shot sensitivity-encoded diffusion data recovery using structured low-rank matrix completion (MUSSELS)[71] have been proposed to calculate the phase variations without acquiring navigators. MUSE reconstructs data from each shot and then estimates a smooth phase map from the reconstructed images of each shot. Finally, it uses the phase map as extra encoding information to solve a joint multi-shot data reconstruction problem with SENSE. Unlike image-based MUSE method, MUSSELS explores the annihilating relations for multi-shot data and corrects for the multi-shot phase variation by constructing a structured low-rank matrix from k space data without the need of explicitly estimating the phase map. Machine learning and deep learning based methods have also been incorporated to improve the MUSSELS results[72].

Though multi-shot EPI enables higher resolution dMRI acquisition, the scan time is increased proportionally to the number of shots, which is not practical, particularly when combined with higher angular resolution dMRI acquisition. To further accelerate the dMRI acquisition, simultaneous multislice echo planar imaging (SMS EPI) methods were proposed[13]. In SMS EPI, multiple slices are excited simultaneously using multiband RF pulses and acquired at the same time, thus reducing the scan time by the SMS acceleration factor (shown in Figure 2.15(a)). To

separate the signals from different slices, coil sensitivity information along slice-axis is needed. However, usually the imaging FOV along the slice direction is smaller than along the phase encoding, which leads to more similar coil sensitivity and larger g factor at the same acceleration factor compared to in-plane under-sampling. When the SMS acceleration factor is high or when SMS is combined with in-plane acceleration, it's challenging to correct for the aliasing artifacts. To solve this problem, Blipped-controlled aliasing in parallel imaging (Blipped-CAIPI) method is proposed[14], which modulates the phase shifts of each phase encoding line by adding gradient blips to create different image shifts for different slices within one band (shown in Figure 2.15(b)). In this way, the g-factor is significantly reduced. With blipped-CAIPI method, it's possible to achieve SMS factor of 2-3 on normal MRI scanners for dMRI acquisition. SMS data can be reconstructed using SENSE method by adapting the sensitivity maps. GRAPPA-based methods have also been proposed for SMS reconstruction including SENSE-GRAPPA which rearranges the calibration data to an extended FOV to unaliase the images; slice-GRAPPA which trains slice specific GRAPPA kernels to entangle the overlapping slices followed by 1D GRAPPA for phase encoding undersampling and 3D GRAPPA which uses a 3D kernel to directly reconstruct the 3D data[15]. To further improve acceleration performance, regularized reconstruction methods have also been employed, including low rank matrix completion and total variation to constrain the reconstruction for improved image quality[18, 19].

Apart from k space data properties, q space relations have also been explored to help the reconstruction of k space undersampled data. These methods use q space information as priors for the constrained kspace reconstruction such as applying compressed sensing exploring the sparsity between q space data [21, 22]; employing SNR-efficient spatial smoothing which leverages the structural similarity between dMRI images[23]; utilizing spherical ridgelets to exploits q-space data redundancy information [24] and using deep learning network to pre-learn a signal manifold prior from the diffusion measurement based on a biophysical models [25–27]. These methods have been demonstrated for both multi-shot EPI and SMS-EPI.

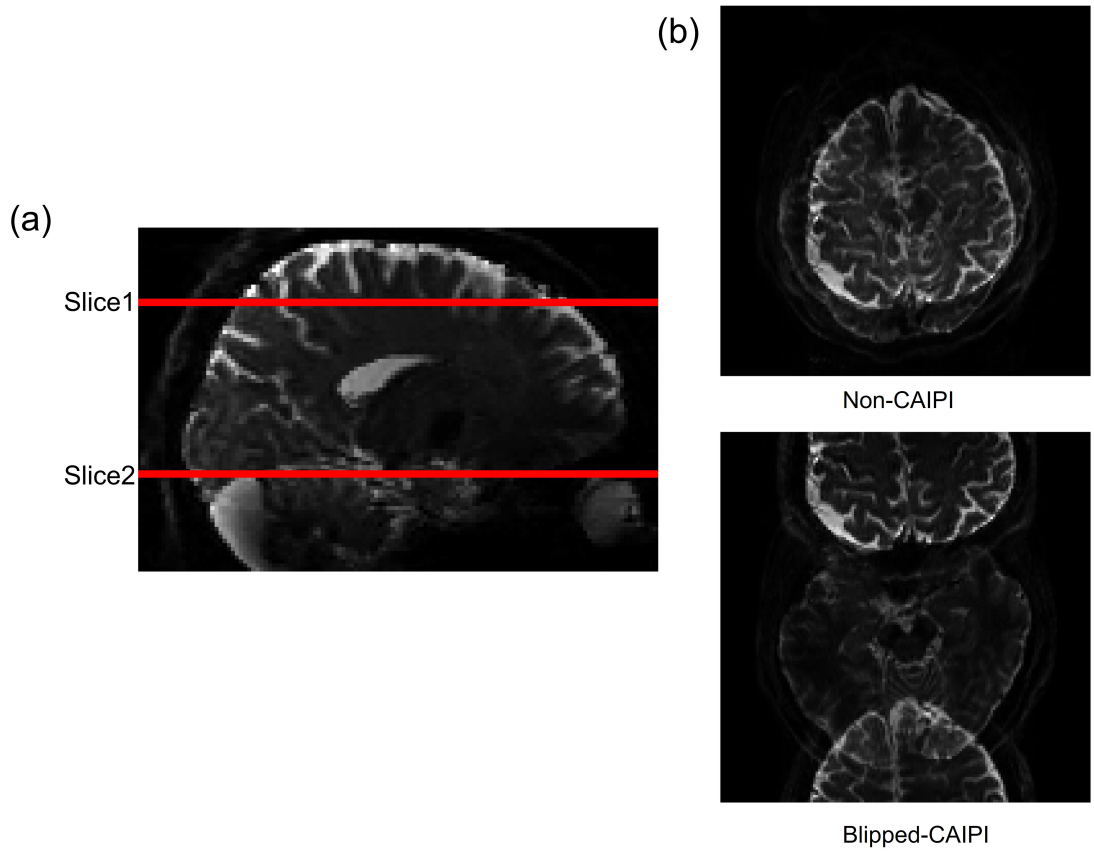

Figure 2.15: Illustration of SMS EPI sequence.(a)Two slices are exited at the same time.(b) Without blipped-CAIPI, two excited slices overlap with each other while blipped-CAIPI leads to shift between slices.

A recent work in our group uses Gaussian Process to exploit the q space data intrinsic smoothness without making signal model assumptions and achieve good performance under high acceleration factor for single-shell dMRI acquisition[73].

Non-cartesian imaging techniques have also been used for dMRI acquisition. Spiral acquisition has a higher spatial encoding efficiency by efficiently using both gradients to traverse k-space much faster and provides higher SNR due to its shorter TE [74–76]. However, the spiral acquisition is sensitive to B0 field inhomogeneity which leads to blurring artifacts in the obtained images. Single-shot spiral, due to its long readout duration, is severely affected and the achievable resolution is limited. Similarly to EPI, multi-shot spiral techniques have been developed with various sampling strategies to improve the achievable resolution by shortening the readout time[77, 78]. Like multi-shot EPI, multi-shot spiral acquisition also suffers from

shot-to-shot phase variation, Navigator-based and navigator-free methods have been developed to correct for the variation. For example, Variable density spirals (VDS) samples the center of k space data densely[79], which provides navigator information. Methods like MUSE and POCS-ICE can be used to correct for uniform density spiral (UDS)[80]. Deblurring algorithms have also been developed to mitigate the blurring caused by static B_0 off-resonance[81]. Spiral acquisition has the potential to achieve high resolution dMRI with the higher SNR efficiency, though efforts are still needed to further correct for blurring artifacts[82].

Apart from 2D acquisition, 3D acquisition techniques are also used for dMRI acquisition. By adding a second phase encoding gradient along the slice selection direction, it's possible to form a 3D k space and use Fourier transform to resolve thin slices. Usually, multi-shot EPI is used to cover the 3D k space. However, multi-shot EPI is sensitive to motion-induced phase and it's difficult to accurately estimate phase information varying in 3D space while a 3D navigator acquisition is time-consuming. Besides, to maximise the scan efficiency, 3D single-slab acquisition needs to operate with a very short TR, e.g., 100-200ms, which is associated with very low SNR efficiency.

Thus, multi-slab acquisitions have been proposed to solve these problems[83–87]. The imaging volume is divided into multiple thin slabs and excited individually during each repetition. Within each slab, the motion induced phase along the slice direction typically varies very slowly, representing a constant phase offset. Therefore, a 2D phase navigator is usually sufficient for correcting motion induced phase in 3D multi-slab acquisition and providing a high-quality image. Besides, by changing the number of slabs, it's possible to obtain a short TR for optimal SNR efficiency, which facilitates high resolution dMRI acquisition. Generalized slice dithered enhanced resolution: Simultaneous multislice (gSlider-SMS) is another technique aiming to achieve high resolution multi-slab acquisition. This technique excites multiple thin slabs together and then uses blipped-CAIPI to reconstruct each slab.A novel slab RF encoding is used to encode different partitions in each slab for reconstruction to achieve high resolution in the partition direction[88].

2.2.3 Gaussian Process for dMRI reconstruction

Gaussian processes(GP) describes the joint distribution of infinite-dimensional random variables, such that any finite collection of random variables follows a multivariate Gaussian distribution. Thus, it can be viewed as an infinite-dimensional extension to multivariate Gaussian distributions. Instead of using a mean vector and a covariance matrix as in multivariate Gaussian distribution, GP models a distribution over functions within a continuous domain by using a mean function and a covariance function to describe the data relations[89]. GP is a data-driven model that, rather than fitting a single function, produces an infinite set of functions that all describe the data. Specifically, each function fits the data exactly at the measured points and the collective set of functions follow a multi-variate Gaussian distribution away from the measured points.

With known mean function and covariance function, GP can predict unseen data from a training dataset or noisy observation dataset, which can provide a prior distribution of dMRI signals. Considering acquired noisy dMRI signal y from N diffusion volumes and the target clean signal x, assuming x follows the multivariate Gaussian distribution:

$$\mathbf{x} \sim N\left(\mu, \mathbf{\Sigma}\right) \tag{2.48}$$

based on Bayes theorem, a posterior distribution can be calculated by updating the prior distribution with the likelihood from the data.

$$p(x|y) = \frac{p(y|x)p(x)}{p(y)} \tag{2.49}$$

assuming y contains Gaussian noise with variance σ^2,$p(y|x)$ can be described as:

$$p(y|x) \sim N\left(\mathbf{x}, \boldsymbol{\sigma^2}\mathbf{I}\right) \tag{2.50}$$

By the Maximum A Posteriori (MAP) probability, an estimate of q space signal can be obtained. With this formulation, it's possible to reconstruct dMRI images based on Gaussian Process estimated reconstruction.

Note that Gaussian Process offers a non-parametric way with uncertainty mapping to describe the distribution of data, thus doesn't rely on any prior assumption on the distribution patterns, which introduces less bias in the reconstructed dMRI data compared to model-based reconstruction which assumes the data follow certain signal models. Besides, Gaussian Process estimated the data with Bayes theorem, thus no manual tuning of GP prior weighting is needed in the MAP optimisation. In conclusion, GP offers a flexible data-driven technique to estimate dMRI signals, which causes less bias in dMRI reconstruction.

3

Accelerated multi-shell diffusion MRI with Gaussian process estimated reconstruction of multi-band imaging

Contents

This chapter describes a robust reconstruction method we propose exploiting sharing information across shells to increase the acquisition speed of multi-shell diffusion MRI, enabling rapid tissue microstructure mapping. Gaussian Process can exploit the q space smoothness in a data-driven way and provide q space

signal estimation based on the signals from a q space neighbourhood. The Diffusion Acceleration with Gaussian process Estimated Reconstruction (DAGER) method[27] uses the signal estimation from Gaussian processes as a prior in a joint k-q reconstruction framework and improves image quality under high acceleration factors compared to conventional (k-only) reconstruction. In this work, we extend the DAGER method to multi-shell condition by introducing a multi-shell covariance function and correcting for Rician noise distribution in magnitude data when fitting the Gaussian process model. The method was evaluated with both simulation and in vivo data. Simulation and in-vivo results demonstrate that the proposed method can significantly improve the image quality of reconstructed multi-shell dMRI data with high acceleration both in-plane and slice-wise, achieving a total acceleration factor of 12. The improvement of image quality allows for more robust diffusion model fitting compared to conventional reconstruction methods, enabling advanced multi-shell diffusion analysis within much shorter scan time. This chapter is based on a peer-reviewed journal paper we published in Magnetic Resonance in Medicine[90].

3.1 Introduction

Diffusion-weighted MRI (dMRI) is a non-invasive technique that can characterise tissue microstructure and delineate structural connectivity by measuring the movement of water within biological tissues, making it an essential tool for basic and clinical neuroscience research [1, 2, 10, 51, 91]. The acquisition time of a dMRI scan is determined by the number of diffusion directions (i.e., q space samples) and the scan time per direction (acquiring k space). Due to the desirability of both high spatial and angular resolution (k- and q space, respectively), image acceleration has become critical to dMRI acquisition. Advanced diffusion MRI models (e.g., DKI, NODDI, CHARMED [7, 8, 92]) provide higher specificity about tissue microstructure compared to simple models (e.g., DTI). However, fitting these advanced models requires acquisitions of a large number of q space samples over many diffusion directions and across multiple b shells, leading to long scan times [5, 6, 93]. dMRI signal is typically acquired with 2D single-shot EPI due to its

rapid acquisition speed, for which the scan time of each q space sample is coupled with the number of slices. Consequently, achieving higher resolution (thinner slices) with the same brain coverage results in longer scan time per direction. When the total scan time is limited, this creates a fundamental trade-off between spatial resolution, anatomical coverage, and model specificity.

Various acquisition and reconstruction methods have been developed to speed up dMRI scans and mitigate this trade-off. Conventional parallel imaging methods such as SENSE and GRAPPA [11, 12] have been applied to accelerate dMRI by under-sampling in k space. However, as more than 50% of dMRI sequence timing is dedicated to diffusion sensitizing gradients rather than readout, in-plane under-sampling is not as effective in reducing scan time. A major advance in dMRI acceleration is Simultaneous multislice (SMS) imaging [13], which reduces the scan time by acquiring multiple slices at the same time and thus effectively sharing the diffusion sensitizing gradients across slices. With blipped-CAIPI sampling [14] SMS allows 2-3X slice acceleration for dMRI without significantly increased g-factor SNR penalties. However, due to the intrinsically low SNR of dMRI data, achieving high slice acceleration (i.e., 4 or higher) is still challenging. This is particularly problematic when combined with in-plane accelerations because the two approaches compete for the use of coil sensitivity information, leading to a highly ill-conditioned reconstruction problem. Methods enforcing some prior information in the spatial domain can potentially be employed to alleviate the problem [94–98]. But the slice acceleration achievable in dMRI is still highly limited compared to other MRI modalities. Using large cohort studies as an example, the UK Biobank [16] and Human Connectome Project [17] use a slice acceleration factor of 2 or 3 for dMRI, but an acceleration factor of up to 8 for functional MRI.

Acceleration methods have also been developed to reduce the number of required q space directions. To exploit the data redundancy, different methods like compressed sensing [99, 100] and dictionary learning [101] have been used to improve the estimation of diffusion metrics from a reduced number of q space samples. Deep

learning-based methods have been also developed to improve the accuracy of diffusion metrics estimation from a reduced number of diffusion directions [102–105].

Finally, joint k-q acceleration methods have been proposed to leverage the information redundancy in both k space and q space simultaneously to achieve a higher acceleration factor[21–27, 73] by jointly reconstructing k space data at different q space locations. Diffusion Acceleration with Gaussian process Estimated Reconstruction (DAGER) [27] is a model-independent joint k-q reconstruction method that exploits the smoothness in q space to interpolate signals in a data-driven way, which enables high acceleration factor. DAGER uses Gaussian-Processes (GPs) to model dMRI signals, an approach that has been successfully applied to correct for subject motion and eddy current distortions [106]. Whereas some other joint k-q reconstruction methods use priors in the context of a specific signal model, DAGER does not make assumptions about the form of dMRI signal. It also doesn't impose spatial-smoothing priors in the reconstruction but only data-driven q space smoothness fitted by Gaussian Processes. Besides, DAGER uses a Bayesian framework to automatically estimate the reconstruction hyperparameters from the data. This avoids the manual tuning of regularization parameters.

However, the original DAGER method only exploits information redundancy between different diffusion directions within a single shell in q space (i.e., a single b-value). For multi-shell dMRI acquisitions, DAGER currently reconstructs each shell independently, which may require a large number of diffusion directions. Since signal also varies smoothly with q space radius in addition to angle, exploiting information across shells in the reconstruction can reduce the needed number of diffusion directions for each shell and improve the image quality particularly for outer q-shells due to their lower SNR. In this work, we propose to extend the GP model used in the original DAGER to enable information sharing between shells to improve reconstruction at high acceleration for multi-shell acquisition. In addition, the original DAGER framework assumes Gaussian noise, which may underestimate the noise variance given that magnitude data (with a Rician distribution) is used in GP fitting. This assumption is particularly problematic for low-SNR data, such as

at high b-values. We integrate a variance-stabilizing transformation [107, 108] to improve the accuracy of Gaussian Process fitting under Rician noise conditions. A data-driven multi-shell diffusion reconstruction method is developed that integrates these two extensions of DAGER. The method, which we name multi-shell DAGER (ms-DAGER), is evaluated using numerical simulations and in vivo scans. We demonstrate robust image quality and microstructure model fitting at 1.25-1.5 mm resolution using high multi-slice and in-plane accelerations (SMS = 4 × R = 3).

3.2 Theory

3.2.1 GP modelling of dMRI signal

A Gaussian process (GP) is a data-driven model that, rather than fitting a single function, produces an infinite set of functions that all describe the data. Specifically, each function fits the data exactly at the measured points and the collective set of functions follow a multi-variate Gaussian distribution away from the measured points [89]. dMRI signals exhibit smoothness in q space as shown in Figure 3.1.(a) – that is, they have a covariance structure – that can be described using a multi-variate Gaussian. GP models are able to capture this structure in a way that enables the prediction of the mean and variance of the dMRI signal at unseen q space locations. With GP modelling, we assume that dMRI signals $\mathbf{u}$ at a set of $q = [q_1, q_2, ..., q_{N_d}]$ follows a multivariate Gaussian distribution:

$$\mathbf{u} \sim N(\mu, \mathbf{\Sigma}) \tag{3.1}$$

which is determined by a mean vector μ (N_d×1) and a covariance matrix $\mathbf{\Sigma}$ (N_d×N_d). Here, $\mathbf{u}$ represents dMRI signals from a single voxel for all dMRI directions and N_d is the number of dMRI directions.

The GP covariance matrix $\mathbf{\Sigma}$ in Eq.3.1 is parametrized using a covariance function C. For multi-shell dMRI acquisition consisting of multiple b values (and directions), a valid covariance function between two q space locations (q,q') can be defined as:

$$C\left(q, q^{'}\right) = C_\theta\left(\theta; a\right) C_b\left(b, b^{'}; l\right) \tag{3.2}$$

where q and q' refer to q space locations at two b shells (b and b') with an angular distance of θ, C_θ is a spherical covariance function describing relations between dMRI data within a shell and C_b is a squared-exponential function describing relations of dMRI data between shells [109]:

$$C_\theta(\theta; a) = \begin{cases} 1 - \frac{3\theta}{2a} + \frac{\theta^3}{2a^3} & \text{if } \theta \leq a \\ 0 & \text{if } \theta > a \end{cases} \tag{3.3}$$

$$C_b(b, b'; l) = \exp\left(-\frac{(\log b - \log b')^2}{2l^2}\right) \tag{3.4}$$

Where a is a hyperparameter controlling signal smoothness within shell and serves as an angular threshold, l is a hyperparameter controlling signal smoothness across shells.

Because dMRI measurements reflect both true signal variation and noise, two more hyperparameters are included in the covariance function to represent noise σ_n^2 and signal variation λ. The covariance matrix can be calculated as:

$$\mathbf{\Sigma_y} = \mathbf{\Sigma} + \sigma_n^2 \mathbf{I} \tag{3.5}$$

$$\mathbf{\Sigma_{i,j}} = \lambda C(q_i, q_j) \tag{3.6}$$

where $\mathbf{\Sigma_y}$ denotes the covariance matrix for noisy dMRI data $\mathbf{y}$, and $\mathbf{I}$ is an identity matrix. In multi-shell condition, while the underlying noise level should be similar for different shells, the estimation of σ_n^2 from magnitude images is affected by Rician noise bias, which depends on signal intensity and thus varies between shells. To account for this effect, unique σ_n^2 values are estimated for different shells.

3.2.2 GP estimation of dMRI signals

GP modelling allows us to construct a prior distribution of dMRI signals in q space. Based on Bayes theorem, a posterior distribution can be calculated by updating the prior distribution with the likelihood from the data. The Maximum A Posteriori (MAP) probability provides an estimate of q space signal based on this posterior distribution [110]:

$$\overline{\mathbf{u}} = \arg\min_{\mathbf{u}} \frac{1}{2\sigma_n^2} \|\mathbf{u} - \mathbf{y}\|_2^2 + \frac{1}{2}(\mathbf{u} - \mu)^H \mathbf{\Sigma^{-1}} (\mathbf{u} - \mu) \tag{3.7}$$

Where $\overline{\mathbf{u}}$ is the MAP point estimate, $\mathbf{y}$ is the noisy data.

3.2.3 Multi-shell-DAGER reconstruction

Inspired by the use of GPs in dMRI pre-processing, DAGER incorporates GPs into the earlier step of image reconstruction and extends it to multi-coil acquisitions. DAGER uses the GP-estimated dMRI signal as a prior and solves the following reconstruction problem:

$$\mathbf{u} = \arg\min_{\mathbf{u}} \left(\frac{1}{2\sigma_k^2} \|\mathbf{\Omega F S u} - \mathbf{d}\|_2^2 + \frac{1}{2} (\mathbf{P}^H \mathbf{u} - \boldsymbol{\mu})^H (\mathbf{\Sigma} \otimes I_N)^{-1} (\mathbf{P}^H \mathbf{u} - \boldsymbol{\mu}) \right) \quad (3.8)$$

where $\mathbf{u}$ is the unknown image, Ω refers to undersampling operator, F refers to Fourier transform, S refers to coil sensitivity encoding, σ_k^2 is the noise variance in the k space data, which can be calculated from σ_n^2 as in [27], d is the acquired k space signal, μ is the mean value of GP prediction, $\mathbf{\Sigma}$ is the GP covariance matrix and N is the number of voxels, H is the conjugate operation and $\otimes$ is Kronecker product. P represents the motion induced phase error, which is different between diffusion directions. DAGER iteratively solves hyperparameter estimation and image reconstruction[27]. In this work, we extend DAGER to incorporate multi-shell information sharing in the reconstruction framework, resulting in ms-DAGER. The original single-shell covariance matrix $\mathbf{\Sigma}$ in Eq.3.8 is replaced with the multi-shell covariance matrix $\mathbf{\Sigma}$ defined in Eq.3.2.

3.2.4 Correction for Rician noise fitting

The Gaussian Process assumes Gaussian noise in the data. However, in practice GP fitting is performed on magnitude images, where noise follows a Rician distribution. In scenarios where the noise level is high, the noise variance σ_k^2 in Eq.3.8 estimated from GP model can deviate significantly from the true noise variance, impacting the accuracy of GP fitting.

To mitigate this issue, we propose to incorporate the noise estimation from the variance-stabilizing transformation (VST) method to improve the noise estimation accuracy. The variance-stabilizing transformation defines a nonlinear function $f(z)$ to map the Rician random variable z to new values with variances that are independent of signal intensity (stabilized). The nonlinear mapping function $f(z)$

and noise estimation are jointly optimised by minimizing a loss function consisting of a main term controlling the accuracy of the transformation (variance becomes independent of signal intensity) along with penalty terms to enhance the robustness of the estimation process [107]. During the optimisation of $f(z)$, an estimation of noise variance $\sigma_n^{'2}$ for the Rician noise can be derived. For the first iteration of the reconstruction, we applied VST to get $\sigma_n^{'2}$ from the initial SENSE reconstruction. Then $\sigma_n^{'2}$ was used as an initial guess for the GP hyperparameter optimisation to get noise variance in GP model σ_n^2. Noise variance in the k space data σ_k^2 was derived from σ_n^2 as in [107] and used in Eq.3.8 as the GP prior weighting for the optimisation. For later iterations, we applied VST to calculate $\sigma_n^{'2}$ from the reconstruction result of the previous iteration and then repeated the above steps.

3.3 Method

3.3.1 Simulation

We first evaluated the performance of ms-DAGER using realistic simulations based on HCP dMRI data consisting of 3 shells (1000, 2000 and 3000 s/mm^2) and 270 directions[111]. The data was fitted with the ball-and-stick model which was used to generate simulation data with the same model[112]. A 100-direction dataset was generated with 50 b=1000s/mm^2 and 50 b=2000s/mm^2 directions uniformly sampled in q space, which was used as a reference. Datasets with 36 and 64 directions were simulated by uniformly undersampling the 100-direction dataset. For ms-DAGER reconstruction, we optimised k-q undersampling using a graph model [113] that aims for each q space neighbourhood (across directions and shells) to have highly diverse k space undersampling patterns. Figure 3.1(b) shows the k space sampling using in-plane R = 2 and SMS = 3 (total under-sampling factor 6) as an example. Here each colour refers to a different sampling pattern. In SMS-EPI acquisition, multiple slices are excited simultaneously. To reduce noise amplification at higher slice acceleration factors, blipped-CAIPI technique is used by applying blipped gradient on the slice direction in addition to the phase-encoding gradient during the EPI readout, creating a FOV shift between slices.

SMS-EPI with blipped-CAIPI can be equivalently formulated as a 3D encoding problem of all simultaneously excited slices using CAIPRIHNA[114], where gradient blips along the slice direction impose a phase variation akin to phase encoding along kz [115, 116] ('partition encoding') in 3D imaging. The k_z encoding step, $\Delta k_z = \frac{1}{FOV_{zSMS}}$, where FOV_{zSMS} is calculated as the SMS factor times the distance between two adjacent slices. In Figure 3.1(b), a 3D k space was used to illustrate our under-sampling strategy, where each colour corresponds to a unique CAIPRIHNA under-sampling sampling pattern with in-plane R = 2, SMS = 3 and an inter-slice image shift of $FOV_y/3$. For different diffusion directions within a local q space neighbourhood, different sampling patterns were used by adding different shifts along k_y and k_z directions. This allows diverse k space sampling patterns for each local q space neighbourhood. Undersampled multi-channel datasets were simulated with sensitivity maps from an 8-channel head coil and a total undersampling factor of 12 (in-plane R = 3 and through-plane SMS = 4) with added noise. This simulation intends to deliberately test ms-DAGER's ability to exceed the theoretical limits by using a total acceleration that exceeds coil count.

To evaluate potential angular smoothing effects introduced by the Gaussian Process prior, we calculated the covariance between directions as a function of angular distance. We also calculated the point-by-point intensity ratio between direction-averaged images of different shells to evaluate the cross-shell smoothness.

3.3.2 In vivo experiment

Seven subjects were scanned on a Siemens 7T scanner. Informed consent in accordance with local ethics was obtained before each scan. A 2D spin-echo dMRI sequence was modified to include SMS acquisition and blipped-CAIPI encoding with highly variable k space undersampling patterns for each q space neighbourhood. A 32-channel coil was used with coil sensitivities measured using a GRE sequence. The dMRI data were acquired with in-plane acceleration R = 3 and multi-slice acceleration SMS = 4 (total acceleration factor = 12). Three subjects were scanned with 1.25 mm isotropic resolution (TE = 70 ms) and four were scanned with 1.5

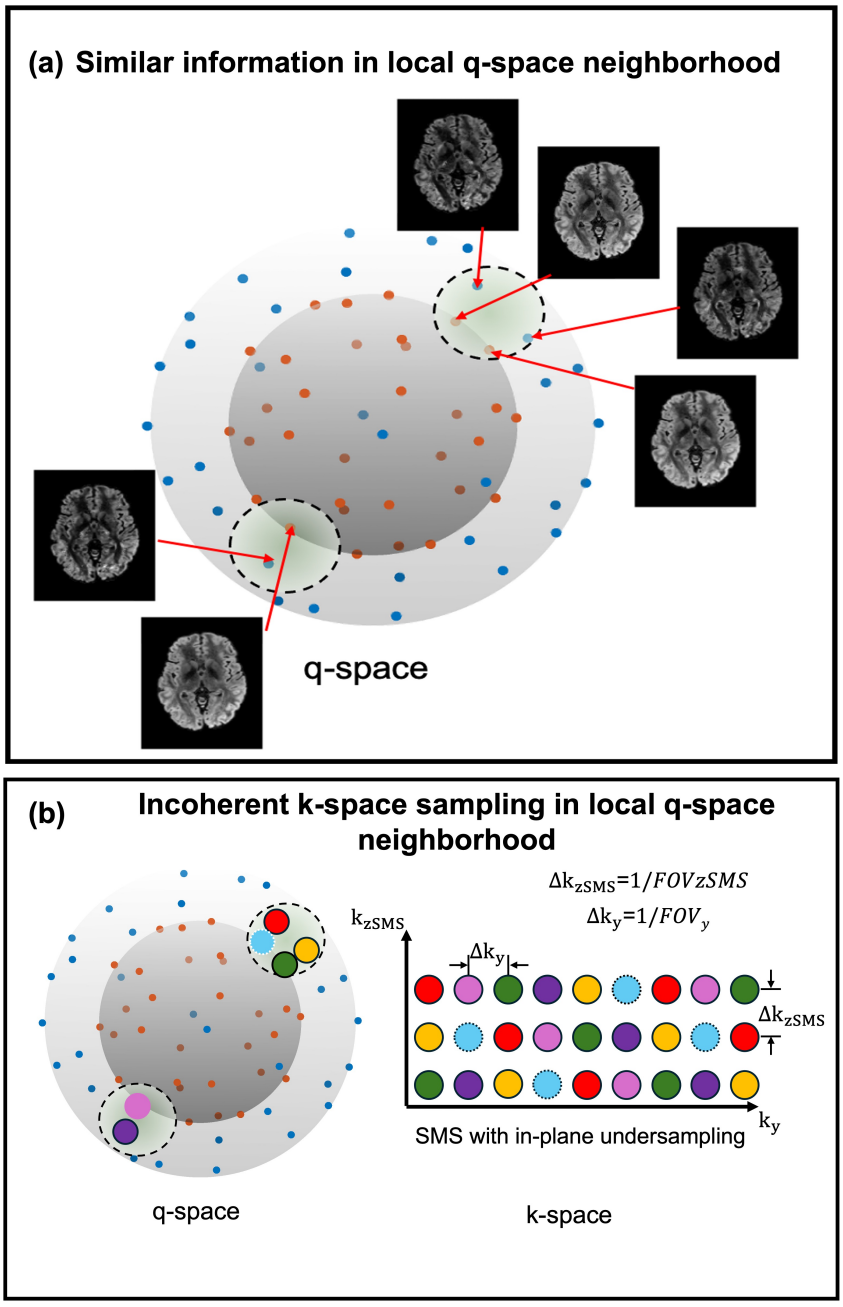

Figure 3.1: ms-DAGER reconstruction utilizes local smoothness in q-space. a) dMRI images that are near to each other in q-space within a shell and across shells have sharable information, which can be leveraged in a joint k-q reconstruction for accelerated dMRI. Antipodal symmetry property can be incorporated as q space points at the opposite sides of the sphere share the same diffusion contrast. Blue and orange points refer to samples on different q space shells. b) To enhance the joint k-q reconstruction, q space neighborhood (across directions and shells) is designed to have highly diverse k space undersampling patterns. Each color corresponds to a different sampling pattern in k-space. Here, SMS = 3 (acquired with blipped-CAIPI) with in plane R = 2 is used for illustration.

mm isotropic resolution (TE = 68 ms). Other parameters: TR = 3500 ms, partial Fourier 6/8, 84 slices over 21 multi-slice sets.

The protocols were designed to evaluate the performance of ms-DAGER with a reduced number of diffusion directions (with fixed resolution) and different resolutions (with fixed diffusion directions). For the 1.5mm protocol, we acquired three dMRI datasets with 100, 66 and 36 diffusion directions staggered across two shells (b = $1000s/mm^2$ and $2000s/mm^2$) using optimised k-q sampling patterns and equal number of directions for each shell (50 b = $1000s/mm^2$ and 50 b = $2000s/mm^2$, etc.). The q space points for the 66-direction dataset were obtained by optimally undersampling those of 100-direction dataset, while the q space points of the 36-direction dataset were separately designed for uniform angular coverage. The 1.25mm dataset was acquired with the same q space sampling except for omitting the 36 direction set. A 3-shell in vivo dataset at 1.5mm resolution was also acquired for subject 1 with 40 diffusion directions for each b-shells across b = 1000/2000/3000 s/mm^2 to evaluate the performance for more shells (same parameters as above except TE = 78ms). Seven b = 0 volumes were also acquired, including one volume acquired with reversed phase-encoding direction for distortion correction with the FSL's topup [117, 118].

For each subject, we acquired a high-SNR reference consisting of two repetitions of non-slice-accelerated ("single-band") data with matched TR (covering 21 slices to reduce scan time) and in-plane acceleration. For one subject, a whole-brain single-band reference image was also acquired with one repetition.

To compare our method with more commonly used accelerations, we acquired SMS =2 whole-brain data, along with our proposed SMS =4 whole-brain data for comparison, single band data was also acquired as reference. To compare ms-DAGER method with the previous single-shell DAGER (ss-DAGER), an additional set of data were acquired from one subject using separately optimised k space sampling patterns for each shell (which is optimal for single-shell DAGER) for a fair comparison with ms-DAGER using the same q space sampling pattern. The details of the protocols are listed in Figure 3.2.

	Subj. ID	TE (ms)	TR (ms)	Resolution (mm^2)	MB	PAT	Partial Fourier	b value ($s \cdot mm^{-2}$)	Diffusion directions	Ave	Scan time
1.5 mm protocol	Subj. 1 2 3 4	68	3500	1.5×1.5×1.5	4	3	6/8	1000,2000	100/66/36	1	350s/231s/126s
		68	3500	1.5×1.5×1.5	1	3	6/8	1000,2000	100	2	700s
		68	5000	1.5×1.5×1.5	2	3	6/8	1000,2000	66	1	330s
		68	3500	1.5×1.5×1.5	1	3	6/8	0	1 (AP)	6	21s× 4(bands)
		68	3500	1.5×1.5×1.5	1	3	6/8	0	1 (PA)	1	3.5s× 4(bands)
	Subj. 3	68	3500	1.5×1.5×1.5	1	3	6/8	1000,2000	66	1	231s× 4(bands)
	Subj. 1	78	3500	1.5×1.5×1.5	4	3	6/8	1000,2000,3000	120	1	420s
1.25 mm protocol	Subj. 5 6 7	70	3500	1.25×1.25×1.25	4	3	6/8	1000,2000	100/66	1	350s/231s
		70	3500	1.25×1.25×1.25	1	3	6/8	1000,2000	100	2	700s
		70	5000	1.25×1.25×1.25	2	3	6/8	1000,2000	66	1	330s
		70	3500	1.25×1.25×1.25	1	3	6/8	0	1(AP)	6	21s× 4(bands)
		70	3500	1.25×1.25×1.25	1	3	6/8	0	1(PA)	1	3.5s× 4(bands)

Figure 3.2: In vivo acquisition protocols.

3.3.3 Reconstruction implementation

The motion induced phase error P in Eq.3.8 was estimated using a method similar to MUSE [70]. For each diffusion direction, an initial SENSE reconstruction is performed and a smooth phase map is then estimated from the k space center.

The dMRI signal is identical at opposite points on a q space sphere, a property known as "antipodal symmetry". We leverage this property during ss-DAGER and ms-DAGER reconstruction by extending the local neighbourhood around each direction to include the region around its antipodal reflection, as shown in Figure 3.1(b).

Since brain white matter and gray matter tissues have different diffusivity property, the hyperparameters were separately updated for these two types of tissues using gray matter and white matter masks generated using FA and MD thresholds (FA $>$ 0.2,MD $>$ 0.0003 mm^2/s for white matter regions; FA $<$ 0.2, MD $<$ 0.0009 mm^2/s for gray matter regions). In other parts inside the brain, we used the same hyperparameters as for gray matter.

In this work, we used VST to estimate the noise variance directly from magnitude data with the aim of improving the initial noise variance estimation for the GP fitting. VST estimates the noise variance in a voxel-wise way. To account for spatially-varying noise amplification during parallel imaging reconstruction, we calculated the g-factor from the initial SENSE reconstruction and divided the VST-estimated noise standard deviation by the g-factor at corresponding spatial

locations. The averaged noise variance from all spatial locations was used as an initial likelihood estimation in Gaussian Process parameter fitting.

3.3.4 Post-processing

For the in vivo data, Gibbs ringing artifacts were removed using degibbs3D from mrtrix3 (https://www.mrtrix.org/) followed by correction for susceptibility-induced distortions, eddy currents and motion using FSL's topup and eddy tools. To better compare the reconstruction performance, in the paper we showed all the raw DWI images directly after reconstruction without performing FSL's topup and eddy tools.Diffusion images from one randomly selected representative diffusion direction from each shell are shown for each subject. But To mitigate the impact of motion and distortion difference between the reference data and the under-sampled data, raw dMRI images were processed with FSL's topup and eddy tools before calculating difference maps. DKI and NODDI metrics were calculated using DIPY (https://dipy.org/) and FSL [119], respectively. Since q space sampling can influence dMRI model fitting[120], to evaluate the impact of reconstruction methods on dMRI model parameters, difference maps and overall errors for whole brain were calculated for the direction-matched pairs (i.e., 100-dir single band 2-average reference, 100-dir SENSE and 100-dir ms-DAGER).We also fitted the data using the ball and stick model with Bedpostx [112]. For one subject, we compared the whole brain tractography results between the reconstructed images and the single band whole brain reference images using autoPtx toolbox [121]. Weighted-DICE values[122] were calculated to quantitatively evaluate tractography results:

$$D(w_i, w_j) = \frac{\sum_{v'} w_{i,v'} + \sum_{v'} w_{j,v'}}{\sum_v w_{i,v} + \sum_v w_{j,v}} \tag{3.9}$$

where w_i and w_j are the same fascicle but extracted from different datasets and each voxel in w_i and w_j contains a value between 0 and 1 expressing the fraction of tracts passing through. v is a voxel index and v' stands for the voxels within the intersection of w_i and w_j.

3.4 Results

Figure 3.3 shows simulation results with 100, 64 and 36 directions. Compared to SENSE, ms-DAGER and original single-shell DAGER (ss-DAGER) provide improved image quality with significantly reduced noise level for all protocols. However, as the number of directions decreases (e.g., 64 and 36 directions), ss-DAGER suffers from increased image errors because fewer directions are available from ss-DAGER for pulling information in a given shell. In comparison, ms-DAGER provides relatively high image quality even with 36 directions due to its ability to draw information from multiple shells. This behaviour is quantified with normalized Root-Mean-Square-Error (nRMSE) values, which increase rapidly for ss-DAGER as the number of diffusion directions decreases, but remain similar for ms-DAGER, demonstrating improved robustness of ms-DAGER.

Because ms-DAGER leverages information from nearby directions and b-shells to improve the reconstruction, it risks introducing smoothness across both angle and shell. We investigated these two types of smoothness in ms-DAGER using simulation data. To investigate angular smoothness, angular covariance of the simulated ground truth dMRI signal and the ms-DAGER reconstruction were compared (Figure 3.4(a). Because noise will decrease the covariance values and confound the smoothness evaluation, a noise-free simulation was used in this investigation. The covariance is plotted for all pairs of directions on the same b-shell as a function of their angular difference in q space. ms-DAGER demonstrates highly consistent angular covariance profile for 100, 66 and 36 diffusion directions with respect to reference, indicating that ms-DAGER is introducing minimal angular smoothness. The discrepancy increases slightly at a low number of directions (e.g., 36-dir) because ms-DAGER has fewer points in a local neighbourhood to exploit information redundancy. Cross-shell smoothness was evaluated by assessing the intensity ratio between different shells (Figure 3.4(b)). We calculated the point-by-point intensity ratio between direction-averaged b = 1000 s/mm^2 images and direction-averaged b = 2000 s/mm^2 images for the simulated ground truth and ms-DAGER reconstruction within a white matter mask. Histograms are shown for two different noise levels (SNR 20

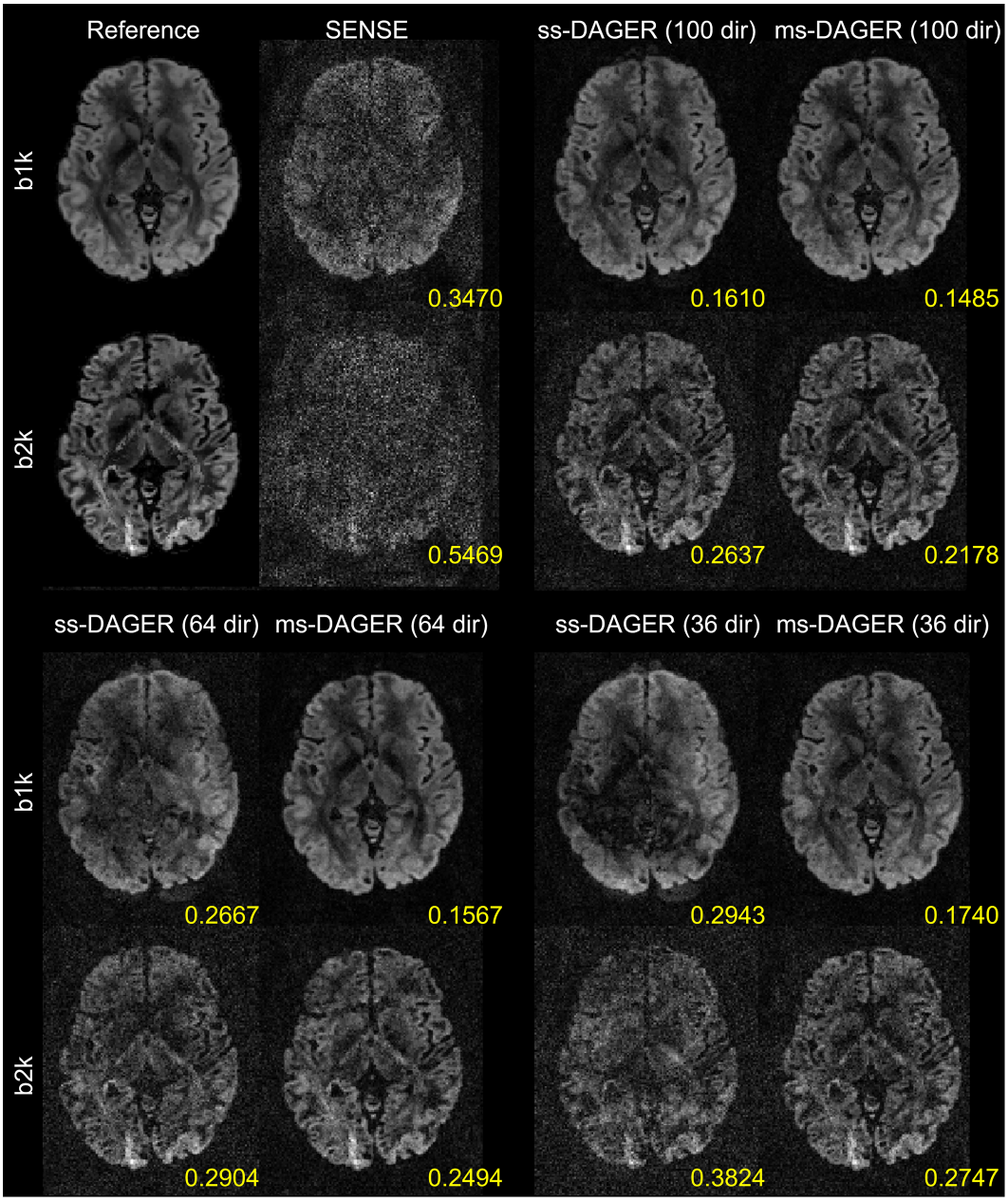

Figure 3.3: Reconstruction results of the 100/64/36-direction simulation data with undersampling factor R =12 (SMS = 4, R = 3). Reconstructed b = $1000 s/mm^2$ ('b1k') and b = 2000 s/mm^2 ('b2k') images from SENSE, ss-DAGER, and ms-DAGER are shown for each method. Note that ms-DAGER produces the highest SNR and the least artifacts. Compared to ss-DAGER, ms-DAGER allows improved reconstruction by exploring shared information across shells, particularly with a small number of directions (i.e., 64 and 36 directions).

and 40 based on fully sampled data) and different numbers of diffusion directions. Cross-shell smoothness would lead to reduced ratio compared to the ground truth. The intensity ratio between two shells was slightly decreased with ms-DAGER (3.8% at most, for 36 directions), indicating minimal cross-shell smoothing.

In Figure 3.5 we compared the noise estimation accuracy and effects on reconstruction with and without using VST by adding different levels of Gaussian noise to the complex simulation data (noise standard deviation 1-16 refers to SNR 30 to 1.875). As shown in Figure 3.5(a), with the increasing of noise levels added to the simulation, the results without using VST (w/o VST) show strong negative bias, which increases with the ground truth noise standard deviation, revealing a large underestimation effect at high noise levels. In comparison, VST based method (w/ VST) provides a more robust estimation of noise standard deviation. As shown in Figure 3.5(b), the nRMSE values between reconstruction results and the ground truth at different noise levels are decreased with the introduction of VST.

Figure 3.6 shows the reconstruction results for the 1.5 mm in vivo data from subject 1 with 36- directions using SENSE, ss-DAGER and ms-DAGER. The k space undersampling patterns are separately optimised for ss-DAGER and ms-DAGER (the q space sampling patterns are identical). Compared to SENSE, both ss-DAGER and ms-DAGER methods significantly improve the image quality. However, the ss-DAGER reconstruction is noisier than ms-DAGER, particularly for the b = 2000 s/mm^2 shell, whereas ms-DAGER provides similar data quality to the high-SNR single band reference (2 averages). Figure 3.7 shows the difference map between reconstruction results from different methods with the reference as in Figure 3.6 by subtracting the raw dMRI images between reference data and reconstruction results after registration to reduce motion-induced inconsistency. These results demonstrate the advantage of ms-DAGER over original DAGER when the number of diffusion directions is small.

Figure 3.8 shows an axial slice of the reconstruction results without EPI distortion correction for the 1.5 mm in vivo data from subject 2 with 100, 66 and 36 directions. Compared to the SENSE results, ms-DAGER provides significantly improved SNR

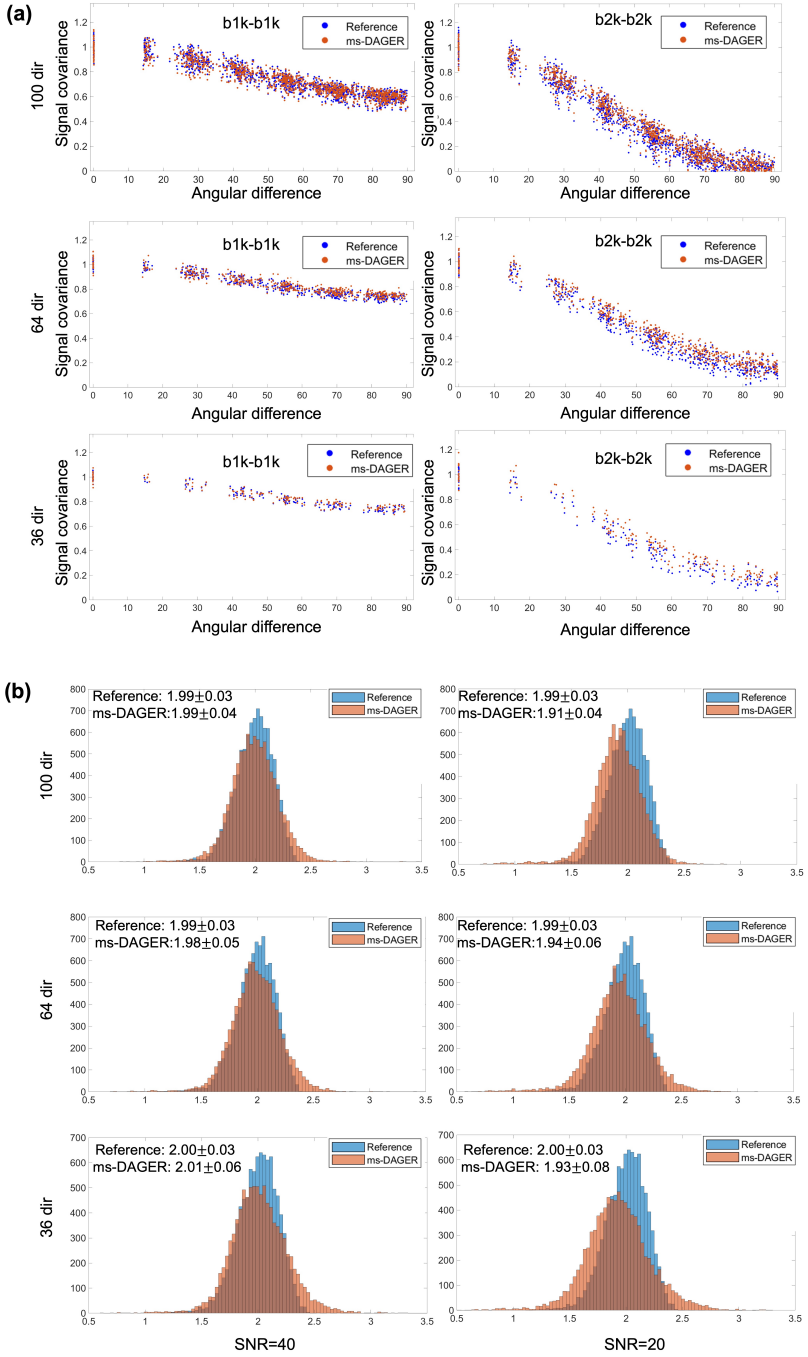

Figure 3.4: (a) Signal covariance of dMRI images. Whole-brain white matter of the simulation data was used for the covariance calculation. Each point represents 1 diffusion direction. For each data set, the covariance is normalized by the median of signal variances (angular distance = 0°). ms-DAGER reconstructed images demonstrate consistent covariance with the reference at both b = $1000s/mm^2$ ('b1k') and b = $2000s/mm^2$ ('b2k') shells. (b) Histogram of point-by-point intensity ratio between direction-averaged b1k images and direction-averaged b2k images, calculated with whole-brain white matter signal of the simulation data. High noise level and low noise level refers to SNR = 20 and SNR = 40 data (SNR calculated based on fully sampled data).

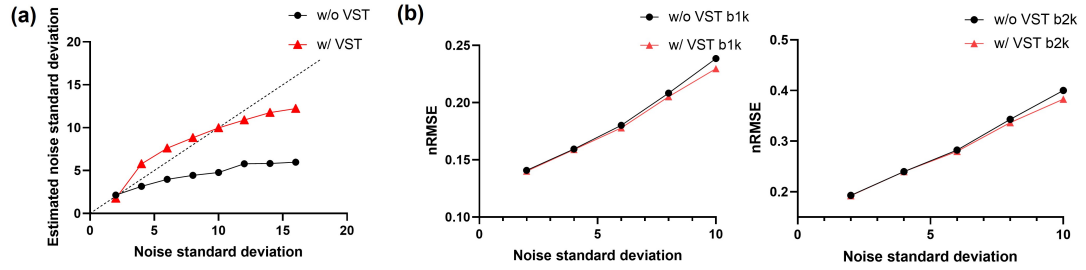

Figure 3.5: (a) Comparison of noise standard deviation estimation for the simulation data. Different noise levels were added to the ground truth. The noise estimation with VST (w/ VST) and without VST (w/o VST) are shown. VST allows more robust estimation of noise standard deviation, particularly at high the noise levels. (b) nRMSE values between ground truth and reconstruction results with and without using VST for noise standard deviations of 2, 4, 6, 8, 10. With the increase of noise levels, the method using VST shows better performance compared to the method without using VST.

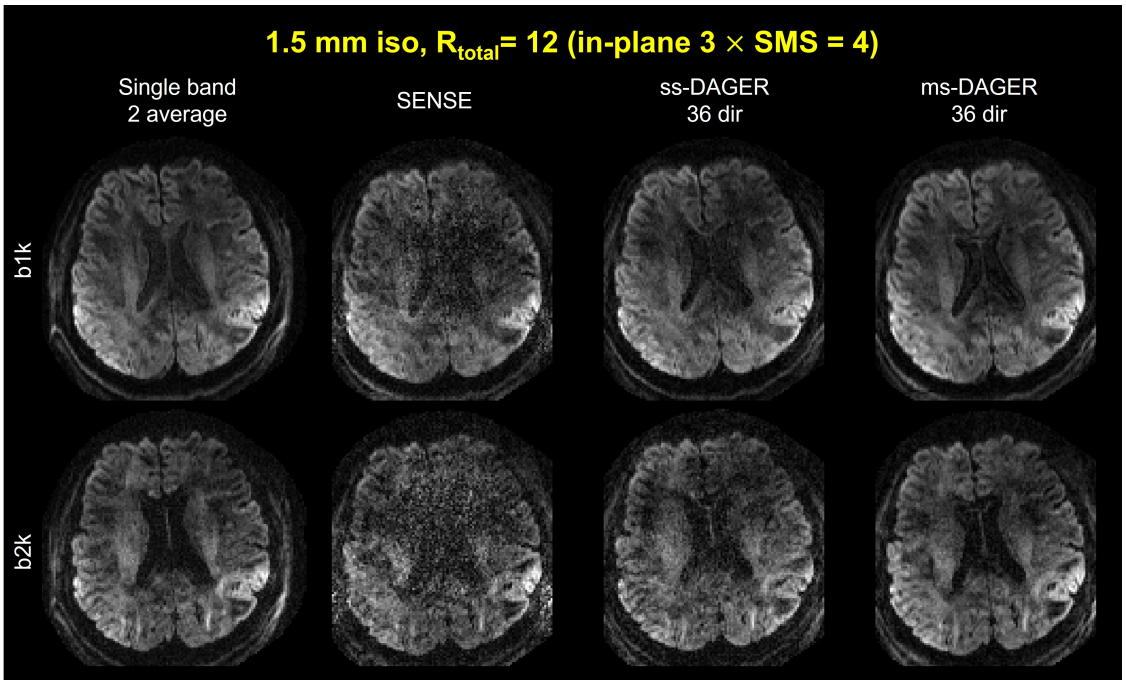

Figure 3.6: Reconstruction results of the 36-direction 1.5 mm isotropic resolution in vivo data. Single band reference images with 2 averages, SENSE, single shell DAGER (ss-DAGER) and ms-DAGER results at b=1000s/mm^2 ('b1k') and b=2000s/mm^2 ('b2k') are shown. Compared to ss-DAGER, ms-DAGER further improves the image quality when the number of diffusion directions is small.

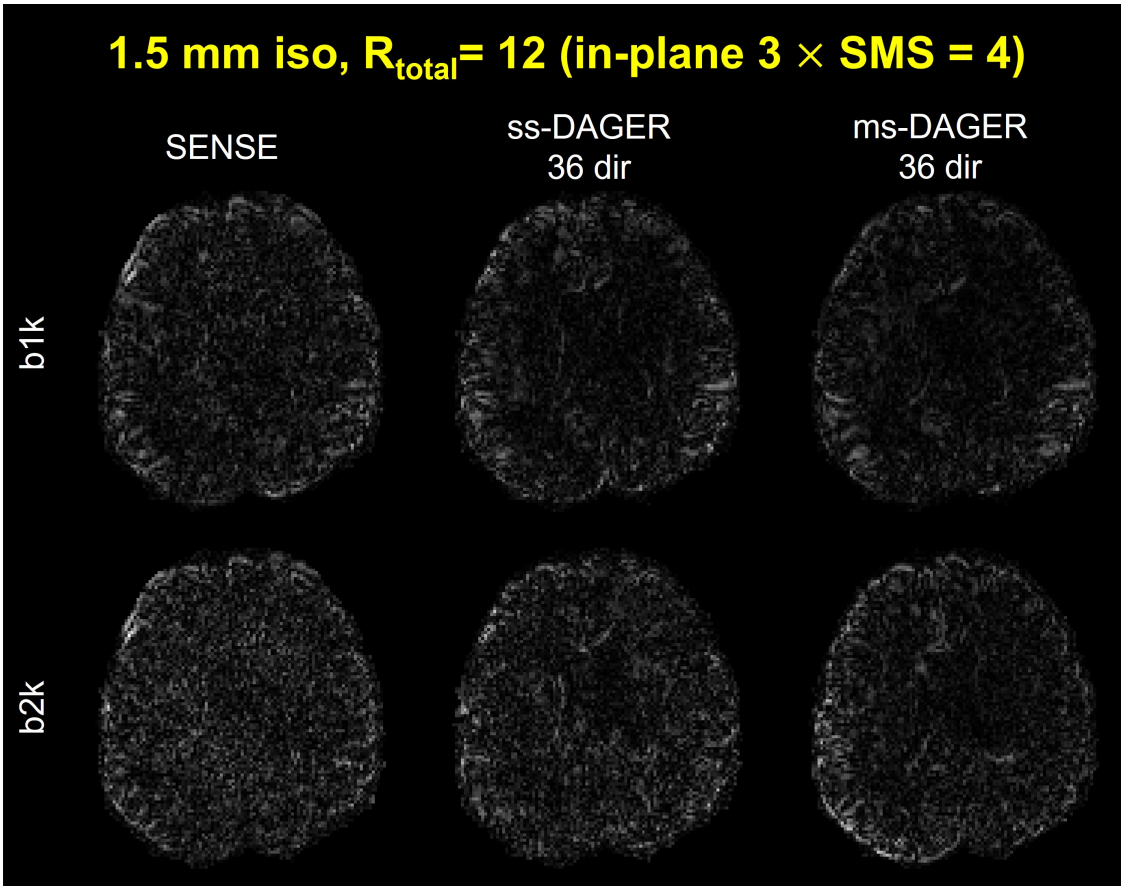

Figure 3.7: Difference maps between reference and reconstruction results of the 36-direction 1.5 mm isotropic resolution in vivo data shown in Figure 3.7. Compard to SENSE and ss-DAGER, ms-DAGER shows least error.

and reduced artifacts, with consistent structure details to the high SNR single-band reference. The difference map between reconstruction results and the reference are also shown in Figure 3.8. Even with a small number of diffusion directions as 36 directions, the results still show comparable quality to the high SNR reference.

ms-DAGER reconstruction results for two other subjects (1 and 4) with 1.5mm isotropic resolution are shown in Figure 3.9 and 3.10 respectively. Difference maps between reference and reconstruction results are also shown. ms-DAGER consistently improves the image quality compared to SENSE and shows comparable data quality to the high SNR reference images for different numbers of diffusion directions, which demonstrates that ms-DAGER works robustly for different subjects.

In Figure 3.11, we compare our method with a SMS acceleration factor of 2, as is currently common practice, along with a single band whole-brain reference from

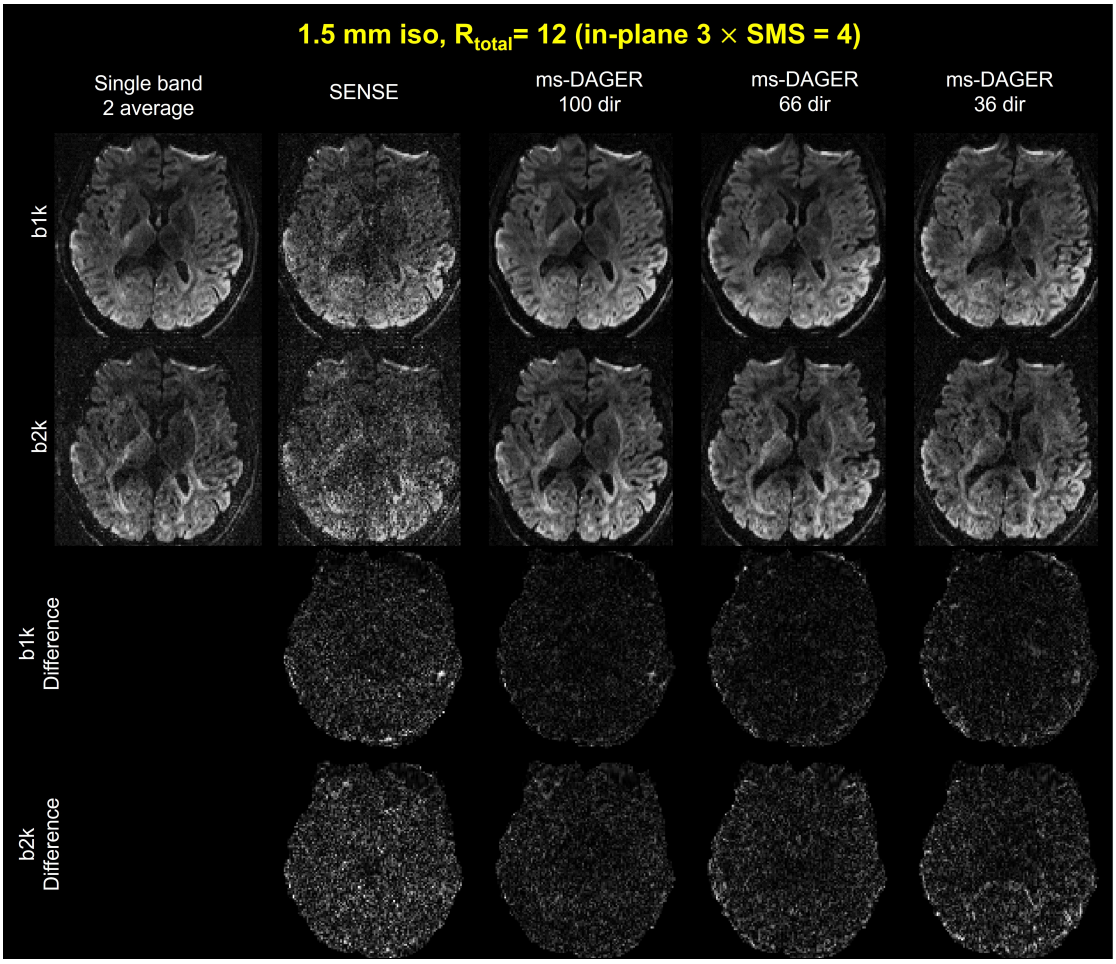

Figure 3.8: 1.5 mm isotropic resolution in vivo data with different number of directions. Single band reference images with 2 averages, SENSE and ms-DAGER with different number of directions are shown at b=1000s/mm^2 ('b1k') and b=2000s/mm^2 ('b2k').Difference maps between reference and reconstruction results are also shown.ms-DAGER improves image quality compared to SENSE and provides consistent detailed structural information with the reference images.

subject 3. Sagittal, and coronal views are shown. Here, the single band reference was acquired with only one average due to scan time constraints. All data were acquired with the same in-plane acceleration factor of 3. As shown in Figure 3.11, the 12-fold acceleration data reconstructed using ms-DAGER show comparable image quality to the 3-fold accelerated single band reference and improved SNR compared to the 6-fold accelerated SMS = 2 data, particularly for the higher b value shell. Note the image contrast is slightly different between protocols due to TR difference.

Figure 3.12 shows the reconstruction results for the 1.25mm in vivo data for subject 5. The difference maps between reference and reconstruction results

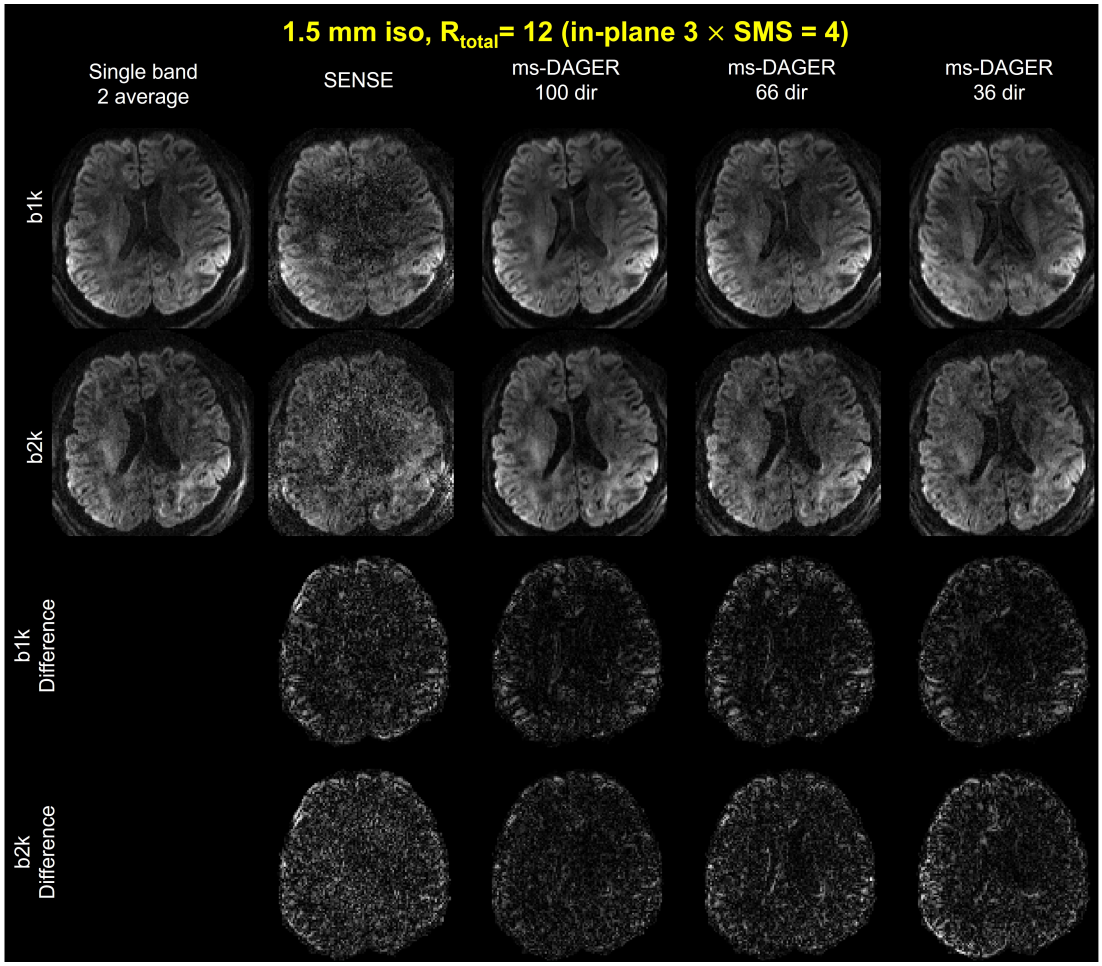

Figure 3.9: Reconstruction results of the 1.5 mm isotropic resolution in vivo data from subject 1. Single band reference images with 2 average, SENSE and ms-DAGER results are shown b=1000s/mm^2 ('b1k') and b=2000s/mm^2 ('b2k') images are both shown. Difference maps between reconstruction results and reference are shown. ms-DAGER consistently improve image quality compared to SENSE for both subjects.

are also shown in Figure 3.12. The image quality is extremely poor in SENSE reconstruction, which is dominated by noise. ms-DAGER significantly improves the image quality for 100-dir data and 66-dir data, showing consistent structure details compared to reference.

DKI fitting results, including mean kurtosis (MK), axial kurtosis (AK) and radial kurtosis (RK) are demonstrated in Figure 3.13, SENSE reconstructions have inflated MK and AK values compared to the reference while ms-DAGER produces results consistent with the reference for matched number of directions. As the number of directions reduces, DKI maps with ms-DAGER have more outliers (i.e.,

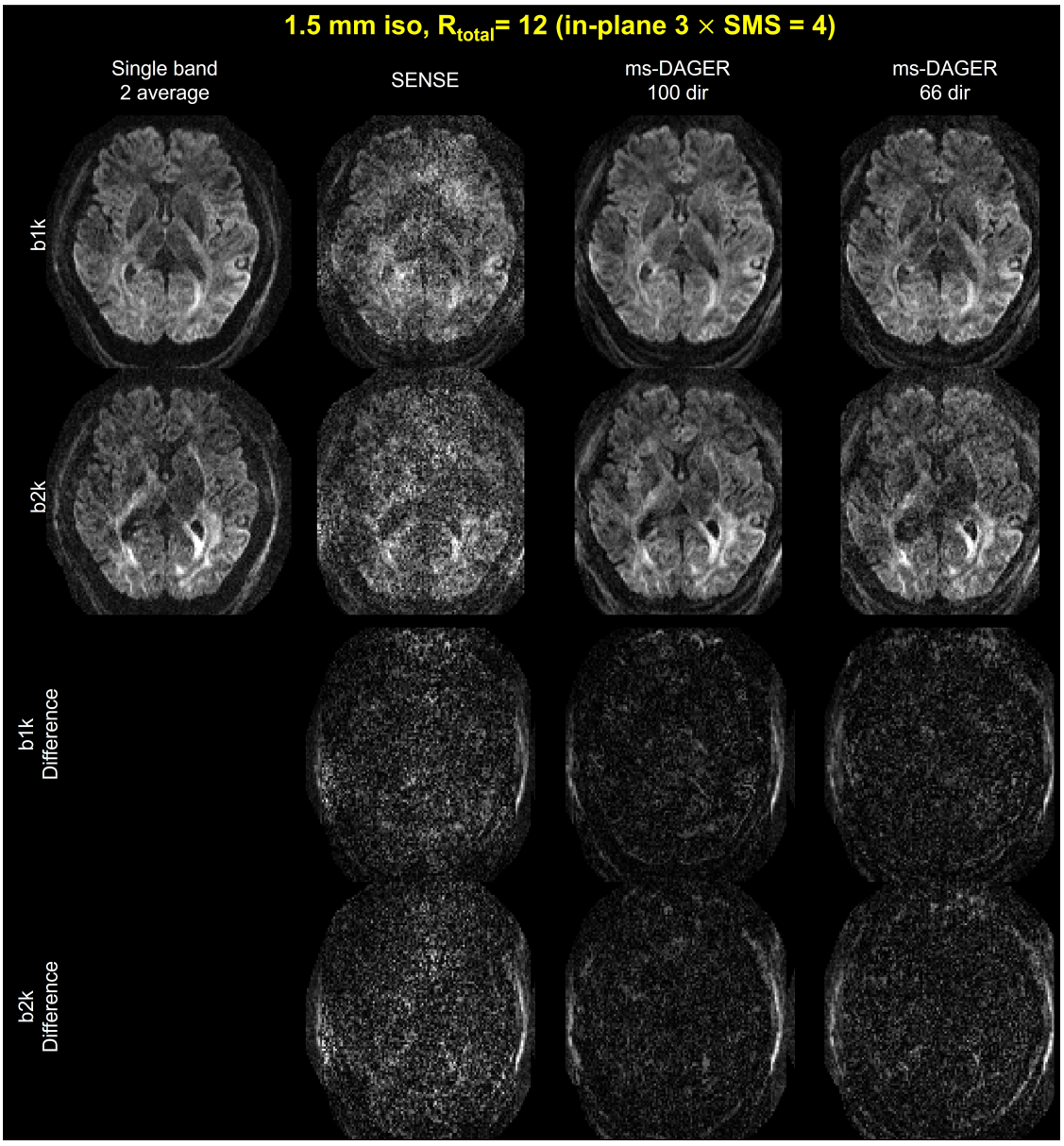

Figure 3.10: Reconstruction results of the 1.5 mm isotropic resolution in vivo data from subject 4. Single band reference images with 2 average, SENSE and ms-DAGER results are shown b=1000s/mm^2 ('b1k') and b=2000s/mm^2 ('b2k') images are both shown. Difference maps between reconstruction results and reference are shown. ms-DAGER consistently improve image quality compared to SENSE for both subjects.

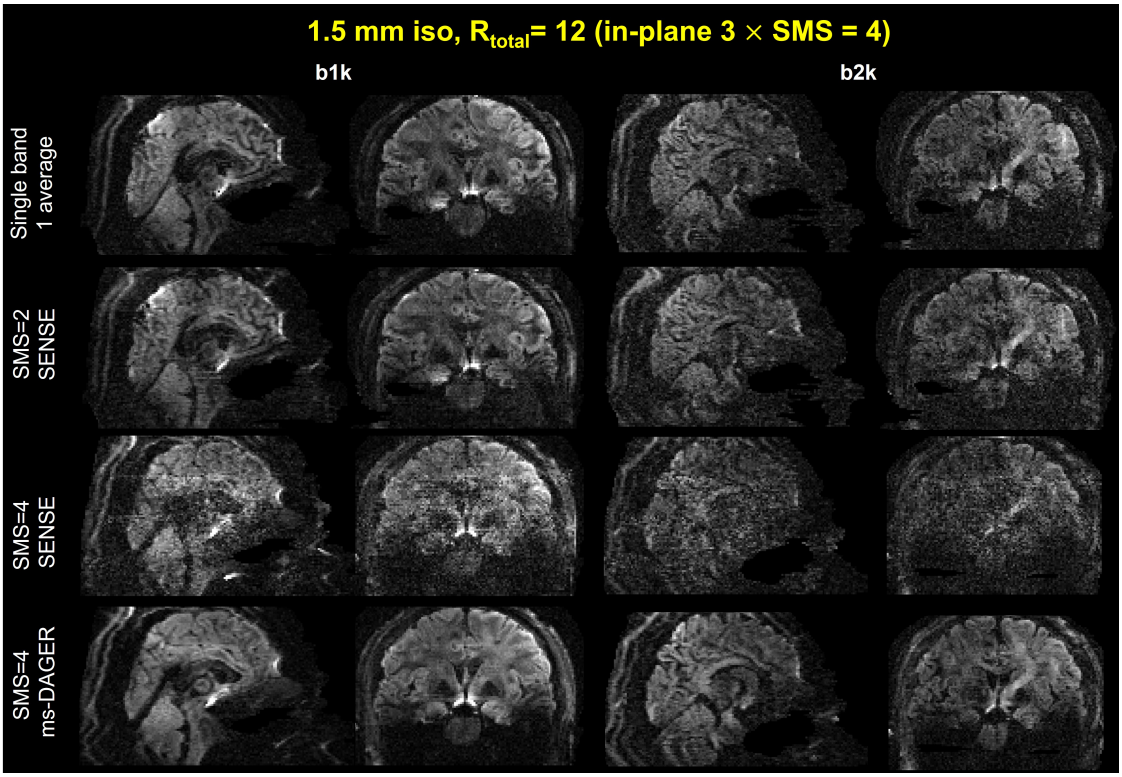

Figure 3.11: Coronal and sagittal slices of 1.5 mm isotropic resolution in vivo data. Single band reference images with 1 average, SMS = 2 SENSE, SMS = 4 SENSE and SMS = 4 ms-DAGER results are compared. b = 1000 s/mm^2 ('b1k') and b = 2000 s/mm^2 ('b2k') images are both shown. ms-DAGER provides improved SNR compared to SMS = 4 and SMS = 2 SENSE, with comparable data quality to the reference images. Note image contrasts are slightly different between methods due to different TR used.

black dots in the maps, indicating fitting failures), but the overall spatial patterns are consistent with the high-SNR reference.

Figure 3.14 compares NODDI modelling fitting results from subject 2, specifically maps for isotropic fraction (fiso), intra-cellular fraction (fintra), and orientation dispersion index (ODI). ms-DAGER produces parameter maps that are consistent with the high-SNR reference while providing full brain coverage with a much shorter scan time. The degraded data quality in SENSE reconstruction (e.g., in Figures, 3.8 and 3.12) leads to instability in the modelling fitting, including overestimated fintra and large errors in thalamus (white arrow) for ODI due to the high noise level. In comparison, ms-DAGER provides parameter maps that are consistent with the reference with matched number of directions. When the number of directions reduces, ms-DAGER provides robust NODDI fitting despite significantly reduced

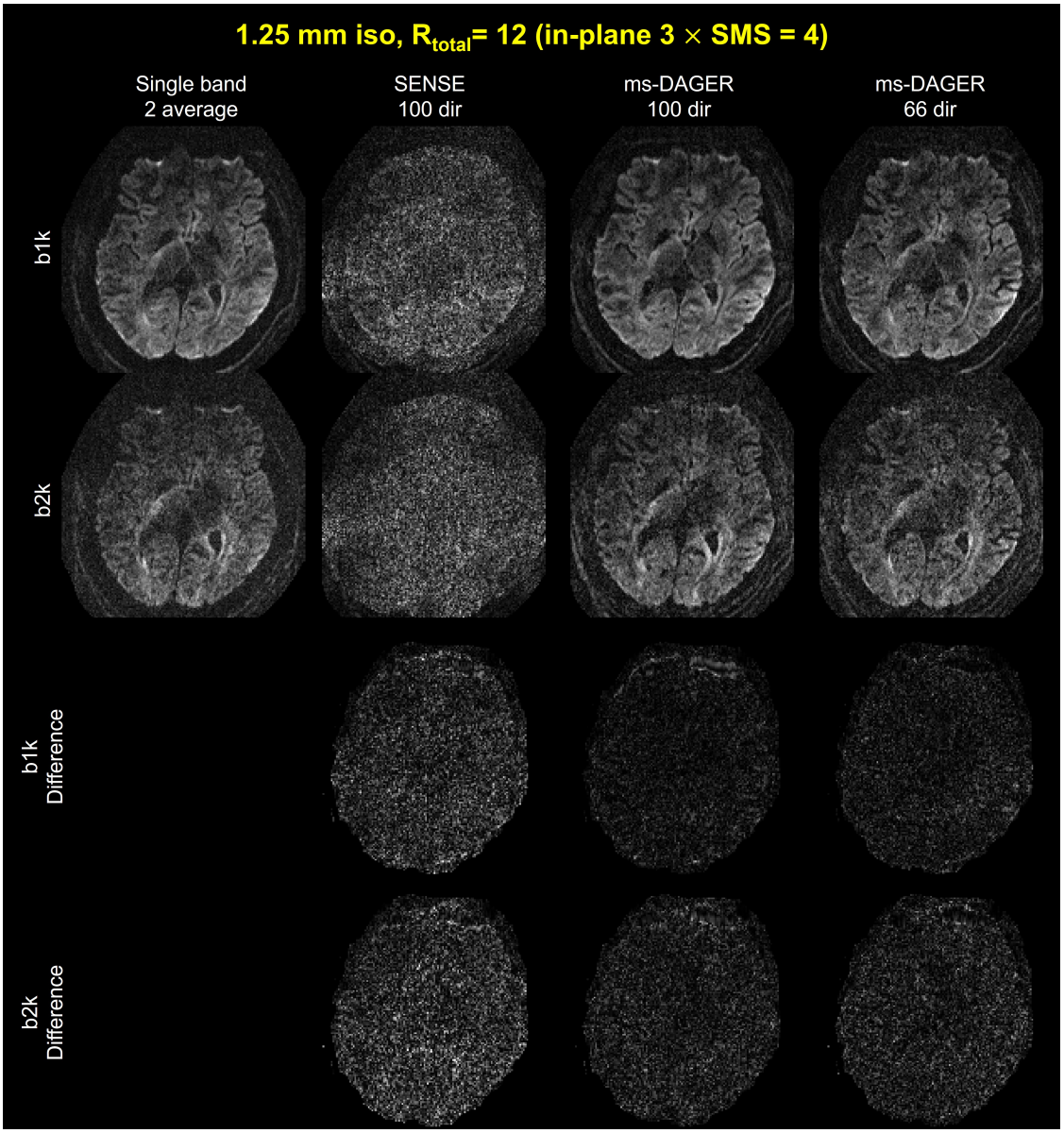

Figure 3.12: Reconstruction results for the 1.25 mm isotropic resolution in vivo data. Single band reference images with 2 average, SENSE and ms-DAGER results for different number of diffusion directions are shown. b=1000s/mm^2 ('b1k') and b=2000s/mm^2 ('b2k') images are both shown. Difference maps between reference and reconstruction results are also shown. Despite low SNR at 1.25mm resolution, ms-DAGER provides robust reconstruction from highly-undersampled multi-shell datasets.

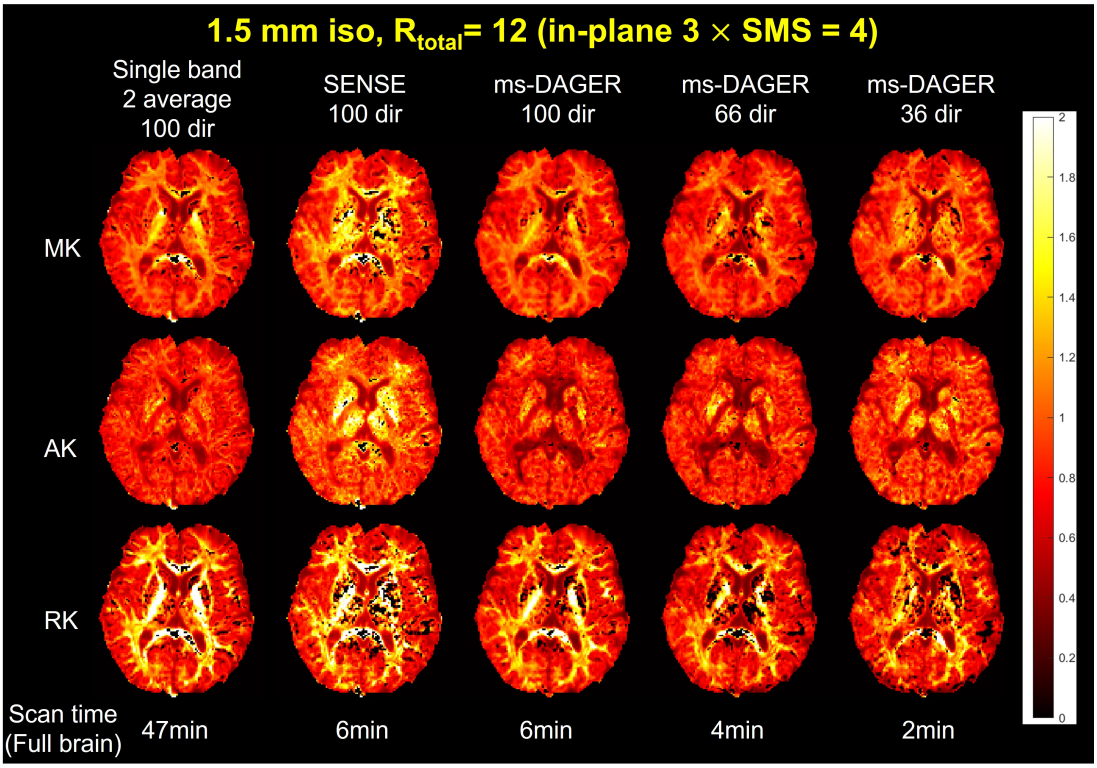

Figure 3.13: DKI fitting results for the 1.5 mm isotropic resolution in vivo data. Mean kurtosis (MK), axial kurtosis(AK) and radial kurtosis(RK) maps are shown calculated from single band reference images with 2 average, SENSE and ms-DAGER for different numbers of diffusion directions. ms-DAGER accelerated reconstruction generates similar DKI metric maps as the 2 average single-band reference with a much shorter scan time.

scan time (e.g., 2min for 36-dir ms-DAGER versus 47min for 100-dir reference).

Figure 3.15 shows the difference map and median absolute error values for DKI and NODDI fitting results from direction-matched datasets from subject 2. Compared to SENSE, ms-DAGER can improve the parameter fitting accuracy and reduce the error values.

Figure 3.16 shows the ball and stick model fitting results using FSL's Bedpostx tool for the 1.5mm in vivo data from Subject 2, including both primary and secondary fiber populations. With 100 diffusion directions, both SENSE and ms-DAGER capture similar primary fiber populations. However, due to the high noise level in the SENSE reconstruction, the number of voxels with a robust secondary fiber population is significantly decreased as Bedpostx filters out secondary fiber population if they are unsupported by the data due to low SNR. In comparison,

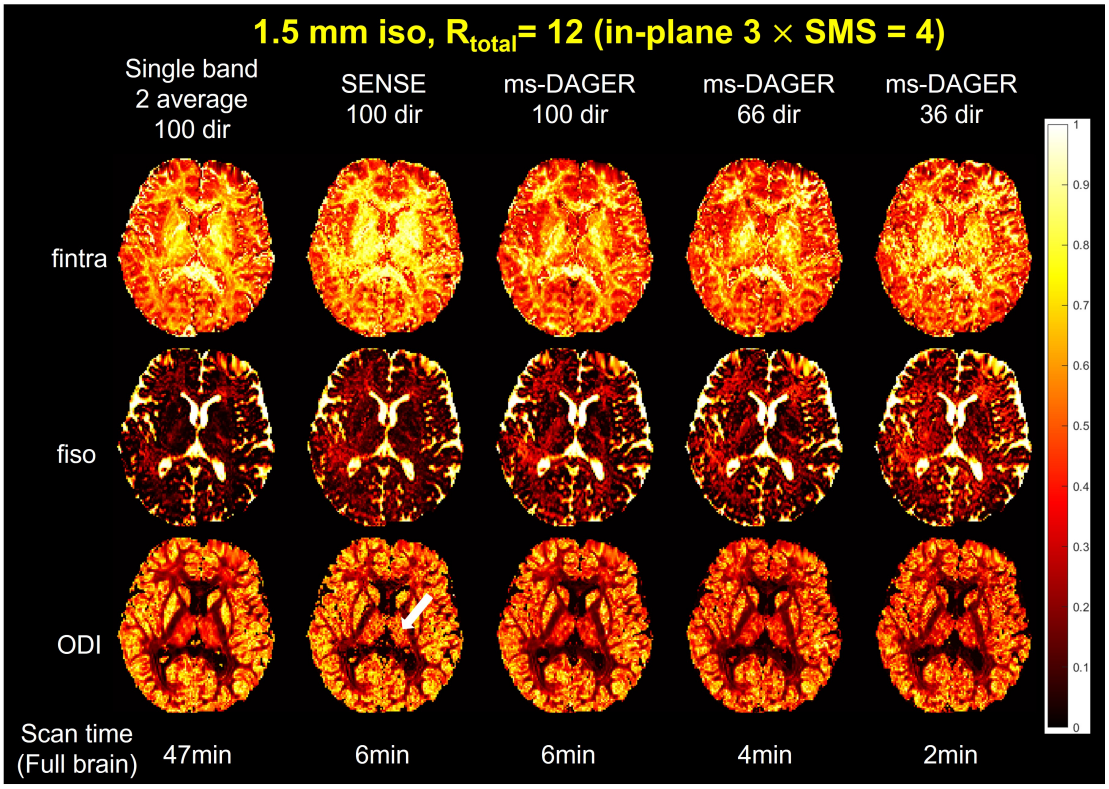

Figure 3.14: NODDI fitting results for the 1.5 mm isotropic resolution in vivo data. CSF volume fraction(fiso), intra-cellular volume fraction(fintra) and orientation dispersion index (ODI) from NODDI fitting are shown, which were calculated from single band reference images with 2 average, SENSE and ms-DAGER results for different numbers of diffusion directions. ms-DAGER accelerated reconstruction produces comparable NODDI metric maps as the single-band reference with a much shorter scan time.

ms-DAGER results identify a secondary population in many more voxels, which have consistent patterns to the reference. As shown in the images, the orientations of secondary fibers are also consistent with the high SNR reference results.

Figure 3.17 shows tractography results for subject 3. autoPtx is used to track the fibers for 66-dir whole-brain single band reference data (16 min) along with SMS 4 66-dir whole-brain data (4 min) reconstructed using SENSE and ms-DAGER. Most fiber bundles are properly delineated from the single band reference data. Compared to the reference, many tracts are either incomplete or missing when using SMS 4 SENSE reconstructions for example acoustic radiation tracts (Figure 3.17, middle column, in green), forceps minor (Figure 3.17, left column, in yellow), inferior frontal-occipital fasciculus (Figure 3.17, right column, in green) are absent.

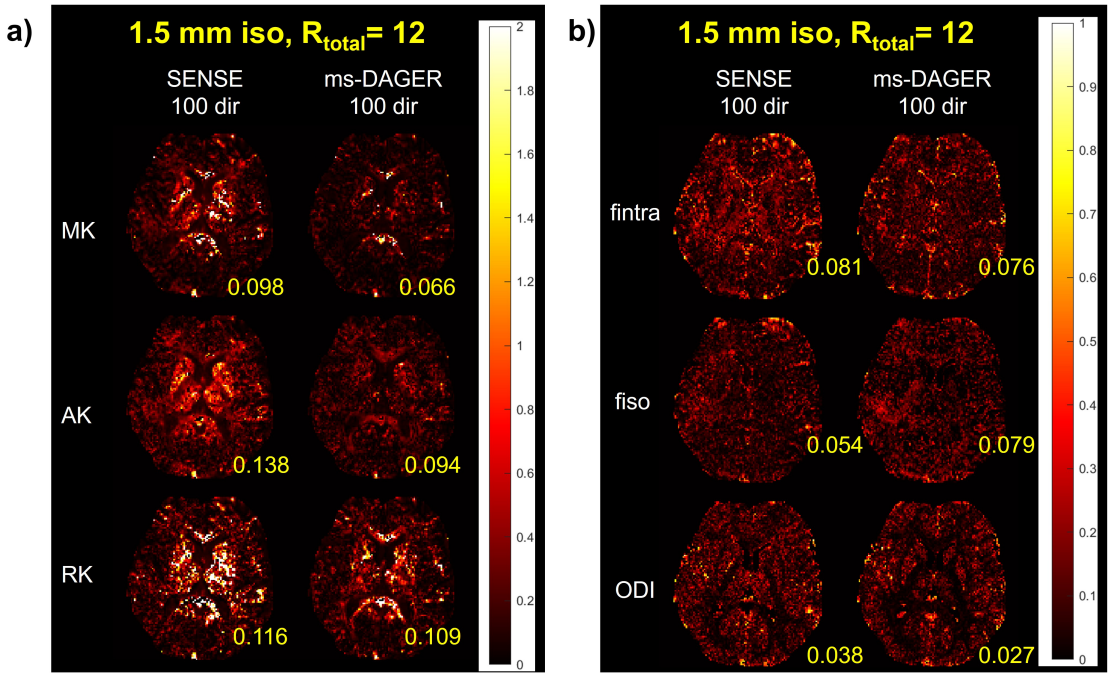

Figure 3.15: a)Error maps between DKI fitting results from reference and reconstruction results for the 1.5 mm isotropic resolution in vivo data from subject 2. Median absolute error values are also shown for Mean kurtosis (MK), axial kurtosis(AK) and radial kurtosis(RK). b)Error maps between NODDI fitting results from reference and reconstruction results for the 1.5 mm isotropic resolution in vivo data shown in Figure 3.10. Median absolute error values are also shown for CSF volume fraction(fiso), intra-cellular volume fraction(fintra) and orientation dispersion index (ODI).

ms-DAGER reconstructions with a much shorter scan time capture most tracts, consistent with single band reference. Weighted-DICE values were calculated to compare the overlap between tracts from the reference and those obtained from SENSE and ms-DAGER, respectively. As shown in Table 3.1, compared to SENSE, ms-DAGER improves the weighted-DICE values for all tracts, demonstrating much better alignment with the reference.

3.5 Discussion

In this work, we propose a robust acceleration method for multi-shell dMRI to improve acquisition efficiency while preserving image fidelity. This method builds on our previous single-shell DAGER approach, using Gaussian processes to model smoothness of the dMRI signal in q space neighbourhoods and leverage the

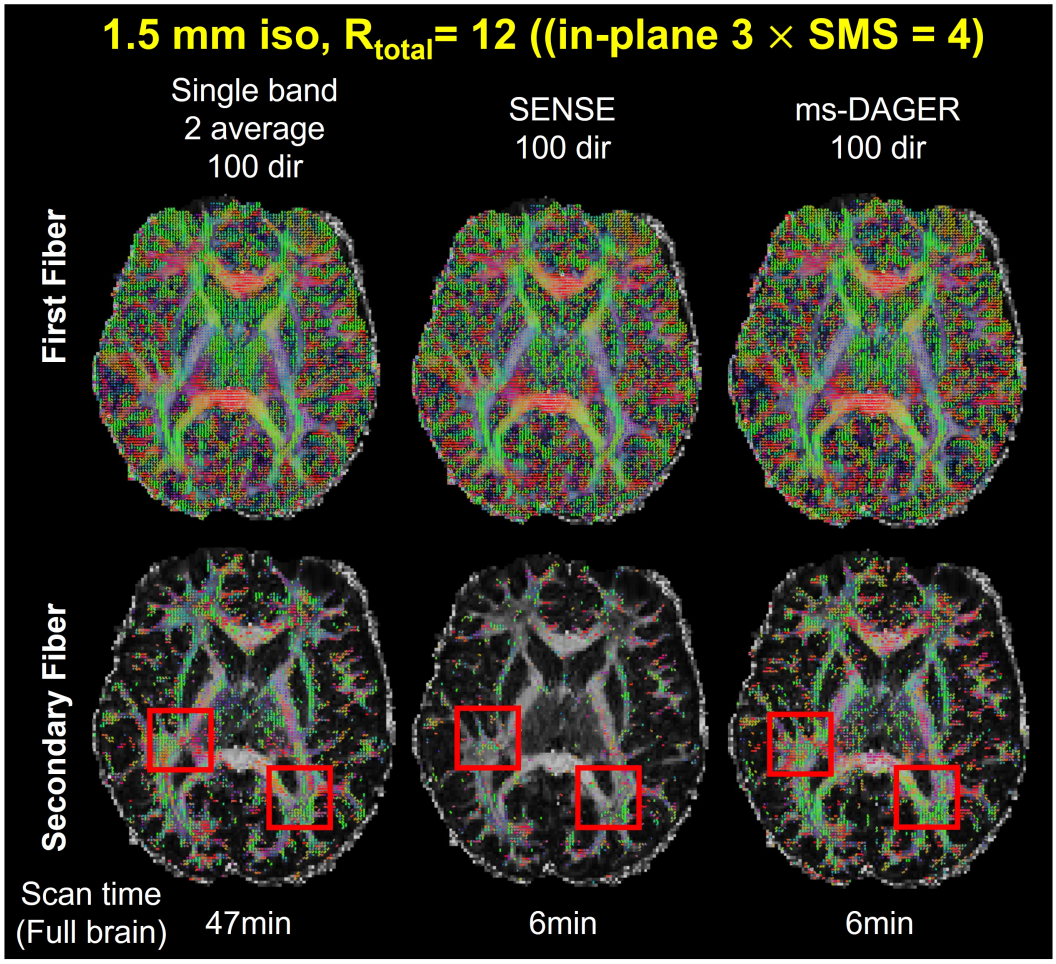

Figure 3.16: Ball and stick fitting results for the 1.5 mm isotropic resolution in vivo data from subject 2. The first fiber and second fiber populations calculated from single band reference images with 2 average, SENSE and ms-DAGER results are shown. ms-DAGER recovers a large number of second fiber population, consistent with the single-band reference, while SENSE results fail to capture many second fibers.

associated covariance structure in image reconstruction. Simulation and in vivo results demonstrate that the proposed method can effectively preserve the SNR and suppress artifacts even at a high acceleration factor of 12 (SMS = 4 and in-plane R = 3). Unlike single-shell DAGER, ms-DAGER jointly reconstructs multiple shells to exploit information redundancy both within and across shells, allowing more efficient information sharing. To achieve robust model parameter estimation at low SNR, which is common to high-b values and high resolution dMRI, we further integrate a variance-stabilizing transformation to improve the accuracy of noise variance estimation when optimizing Gaussian Processes hyperparameters.

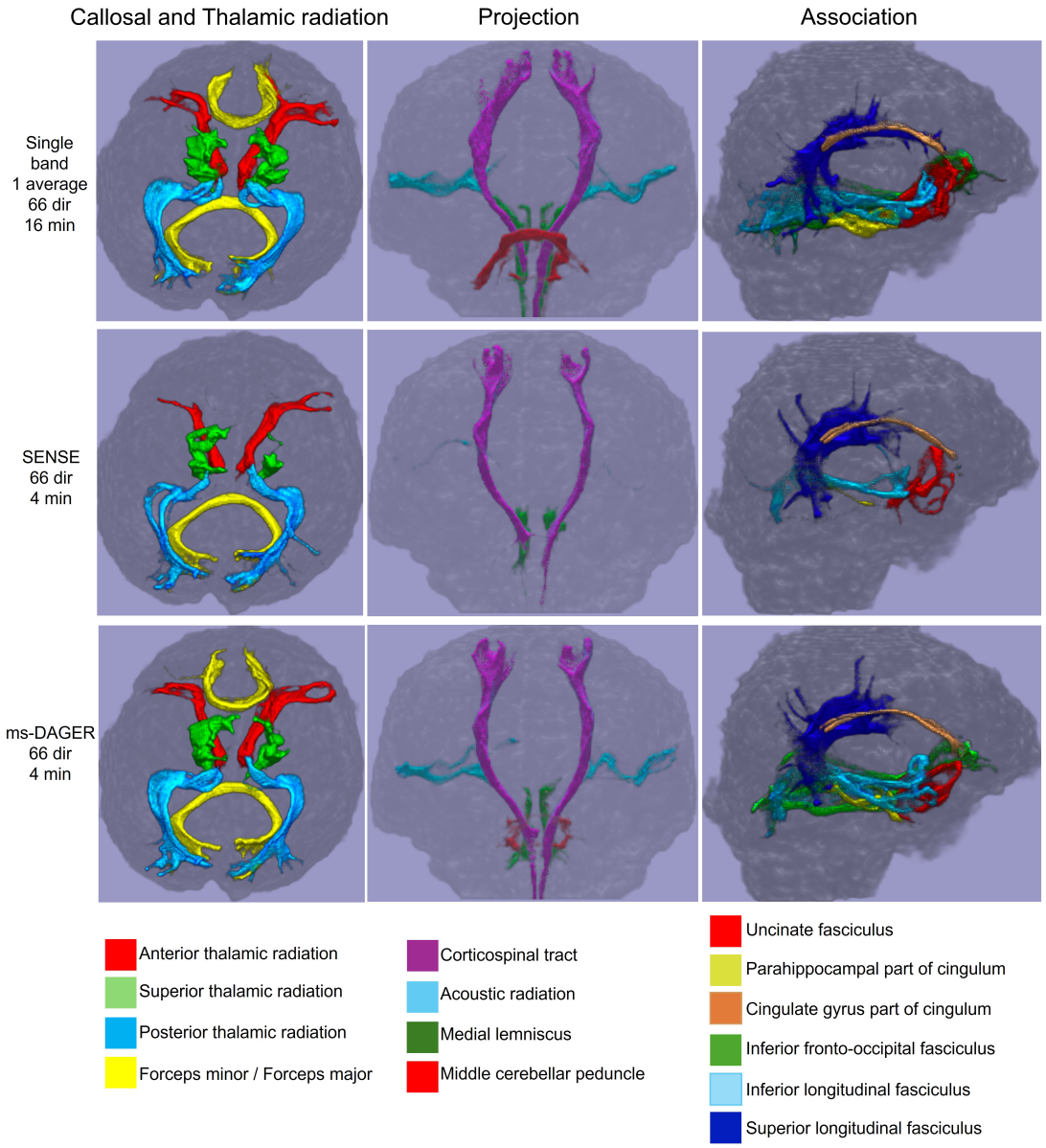

Figure 3.17: Fiber tracking results for the 1.5 mm isotropic resolution in vivo data using autoPtx. Single band reference, SENSE and ms-DAGER for SMS = 4 data are shown respectively. 14 major white matter pathways (constituting 27 separate tracts in right and left hemispheres) are rendered in superior (thalamic radiation and callosal fibers), anterior (projection) and lateral (association fibers) views. Compared to Single band, several fibers are totally missing in the SENSE results due to the high noise level while ms-DAGER manages to recover most of the fiber tracts.

Tracts	SENSE	ms-DAGER
atr	0.8200	0.9526
str	0.8672	0.9629
ptr	0.7159	0.9345
fmi/fma	0.7613	0.8995
cst	0.9285	0.9779
ar	0.3820	0.8093
ml	0.7181	0.7253
mcp	0.0000	0.3515
unc	0.5765	0.7561
cgh	0.3121	0.7368
cgc	0.9711	0.9714
ifo	0.4733	0.8548
ilf	0.3778	0.7964
slf	0.8984	0.9550

Table 3.1: Weighed DICE values comparing tracts from the reference data and results from SENSE and ms-DAGER.

One major concern for joint k-q reconstruction is that when sharing information across different q space points, there might be extra smoothing introduced beyond what is intrinsic to the data. This could introduce bias to model parameters reflecting fiber dispersion if angular smoothness is introduced or metrics reflecting non-Gaussianity if cross-shell smoothness is introduced. In this study, we investigated within-shell angular and cross-shell smoothness using simulated datasets. As shown in Figure 3.4, the ms-DAGER reconstruction only slightly increases the covariance between different directions and affects intensity ratio between shells compared to the reference, indicating that Gaussian Process is able to learn and exploit the smoothness intrinsic to the data without introducing much smoothing.

Noise estimation plays a key role as a hyperparameter in GP fitting. In the context of ms-DAGER, the estimated noise level is directly used as a regularization factor on the data consistency term (σ_k^2 in Eq.3.8). Hence, estimating noise level accurately is crucial to reconstruction quality. In this work, we used VST to mitigate the noise variance estimation bias due to the Rician distribution in magnitude

images when the noise level is high. We assessed the accuracy of noise estimation using simulated data with ground truth noise std from 1 to 10 in Figure 3.5. The results show that VST can improve noise estimation and hence improve image reconstruction accuracy.

One impact that ms-DAGER could have is to facilitate use of multi-shell dMRI models within clinically feasible scan times. Due to the noise amplification when reconstructing high acceleration factors, results from traditional parallel imaging methods like SENSE provide unreliable fits to models like NODDI or DKI, as shown in Figure 3.13 and Figure 3.14. ms-DAGER can significantly improve the image quality and maintain diffusion contrast information under these conditions of high acceleration, enabling more accurate results for both multi-shell model fitting and fibre tracking.

Figure 3.18 shows the DKI results of 1.25mm in vivo data of subject 5. DKI fitting results from SENSE are corrupted by noise, showing large errors. In comparison, ms-DAGER produces more consistent results compared to the high SNR reference, though there are some outliers (black dots) due to the high noise level. Figure 3.19 shows the NODDI fitting results of 1.25mm in vivo data of subject 5. Figure 3.20 shows the difference map and median absolute error values for DKI and NODDI fitting results from direction-matched datasets in Figure 3.18 and Figure 3.19. SENSE results cannot support reliable NODDI fitting, leading to large errors in the parameter maps. In comparison, ms-DAGER allows better NODDI fitting even with a smaller number of diffusion directions of 66. The ODI parameters with ms-DAGER are slightly under-estimated compared to the high SNR reference, and the biases may be caused by the relatively low SNR at higher resolution. To investigate this effect, we also tested on other subjects (subjects 6 and 7). Figure 3.21 and 3.22 show the reconstructed images and NODDI fitting results for subjects 6 and 7 with 1.25 mm isotropic resolution, the model fitting results consistently show significant improvements compared to SENSE results and high reproducibility across subjects. Figure 3.23 shows the difference maps between reference and reconstruction results for the two subjects (subjects 6 and 7) in Figure 3.21. Figure 3.24 shows the

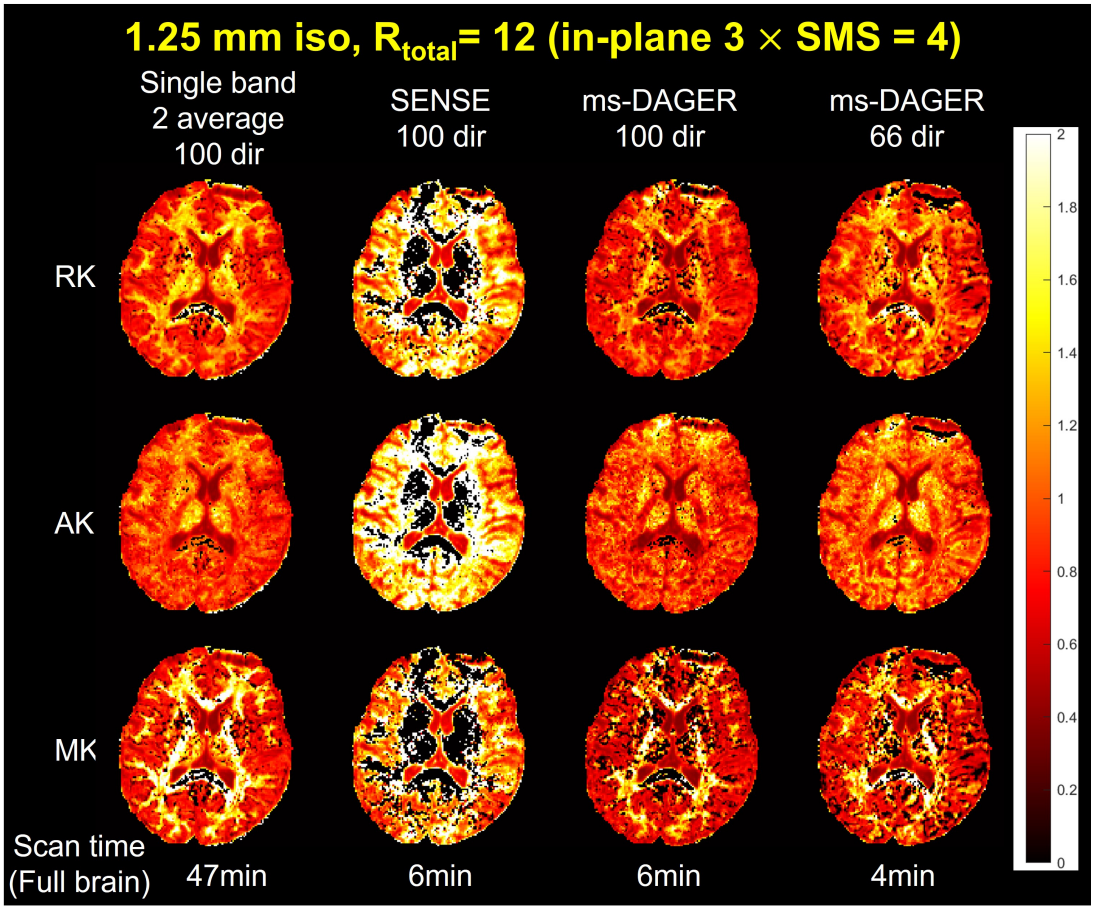

Figure 3.18: DKI fitting results for the 1.25 mm isotropic resolution in vivo data. Mean kurtosis (MK), Axial kurtosis(AK) and Radial kurtosis(RK) maps calculated from Single band reference images with 2 average, SENSE and ms-DAGER results are shown. Compared to SENSE, ms-DAGER produces more consistent results with reference using much shorter scan time.

difference map and median absolute error values for NODDI fitting results from direction-matched datasets in Figure 3.22. A summary of median absolute error values for NODDI fitting results across subjects is shown in Figure 3.25.

Although ms-DAGER improves overall image quality and model fitting results, the ODI maps of ms-DAGER appear to be less consistent with the reference in the cortex. This is likely due to the higher noise level in the ms-DAGER reconstructed images compared to the high-SNR reference. Low SNR can introduce bias in NODDI-ODI estimation, and this bias is dependent on the underlying ODI values: larger ODI values are prone to significant negative bias, while smaller ODI values are associated with small bias[7] . This mirrors the noise-induced bias in the estimated

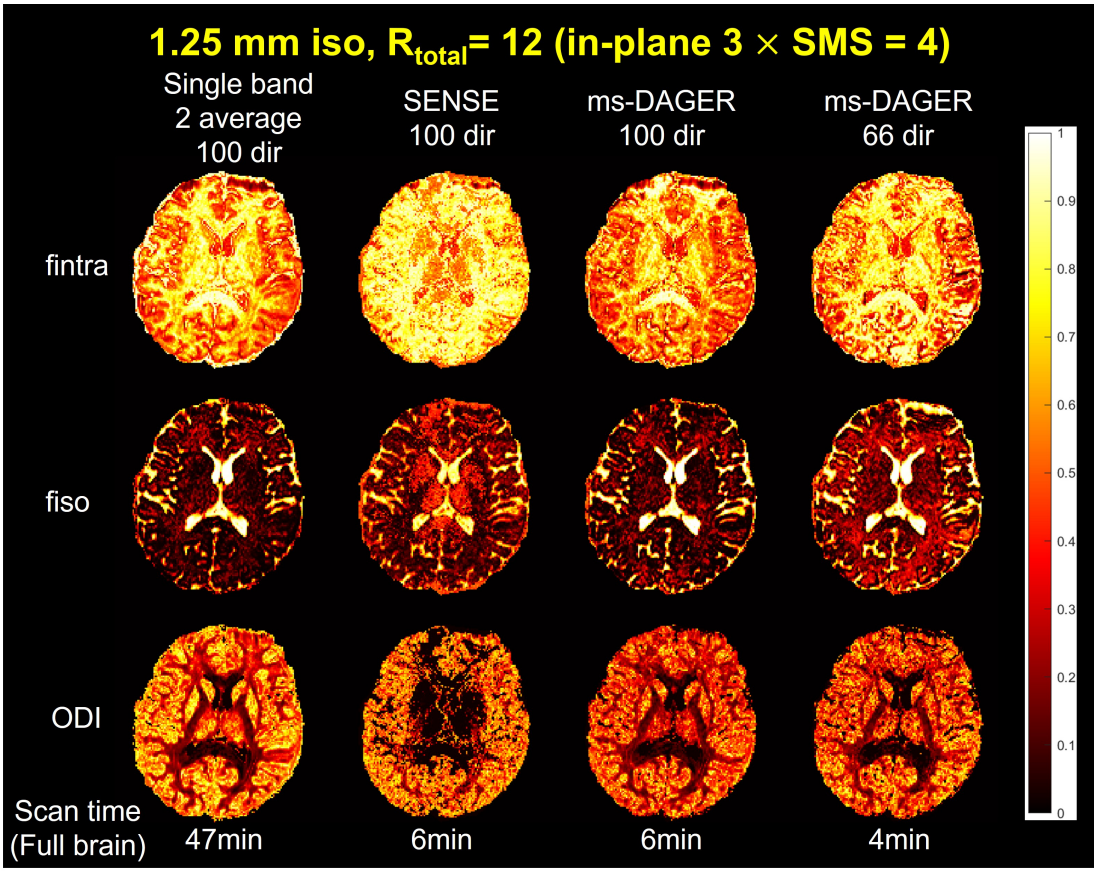

Figure 3.19: NODDI fitting results for the 1.25 mm isotropic resolution in vivo data. CSF volume fraction(fiso), intra-cellular volume fraction(fintra) and orientation dispersion index (ODI) from NODDI calculated from Single band reference images with 2 average, SENSE and ms-DAGER results are shown. Though bias exists in ODI maps, ms-DAGER can produce improved fitting results compared to SENSE results which are significantly corrupted by noise.

FA, which is dependent on the underlying FA values [123] . Since the underlying ODI values are higher in cortex than in white matter, the estimated ODI values in cortex are more susceptible to bias. This effect is further exacerbated when using a reduced number of directions with low SNR (e.g., 32 and 64 direction datasets). To validate our assumption, we performed a simulation by adding different levels (SNR = 15 and 7.5 respectively) of noise to the noise-free reference (33 b1k and 33 b2k directions) data and then fit the NODDI model. The ODI maps are shown in Figure 3.26 (a) and the boxplots of ODI for white matter and gray matter regions are shown in Figure 3.26(b). The results show that as the noise level increases, the ODI values in white matter regions deviate modestly from the reference, while in gray

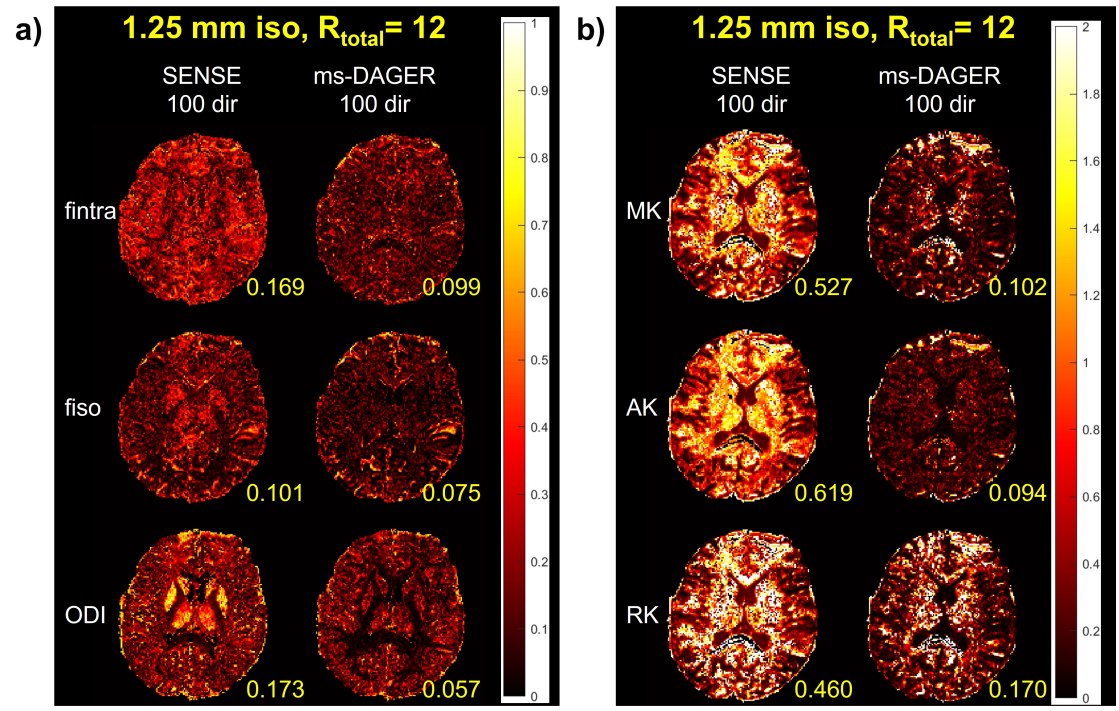

Figure 3.20: a)Error maps between NODDI fitting results from reference and reconstruction results for the 1.25 mm isotropic resolution in vivo data shown in Figure 3.19. Median absolute error values are also shown for CSF volume fraction(fiso), intracellular volume fraction(fintra) and orientation dispersion index (ODI).b)Error maps between DKI fitting results from reference and reconstruction results for the 1.25 mm isotropic resolution in vivo data shown in Figure 3.18. Median absolute error values are also shown for Mean kurtosis (MK), axial kurtosis(AK) and radial kurtosis(RK).

matter regions, ODI values significantly decrease. This aligns with the in vivo data, where ODI maps from ms-DAGER appear to be more consistent with high-SNR reference in the white matter than in the cortex. In this work, we primarily focused on dMRI protocols with two b-shells, which are commonly used in dMRI studies due to their compatibility with a large range of dMRI modelling fitting approaches and feasible acquisition times. We tested the performance of ms-DAGER with a set of 3-shell data (b = 1000, 2000, 3000s/mm^2). The preliminary results shown in Figure 3.27 demonstrated that the image quality of higher b value shell can be improved by sharing information across shells even at b = 3000s/mm^2. Our current study has some limitations. Firstly, the proposed method has not considered eddy currents. Eddy current effects can lead to geometric distortions and phase mismatch between diffusion directions and b values. The phase mismatch for

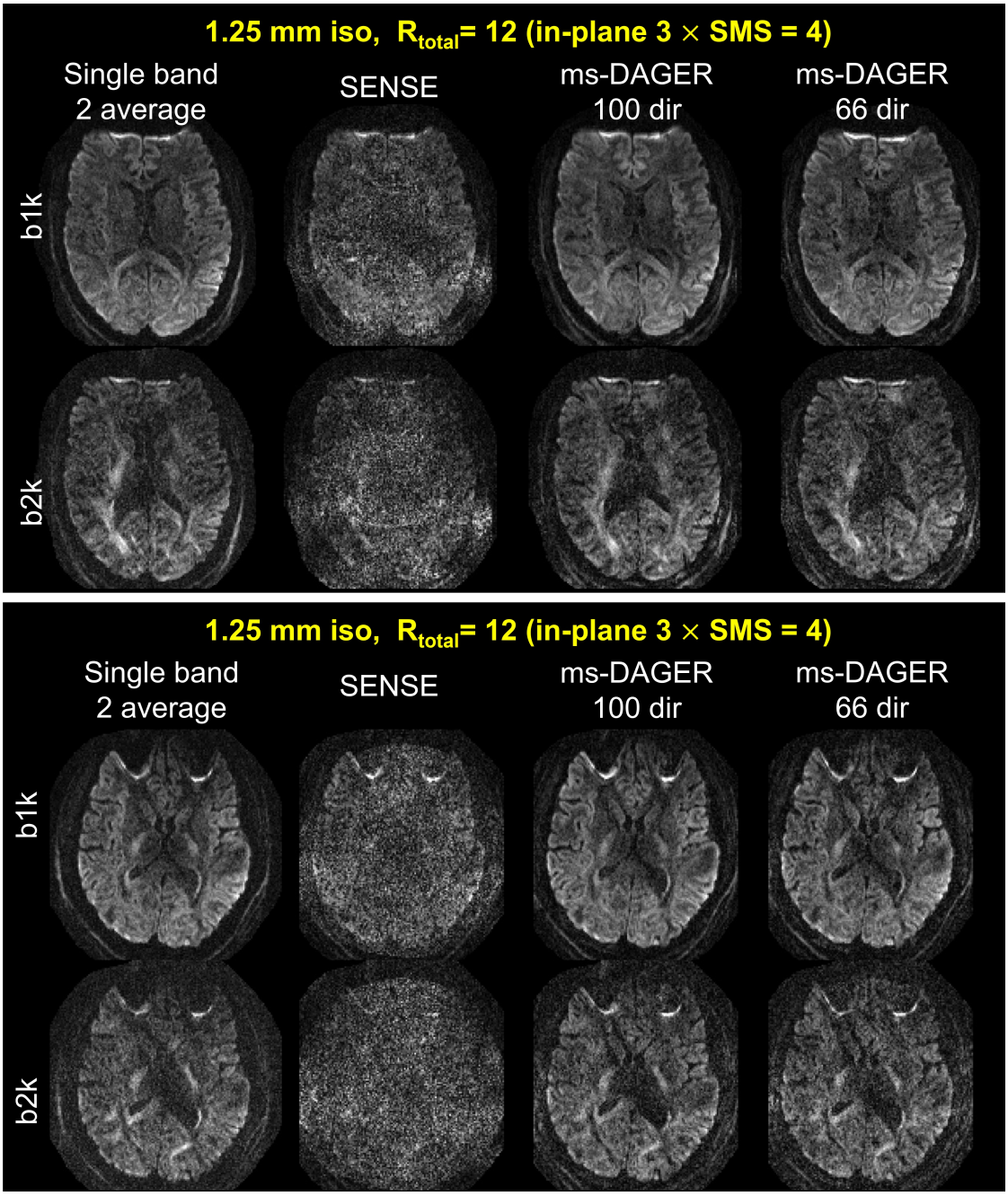

Figure 3.21: Reconstruction results for the 1.25 mm isotropic resolution in vivo data from two other subjects (subjects 6 and 7) . Single band reference images, SENSE and ms-DAGER results are shown. b=1000s/mm^2 ('b1k') and b=2000s/mm^2 ('b2k') images are both shown. ms-DAGER can consistently improve image quality.

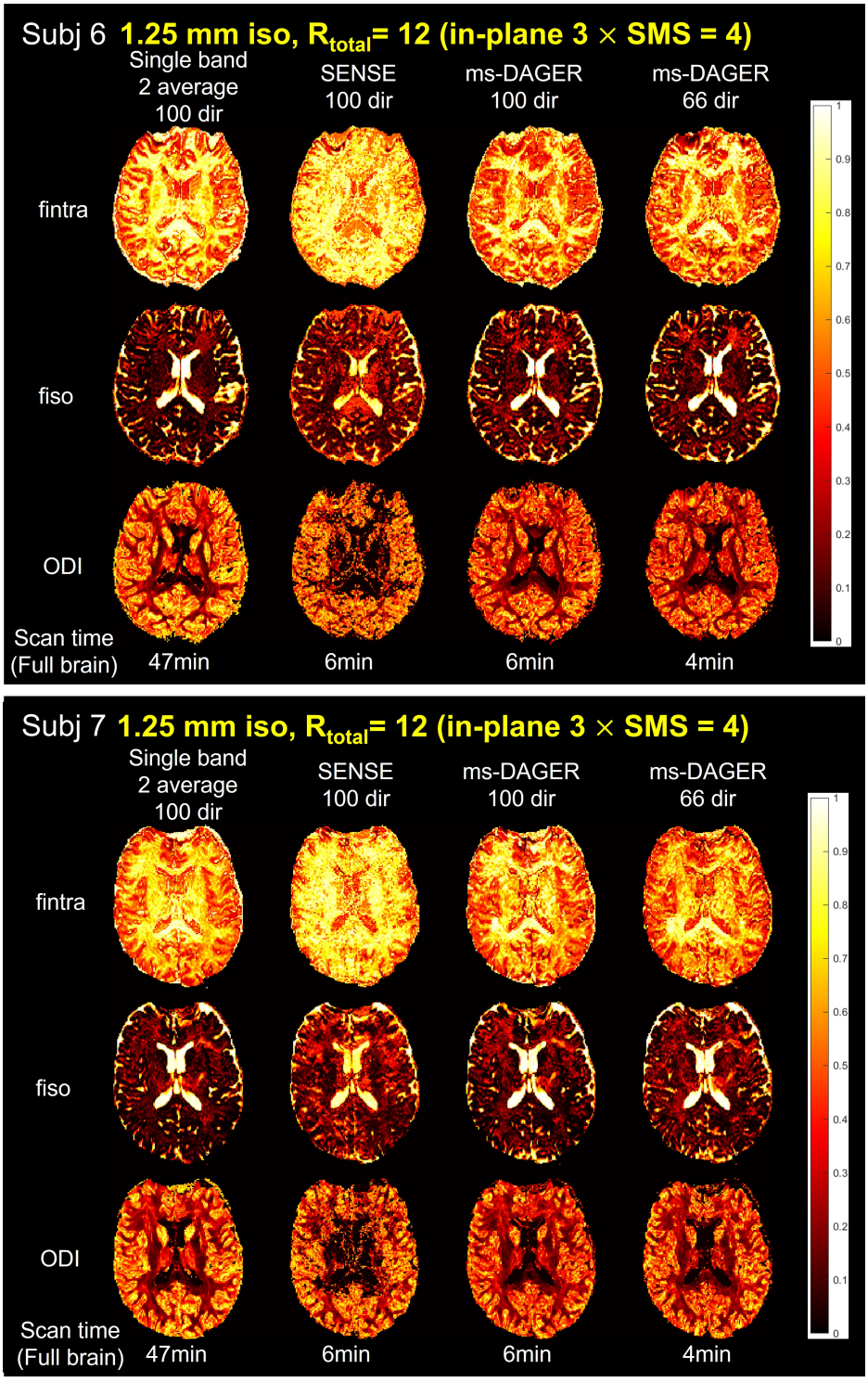

Figure 3.22: NODDI fitting results for the 1.25 mm isotropic resolution in vivo data for other subjects (subjects 6 and 7). CSF volume fraction(fiso), intra-cellular volume fraction(fintra) and Orientation dispersion index (ODI) from NODDI calculated from Single band reference images with 2 average, SENSE and ms-DAGER are shown are shown. Compared to SENSE, ms-DAGER consistently improve the fitting accuracy, showing high reproducibility across subjects

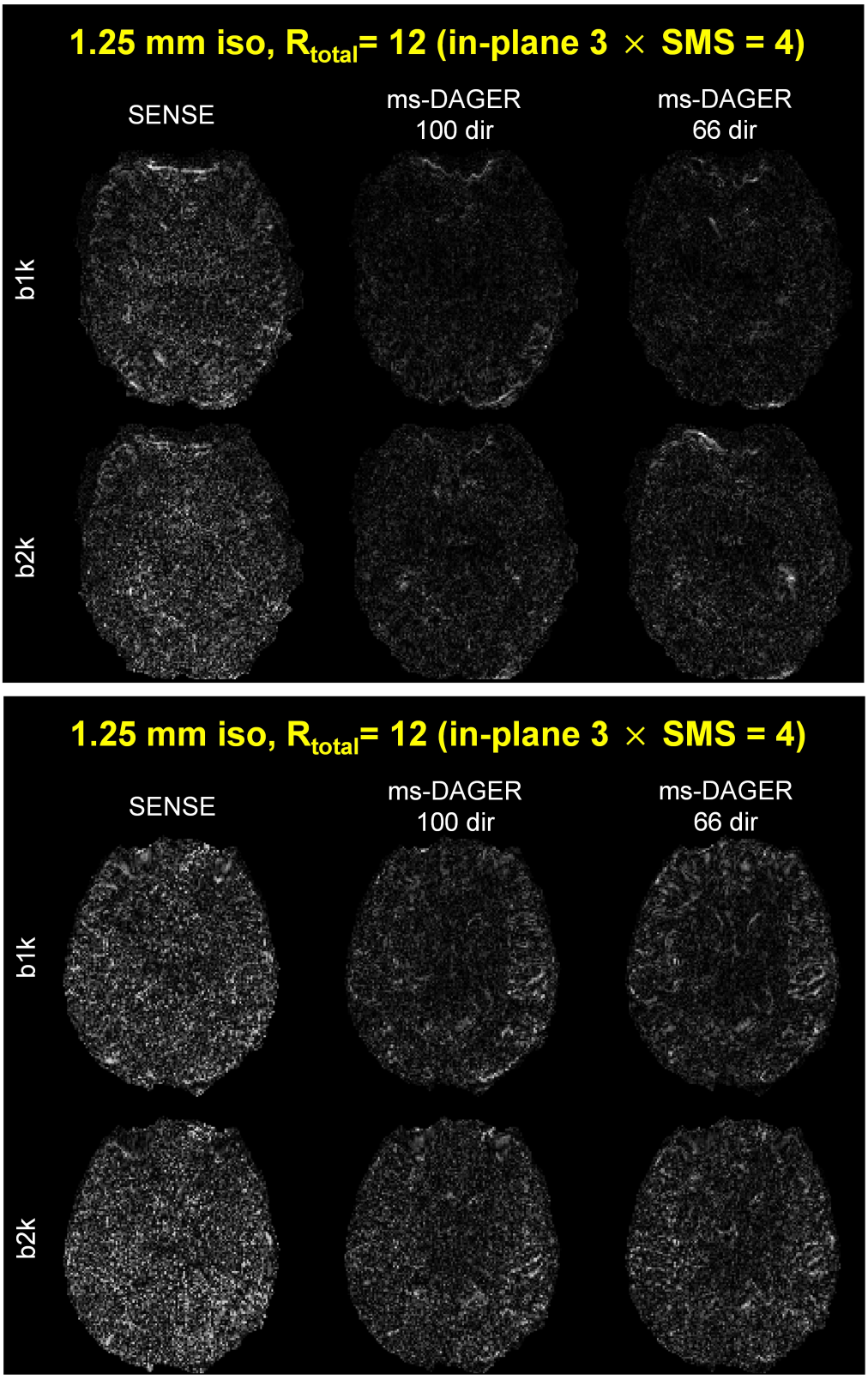

Figure 3.23: Difference maps between reference and reconstruction results for 1.25 mm isotropic resolution in vivo data from two other subjects (subjects 6 and 7) shown in Figure 3.21. Note that ms-DAGER method largely reduce the error compared to SENSE.

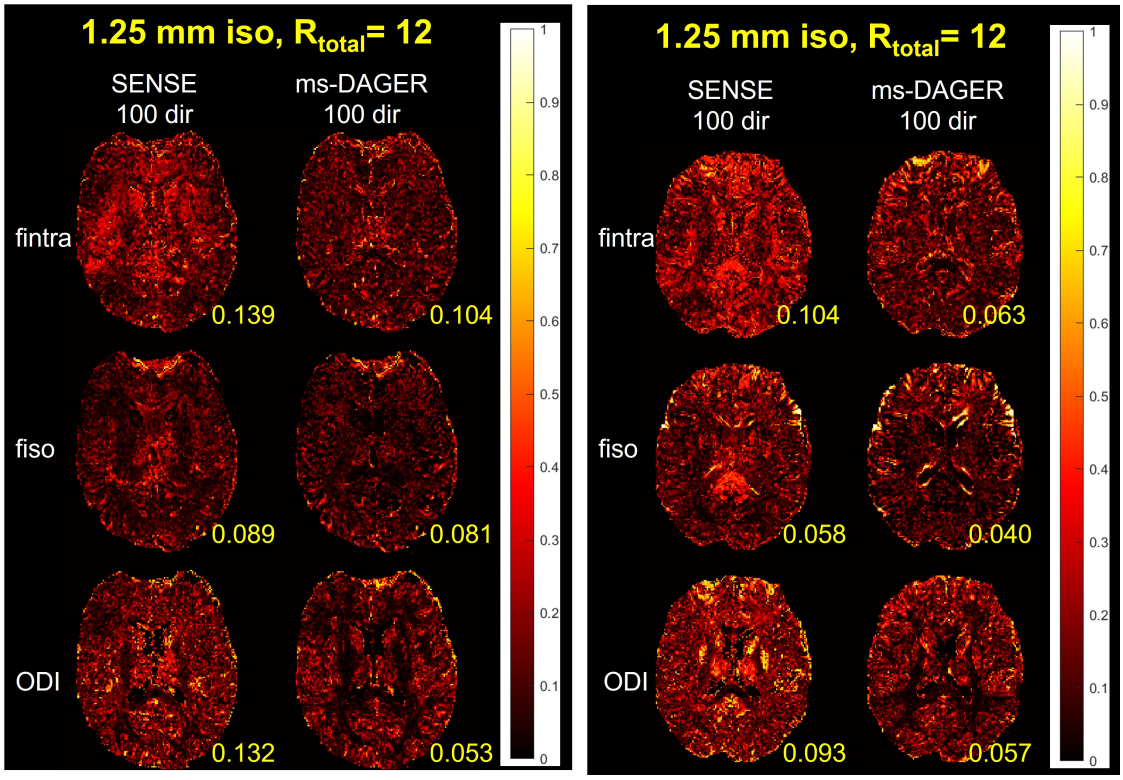

Figure 3.24: Error maps between NODDI fitting results from reference and reconstruction results for the other 1.25 mm isotropic resolution in vivo data shown in Figure 3.22 (subjects 6 and 7). Median absolute error values are also shown for CSF volume fraction(fiso), intra-cellular volume fraction(fintra) and orientation dispersion index (ODI).

different directions is captured in the phase error term P in Eq.3.8, thus corrected during the reconstruction. For the distortions effect, we used a high in-plane acceleration factor R = 3 in all our in vivo scans, resulting in modest eddy current induced distortions. We investigated this effect with a phantom scan using in-plane acceleration factor R = 3 as used for in vivo scans with the identical EPI readout and calculated the between-volume voxel shift. The results showed a max shift of 0.292 pixel with a standard deviation of 0.234 pixel, which did not introduce a major bias in the joint k-q reconstructions performed in this work. Second, we have not accounted for potential subject motion, which will have similar (but less predictable) impact on the k-q framework. In the present work, we used experienced subjects who were instructed to remain as still as possible. In examining our SENSE results, we did not observe substantial motion in any of our subjects, which may in part reflect the relatively short scan times. The high quality of ms-DAGER results

	Subj. ID	fiso	fintra	ODI
SENSE	Subj. 5	0.101	0.169	0.173
	Subj. 6	0.089	0.139	0.132
	Subj. 7	0.058	0.104	0.093
ms-DAGER	Subj. 5	0.075	0.099	0.057
	Subj. 6	0.081	0.104	0.053
	Subj. 7	0.040	0.063	0.057

Figure 3.25: Summary of the median absolute error values across subjects for NODDI fitting results. The improvement of fitting accuracy by ms-DAGER is consistent across subjects.

with crisp image edges also suggests negligible impact of eddy current distortions and motion. Nevertheless, eddy current induced distortions will be stronger with lower in-plane acceleration and motion will present in less compliant subjects. We will investigate the effects of the resulting mismatches and extend DAGER to include a correction framework in future work. Finally, the computation time of the current MATLAB implementation is long, which can be improved with algorithmic optimisation, parallel computing, and more efficient implementation.

3.6 Conclusion

We have proposed a novel reconstruction method based on Gaussian Processes to accelerate multi-shell dMRI data acquisition. Based on simulations and in vivo data, our proposed method enables multi-shell dMRI data with high spatial and angular resolution in shorter scan times compared to conventional methods. These data are of

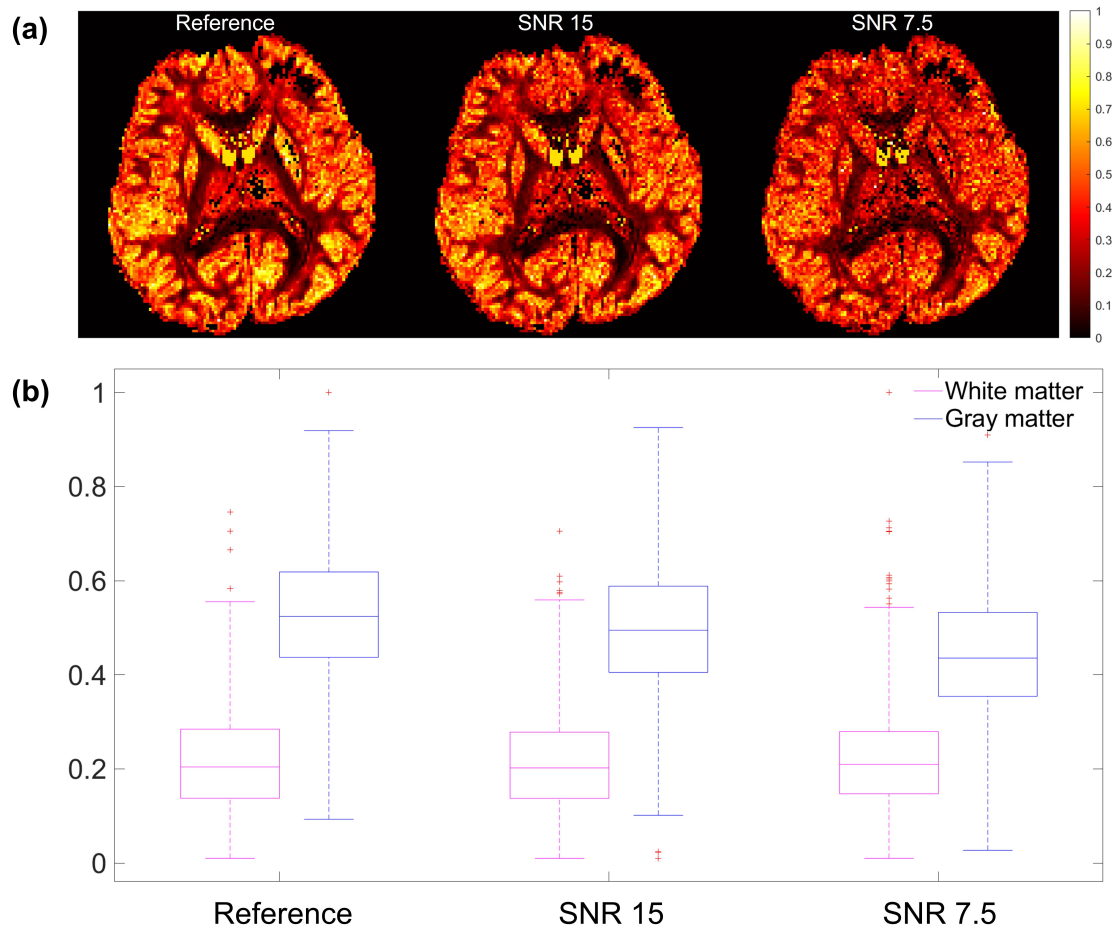

Figure 3.26: (a) ODI maps from NODDI fitting of simulation data with different noise levels (SNR 15 and SNR 7.5). The noisy datasets and the noise-free reference were fitted with NODDI. (b) Box plots showing ODI distribution within white matter region and gray matter region, respectively, for different noise levels.

sufficient quality to support advanced modelling of microstructure and tractography.

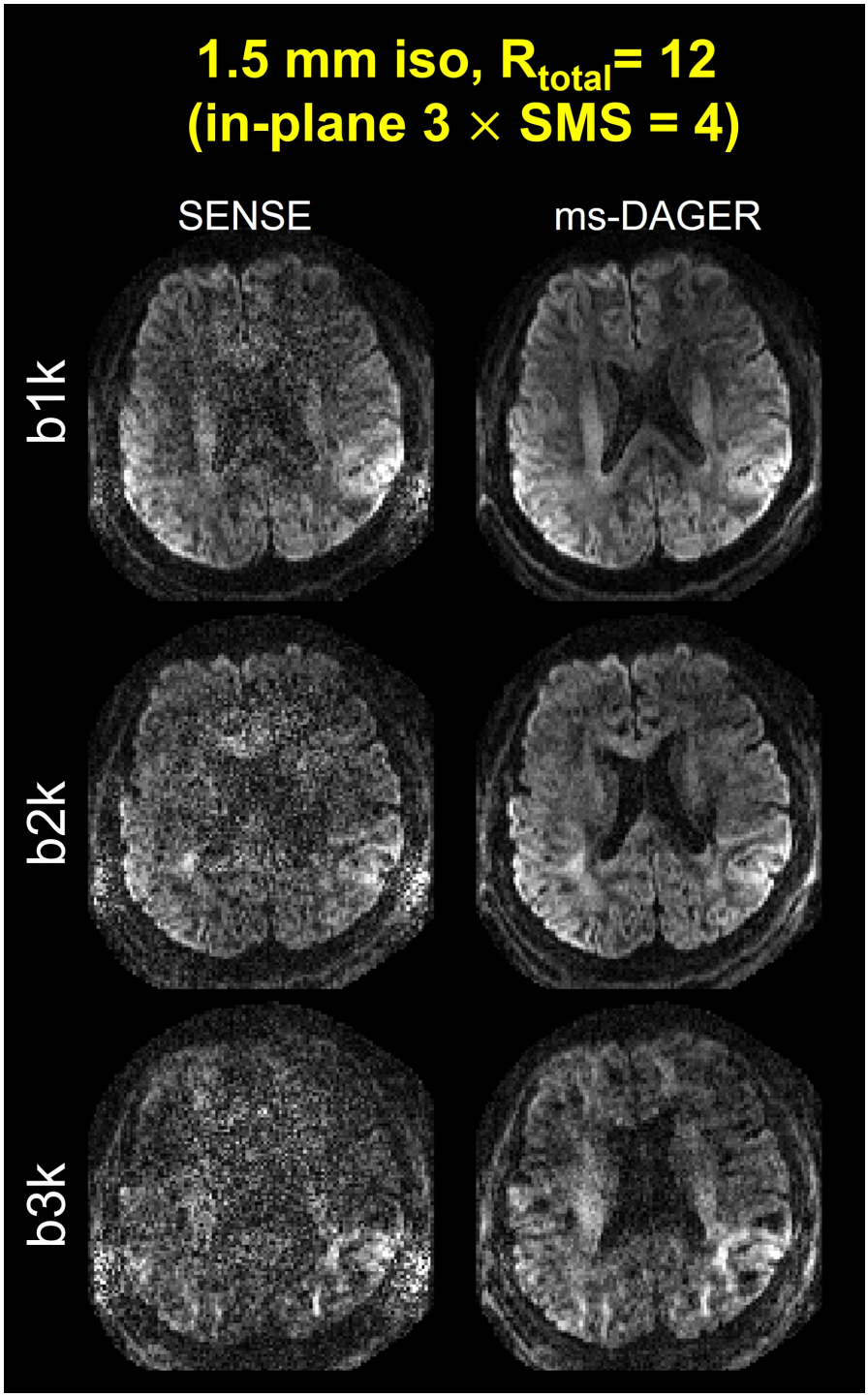

Figure 3.27: Reconstruction results for the 1.5 mm isotropic resolution 3-shell in vivo data. SENSE and ms-DAGER results are shown. b = 1000 s/mm^2 ('b1k'), b = 2000 s/mm^2 ('b2k') and b = 3000 s/mm^2 ('b3k')images are both shown. The image quality of higher b value shell can be significantly improved compared to SENSE with the help of cross-shell information sharing.

4

Eddy current and motion robust joint k-q reconstruction for accelerated multi-band diffusion MRI

Contents

This chapter describes a joint k-q reconstruction method we propose which is robust to eddy current distortion and motion for accelerated multi-shell dMRI acquisition. Eddy current distortion correction and motion correction are incorporated into the joint k-q reconstruction framework to correct for inter-volume mismatches which cause errors when sharing information in q space. An efficient

optimisation algorithm is also proposed which splits the joint motion correction and Gaussian Process estimated reconstruction into two sub-problems to improve computational efficiency. Simulation and in vivo results demonstrate that our proposed method enables robust joint k-q reconstruction under high acceleration factor (12 x) in the presence of inter-volume subject motion and strong eddy current effects. The improvement of image quality allows for more robust diffusion model fitting compared to conventional reconstruction methods, enabling advanced multi-shell diffusion analysis within a much shorter scan time. The proposed method can facilitate future application of multi-shell diffusion MRI analysis for less cooperative subjects and patients.

4.1 Introduction

Diffusion-weighted MRI (dMRI) allows non-invasive assessment of tissue microstructure and structural connectivity by measuring the motion of water molecules in biological tissues, which is widely used in basic and clinical neuroscience research [1, 2, 51, 91]. Recently, advanced dMRI models [5–8, 93] have been proposed which provide improved specificity and sensitivity in characterising tissue microstructure compared to simpler models (e.g., Diffusion Tensor Imaging[56]). However, these models typically require the acquisition of a large number of diffusion directions across multiple b shells, leading to significantly longer scan times, which poses a barrier to the clinical adaption. Therefore, accelerating data acquisition is critical for clinical translation of advanced dMRI modelling methods.

Two-dimensional (2D) single-shot EPI is commonly used in dMRI acquisition due to its rapid acquisition speed. However, as dMRI scan time is dominated by the long diffusion encoding time and 2D single-shot EPI acquires image slices sequentially, achieving higher resolution (thinner slices) with a large brain coverage requires long scan time per direction. When the total scan time is limited, this leads to a trade-off between spatial resolution and model specificity.

Many efforts have been made to accelerate the dMRI scans and mitigate this trade-off [10] including parallel imaging[11, 12]. A major advance in dMRI

acceleration is Simultaneous multislice (SMS) imaging [13, 14] which significantly reduces scan time by acquiring multiple slices simultaneously and using shared diffusion encoding. However, since dMRI data has intrinsically low SNR, the slice acceleration factor that is commonly used in dMRI is limited to 2 or 3 compared to other MRI contrasts [16, 17].

To achieve higher acceleration for dMRI, joint k-q reconstruction methods have been proposed [21–27, 73]. These methods jointly reconstruct k space data from different q space locations, exploiting the shared information in q space to enhance k space reconstruction for highly undersampled data. Diffusion Acceleration with Gaussian process Estimated Reconstruction (DAGER) is a joint k-q reconstruction method without explicit model assumption, which uses Gaussian-Process (GP) to exploit the smoothness of diffusion signals in q space to interpolate signals in a data-driven way [27]. Recently, extension of DAGER to multi-shell condition (ms-DAGER)[90] has also been proposed, which uses signal relations between diffusion directions and across different shells, showing promising results enabling highly-accelerated multi-shell dMRI acquisition.

However, since joint k-q reconstruction methods reconstruct all diffusion volumes simultaneously, they are sensitive to the inter-volume geometric mismatch, which undermines the assumption of q space smoothness. If not corrected, joint reconstruction may lead to blurring and other image artifacts in the reconstructed results. Two primary sources of such inter-volume geometric mismatch in dMRI scans are subject bulk motion and eddy current induced distortions. First, bulk motion (i.e., rotation and translation) is common during MRI scans, particularly in less cooperative subjects or long scan sessions [124, 125], which causes changes in subject position during acquisition, leading to inter-volume misalignment. Second, eddy current induced by rapid switching of diffusion encoding gradients can produce distortions that are diffusion direction and b value dependant, leading to additional geometric inconsistency across diffusion volumes [126]. Thus, motion correction and eddy current distortion correction need to be incorporated into the joint k-q reconstruction to make it robust to inter-volume mismatch.

Many researchers have explored different ways of motion correction including prospective methods in MRI acquisition with navigators or external hardware to get motion estimates[127–133] or retrospective methods in MRI reconstruction with extra navigators or data-driven approaches to learn motion estimates [28, 134–140]. And post-processing methods have also been proposed to correct for inter-volume motion [141–143] in fMRI and dMRI, which estimate the motion parameters from reconstructed image series and apply transformation to them. Meanwhile, for eddy current distortion correction, post-processing techniques including using field mapping information, field monitoring and deep learning networks [106, 144–147] have also been proposed to correct for inter-volume distortions in reconstructed image series.

However, the inter-volume motion correction and eddy current correction in joint k-q reconstruction for dMRI hasn't been incorporated before. One challenge for this problem is that it's difficult to obtain accurate motion and eddy current estimates from highly undersampled data during reconstruction when the image quality is low. Another critical challenge is the high computational burden for the combined correction and reconstruction problem. Without the presence of motion, parallel computing can be used in joint k-q reconstruction for optimisation at different spatial locations. For example, we can split the original optimisation problem into smaller segments each containing data from one readout line. However, motion correction and eddy current necessitates a combined motion- and spatial- encoding matrix that includes all spatial locations, diffusion volumes and coils in the forward model of the optimisation problem, increasing computational demands significantly.

In this research, we propose a motion-robust and eddy-current corrected joint k-q reconstruction method for multi-shell dMRI acceleration in the presence of motion and strong eddy current distortions. To tackle the challenge that it's difficult to get accurate motion and eddy current field estimates for the highly accelerated data with degraded image quality, we propose to perform rigid motion and eddy-current distortion estimation within an iterative reconstruction framework, where the motion and eddy current estimates are iteratively updated along with

the reconstruction results. Besides, to reduce the computational burden, we also develop an efficient algorithm to substantially reduce the computational burden of the reconstruction by splitting the original optimisation problem into several sub-problems which enables parallel computing and reduces memory burden.

4.2 Theory

4.2.1 Multi-shell DAGER (ms-DAGER)

A Gaussian process (GP) is a data-driven model that, rather than fitting a single function, produces an infinite set of functions that all describe the data. Specifically, each function fits the data exactly at the measured points and the collective set of functions follow a multi-variate Gaussian distribution away from the measured points. dMRI signals have a covariance structure that can be described using a multi-variate Gaussian distribution due to the smoothness in q space. Thus, the mean and variance of the dMRI signal at unseen q space locations can be predicted with GP models given this structure[106].

Multi-shell DAGER uses the GP-estimated dMRI signal as a prior and solves the following reconstruction problem in a Bayesian framework:

$$\mathbf{u} = \arg\min_{\mathbf{u}} \left(\frac{1}{2\sigma_k^2} \|\mathbf{\Omega F S u} - \mathbf{d}\|_2^2 + \frac{1}{2} (\mathbf{P}^H \mathbf{u} - \boldsymbol{\mu})^H (\mathbf{\Sigma} \otimes I_N)^{-1} (\mathbf{P}^H \mathbf{u} - \boldsymbol{\mu}) \right) \quad (4.1)$$

where $\mathbf{u}$ is the unknown image, Ω refers to undersampling operator, F refers to Fourier transform, S refers to coil sensitivity encoding, σ_k^2 is the noise variance in the k space data, which can be calculated from σ_n^2 as in [27], d is the acquired k space signal, μ is the mean value of GP prediction, $\mathbf{\Sigma}$ is the GP covariance matrix and N is the number of voxels, H is the conjugate operation and $\otimes$ is Kronecker product. P represents the motion induced phase error, which is different between diffusion directions. Note that, when the inter-volume motion and eddy current-induced distortions exist among different diffusion volumes, there will be errors during fitting GP prior since it uses data from different volumes to explore sharing information at different q space locations. This will lead to blurring and artifacts in the reconstructed images as shown in Figure 4.1(a).

4.2.2 Motion-robust multi-shell DAGER (mr-ms-DAGER)

In this work, we aim to integrate motion and eddy current correction into multi-shell DAGER to accelerate multi-band dMRI acquisitions in the presence of strong eddy current and motion.

To begin with, eddy current effects lead to both phase mismatch and geometric distortions between different q space points. The phase mismatch for different volumes is captured in the phase error term P in Eq.4.1, thus corrected during the reconstruction. For the distortion effect, assuming that the eddy current induced field map offset is $\triangle f$, a phase term Φ in k space is generated as the following equation:

$$\Phi_k = \exp(-i \cdot 2 \cdot \pi \cdot \triangle f \cdot t_k) \tag{4.2}$$

Where t_k is the echo time of the k th phase encoding line. Due to the different field offsets in different diffusion directions, the distortions vary among volumes, leading to geometric mismatches. Thus, we propose to incorporate the phase term Φ into the forward model to model the eddy current effects.

Secondly, for the motion correction, in this work we focus on the rigid motion caused by participant head motion during scans. To model the rigid transformation, we incorporate a rigid motion operator $\mathbf{T}$ as in [28], which uses convolution-based interpolation technique to perform rotations without any gridding. The rigid motion is split into three consecutive shearing applied in hybrid image/k space and translation in k space. The 3D rigid transformation is represented as:

$$\begin{aligned}\mathbf{T}^H =& F^H U F F_2^H V^{\tan} F_1 F_2^H V^{\sin} F_3 F_2^H V^{\tan} F_2 \times F_3^H V^{\tan} F_2 F_3^H V^{\sin} F_1 F_3^H V^{\tan} F_3 \\ & \times F_1^H V^{\tan} F_3 F_1^H V^{\sin} F_2 F_1^H V^{\tan} F_1\end{aligned} \tag{4.3}$$

where F is the 3D Fourier transform and F_j is the Fourier transform along dimension j. The U and V are the diagonal matrices for translation and shearing operation along different axes. whose diagonal vectors u_s and v_s determined by:

$$
\begin{aligned}
\mathbf{u}_s &= e^{-j(q_{1s}k_1+q_{2s}k_2+q_{3s}k_3)} \\
\mathbf{v}_{1s}^{\tan} &= e^{j\tan(\theta_{1s}/2)k_2}\mathbf{r}_3 \qquad & \mathbf{v}_{1s}^{\sin} &= e^{-j\sin(\theta_{1s})k_3}\mathbf{r}_2 \\
\mathbf{v}_{2s}^{\tan} &= e^{j\tan(\theta_{2s}/2)k_3}\mathbf{r}_1 \qquad & \mathbf{v}_{2s}^{\sin} &= e^{-j\sin(\theta_{2s})k_1}\mathbf{r}_3 \\
\mathbf{v}_{3s}^{\tan} &= e^{j\tan(\theta_{3s}/2)k_1}\mathbf{r}_2 \qquad & \mathbf{v}_{3s}^{\sin} &= e^{-j\sin(\theta_{3s})k_2}\mathbf{r}_1
\end{aligned}
\tag{4.4}
$$

where k_l is the k-space coordinate along dimension l, r_l is the spatial coordinate along dimension l,θ_l and q_l are the rotation and translation parameters respectively.

To correct for motion-induced mismatch between diffusion volumes in the reconstruction, we incorporate the inverse motion operator $\mathbf{T}^H$ which transforms the data from native (motion) space to aligned space for GP fitting into Eq.4.1 in the forward model:

$$
\mathbf{u} = \arg\min_{\mathbf{u}} \left(\frac{1}{2\sigma_k^2} \|\mathbf{\Omega\Phi FSu} - \mathbf{d}\|_2^2 + \frac{1}{2}(\mathbf{T}^H\mathbf{P}^H\mathbf{u} - \boldsymbol{\mu})^H(\mathbf{\Sigma} \otimes I_N)^{-1}(\mathbf{T}^H\mathbf{P}^H\mathbf{u} - \boldsymbol{\mu}) \right)
\tag{4.5}
$$

For simplicity we define$\mathbf{A} = \mathbf{\Omega\Phi FSu}$. We name this method as motion-robust multi-shell DAGER (mr-ms-DAGER). With this formulation, motion operator $\mathbf{T}^H$ is on the forward encoding operator. The combined motion ($\mathbf{T}^H$ $\mathbf{P}^H$) and spatial encodings ($\mathbf{A}$) in the forward model includes voxels from all diffusion volumes across all spatial locations from all coils. Thus, direct inversion for the optimisation problem is computationally challenging ($\geq$ 80 GB memory for 1.5 mm resolution, 32-coil, 66-directions).

4.2.3 Computationally efficient optimisation algorithm

To improve computational efficiency, we split the reconstruction formulation into the following steps by incorporating another variable $\mathbf{v_k}$ representing a motion-corrected GP prior in the aligned space based on variable splitting:

Step-1: For iteration k, we first use FSL's [118] eddy to estimate the volume-to-volume rigid motion parameters (translation and rotation along three spatial axes) along with the eddy current induced field offset $\triangle f$ using reconstruction result $\mathbf{u_{k-1}}$ from the previous iteration (SENSE reconstruction results for the initial iteration), and then construct a rigid motion operator $\mathbf{T}^H$ based on the

estimated rigid motion parameters. After that, GP prior $\mathbf{v_k}$ is updated in the aligned space using a Bayesian framework:

$$\mathbf{v}_k = \arg\min_{\mathbf{v}} \left(\frac{\rho}{2} \|\mathbf{v} - \mathbf{T}^H \mathbf{P}^H \mathbf{u}_{k-1}\|_2^2 \right) + \frac{\sigma_k^2}{2} (\mathbf{v} - \boldsymbol{\mu})^H (\boldsymbol{\Sigma} \otimes \mathbf{I}_N)^{-1} (\mathbf{v} - \boldsymbol{\mu}) \quad (4.6)$$

Here, ρ is a convergence controlling parameter and gradually increases with more iterations.

Step-2: The updated GP prior $\mathbf{v_k}$ is transformed to the native space by applying the motion operator $\mathbf{T}$. It's used for later constrained reconstruction of k space data to solve $\mathbf{u_k}$. Here phase term Φ is updated based on $\triangle f$ obtained in step-1:

$$\mathbf{u}_k = \arg\min_{\mathbf{u}} \left(\frac{1}{2} \|\mathbf{A}\mathbf{u} - \mathbf{d}\|_2^2 + \frac{\rho}{2} \|\mathbf{P}^H \mathbf{u} - \mathbf{T}\mathbf{v}_k\|_2^2 \right) \quad (4.7)$$

An overview of these steps is shown in Figure 4.1(b). Note that, in Eqs. 4.6 and 4.7, $\mathbf{T}$ and $\mathbf{T}^H$ operators are no longer applied to the unknowns, so there is no need to inverse the large encoding matrix containing $\mathbf{T}$ and $\mathbf{T}^H$. The motion-related terms in all equations can be calculated before solving the optimisation problem and served as a constant term, allowing efficient computation using parallel computing for each optimisation.

4.3 Method

4.3.1 Simulation

We first evaluated the performance of mr-ms-DAGER using realistic simulations. Motion corrupted data were simulated based on conventional 2D 1.5 mm isotropic resolution in vivo dMRI dataset without slice acceleration and with 33 b = 1000 s/mm^2 and 33 b = 2000 s/mm^2 uniformly sampled q space points acquired on a Siemens 7T scanner. FSL's eddy was performed to correct for eddy current distortion and motion in the data followed by performing MPPCA denoising [148] implemented in Mrtrix3(https://www.mrtrix.org/). We used the denoised and eddy-corrected data as the motion-free reference image. For mr-ms-DAGER reconstruction, we optimised k-q undersampling using a graph model [113] that aims for each q

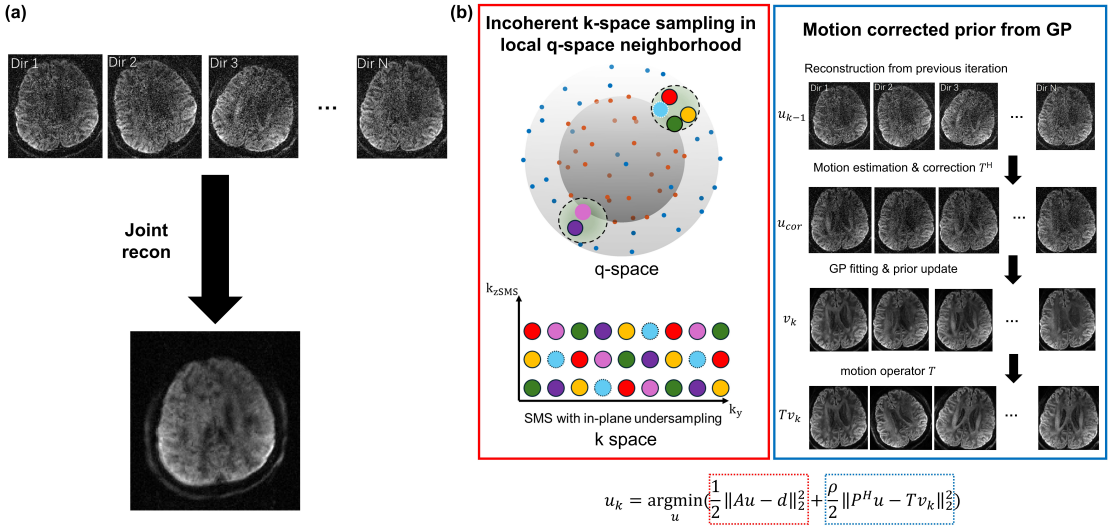

Figure 4.1: (a)Joint k-q reconstruction for diffusion volumes with mismatches. Blurring artifacts are introduced in the results. (b)Flowchart of the proposed mr-ms-DAGER method. On the left shows the incoherent k space undersampling patterns in local q space neighbourhood. On the right shows how the GP prior is derived. The dMRI data from native space are firstly corrected into motion-free space and then fit a GP prior. The GP prior is then transformed back to the motion space for the constrained reconstruction.

space neighbourhood (across directions and shells) to have highly diverse k space undersampling patterns as in our previous works[27, 90]. A $\frac{FOV}{4}$ shift CAIPI pattern is used. Multi-channel datasets were simulated with 32-channel head coil sensitivity maps and a total acceleration factor of 12 (in-plane R = 3, SMS = 4) with added noise. Random 3D rigid motion was added to each volume (maximum translation 2mm and maximum rotation angle 5°) in the simulation data.

4.3.2 In vivo acquisition

Four subjects were scanned on a Siemens 3T scanner. Informed consent in accordance with local ethics was obtained before each scan. A 2D spin-echo dMRI sequence was modified to include SMS acquisition and blipped-CAIPI encoding with highly variable k space undersampling patterns for each q space neighbourhood. A 32-channel coil was used with coil sensitivities measured using a segmented EPI sequence. The dMRI data were acquired with in-plane acceleration R = 2 and multi-slice acceleration SMS = 6 (total acceleration factor = 12). The subjects were scanned with 1.5 mm isotropic resolution (TE = 65 ms). Other parameters:

TR = 1.8 s, partial Fourier 6/8, 90 slices over 15 multi-slice sets. For each subject, accelerated dMRI data were acquired twice. In the first session, the subjects were instructed to keep still and in the other session, the subjects were instructed to perform head motion (both translation and rotation) during the scan by pointing their nose to a marker shown on the screen in the scanner which moves to a new position each 30 s as shown in Fig 4.2. 3D rigid motion is performed during the scan.. For each subject, we acquired a high-SNR reference of non-slice-accelerated ("single-band") data with matched TR (covering 15 slices to reduce scan time) and in-plane acceleration R = 2 without guided motion.

We acquired two dMRI datasets with 100 and 66 diffusion directions staggered across two shells (b = 1000 s/mm^2 and 2000 s/mm^2) using optimised k-q sampling patterns and an equal number of directions for each shell (50 b = 1000 s/mm^2 and 50 b = 2000 s/mm^2 etc.) to test the performance of mr-ms-DAGER for subject 1 to subject 4.

Seq	Accelerated DWI	Singleband Ref	Singleband b0
TE (ms)	65	65	65
TR (ms)	1800	1800	1800
Resolution (mm^3)	1.5×1.5×1.5	1.5×1.5×1.5	1.5×1.5×1.5
MB	6	1	1
PAT	2	2	2
Partial Fourier	6/8	6/8	6/8
b value ($s \cdot mm^{-2}$)	1000,2000	1000,2000	0
Diffusion directions	100/66	100	6 AP + 1 PA
Scan time	180s/118.8s	180s x 6 (6 bands)	12.6s x 6 (6 bands)

Table 4.1: In vivo acquisition protocols

4.3.3 Reconstruction Implementation

We perform motion and eddy current field estimation in an iterative way. For the initial iteration, we used BM4D [149] to denoise initial reconstruction results from SENSE and used FSL's eddy to estimate the parameters based on denoised images. Then for each iteration, we used FSL's eddy to update the parameters using the reconstruction results from last iteration. For the first three iterations,

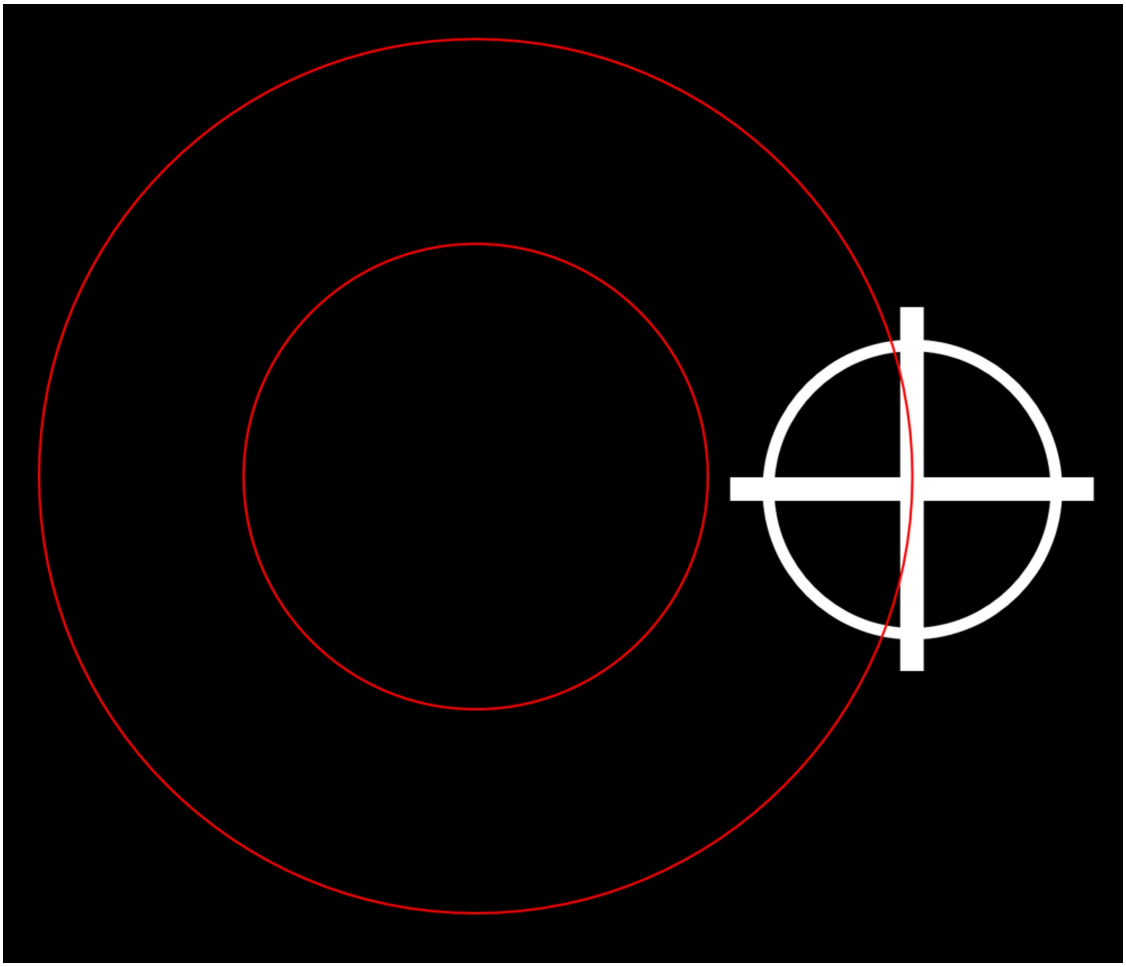

Figure 4.2: Motion guidance for in vivo scans. The subjects are asked to point their nose to the marker which moves each 30s on the screen.

BM4D was used to denoise the reconstruction results to get more accurate motion and eddy current field estimates.

Due to the degraded image quality of highly accelerated dMRI data, during the starting iterations, the eddy current field and motion estimates may not be accurate. Thus joint reconstruction may introduce bias and blurring into the reconstructed images, which accumulates in later iterations. When the motion is mild, the effects may be negligible but when the motion is large, the reconstructed images may be severely affected, leading to residual artifacts in the reconstruction results even after many iterations. To tackle this problem, we firstly perform joint reconstruction for several iterations to get more accurate motion estimates from higher SNR reconstruction results. Then we used these motion estimates and started

with the initial data (SENSE results) again to perform iterative reconstruction. In this way, the accumulated artifacts caused by the bias of motion estimates from initial iterations can be reduced.

When motion happens, the diffusion sensitizing direction from the diffusion weighting gradient deviates from the designed diffusion direction vector, leading to different diffusion contrasts. Thus, when fitting the GP prior, we used the corrected directions of diffusion weighting obtained from FSL's eddy to calculate the covariance function between different volumes.

4.3.4 Post-processing

For the in vivo data, Gibbs ringing artifacts were removed using degibbs3D from mrtrix3 (https://www.mrtrix.org/) followed by correction of distortions and motion using FSL's eddy tools (note that after mr-ms-DAGER reconstruction, the reconstructed images are still in motion space). NODDI metrics were calculated using FSL[119].We also fitted the data using the ball-and stick model with Bedpostx [112]. Finally, we compared the whole brain tractography results between the reconstructed images and the single band whole brain reference images using autoPtx toolbox[121].

4.4 Result

Reconstruction results for motion-corrupted simulation data are shown in Figure 4.3. Figure 4.3(a) compares the reconstructed DWI images from SENSE, ms-DAGER and mr-ms-DAGER. Compared to SENSE, ms-DAGER and mr-ms-DAGER improves image SNR by sharing information between different diffusion directions. However, due to the existence of geometric mismatches caused by motion, the jointly fitted GP prior introduces blurring into ms-DAGER while mr-ms-DAGER method corrects for the inter-volume mismatch, showing structural details consistent with the reference. Motion parameter estimates are shown in Figure 4.3(b). Due to the lower image SNR at first iterations, the motion parameter estimates show errors compared to the ground truth. However, after 4 iterations, estimation of all motion parameters

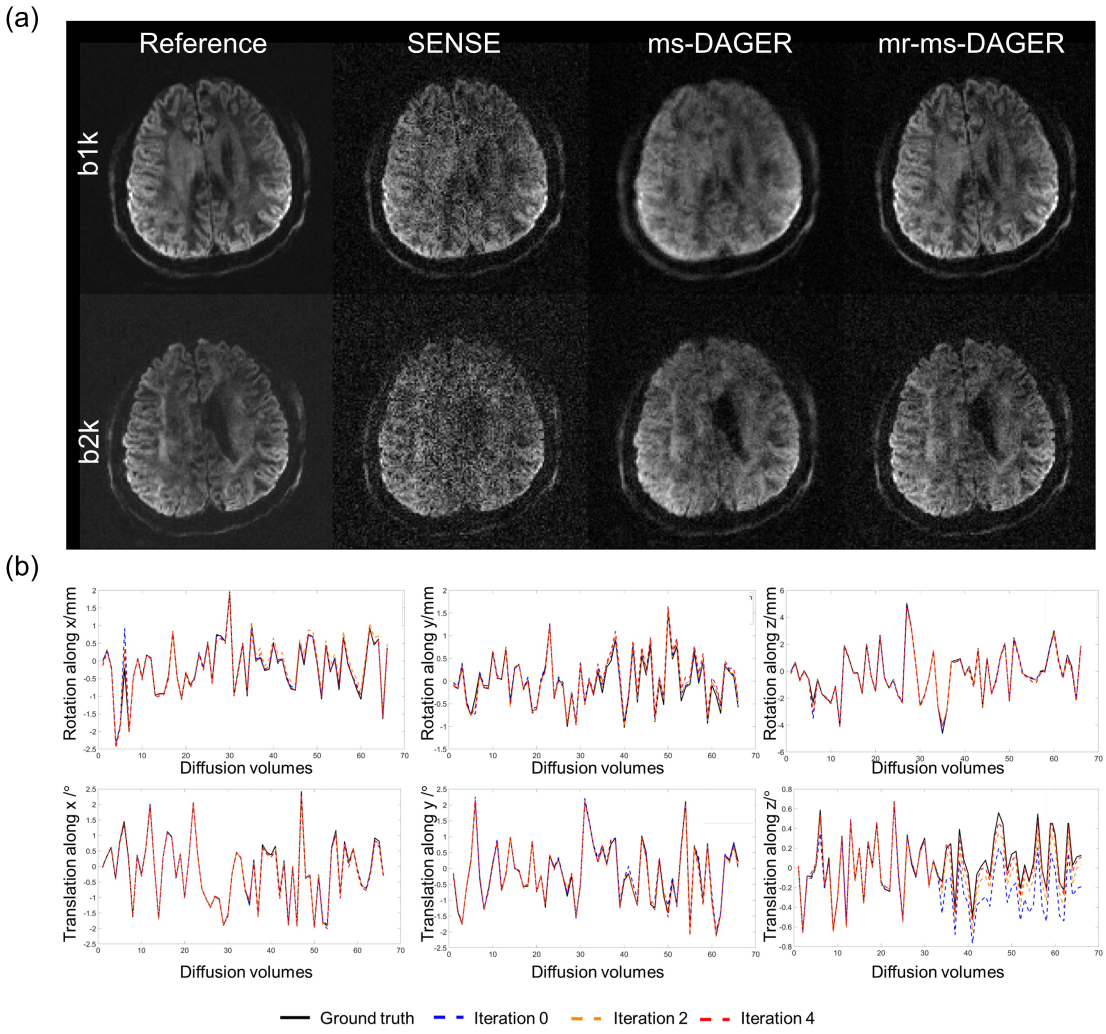

Figure 4.3: (a)Reconstruction results when random 3D rigid motion exists across all volumes. Reference images, SENSE images, multi-shell DAGER (ms-DAGER) and motion robust multi-shell DAGER (mr-ms-DAGER) results are shown. b = 1000 s/mm^2 ('b1k') and b = 2000 s/mm^2 ('b2k') images are both shown. (b) Motion parameter estimation results. eddy-estimated results based on images from different iterations along with the ground truth are shown. The motion has six degrees of freedom. (rotation along x,y,z and rotation along x,y,z)

converges to the ground truth as the image SNR increases, demonstrating the effectiveness of jointly updated motion estimates and reconstruction.

In this work, we proposed an efficient algorithm by splitting the original optimisation problems into sub-problems in native (motion) space and aligned space respectively. To test the influence of this framework, we compared the mr-ms-DAGER method with the previously proposed multi-shell DAGER method (ms-

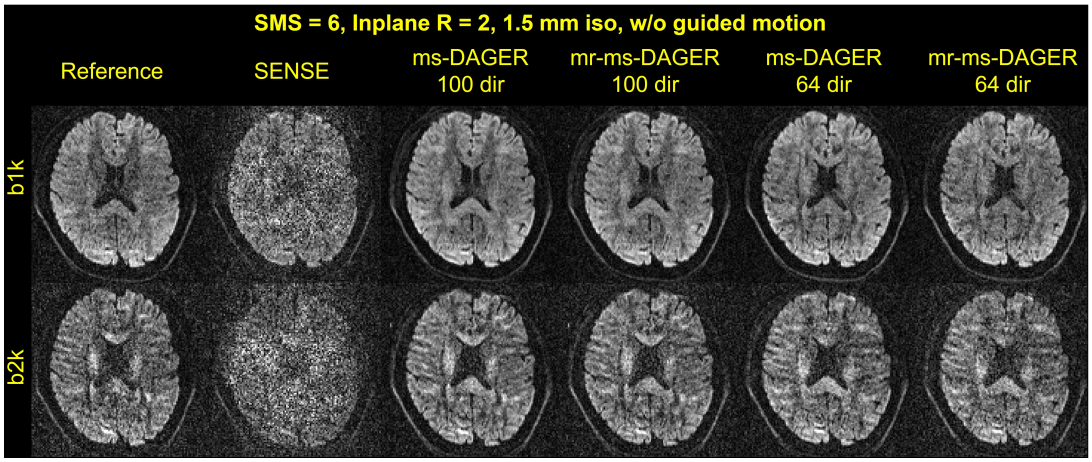

Figure 4.4: Reconstruction results for subject 1 data without guided motion evaluating mr-ms-DAGER framework. Singleband reference images, SENSE images, multi-shell DAGER (ms-DAGER) and motion-robust multi-shell DAGER (mr-ms-DAGER) results are shown. b = 1000 s/mm^2 ('b1k') and b = 2000 s/mm^2 ('b2k') images are both shown. Note that the 64-dir datasets have different diffusion directions compared to reference. mr-ms-DAGER and ms-DAGER show similar results consistent with the reference and improve SNR significantly compared to the SENSE results, validating the proposed computational efficient optimisation framework.

DAGER) with eddy current correction on the 100-dir and 64-dir datasets acquired without guided motion for subject 1. As shown in Figure 4.4, reconstruction results for b = 1000 $s/mm^2$and b = 2000 s/mm^2 ('b1k' and 'b2k') are shown. Without guided motion, mr-ms-DAGER produces similar results compared to reference and ms-DAGER, improving the image quality significantly compared to SENSE, thus validating the proposed variable splitting optimisation framework. Note that the 64-dir result and reference have different contrasts due to different directions chosen.

Figure 4.5 compares the mr-ms-DAGER method with and without incorporating eddy current correction using the 100-direction dataset acquired without guided motion from subject 2. b = 1000 s/mm^2 ('b1k') and b = 2000 s/mm^2 ('b2k') images are both shown. As shown in the figure, mr-ms-DAGER without incorporating eddy current correction produces blurry boundaries pointed by the red arrows compared to the reference images due to geometric distortions induced by eddy current. Meanwhile, mr-ms-DAGER with eddy current correction produces consistent structure pointed by the red arrows compared to reference, demonstrating the benefit of incorporating eddy current correction into reconstruction.

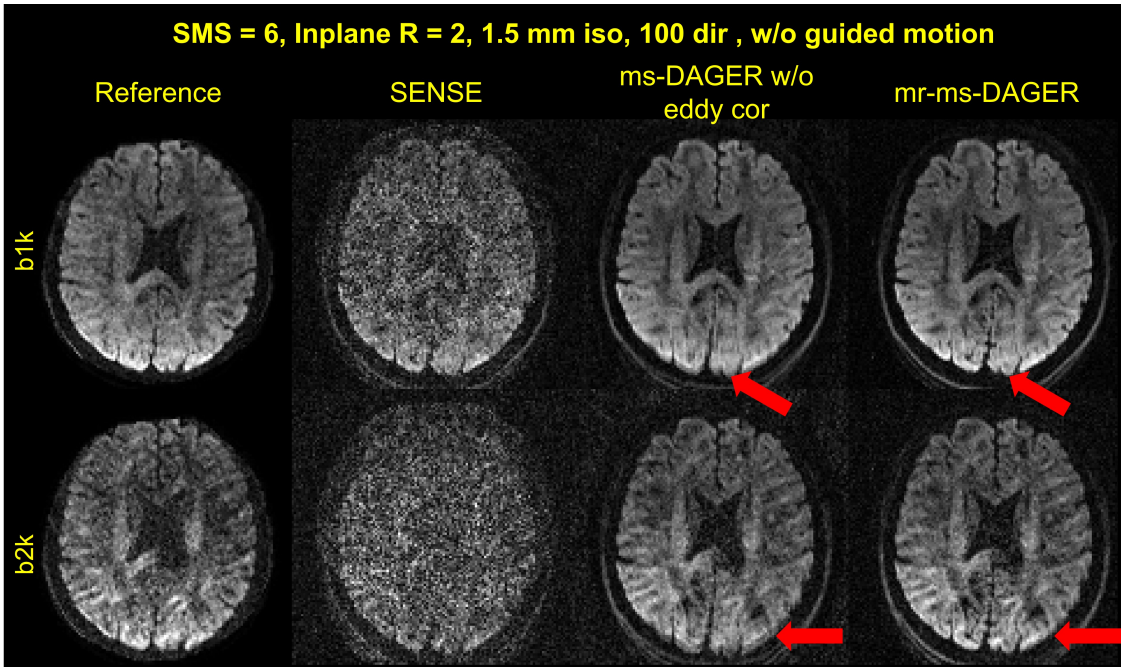

Figure 4.5: Reconstruction results for subject 2 evaluating eddy current correction. Singleband reference images, SENSE images, multi-shell DAGER without eddy correction (ms-DAGER w/o eddy cor) and motion-robust multi-shell DAGER with eddy correction (mr-ms-DAGER) results are shown. b = 1000 s/mm^2 ('b1k') and b = 2000 s/mm^2 ('b2k') images are both shown. As shown in the regions marked by the red arrows, ms-DAGER without eddy correction produces blurry boundaries while mr-ms-DAGER with eddy correction can recover detailed structure information consistent with the reference.

Figure 4.6 shows the reconstruction results for b = 1000 s/mm^2 and b = 2000 s/mm^2 ('b1k' and 'b2k') from SENSE, ms-DAGER and mr-ms-DAGER for subject 1 with a mild level of motion for 100-dir dataset (maximum rotation 4.2°, displacement 0.5 mm). As motion exists between reference scans and the accelerated scans, to better illustrate the comparison on the structure details, we firstly used FSL's mcflirt to register the images from different methods and got the rigid transform parameters. Then we used the motion operator as in Eq.4.3 to align the images with the transform parameters to avoid the smoothing effects the registration step may introduce. Compared to SENSE, both ms-DAGER and mr-ms-DAGER significantly improve the image SNR. However, due to the existence of motion, ms-DAGER shows blurred structure details compared to reference as marked by the red boxes. Meanwhile, mr-ms-DAGER corrects for the inter-volume mismatch, showing more consistent structure details with the reference.

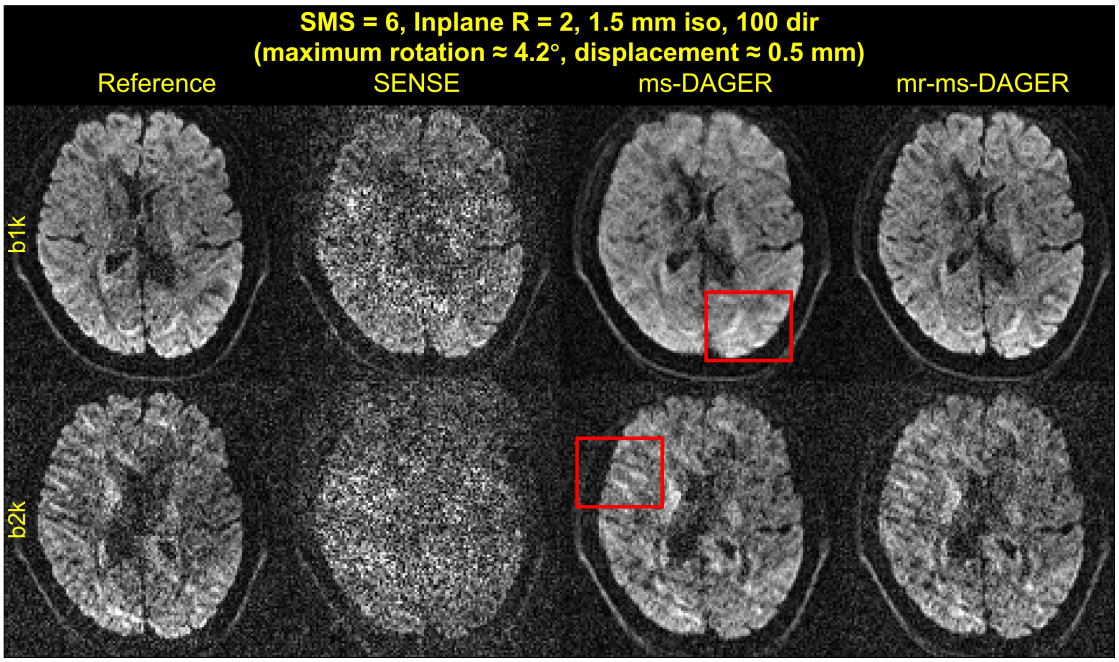

Figure 4.6: Reconstruction results for 100-dir dataset from subject 1 with mild level of motion (maximum rotation 4.2°, displacement 0.5 mm) during the scan. Singleband reference images, SENSE images, multi-shell DAGER (ms-DAGER) and Motion robust multi-shell DAGER (mr-ms-DAGER) results are shown. b = 1000 s/mm^2 ('b1k') and b = 2000 s/mm^2 ('b2k') images are both shown. ms-DAGER produces blurred structure details due to the inter-volume mismatch while mr-ms-DAGER still shows sharp structure edges similar to the reference as marked by the red boxes.

Figure 4.7 shows the reconstruction results for b = 1000 s/mm^2 and b = 2000 s/mm^2 ('b1k' and 'b2k') from SENSE, ms-DAGER and mr-ms-DAGER for subject 1 with a mild level of motion for 64-dir dataset(maximum rotation 1.9°, displacement 0.4 mm). With a reduced number of directions, both ms-DAGER and mr-ms-DAGER can still improve image quality and reduce artifacts using sharing information compared to SENSE. mr-ms-DAGER improves the image sharpness compared to ms-DAGER which suffers from inter-volume mismatch.

Figure 4.8 shows the parameters from NODDI fitting for 100-dir subject 1 dataset with mild motion (maximum rotation 4.2°, displacement 0.5mm), specifically, maps for isotropic fraction (fiso), intra-cellular fraction (fintra), and orientation dispersion index (ODI). Due to the high total acceleration (12x), SENSE results are severely corrupted by noise for all maps. ms-DAGER results show more bias due to motion artifacts in the reconstruction as marked by the blue box as it loses detailed

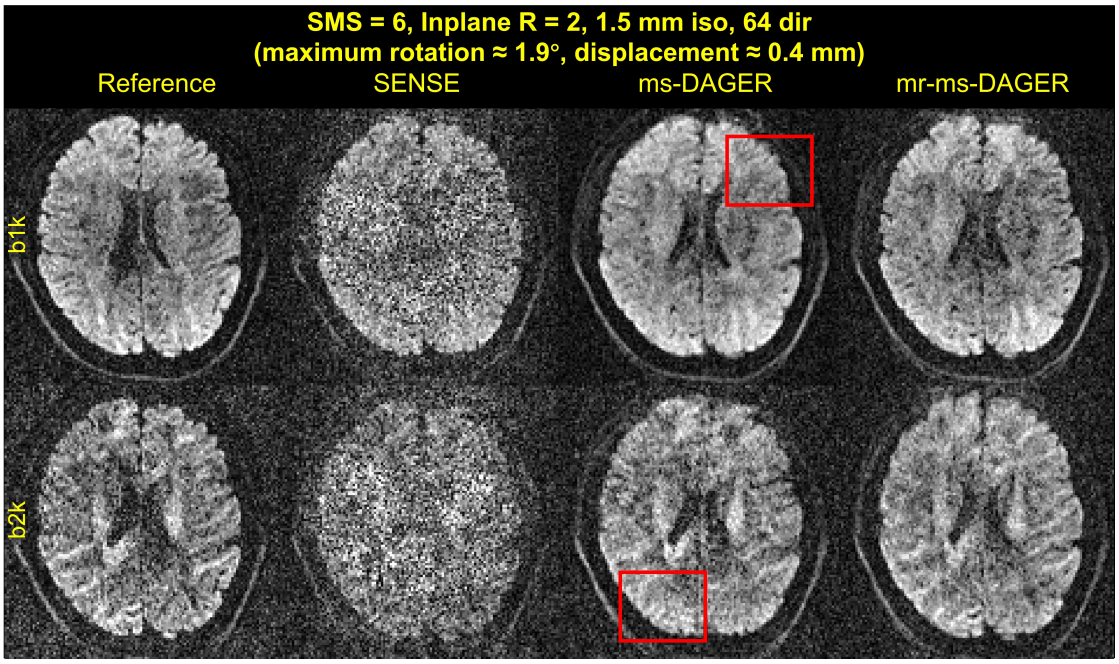

Figure 4.7: Reconstruction results for 64-dir dataset from subject 1 with mild level of motion (maximum rotation 1.9°, displacement 0.4 mm) during the scan. Singleband reference images, SENSE images, multi-shell DAGER (ms-DAGER) and Motion robust multi-shell DAGER (mr-ms-DAGER) results are shown. b=1000ss/mm^2 ('b1k') and b=2000ss/mm^2 ('b2k') images are both shown. Though the number of diffusion volumes is decreased, mr-ms-DAGER still improves the SNR and showing similar structural details compared to reference, demonstrating improved sharpness in the regions compared to ms-DAGER marked by the red boxes.

information in ODI map while mr-ms-DAGER demonstrates more robust fitting results consistent with the reference in a much shorter scan time.

Figure 4.9 shows the reconstruction results for b = 1000 s/mm^2 and b = 2000 s/mm^2 ('b1k' and 'b2k') from different methods for 100-dir dataset from subject 2 who showed a higher level of motion during scan(maximum rotation 10.8°, displacement 4 mm). ms-DAGER and mr-ms-DAGER can suppress noise with joint reconstruction but with larger mismatches between different diffusion volumes, more obvious blurring effects can be found in the ms-DAGER results, which may lead to error in the later fitting analysis. mr-ms-DAGER, however, can still preserve sharp boundary details, showing similar image quality as the single-band reference images.

Figure 4.10 shows the reconstruction results for b = 1000 s/mm^2 and b=2000 s/mm^2 ('b1k' and 'b2k') from different methods for 64-dir dataset from subject 2 who

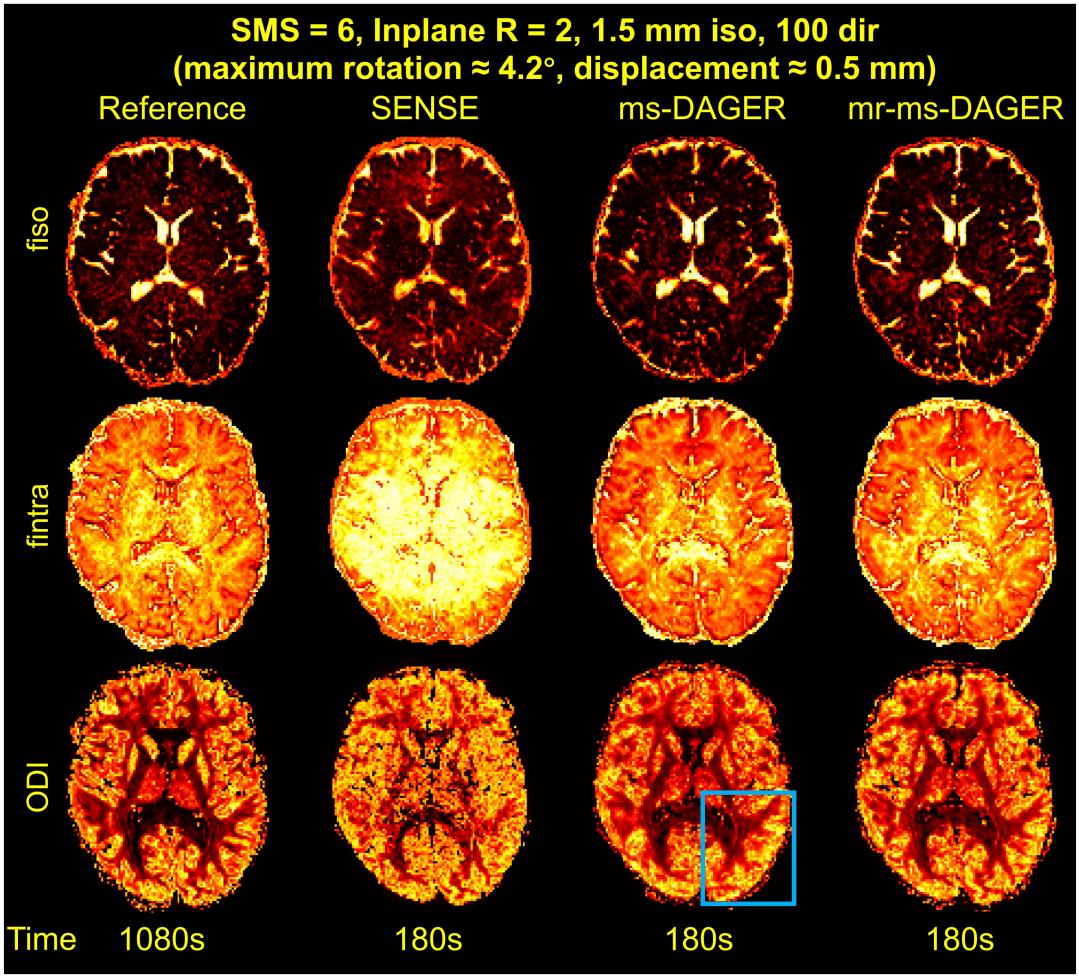

Figure 4.8: NODDI fitting results for subject 1 with mild motion level (maximum rotation 4.2°, displacement 0.5mm) during the scan. Isotropic fraction (fiso), intra-cellular fraction (fintra), and orientation dispersion index (ODI) maps from different methods are shown. SENSE results are corrupted by noise while ms-DAGER results are affected by motion-induced artifacts marked by the blue box. mr-ms-DAGER produces similar fitting results compared to reference with a much shorter scan time.

showed higher level of motion during scan(maximum rotation 24.9°, displacement 3.2 mm). ms-DAGER results are severely affected by the large inter-volume motion mismatch, leading to strong artifacts and blurring, and making it hard to distinguish structures. Meanwhile, mr-ms-DAGER can still correct for the inter-volume mismatch during joint reconstruction, and produce consistent results with the reference images in regard to image quality and structure details with a smaller number of diffusion volumes.Note that the structure difference between mr-ms-DAGER and reference is mainly due to the residual misalignment after registration.

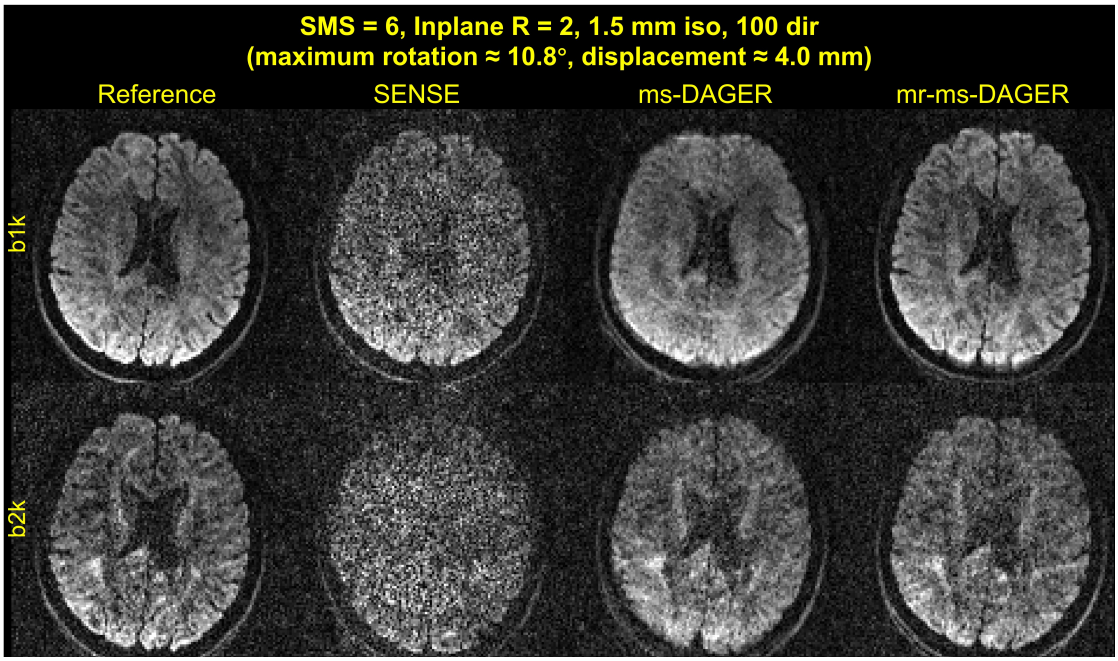

Figure 4.9: Reconstruction results for 100-dir dataset from subject 2 with large level of motion (maximum rotation 10.8°, displacement 4 mm)during the scan. Singleband reference images, SENSE images, multi-shell DAGER (ms-DAGER) and Motion robust multi-shell DAGER (mr-ms-DAGER) results are shown. b = 1000 s/mm^2 ('b1k') and b = 2000 s/mm^2 ('b2k') images are both shown. Severe blurring artifacts caused by the joint reconstruction of volumes with large mismatches can be observed in ms-DAGER results while the mr-ms-DAGER still show consistent structural details compared with reference.

Parameters from NODDI fitting for 100-dir subject 2 dataset with large motion (maximum rotation 10.8°, displacement 4 mm) are demonstrated in Figure 4.11. Fitting results from SENSE are dominated by noise. ms-DAGER results show significant bias in the white matter regions of ODI maps and overestimated fintra as marked by the blue box. Meanwhile, mr-ms-DAGER shows more consistent ODI and fintra maps in white matter regions compared to the reference. Note that due to higher noise level, mr-ms-DAGER shows decreased ODI values in gray matter regions compared to reference as explained in chapter 3.

Figure 4.12 and Figure 4.13 show the first fibre population and secondary fibre population from ball and stick model using FSL's bedpostx tool for subjects 1 and 2. Compared to reference results, SENSE results show significantly decreased secondary fibre population intensity due to the low SNR while the proposed mr-ms-DAGER method produces more consistent results, better recovering the fibre

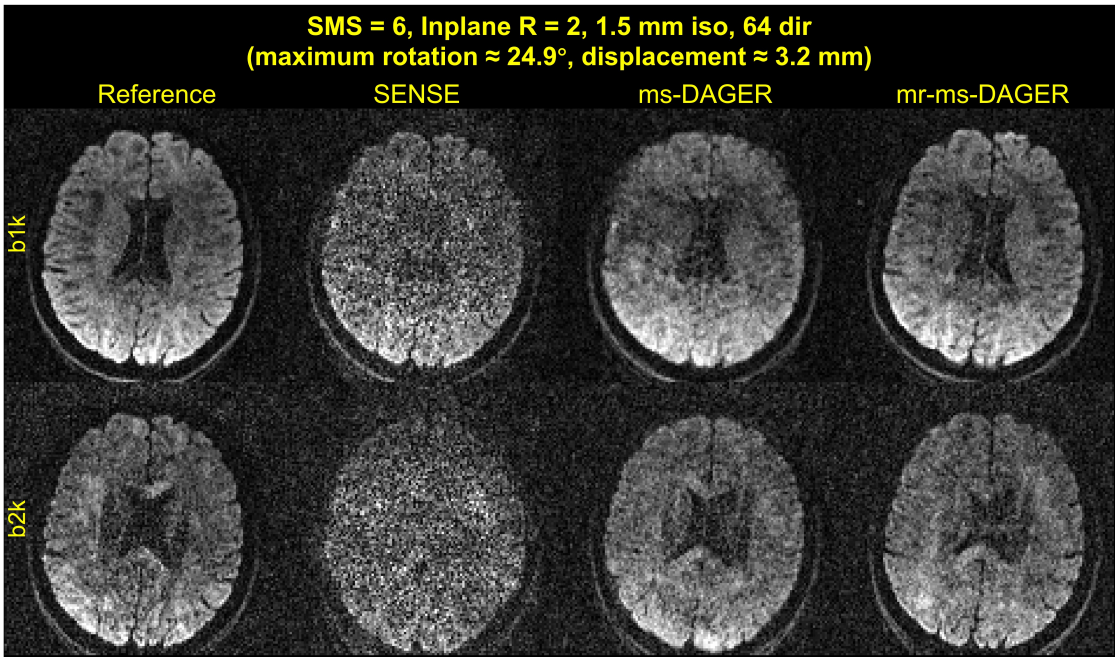

Figure 4.10: Reconstruction results for 64-dir dataset from subject 2 with mild level of motion (maximum rotation 24.9°, displacement 3.2 mm). Singleband reference images, SENSE images, multi-shell DAGER (ms-DAGER) and Motion robust multi-shell DAGER (mr-ms-DAGER) results are shown. b = 1000 s/mm^2 ('b1k') and b= 2000 s/mm^2 ('b2k') images are both shown. ms-DAGER results suffer from strong blurring artifacts while mr-ms-DAGER still shows improved image sharpness with a reduced number of diffusion volumes.

orientation information.

Figure 4.14 shows the tractography results for subjects 1 and 2. 14 major white matter pathways (constituting 27 separate tracts in right and left hemispheres) are shown using autoPtx for 100-dir singleband reference data (18 mins), SENSE reconstructed 100-dir SMS = 6 data(3 mins) and mr-ms-DAGER reconstructed 100-dir SMS = 6 data(3 mins). Most fibre bundles can be tracked from the singleband reference data, while many tracts are either incomplete or missing in the SENSE results for both subjects. For example Corticospinal tract and acoustic radiation tracts (Figure 4.14, left column, in red and yellow), inferior frontal-occipital fasciculus and Inferior longitudinal fasciculus (Figure 4.14, middle column, in green and dark blue), Posterior thalamic radiation (Figure 4.14, right column, in green) are absent. mr-ms-DAGER method, however, produces consistent fiber tracking results compared with the reference at a much shorter scan time, demonstrating its

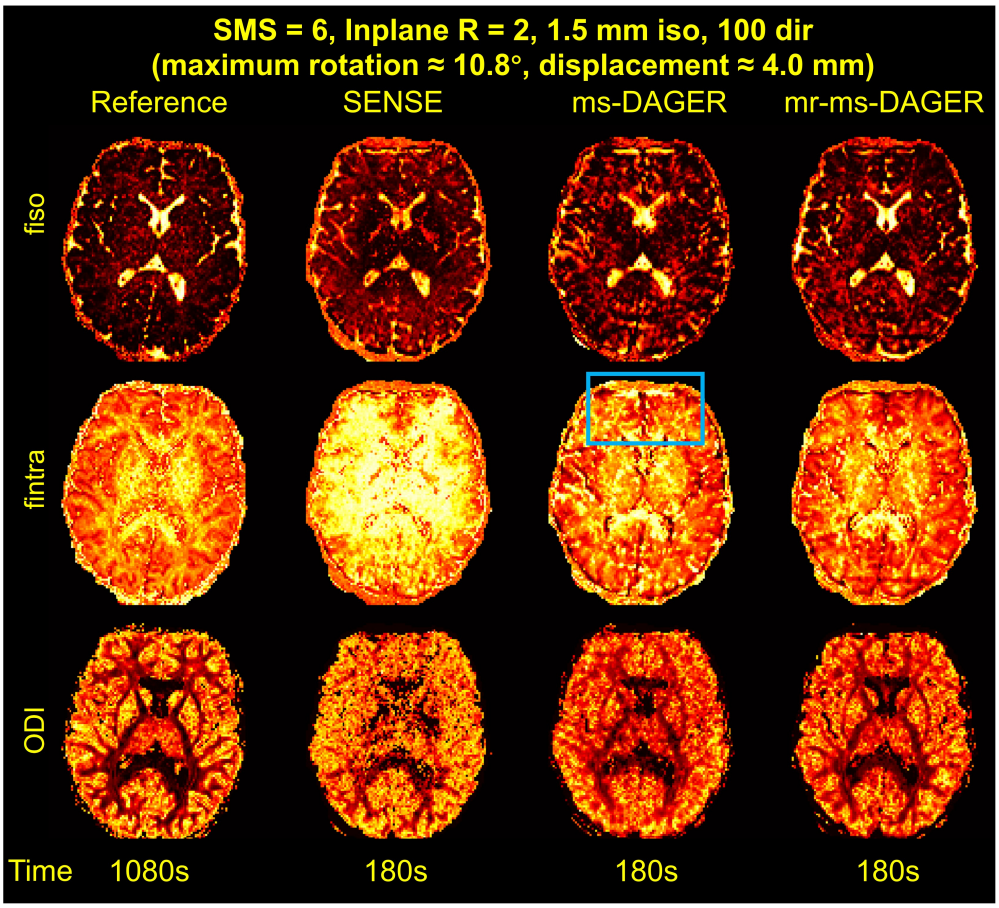

Figure 4.11: NODDI fitting results for subject 2 with large motion level (maximum rotation 10.8°, displacement 4 mm) during the scan. Isotropic fraction (fiso), intra-cellular fraction (fintra), and orientation dispersion index (ODI) maps from different methods are shown. SENSE results are dominated by noise. Bias in the fitting maps can be observed in ms-DAGER results due to the artifacts caused by mismatched volumes during joint reconstruction while mr-ms-DAGER still show comparable results compared to the reference.

ability to improve the diffusion analysis accuracy for highly accelerated data.

Figure 4.15 shows the reconstruction results for b = 1000 s/mm^2 and b = 2000 s/mm^2 ('b1k' and 'b2k') from SENSE, ms-DAGER and mr-ms-DAGER for subject 3 with mild motion levels (maximum rotation 2.2°, displacement 1. 1 mm). Both ms-DAGER and mr-ms-DAGER substantially improve the image quality compared to SENSE, yet blurring artifacts can be found in ms-DAGER as demonstrated by the red boxes.

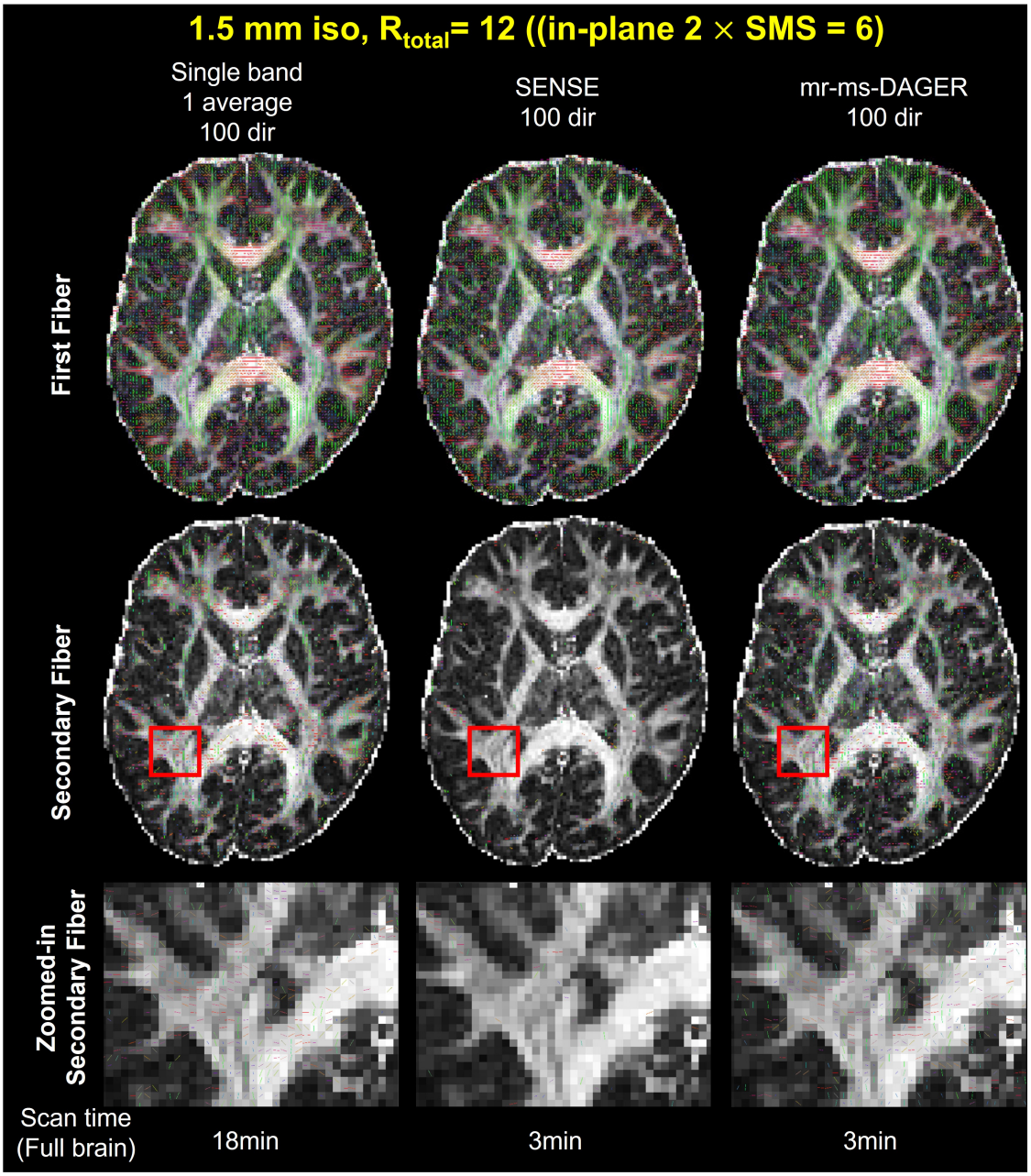

Figure 4.12: Ball and stick model fitting results for subject 1 motion data. Compared to reference, SENSE results lack secondary fibre population information while mr-ms-DAGER shows consistent patterns with the reference.

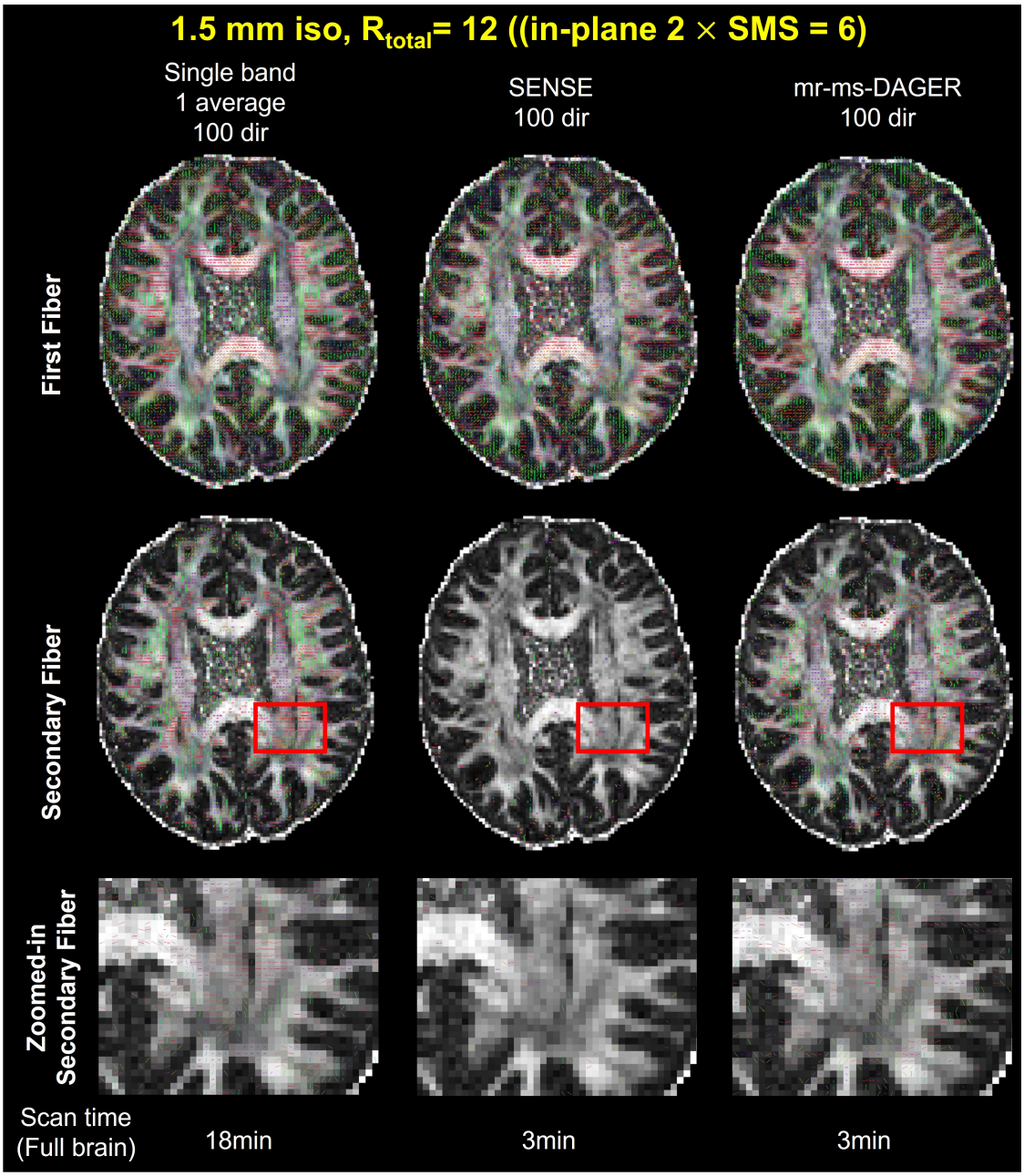

Figure 4.13: Ball and stick model fitting results for subject 2 motion data. mr-ms-DAGER preserves the secondary fibre population information while SENSE results are affected by strong noise.

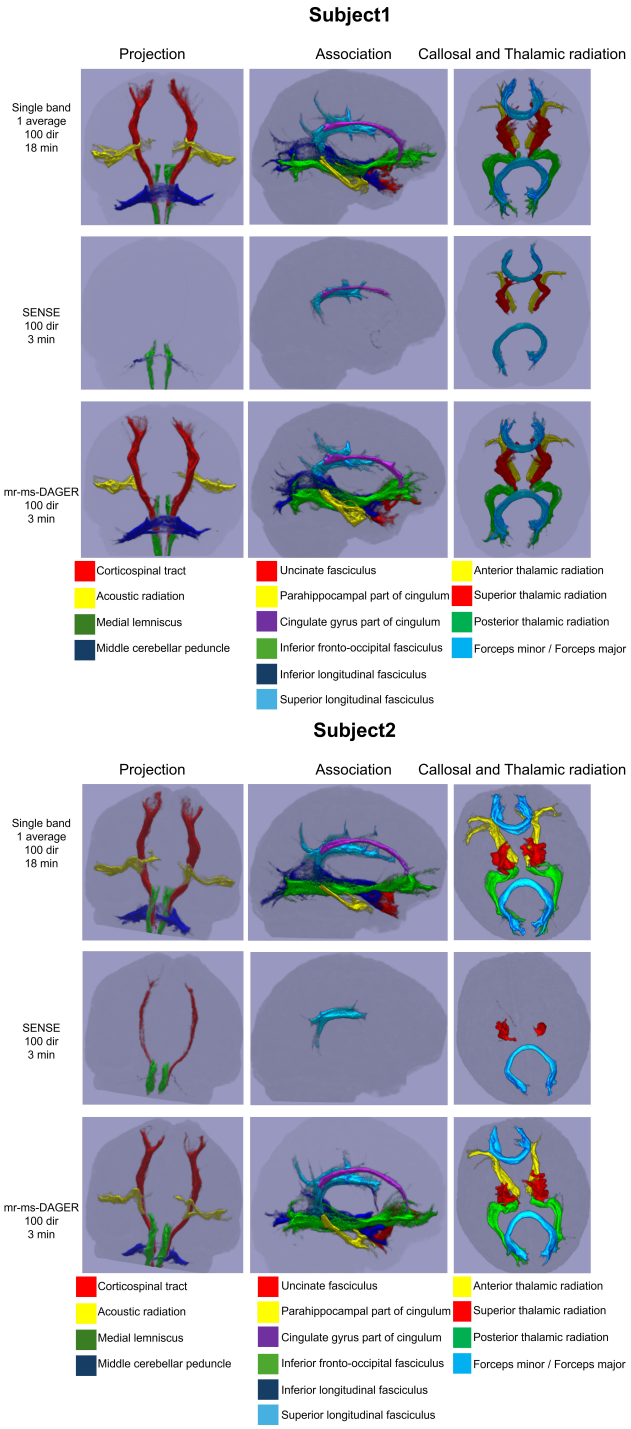

Figure 4.14: Fibre tracking results for subject 1 and subject 2 using autoPtx. Single band reference, SENSE and mr-ms-DAGER results are shown respectively. 14 major white matter pathways (constituting 27 separate tracts in right and left hemispheres) are rendered in superior (thalamic radiation and callosal fibres), anterior (projection) and lateral (association fibres) views. Compared to Single band, several fibres are totally missing in the SENSE results due to the high noise level while mr-ms-DAGER manages to recover most of the fibre tracts.

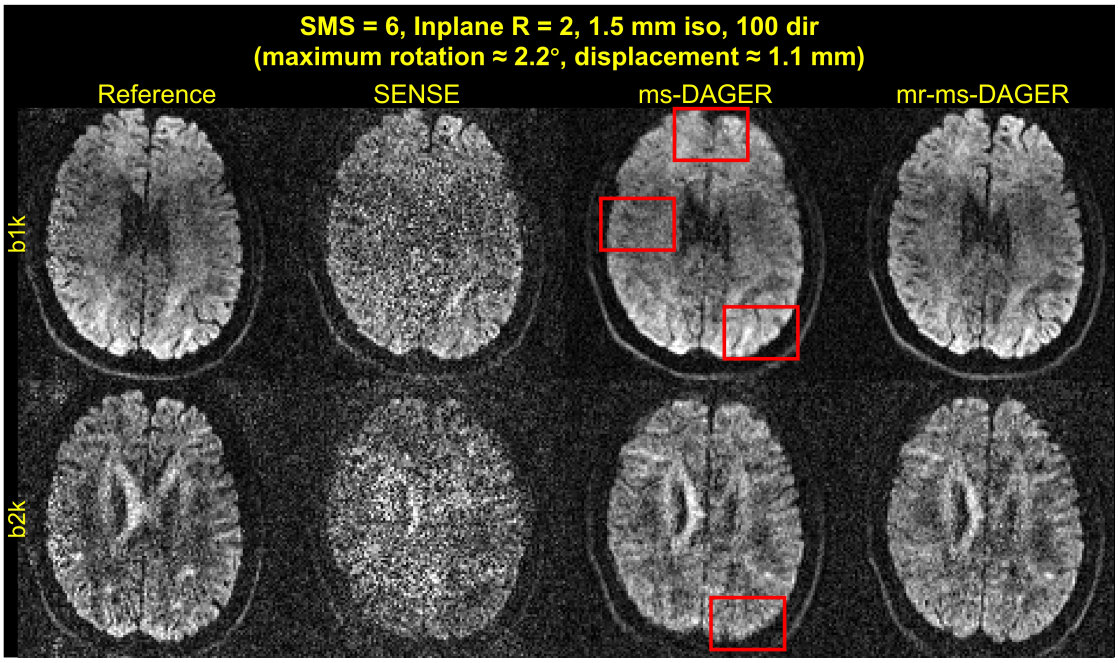

Figure 4.15: Reconstruction results for subject 3 with mild level of motion (maximum rotation 2.2°, displacement 1.1 mm)during the scan. Singleband reference images, SENSE images, multi-shell DAGER (ms-DAGER) and Motion robust multi-shell DAGER (mr-ms-DAGER) results are shown. b = $1000s/mm^2$ ('b1k') and b = $2000s/mm^2$ ('b2k') images are both shown. Though the motion is relatively small, it still leads to blurring in ms-DAGER results as marked in the red boxes.

4.5 Discussion

In this work, we proposed an eddy current distortion and motion robust joint k-q reconstruction method for accelerated multi-shell dMRI acquisition. Previously, by using Gaussian Process to exploit the sharing information among different diffusion volumes, we achieved a high acceleration factor of 12× for in vivo dMRI acquisition[90]. However, the joint k-q reconstruction is vulnerable to geometric mismatches between different diffusion volumes led by motion and eddy current during dMRI scans. Thus, we incorporated motion correction and eddy current correction into the reconstruction framework by iteratively updating motion estimates, eddy current field estimates and images respectively in a data-driven way. Besides, we developed a computational efficient algorithm by splitting the original optimisation framework into sub-problems to avoid inverting a large encoding matrix consisting of spatial locations, diffusion volumes and coils. In this way,

the proposed framework enables parallel computing to accelerate the computing time and reduce memory burden.

There have been quite a few previous works on combined retrospective motion correction and image reconstruction. Motion estimates can be obtained by using additional MRI navigators and incorporated into the reconstruction encoding[135]; or in a data-driven way which estimates motion parameters directly from the acquired data and jointly updates the motion estimates and images during reconstruction[28, 137, 138, 150]. Recently, deep learning based methods have also been proposed to correct for motion artifacts in reconstruction[134, 139, 140]. In this work, instead of proposing a new motion correction method, we focus on developing joint k-q reconstruction methods robust to inter-volume mismatch and incorporate the existing motion correction into the framework in a more computationally efficient way. And the proposed framework can be also be applied to other joint reconstruction methods exploiting inter-volume data relations apart from GP-based reconstruction.

One major challenge for motion-robust joint k-q reconstruction is to get accurate motion estimates from undersampled data. Thus, we investigated the effects of noise on the motion estimates. We added different levels of noise to the simulation data (equivalent SNR of 50, and 10) and tested the mr-ms-DAGER reconstruction method. The iterative motion estimates of data from different noise levels are shown in Figure 4.16. Note that at lower noise level, the motion estimates are more accurate at initial iterations, while for the higher noise level, there are more errors. Regardless, with more iterations, the image quality is improved and the motion estimates gradually converge to the ground truth even for the data with higher noise level.

Eddy current distortion will be more problematic with a in-plane acceleration factor (R = 1 or 2). In our previous study, we investigated the eddy current effects on 7T with an in-plane acceleration factor R = 3. Due to the high bandwidth along phase encoding, eddy current effect is relatively small and eddy current correction may not bring a significant improvement. However, for dMRI protocols typically used at 3T or lower field, R=1 and 2 are typically chosen, where eddy current induced distortion is stronger due to the lower bandwidth along phase encoding. As

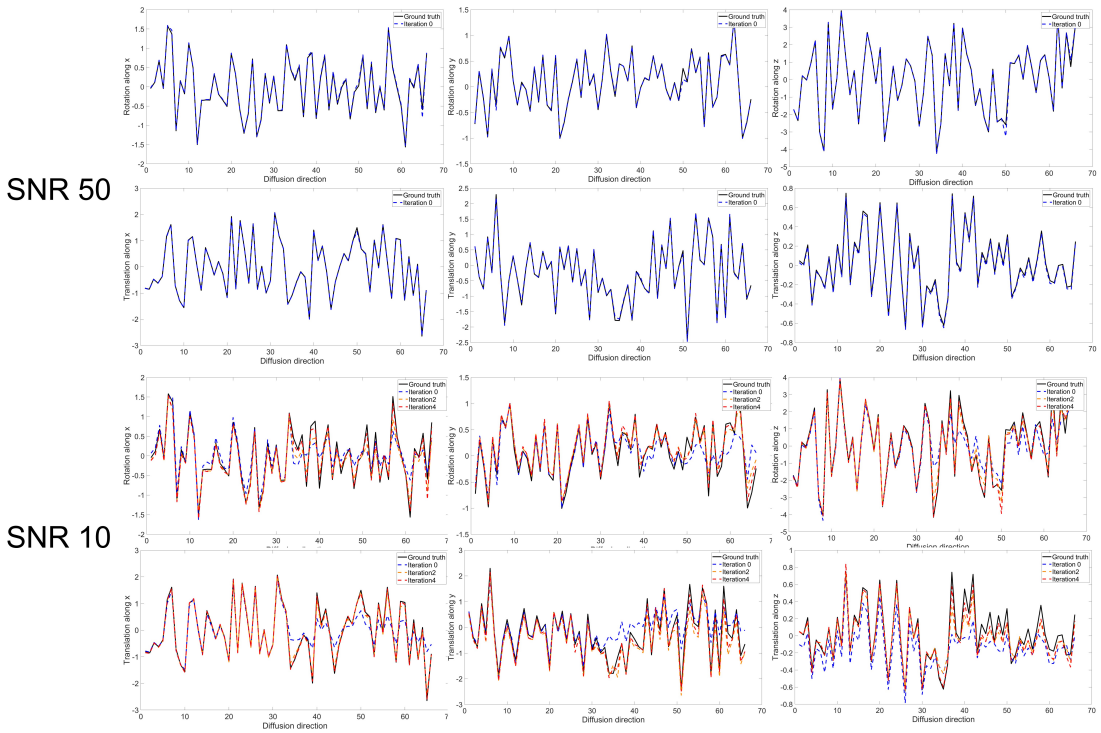

Figure 4.16: Motion estimates from simulation data of different noise levels. Rotation and translation parameters along three axes estimated from different iterations results along with the ground truth are shown. The proposed method achieves robust accurate motion estimation for data with different noise levels.

shown in Figure 4.5, incorporating eddy current correction into the reconstruction benefits the recovery of structural details especially at the edges.

In diffusion MRI, if motion happens during the application of diffusion encoding gradients, the data will be corrupted and cannot be recovered with the proposed method. During the experiments, we noticed that when the subject motion is fast, about 10% of the total diffusion volumes are corrupted when the motion happens during the diffusion encoding. Including these volumes in the joint reconstruction leads to contamination for other volumes within their local neighbourhoods when sharing information. Therefore, data rejection is employed to discard those corrupted volumes to avoid them contaminating other diffusion volumes during joint reconstruction. Currently, visual check is used to find the corrupted volumes. In the future, we plan to use energy-based automatic selection method to reject the severely corrupted volumes. Since the shortened TR enables acquisition of more volumes within the same scan time, a sufficient number of

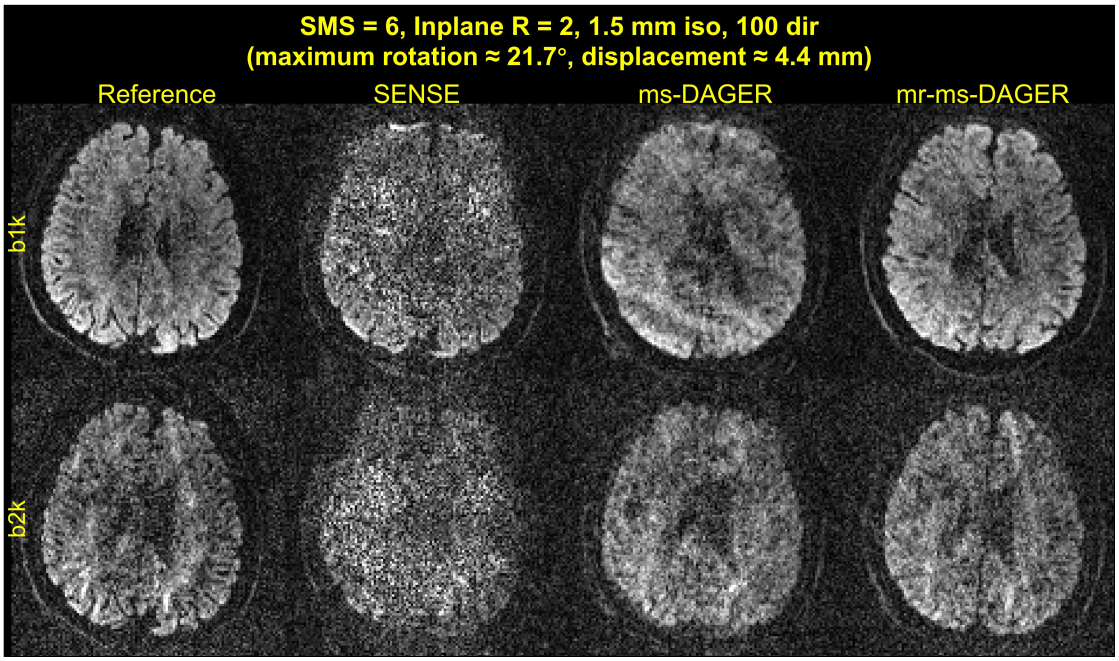

Figure 4.17: Reconstruction results for subject 4 with very high level of motion (maximum rotation 21.7°, displacement 4.4 mm)during the scan. Singleband reference images, SENSE images, multi-shell DAGER (ms-DAGER) and Motion robust multi-shell DAGER (mr-ms-DAGER) results are shown. b = 1000 s/mm^2 ('b1k') and b = 2000 s/mm^2 ('b2k') images are both shown. Strong artifacts can be seen in the ms-DAGER results due to large motion, while mr-ms-DAGER still robustly improve the image SNR and preserve structure details.

diffusion volumes can be still be acquired for advanced diffusion model fitting even when the subjects are less cooperative.

In this work, we used FSL's eddy tool for the motion and eddy current estimation. It can provide accurate estimates even when the motion level is very high. Figure 4.17 shows the reconstruction results for b = 1000 $s/mm^2$and b = 2000s/mm^2 ('b1k' and 'b2k') for subject 4 who showed a high level of motion during scan(maximum rotation 21.7°, displacement 4.4 mm). Note that, due to the very high level of mismatches between volumes, the joint reconstruction without motion correction totally fails, showing strong artifacts, while mr-ms-DAGER still demonstrate high image quality, both improving the SNR compared to SENSE and preserving structure detail information as in single-band reference images. Note that the structural difference between mr-ms-DAGER and reference is mainly due to the residual misalignment after registration. However, when the motion is extremely large (>maximum

rotation 40°, displacement 5 mm), it may become difficult for FSL's eddy tool to predict accurate motion parameters.Thus, other motion estimation techniques can also be explored to provide estimates for the proposed reconstruction framework as the proposed method is compatible with any motion estimation techniques.And the proposed framework can be also be applied to other joint reconstruction methods exploiting inter-volume data relations apart from GP-based reconstruction.

Whether accurate motion estimates can be achieved determines what extents of motion the proposed method can realistically handle. To evaluate it, we further performed tests for FSL's eddy 's capability to estimate motion based on the simulation data. We added different levels of large motion to the reference simulation data and used FSL's eddy to estimate the motion parameters. Two kinds of motion patterns are simulated. The first one is consistent motion where each volume has a different motion state. The second one simulates the condition when the subject suddenly moves at several time points and stops moving during the rest of time.

The consistent motion test results are shown in Fig.4.18. The motion estimation parameters along with the ground truth motion parameters for two different motion levels are shown. FSL's eddy can still provide accurate motion estimates even when the maximum rotation is 60° with 8 mm translation. The sudden motion test results are shown in Fig.4.19. Similarly, FSL's eddy can estimate the inter-volume motion parameters accurately given high input image quality.

To test the method robustness against noise, we added different levels of noise to the sudden motion data (SNR 0.5,1 and 2). Note that, our SMS = 6 accelerated in vivo data have similar noise levels as the SNR 1 data. The motion estimation parameters along with the ground truth motion parameters for each volume are shown in Fig.4.20. With increased noise level, larger errors can be observed in the motion estimates from FSL's eddy. When the maximum rotation is around 25° and translation 5 mm, the motion estimation errors are still small which makes joint reconstruction still feasible. However, when the motion is very large(rotation 60° and translation 8 mm), the residual inter-volume inconsistency leads to strong artifacts in the joint reconstruction if the motion level is very high, which prevents

the improvement of image quality even with more iterations. Without improved input data quality, FSL's eddy can neither predict better motion estimates, which leads to failed reconstruction. Thus, our proposed method may have degraded performance when the motion ranges/magnitudes are larger than 25° rotation and 5 mm translation and the accelerated data show high noise levels.

Regarding the frequencies of motion, for consistent motion in the simulation data, each volume shows different motion states, and the proposed method can correct for the inter-volume motion and provide reconstruction results with reduced blurring artifacts. However, the simulation only simulates different motion positions but not accounting for the contrast corruption if motion happens in diffusion preparation. The proposed method cannot compensate for the corrupted volumes, and they need to be rejected in the reconstruction to avoid contrast contamination. Thus, the proposed method may have degraded performance when the subjects keep moving in the scans like patients with Parkinson's disease.

Since the proposed method is compatible with any motion estimation techniques, other motion estimation techniques including deep learning networks can also be explored to provide estimates for the proposed reconstruction framework when it becomes challenging for FSL's eddy to estimate the motion parameters.

Our method still has some limitations. Firstly, our method only considers the inter-volume motion. When the motion happens during encoding and leads to intra-volume motion, currently the data is rejected to avoid contaminating other diffusion volumes. Other intra-volume motion correction techniques like gradient moment nulling with specially-designed diffusion encoding waveforms may be incorporated into the acquisition to make the scan more robust to motion. Secondly, our current models only consider eddy current induced distortion but not B0 susceptibility induced distortion which may also change between volumes as motion leads to different spatial positions. With small-medium motion, that effect was not strong but it may lead to more artifacts in large motion condition. Susceptibility correction can also be incorporated into the reconstruction framework to further improve the performance. (e.g. using BUDA acquisition [117, 118, 151,

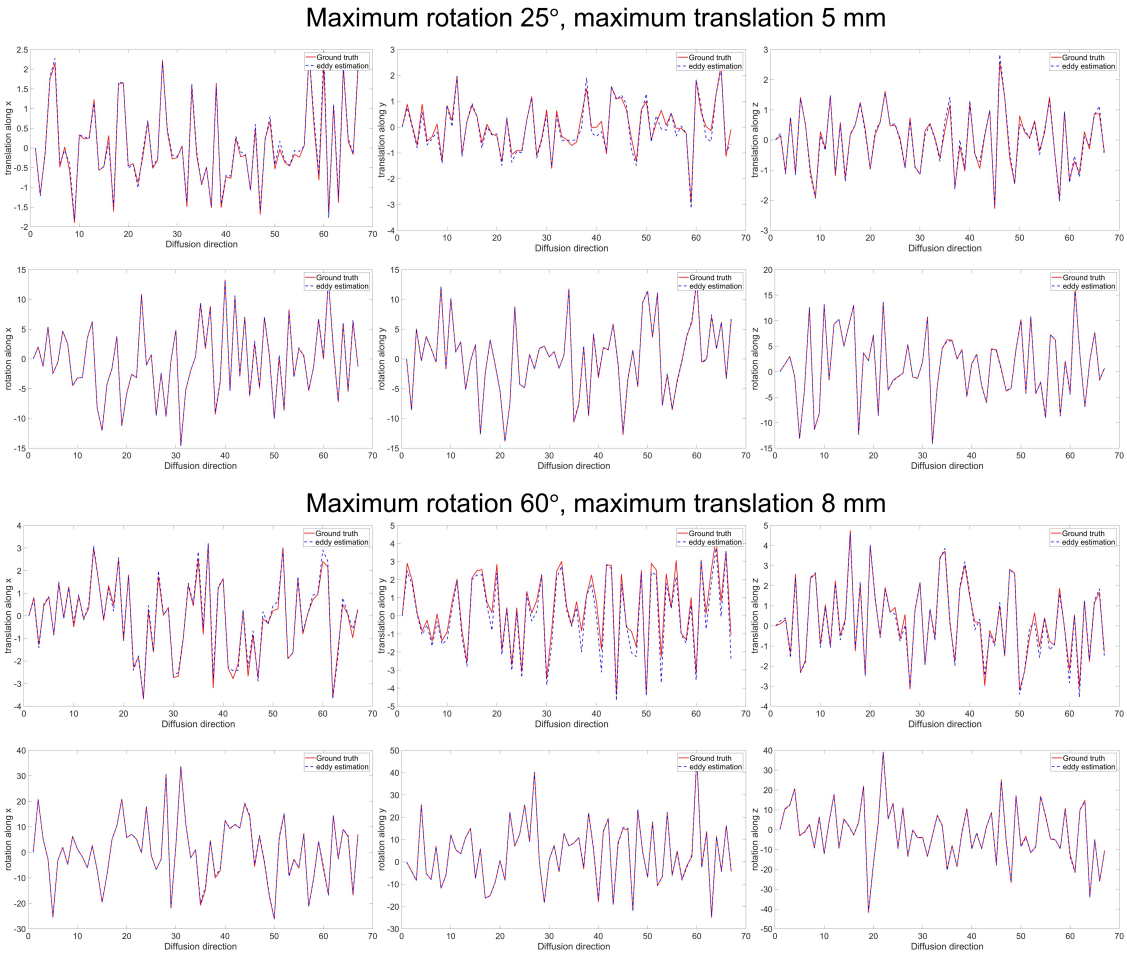

Figure 4.18: Motion estimation test with consistent motion. Random 3D motion is added to each volume of the reference simulation data and then FSL's eddy is used to estimate the motion parameters. Two different levels of large motion are tested. Compared with ground truth, eddy can provide accurate estimates.

152] to provide susceptibility filed map information). Thirdly, we only tested our method on healthy volunteers with guided motion during scan. We will investigate if our method still works well for uncooperative subjects such as patients with different kinds of motion patterns.

4.6 Conclusion

In this work, we proposed an eddy current corrected and motion robust joint k-q reconstruction method for accelerating multi-shell dMRI acquisition. Based on simulation and in vivo data test, our proposed method robustly improves image quality for the multi-shell dMRI data under high acceleration factor compared to

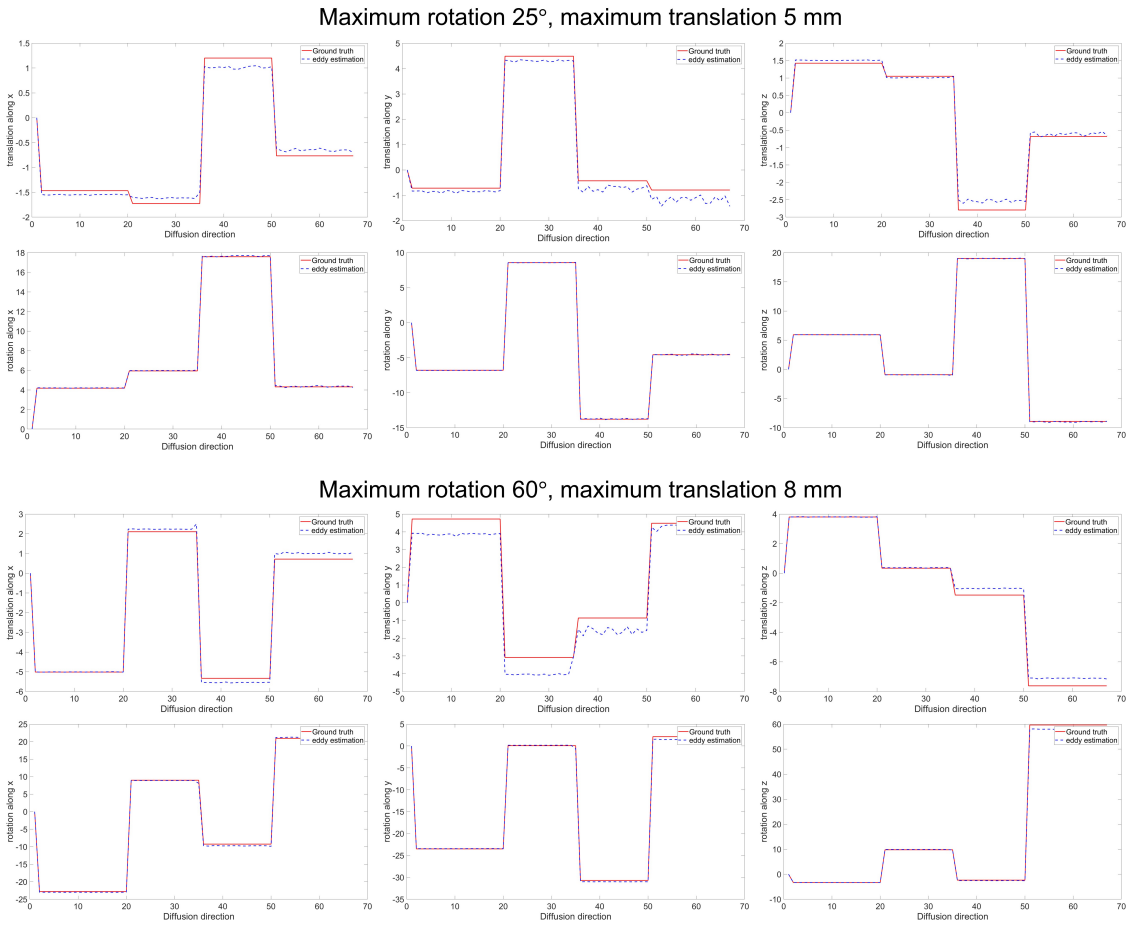

Figure 4.19: Motion estimation test with sudden motion. Random 3D motion is added to serval volumes of the reference simulation data and then FSL's eddy is used to estimate the motion parameters. Two different levels of large motion are tested. Eddy provide consistent results with the ground truth.

conventional methods when motion and strong eddy current distortion exist, which may facilitate the wider application of advanced diffusion analysis models.

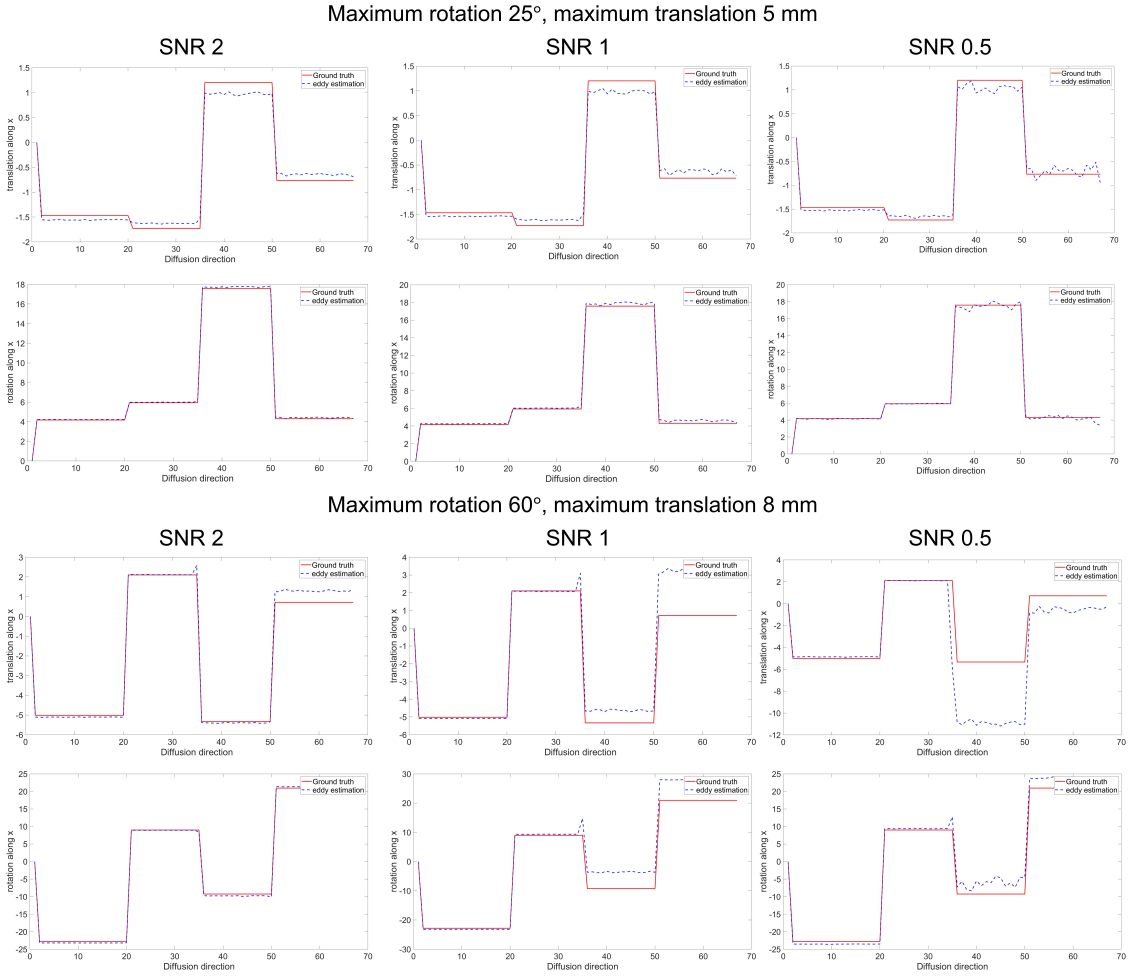

Figure 4.20: Motion estimation test with sudden motion under different noise levels. Random 3D motion and different levels of noise (SNR 2, 1 and 0.5) is added to serval volumes of the reference simulation data and then FSL's eddy is used to estimate the motion parameters. Two different levels of large motion are tested. Increased bias can be observed with higher noise levels. For the maximum rotation 25° and translation 5 mm data, the fitting bias is small yet for maximum rotation 60° and translation 8 mm data, the residual inter-volume inconsistency may lead to strong artifacts.

5

Joint k-q-TE reconstruction for accelerated combined diffusion-relaxometry imaging

Contents

This chapter covers an ongoing project on accelerating combined diffusion-relaxometry MRI. Combined diffusion-relaxometry imaging provides higher microstructure detection specificity compared to using diffusion imaging or relaxometry imaging alone. However, the requirement to acquire higher-dimensional data leads

to significantly increased scan time, making it challenging to apply to practice. In this work, we propose to accelerate multi-TE dMRI acquisition using a joint k-q-TE reconstruction based on Gaussian Process to exploit redundancy in high-dimensional data. We extend the joint k-q reconstruction described in Chapters 3 and 4 and develop a reconstruction in joint k-q-TE space. We use simulation to validate the ability of Gaussian Process to model q-TE data. Then we design an in vivo multi-TE acquisition protocol suitable for practical scans and acquired both healthy volunteers and Traumatic Brain Injury (TBI) patients. The results demonstrate that our proposed method can provide high image quality and comparable fitting accuracy using much shorter scan time with conventional acquisition methods. This work can potentially facilitate the wider applications of combined diffusion-relaxometry MRI for basic and clinical neuroscience studies .

5.1 Introduction

Diffusion MRI (dMRI) probes the random movement of water molecules inside the tissue, sensitizing the signals to microstructure information[1, 2, 10, 51]. dMRI has been widely used as a non-invasive tool for basic and clinical neuroscience research, and many diffusion models have been proposed to map microscopic tissue features to MRI signal based on biophysical models or signal representations[5, 93, 153, 154]. For example, the neurite orientation dispersion and density imaging (NODDI) model [7] has been used in clinical studies for neuro-degenerative diseases like Parkinson's disease, Alzheimer's disease and multiple sclerosis[155–160].

However, it's challenging to obtain accurate microstructure estimation from dMRI signals with high specificity given the complexity of tissue [31]. Due to the practical limitation of MRI image resolution, the acquired signal from one voxel is the combination of signals from multiple microstructural environments. And a change in dMRI signal can be caused by multiple factors including changes in cellular or axonal density, anisotropy, myelination, magnetic transfer and relaxation, which produces high degeneracy when fitting the microstructure parameters. For robust model fitting, commonly used dMRI biophysical models impose priors on the dMRI signals

based on previous knowledge of targeted tissues, e.g., constraining the diffusivity or relaxation terms of complex tissue environments to fixed values. However, these prior assumptions can cause biases in model fitting. For example, many biophysical diffusion models assume the same relaxation time for different compartments. Yet in relativity it varies across compartments and is associated with different signal decays. If not accounted for, it leads to inaccurate parameter estimation.

To tackle these challenges, recently combined diffusion-relaxometry imaging techniques with improved biological specificity have been proposed[31]. MR relaxometry is sensitive to the chemical composition of tissues, also providing information about complex tissue environments[161]. Previously, dMRI and MR relaxometry are usually acquired and analysed independently, but in combined diffusion-relaxometry imaging, diffusion and relaxation properties are measured jointly by performing scans with sequence parameters tuned to be sensitive to both diffusion and relaxation. In this way, the acquired MR contrast encodes both diffusion and relaxation information[162, 163]. During analysis, multi-dimensional information (e.g. diffusivity, T1 relaxation and T2 relaxation) is jointly estimated from the acquired signal, thus making it possible to investigate the correlation between different contrasts.

Compared to independent acquisition of diffusion and relaxometry maps, the multi-dimension combined acquisition enables better characterisation of tissue microstructure. As different compartments become more distinguishable in higher-dimensional space, combined diffusion-relaxometry techniques improve the accuracy of compartment separation and help quantify unique signal contributions from different microstructural environments, thus deriving more accurate microstructure information. Besides, many biophysical diffusion models suffer from biases arising from fixed or constrained parameters. Combined diffusion-relaxometry imaging, however, offers the potential to correct for these biases by directly estimating the previously-constrained parameters based on the information from multi-dimensional data, thus differentiating the signal generated from other mechanisms like relaxation

with diffusion. In this way, the estimated parameters can better reflect the underlying biophysical features.

Many combined diffusion-relaxometry imaging techniques have been applied to study brain microstructure information. Lampinen proposed a minimally constrained white matter model by combing b tensor imaging and T2 imaging[164]. Tract specific T1 mapping was proposed by Leppert et al.[165]. Better crossing fibre information can be extracted with T1-diffusion combined acquisition as proposed by De Santis et al.[166]. Veraart et al. proposed to use combined T2-diffusion imaging to improve intra and extra-axonal tissue compartments separation[167]. Johnson et al. proposed to use combined diffusion tensor, T1 and T2 imaging to disentangle intravoxel components[168]. Previously, NODDI model assumes the same T2 value for all compartments in the model, thus cannot differentiate the signal difference between diffusion effects and relaxation effects. Multi-TE NODDI technique has thus been developed which extends original NODDI model by considering compartment-specific T2 relaxation[169]. Multi-TE NODDI acquires multi-TE dMRI data to fit diffusion and relaxation properties simultaneously and manages to correct for overestimated intra-neurite signal fraction in original models. It also enables brain development study where the T2 values change with brain development. Coelho et al. extended the standard model to multi-TE condition, enabling detection of the free water fraction and offering potential benefits for disease detection such as inflammation, schizophrenia and Parkinson's disease [170].

To obtain the multi-dimensional data, diffusion weighted scans can be repeated with different relaxation encodings (e.g. using different TEs and TIs), thus producing a high-dimensional acquisition space. However, the scan time is significantly increased. Many efforts have been made to improve the acquisition efficiency. Many techniques have explored efficient diffusion-relaxometry sampling schemes by sharing one contrast preparation for multiple readout echoes within one excitation. For example, multiple spin echoes can be acquired after one diffusion preparation for more efficient multi-TE dMRI acquisition. [171, 172]. Besides, a global inversion pulse can be shared by multiple readouts with different TIs using slice-shuffling

technique to accelerate T1-diffusion acquisition[165]. Furthermore, Hutter et al. proposed ZEBRA (Z-location shuffling, multiple echoes and B-interleaving for relaxometry-diffusion acquisitions) technique to combine multiple gradient echoes acquisition, slice-shuffling and interleaved slice-level diffusion encoding to allow for efficient T1-T2*-diffusion acquisition[173]. Other methods try to encode multiple contrasts within highly undersampled acquisition. Wang et al. proposed echo planar time-resolved imaging (EPTI) technique, which uses the k space-temporal correlation to enable highly accelerated relaxometry mapping for T2 and T2*[174]. Recent works have extended this technique to diffusion MRI acquisition[175–177]. Magnetic resonance fingerprinting (MRF) [178] is another fast multi-contrast acquisition method which uses dictionary learning to calculate contrast mapping from highly undersampled spiral acquisition with variable sequence parameters sensitive to different contrasts. Due to the complexity of diffusion signals, diffusion MRF usually only provides ADC value[179–181], yet recent advancements in deep learning methods have enabled extraction of more complicated combined diffusion-relaxometry information from MRF[182]. Meanwhile, other works have explored optimised sampling schemes which use fewer data points to estimate the multi-dimensional information. For example, MADCO (marginal distributions constrained optimisation) framework combines fully sampled 1D acquisitions with sparsely sampled high-dimensional data points, giving accurate estimation while significantly reducing scan time[183]. Machine learning and deep learning based methods have also been explored to optimise sampling patterns[184, 185].

Traditional k space parallel imaging methods like Simultaneous multislice (SMS) imaging can also be combined to improve the scan efficiency [13, 14, 186]. Relations in multi-dimensional space like low rank and sparsity can also be exploited as prior information to improve the reconstruction performance. However, the acquisition of high-dimensional data still takes hours of scan time, limiting its wider applications.

One way to enable further accelerated acquisition is using joint reconstruction for different data points in the sampling space to explore sharing information, instead of reconstructing each image (i.e., one data point in the multi-dimensional space)

independently. Joint reconstruction methods have been proposed for relaxometry imaging and diffusion imaging[21–27, 73, 187–193]. These methods leverage data redundancy and exploit sharing information in diffusion encoding dimension or relaxometry encoding dimension, which improve the image quality at higher acceleration factors. However, in combined diffusion-relaxometry acquisition, due to the scan time limitation, the number of data points along each individual contrast encoding dimension may be very small, thus making it difficult to learn and utilise sharing information. Besides, for data points acquired at high b values and high echo times, the SNR of all data can be very low, posing additional challenges for robust image reconstruction.

To better utilize the shared information in multi-dimensional data to tackle these problems, combined diffusion-relaxometry reconstruction that jointly exploits data redundancy along multiple dimensions can be explored. In this work, we propose to extend our previously developed joint k-q reconstruction method based on Gaussian Process [27, 90] to combined diffusion-relaxometry imaging. Here we focus on multi-TE diffusion MRI to illustrate using joint k-q-TE reconstruction for combined diffusion-relaxometry acceleration. Specifically, we designed a multi-TE multi-shell covariance function to describe the signal relations in q-TE space and developed a fast multi-TE dMRI protocol for in vivo scans. In this preliminary work, we acquired data from both healthy volunteers and Traumatic Brain Injury (TBI) patients to investigate the performance the methods and feasibility for clinical research.

5.2 Developing joint k-q-TE reconstruction

5.2.1 Limitation of TE-independent reconstruction

Previously, we have proposed joint k-q reconstruction methods based on Gaussian processes to accelerate multi-shell dMRI acquisition[27, 90]. Gaussian process (GP) is a data-driven model that exploits the data smoothness without making explicit assumptions of underlying tissue models [89]. High acceleration factors of 12 were achieved at 3T (in plane R = 2, SMS = 6) and 7T (in plane R = 3, SMS = 4) respectively.

However, for multi-TE dMRI acquisition, diffusion volumes need to be acquired at multiple echo times. Due to the limitation of scan time, the number of diffusion volumes for each TE is much smaller, thus limiting the sharing information we can draw from q space at individual TEs. This poses a challenge for individual-TE reconstruction especially for long-TE data which has a lower SNR.

Given the fact that sharing information also exists along TE dimension, as signal decays exponentially characterised by T2 time constant, a joint k-q-TE reconstruction method can be developed to better exploit sharing information in both diffusion and T2 encoding dimensions to improve the reconstruction performance.

5.2.2 GP modelling of multi-TE dMRI signal

GP models the data using an infinite set of functions where each function fits the data exactly at the measured point and any finite collection of functions follows a multi-variate Gaussian distribution. With GP modelling, the multi-TE dMRI signals $\mathbf{u}$ is determined by a mean vector μ ($(N_d N_{TE})\times 1$) and a covariance matrix $\mathbf{\Sigma}$ ($N_d N_{TE} \times N_d N_{TE}$). N_d is the number of dMRI directions and N_{TE} is the number of measured TE values.

Covariance function design

The covariance matrix $\mathbf{\Sigma}$ is parametrized using a covariance function C. We define a valid covariance function between two locations (q,TE;q',TE') in q-TE space as:

$$C\left(q, TE; q', TE'\right) = C_\theta\left(\theta; a\right) C_b\left(b, b'; l\right) C_\tau\left(TE, TE'; \tau\right) \tag{5.1}$$

where q and q' refer to q space locations at two b shells (b and b') with an angular distance of θ, TE and TE' refers to two echo times, C_θ is a spherical covariance function describing angular relations between dMRI data points within a shell, C_b is a squared-exponential function describing relations between data points from different shells and C_τ is a separate squared-exponential function describing relations between data acquired at different echo times[109]:

$$C_\theta(\theta; a) = \begin{cases} 1 - \frac{3\theta}{2a} + \frac{\theta^3}{2a^3} & \text{if } \theta \leq a \\ 0 & \text{if } \theta > a \end{cases} \tag{5.2}$$

$$C_b(b, b'; l) = \exp\left(-\frac{(\log b - \log b')^2}{2l^2}\right) \tag{5.3}$$

$$C_\tau(TE, TE'; \tau) = \exp\left(-\frac{(\log TE - \log TE')^2}{2\tau^2}\right) \tag{5.4}$$

Where a is a hyperparameter controlling signal smoothness within a shell and also serves as an angular threshold; l is a hyperparameter controlling signal smoothness across shells; τ is a hyperparameter controlling signal smoothness across echo times; logarithm is used to scale the b values and TE values.

5.2.3 Validation of covariance modelling

To validate whether the proposed GP model can accurately capture the covariance along the TE dimension in multi-TE dMRI datasets. We performed a simulation study based on a public multi-TE diffusion brain MRI dataset[194]. 30 diffusion directions were acquired from two b value shells (b = 700 and b = 2000 s/mm^2) respectively for eight TEs (62, 72, 82, 92, 102, 112, 122, and 132 ms), resulting in a total diffusion volume number of 480. Data from three healthy volunteers were acquired and the resolution was 2.5 mm isotropic with TR 5.8 s. The acquired data were preprocessed with denoising, susceptibility- and eddy-current-distortion correction. We used the processed data from one subject as a reference to validate our model.

We aim to compare the data covariance derived from the raw image data with that from GP prediction using our model. Specifically, we first fitted a GP model with the reference data and then predicted images at the same directions, b values and TEs as in the reference data using the fitted GP model. Then for each q-space point, we evaluated the covariance values from different echo times. Finally we compared the results with the covariance values calculated from the original reference data. The results can indicate how well the proposed model capture the inherent correlation in the data across TE: a lower covariance indicates reduced correlation by the model, while a higher covariance suggests over-smoothing.

The comparison result is demonstrated in Figure 5.1. The signal covariance is shown as a function of their TE differences and the mean function and standard

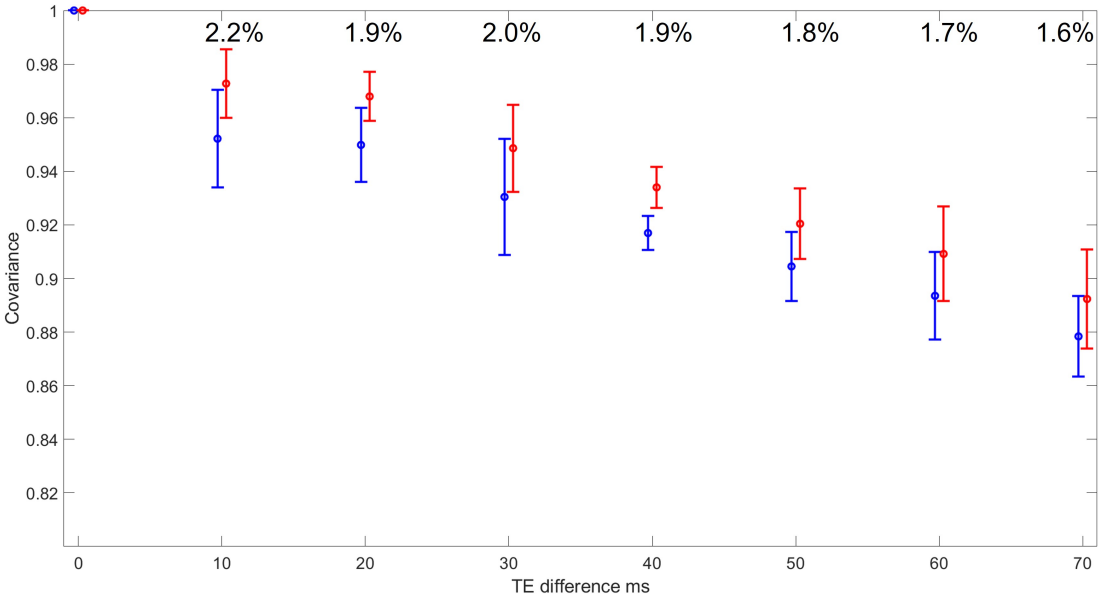

Figure 5.1: Validation of the proposed q-TE covariance function for GP. Signal covariance as a function of TE difference is shown. The covariance is normalized by the median of signal variances (TE difference = 0 ms). The mean function and standard deviation from all q space points are shown. The percentage changes between GP prediction (red) and reference (blue) are also listed in the figure, which show small values.

deviation from all q space points are shown. The percentage changes of the covariance values between GP prediction and reference are calculated for each TE. It is expected that as TE difference increases the covariance between data will decrease. The GP prediction (red) results demonstrate generally consistent covariance profile with the reference (blue), with slightly increased covariance value. Given GP model also inherently denoises the data, this increased covariance may come from the reduced noise fluctuations that is independent across TE. This result indicates that the joint q-TE GP is introducing minimal smoothness along TE dimension.

5.2.4 multi-TE multi-shell DAGER (mte-ms-DAGER)

With the proposed q-TE GP model, we extend our previous DAGER method to multi-TE multi-shell condition named multi-TE multi-shell DAGER (mte-ms-DAGER). mte-ms-DAGER uses the GP-estimated dMRI signal as a prior and solves the following reconstruction problem:

$$\mathbf{u} = \arg\min_{\mathbf{u}} \left(\frac{1}{2\sigma_k^2} \|\mathbf{\Omega\Phi FSu} - \mathbf{d}\|_2^2 + \frac{1}{2}(\mathbf{P}^H\mathbf{u} - \boldsymbol{\mu})^H(\mathbf{\Sigma} \otimes I_N)^{-1}(\mathbf{P}^H\mathbf{u} - \boldsymbol{\mu}) \right) \quad (5.5)$$

where $\mathbf{u}$ is the unknown image, Ω refers to undersampling operator, Φ refers to eddy current-induced phase, F refers to Fourier transform, S refers to coil sensitivity encoding, σ_k^2 is the noise variance in the k space data, which can be calculated from σ_n^2 as in [27], d is the acquired k space signal, μ is the mean value of GP prediction, $\mathbf{\Sigma}$ is the GP covariance matrix and N is the number of voxels, H is the conjugate operation and $\otimes$ is Kronecker product. P represents the motion induced phase error, which is different between diffusion directions. The reconstruction of mte-ms-DAGER follows the same iterative optimisation as in DAGER and ms-DAGER, where reconstructed images from previous iteration are used to update GP model parameters and estimate mean GP prediction for the next iteration.

5.2.5 Simulation

To test the performance of mte-ms-DAGER, we conducted a simulation experiment based on HCP dMRI dataset consisting of 3 shells (1000, 2000 and 3000 s/mm^2) and 270 directions[111]. The data were fitted with the ball-and-stick model which was used to generate simulation data with the same model[112]. Then we segmented the whole brain data into white matter, gray matter and CSF regions based on FA and MD values from DTI fitting. Using T2 values as 60 ms, 75 ms and 250 ms [39]for the three tissue types respectively, we generated 45 b = 1000 s/mm^2 and 90 b = 2000 s/mm^2 directions uniformly sampled in q space and then split them into three uniformly distributed subsets (each with 15 b = 1000 s/mm^2 and 30 b = 2000 s/mm^2) at three echo times (62 ms, 92 ms and 130 ms). We optimised k-q undersampling using a graph model [113] that aims for each q space neighbourhood (across directions, shells and TEs) to have highly diverse k space undersampling patterns to better use complementary information. In Figure 5.2, information is shared in the local q space neighbourhood across TEs. a 3D k space was used to illustrate our under-sampling strategy, where each colour corresponds to a unique CAIPRIHNA under-sampling sampling pattern. It allows diverse k space sampling patterns for each local q space neighbourhood across TEs. Undersampled multi-channel datasets were simulated with sensitivity maps from

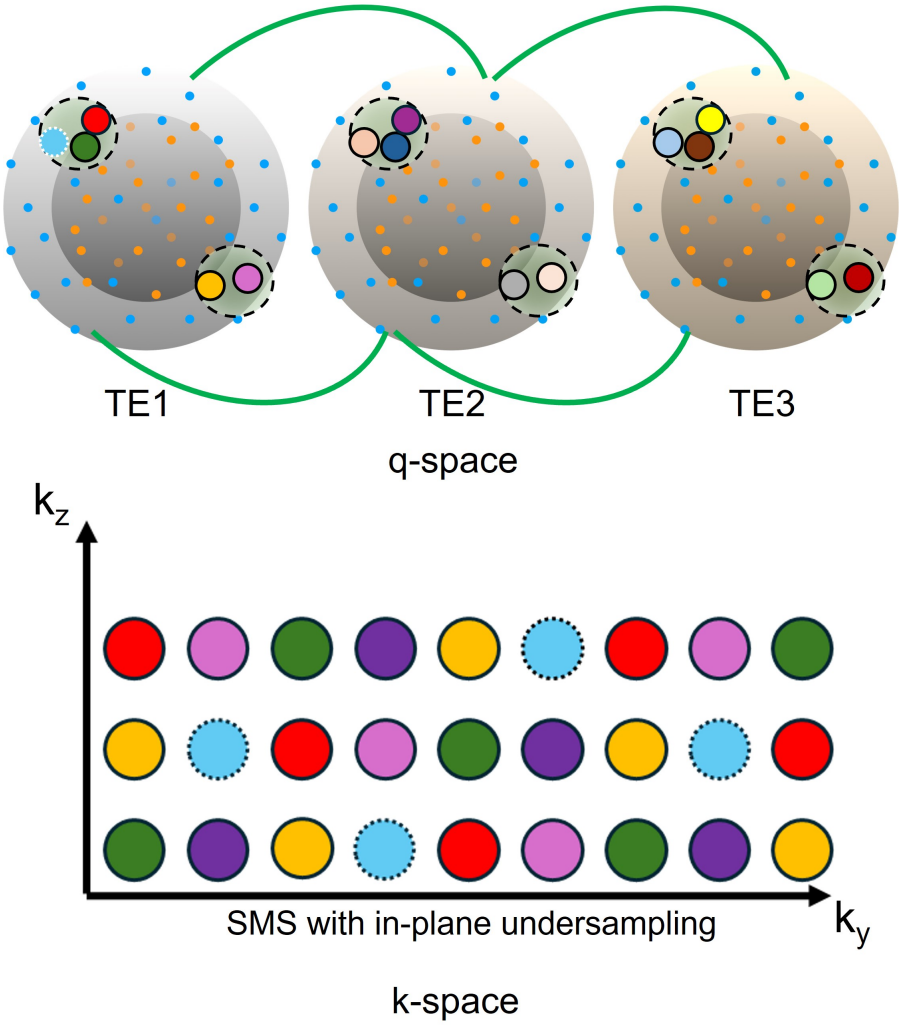

Figure 5.2: To enhance the joint k-q-TE reconstruction, q space neighbourhood (across directions, shells and TEs) is designed to have highly diverse k space undersampling patterns. Each colour corresponds to a different sampling pattern in k-space. Here, SMS = 3 (acquired with blipped-CAIPI) with in plane R = 2 is used for illustration.

an 8-channel head coil and a total undersampling factor of 12 (in-plane R = 3 and through-plane SMS = 4) with added noise.

Figure 5.3 shows the reconstruction results from different methods for the simulation data. b = 1000 s/mm^2('b1k') and b = 2000 s/mm^2('b2k') images at three echo times are shown. Due to the high acceleration factor, SENSE results are corrupted by noise, making it hard to distinguish structure information. TE-by-TE multi-shell DAGER (ms-DAGER) method can improve SNR by using the sharing information in q space, however, due to the limited number of diffusion volumes

per TE, artifacts still exist, especially in higher TE data where the intrinsic SNR is low. Compared to ms-DAGER, mte-ms-DAGER method further suppresses noise and shows consistent structural details with the reference data by exploring the information from multi-TE data.

Normalized Root Mean Square Error (nRMSE) values calculated between reconstruction results from different methods and the reference are shown in Figure 5.4. Note that, both ms-DAGER and mte-ms-DAGER reduce errors compared to SENSE while mte-ms-DAGER shows further improved performance by using cross-TE information compared to ms-DAGER.

5.3 Implementation of fast multi-TE dMRI for in vivo scan

5.3.1 Multi-TE dMRI acquisition

To further test the proposed fast multi-TE dMRI technique, we acquired in vivo data from healthy volunteers and TBI patients for evaluation on a Siemens 3T Prisma scanner. Informed consent in accordance with local ethics was obtained before each scan. A 2D spin-echo dMRI product sequence was modified to enable SMS = 6 acquisition and blipped-CAIPI encoding with highly variable k space undersampling patterns for each q space neighbourhood across TEs. A 32-channel head coil was used with coil sensitivities measured using a segmented EPI sequence. The dMRI data were acquired with in-plane acceleration R = 2 and multi-slice acceleration SMS = 6 (total acceleration factor = 12). Whole brain data were acquired with 2 mm isotropic resolution at 3 echo times (TE = 62 ms, 92 ms and 130 ms). At each TE, 15 b = 1000 s/mm^2 and 30 b = 2000 s/mm^2 directions uniformly sampled in q space were acquired. Other scan parameters: TR = 2200 ms, partial Fourier 6/8, 78 slices over 13 multi-slice sets. The total scan time was about 5 minutes, which was compatible with TBI patient scan. For one healthy volunteer, SMS = 2 reference data were also acquired for multi-TE dMRI, the reference scan time was about 15 minutes.

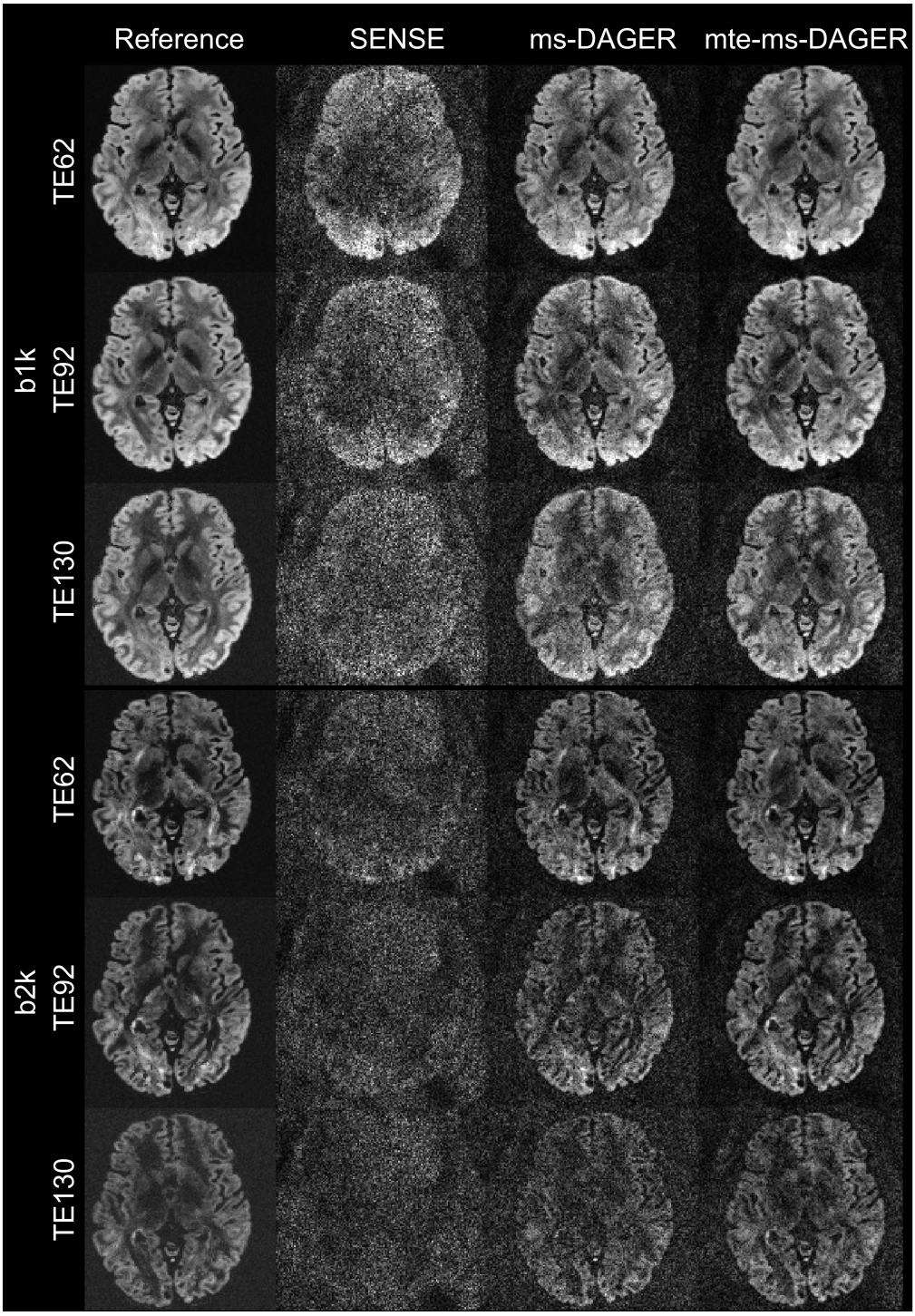

Figure 5.3: Reconstruction results of the simulation data.b = 1000 s/mm^2('b1k') and b = 2000 s/mm^2('b2k') images at three echo times from reference, SENSE,ms-DAGER and mte-ms-DAGER mrthods are shown. SENSE results are dominated by noise while ms-DAGER and mte-ms-DAGER methods can improve image SNR. Compared to ms-DAGER,mte-ms-DAGER further suppresses noise and improves image quality, showing more consistent structural details with the reference data.

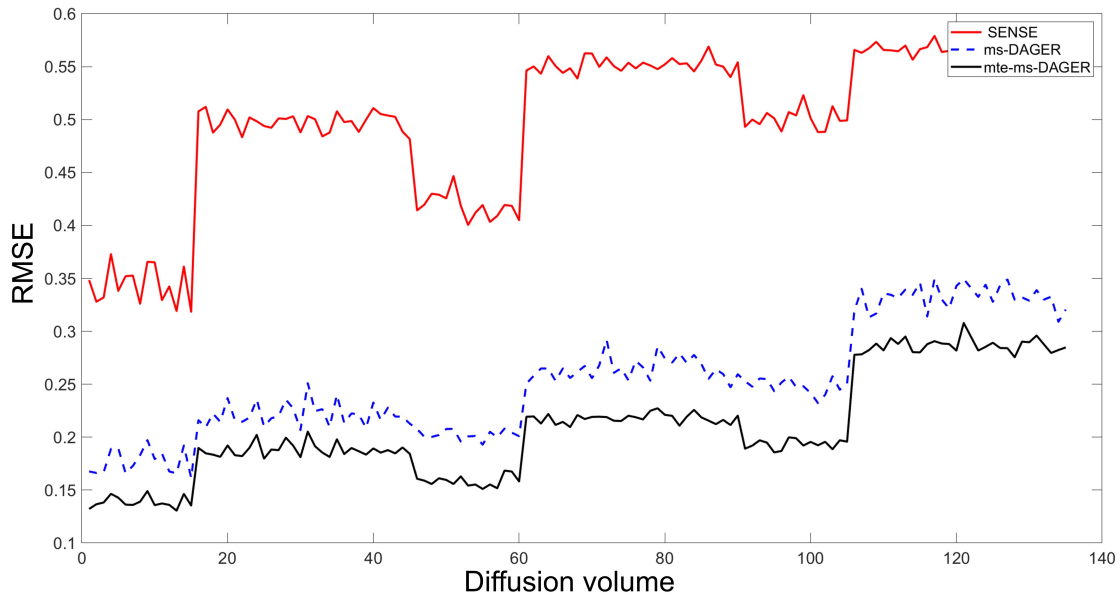

Figure 5.4: nRMSE values between different reconstruction results with the reference data are shown. mte-ms-DAGER shows the lowest error values.

5.3.2 Optimizing b=0 acquisition

Due to the significant contrast difference between b=0 images and diffusion weighted images, b=0 images cannot be reconstructed together with diffusion-weighted volumes in GP-based reconstruction. Therefore, b=0 images were independently reconstructed.

Several strategies for reconstruction b=0 data were considered. First, direct SENSE reconstruction was assessed. However, due to the high g factor at the high acceleration (i.e. 12 folds), b=0 images show strong artifacts, which affect the accuracy of diffusion fitting analysis.

One way to mitigate the g-factor noise amplification is to use a lower SMS acceleration factor. However, to match the TR of b=0 volumes with diffusion weighted volumes, this method would result in a reduced coverage for b=0. To achieve the same brain coverage as the diffusion weighted volumes, the FOV of the b=0 volume can be split into multiple slabs with reduced FOV along slice direction, with each slab being acquired separately using a lower SMS factor. For example, acquiring 6 b=0 slabs to cover the whole brain using single-band acquisition can provide the same brain coverage as a SMS=6 acquisition for diffusion weighted

volume. In this way, the TR-matched high-quality b=0 images reconstructed from SENSE can be used for later analysis steps. However, this acquisition technique requires manual shifting of imaging FOVs of multiple protocols to form the b=0 image, which adds burden to the scan operator and is prone to motion induced errors. Thus, a more robust b=0 acquisition technique is needed.

Instead of using a lower SMS factor with reduced FOV, in this work we propose to acquire b=0 data using the same SMS acceleration as the diffusion weighted volume, but in a multi-shot way to mitigate the g-factor noise amplification. As shown in Figure 5.5(a), similar to the 3D acquisition, 2D-SMS acquisition can be equivalently formulated as a 3D encoding problem of all simultaneously excited slices. By changing the ky and kz shift for acquisition of each shot, the entire 3D k space can be filled using 12 shots (each shot with in-plane acceleration R = 2 and multi-slice acceleration SMS = 6). In this way, we can reconstruct the b=0 images of 6 simultaneously excited slices from the fully sampled 3D k space. Similarly to SMS acquisition, 13 slice sets were acquired to cover the whole brain.

Multi-shot acquisition suffers from the inter-shot phase variation caused by physiological noise such as respiratory motion[195], To mitigate this effect, following N/2 ghost correction, we used MUSE method to correct for the shot to shot phase variation before combining the data from all shots to form the final reconstruction. As filling the full k-space with such multi-shot acquisition strategy would require longer scan time, to accelerate b=0 acquisition, we applied under-sampling with R = 2 along the kz direction, thus acquiring 6 shots instead of 12 shots for each TE (TE = 62, 92 and 130 ms). 6-shot b0 images acquired from one healthy subject at TE = 62 ms are shown in Figure 5.5(b). The total b=0 acquisition time is 52.8 s. By using the multi-shot b0 acquisition, we improved the robustness of the proposed fast multi-TE dMRI acquisition, and minimised the manual operation required for in vivo scan.

5.3.3 Multi-TE analysis

For the reconstructed in vivo data, Gibbs ringing artifacts were removed using degibbs3D from MRtrix3 (https://www.mrtrix.org/) followed by correction for

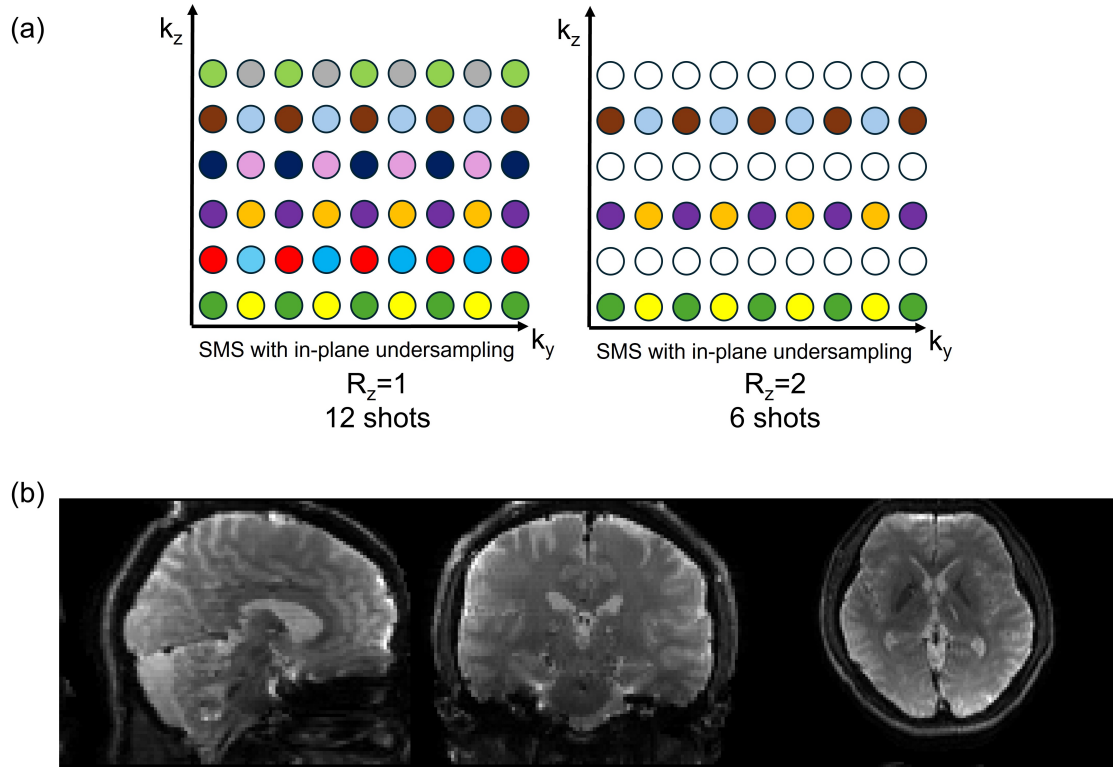

Figure 5.5: Multi-shot b0 acquisition. (a)2D SMS acquisition can be formulated as a 3D k space. Each colour refers to the sampling pattern of one shot. By changing the ky and kz offsets, all kz planes are acquired sequentially to fill in the entire k space and 6 simultaneously excited slices can be reconstructed. On the right, under-sampling with R = 2 along the kz direction is applied, thus 6 shots are acquired in total.(b) 6-shot b0 images acquired from one healthy subject at TE = 62 ms.

susceptibility-induced distortions, and motion using FSL's topup[118] and eddy tools[106]. NODDI metrics were calculated using FSL [119] at each TE. For joint multi-TE dMRI analysis, we fitted the multi-TE standard model using Standard Model Imaging (SMI) toolbox at https://github.com/NYU-DiffusionMRI/SMI [196, 197]. The noise variance input to the Standard Model was estimated using a technique based on random theory [108].

5.4 In vivo result

5.4.1 Healthy volunteers

Figure 5.6 shows the DWI reconstruction results from SENSE and mte-ms-DAGER methods for healthy subject 1. SMS = 2 reference data are also shown for b = 1000

s/mm^2('b1k') and b = 2000 s/mm^2('b2k') at different echo times. SENSE results show strong noise especially in higher b value shell and higher TE. ms-DAGER improves the image SNR, yet noise artifacts still exist in higher TEs as marked by the red box. Meanwhile mte-ms-DAGER significantly improves the image quality, reducing artifacts and recovering more consistent details with SMS = 2 reference images even for higher b value shell and higher TE (note that due to different TR, SMS = 2 shows different contrasts with SMS = 6 accelerated data).

The parameter maps from NODDI fitting for healthy subject 1 at each TE are shown in Figure 5.7. Isotropic fraction (fiso), intra-cellular fraction (fintra), and orientation dispersion index (ODI) maps are shown. Fitting results from SENSE are dominated by noise at higher TEs, where fiso maps and fintra maps show significantly increased values and large dropouts can be found in ODI maps. ms-DAGER improves the results, yet bias is still strong at higher TEs when SNR is low e.g. in white matter of ODI. mte-ms-DAGER demonstrates more robust fitting results which are more consistent with the reference despite a 3-fold reduction of scan time.

Figure 5.8 shows the parameter maps from the multi-TE standard model fitting for healthy subject 1. Fractions for axons and free water (f, f_w), anisotropy (p_2), diffusivity ($D_a, D_e^{\parallel}, D_e^{\perp}$) and compartmental T_2 values ($T_{2a}, T_{2e}^{\parallel}, T_{2e}^{\perp}$) are shown. Compared to the SMS = 2 reference, SENSE results show strong bias, particularly overestimated T_2 values (T_2^e) and diffusivities ($D_e^{\parallel}$), while the proposed mte-ms-DAGER shows more consistent results with the reference for all parameters, though reduced values can be found in white matter tracts in D_a and $D_e^{\parallel}$ maps possibly due to the inaccurate noise estimation input.

Figure 5.9 and Figure 5.10 show the reconstruction results from SENSE, ms-DAGER (TE by TE) and mte-ms-DAGER methods for healthy subject 2. DWI images at 3 echo times (62 ms, 92 ms, 130 ms) of b = 1000 s/mm^2('b1k') and b = 2000 s/mm^2('b2k') shells are shown respectively. SENSE results are dominated by noise while ms-DAGER and mte-ms-DAGER can suppress noise and reduce artifacts. However, in regions pointed by the red arrows, ms-DAGER results suffer

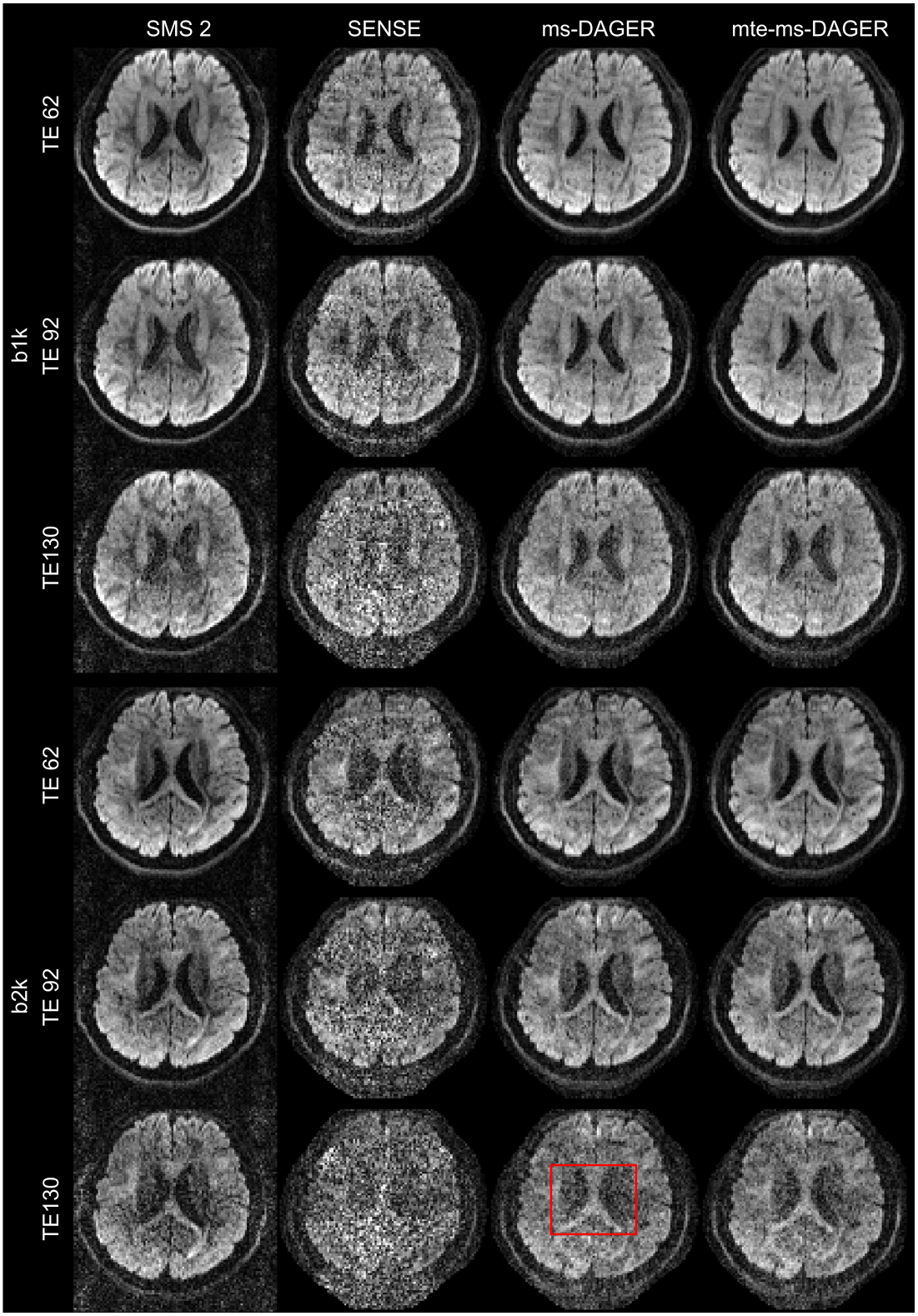

Figure 5.6: Comparison of reconstruction results from SENSE, ms-DAGER and mte-ms-DAGER using the SMS = 6 data for healthy subject 1. SMS = 2 data are also shown as reference. SENSE results are dominated by noise especially for the data of higher b values and higher TEs while mte-ms-DAGER substantially improves image SNR, showing the most consistent results compared to reference. Note that due to difference in TR, SMS = 2 shows different contrasts with SMS = 6 accelerated data

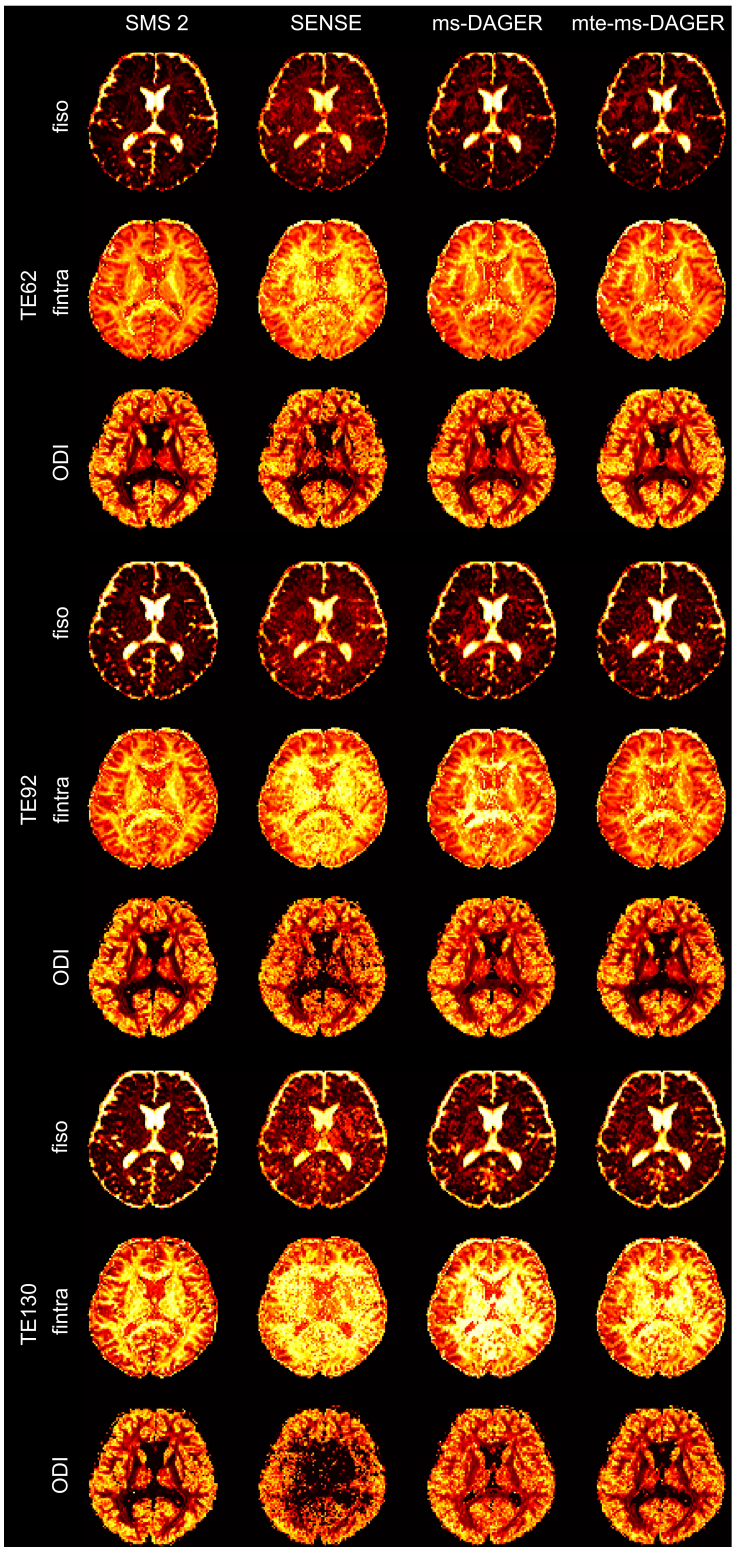

Figure 5.7: Comparison of NODDI fitting results from different reconstruction methods at three TEs for healthy subject 1. Isotropic fraction (fiso), intra-cellular fraction (fintra), and orientation dispersion index (ODI) maps are shown. SENSE results show large bias due to the high noise level, while mte-ms-DAGER demonstrates robust fitting results consistent with the reference.

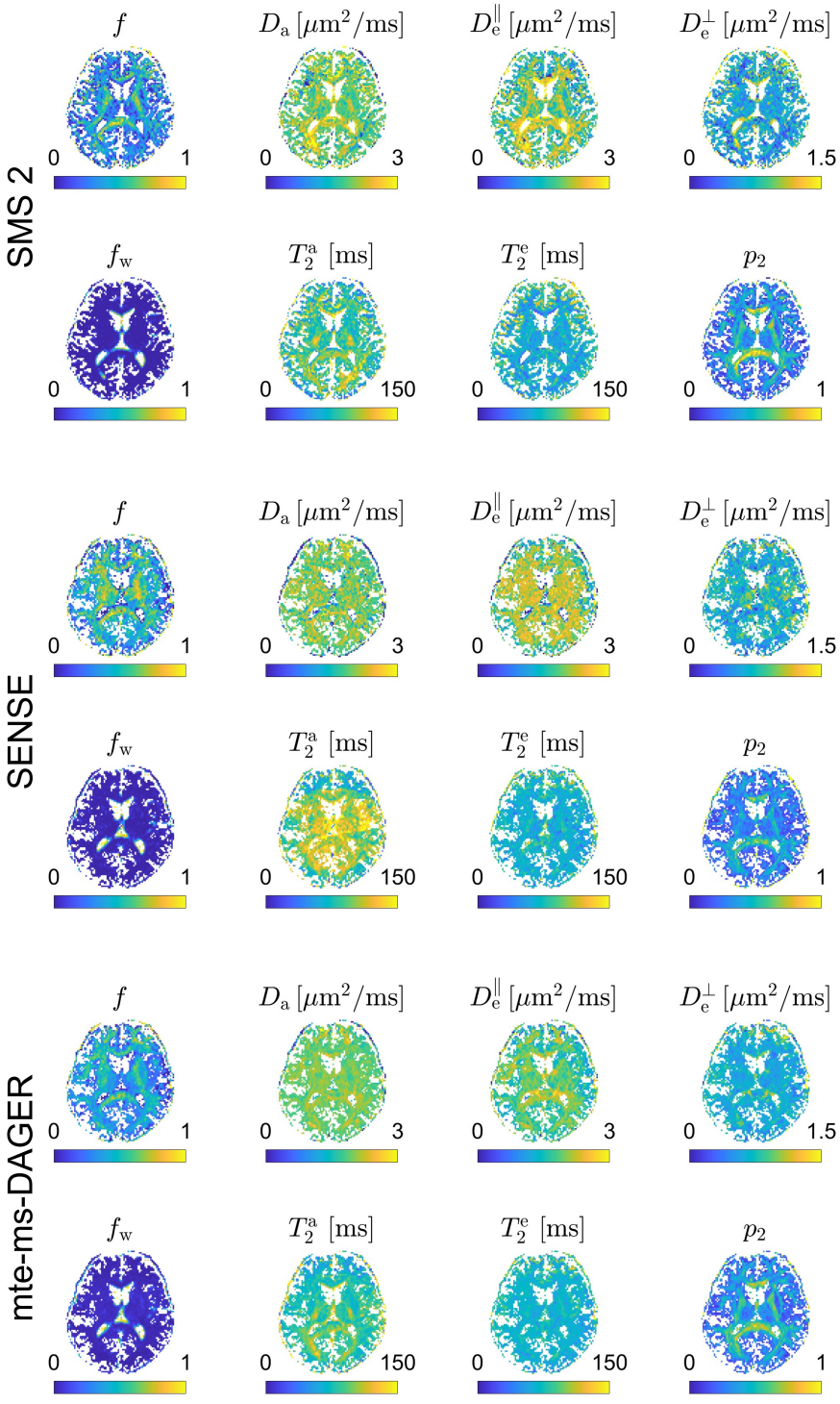

Figure 5.8: Comparison of multi TE Standard model fitting results from different reconstruction methods for healthy subject 1.Fractions for axons and free water (f, f_w,anisotropy(p_2), diffusivity($D_a, D_e^{\parallel}, D_e^{\perp}$) and compartmental T_2 values($T_{2a}, T_{2e}^{\parallel}, T_{2e}^{\perp}$) are shown. SENSE results show overestimated T2 and diffusivity parameters due to the high noise level, while mte-ms DAGER shows less bias in the maps compared to SENSE.A white matter mask is applied.

from strong noise, making the structure details hard to identify, while mte-ms-DAGER further improves SNR compared to ms-DAGER especially in higher TEs by exploiting the cross-TE sharing information.

Figure 5.11 shows the NODDI fitting results for healthy subject 2 at each TE using different reconstruction methods. Large bias in fitting results due to strong noise can be observed from SENSE results for all TEs including overestimated fintra and fiso maps along with dropouts in ODI maps. ms-DAGER and mte-ms-DAGER results both improve the fitting results by improving the image quality while at the highest TE, ms-DAGER shows more bias as overestimated fintra due to the lower SNR from lack of cross-TE information sharing.

Figure 5.12 shows the parameters from the multi-TE standard model fitting for healthy subject 2 using DWI data from three TEs. Consistent with healthy subject 1, SENSE results show overestimated T_2 values and diffusivity $(D_a, D_e^{\parallel})$ due to the high noise level while mte-ms-DAGER reduces the bias during fitting due to improved image quality.

5.4.2 TBI patients

Reconstruction results from SENSE and mte-ms-DAGER for TBI patient 1 b = 1000 s/mm^2('b1k') and b = 2000 s/mm^2('b2k') data at different echo times are illustrated in Figure 5.13. SENSE results suffer from high noise levels caused by the large g factor during reconstruction, making it challenging to identify structural details at high TEs/ high b value. Meanwhile, mte-ms-DAGER improves the image quality at all shells and TEs.

Figure 5.14 shows the parameters from NODDI fitting for patient 1 at each TE. Consistent with healthy dataset, fitting results from SENSE are affected by noise. The ODI maps at TE = 92 and 130 ms show outliers (black dots) due to the high noise level. fintra maps appear to be overestimated. With the improvement of SNR, mte-ms-DAGER demonstrates more robust fitting results, reducing the overestimation and outliers.

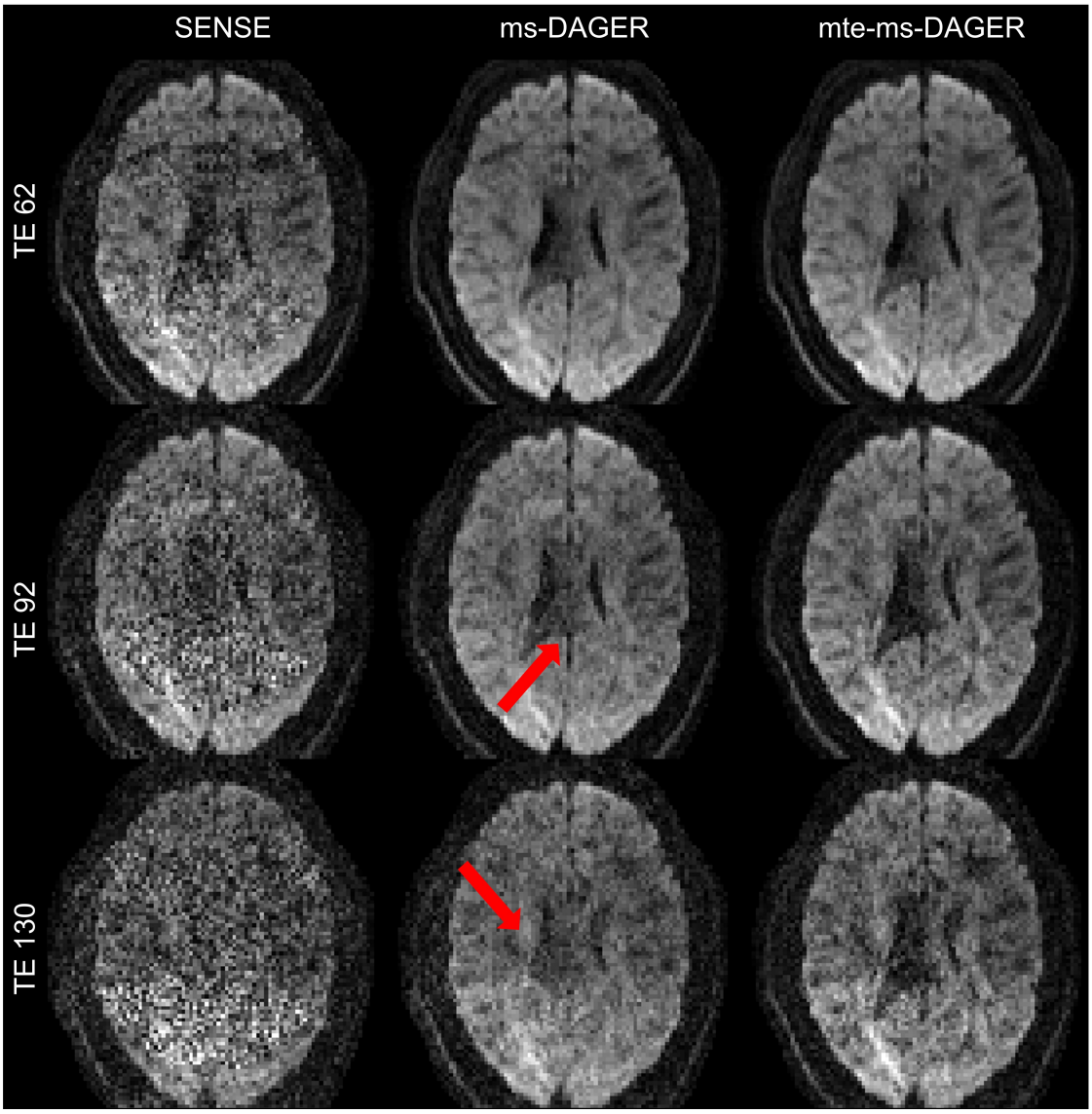

Figure 5.9: Comparison of different reconstruction methods for b = 1000 s/mm^2('b1k') data for healthy subject 2. b1k images at three echo times from SENSE, ms-DAGER(TE by TE) and mte-ms-DAGER reconstruction results are shown. mte-ms-DAGER shows the best SNR compared to SENSE and ms-DAGER by using cross-TE information.Loss of diffusion contrast due to low SNR can be found in the regions pointed by the red arrow.

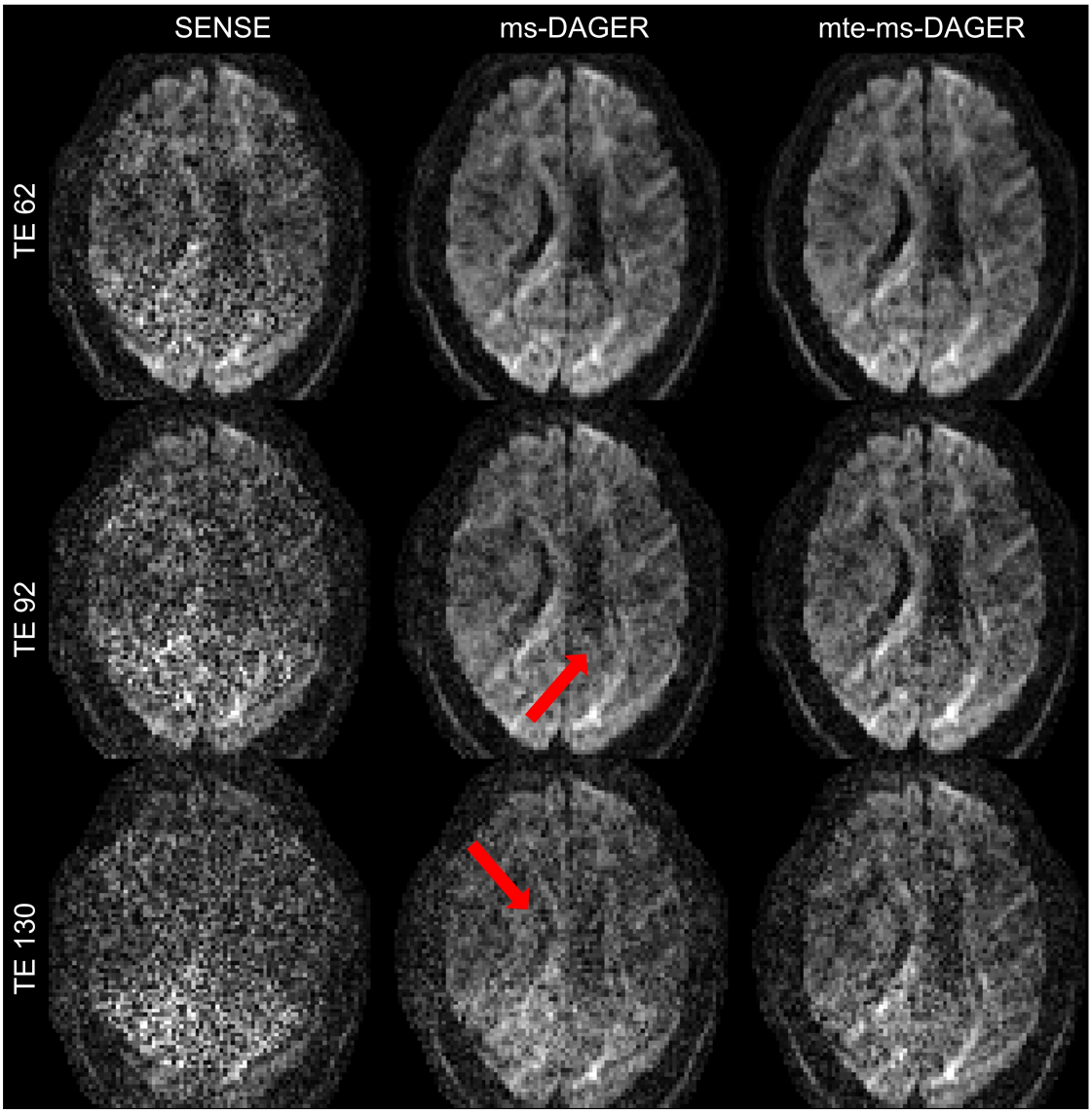

Figure 5.10: Comparison of different reconstruction methods for b = 2000 s/mm^2('b2k') data for healthy subject 2. b2k images at three echo times from SENSE, ms-DAGER(TE by TE) and mte-ms-DAGER reconstruction results are shown. mte-ms-DAGER shows the best SNR compared to SENSE and ms-DAGER by using cross-TE information.Loss of tract contrast due to low SNR can be found in the regions pointed by the red arrow

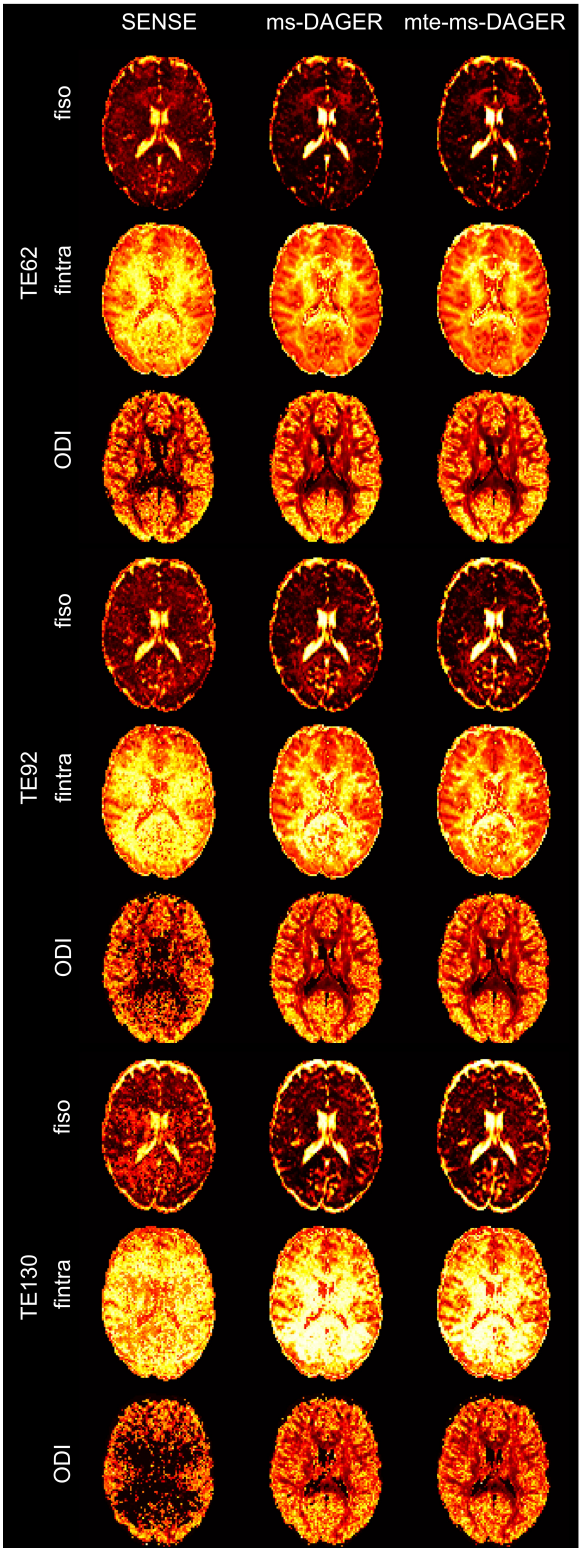

Figure 5.11: Comparison of NODDI fitting results from different reconstruction methods at three TEs for healthy subject 2.Isotropic fraction (fiso), intra-cellular fraction (fintra), and orientation dispersion index (ODI) maps are shown. SENSE results show large bias due to the high noise level, while mte-ms DAGER shows less bias in the higher TE maps compared to ms-DAGER.

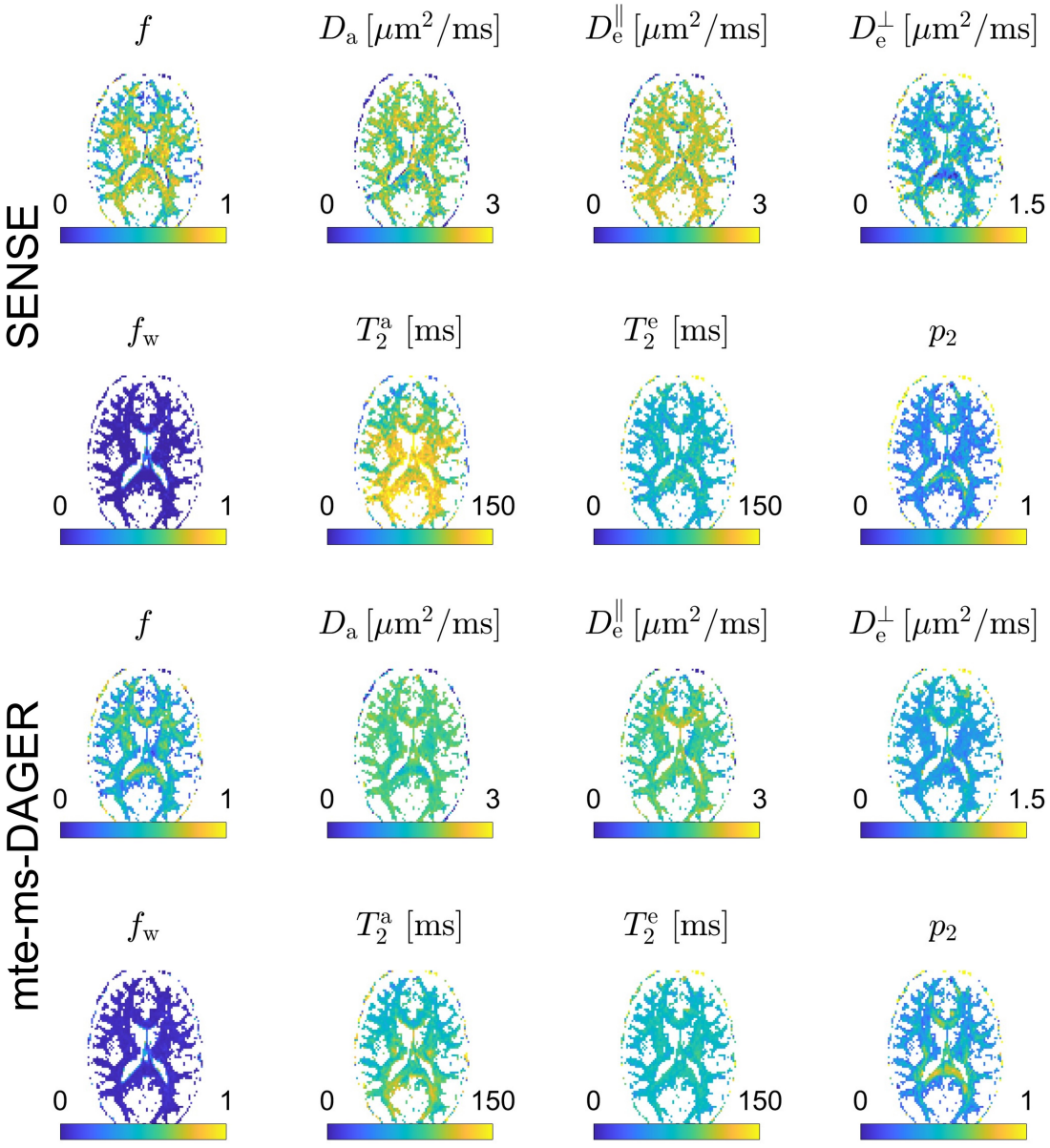

Figure 5.12: Comparison of multi TE Standard model fitting results from different reconstruction methods for healthy subject 2.Fractions for axons and free water (f, f_w,anisotropy(p_2), diffusivity(D_a, $D_e^{\parallel}$, $D_e^{\perp}$) and compartmental T_2 values(T_{2a}, $T_{2e}^{\parallel}$, $T_{2e}^{\perp}$) are shown. SENSE results show large bias due to the high noise level, while mte-ms DAGER shows less bias maps.A white matter mask is applied.

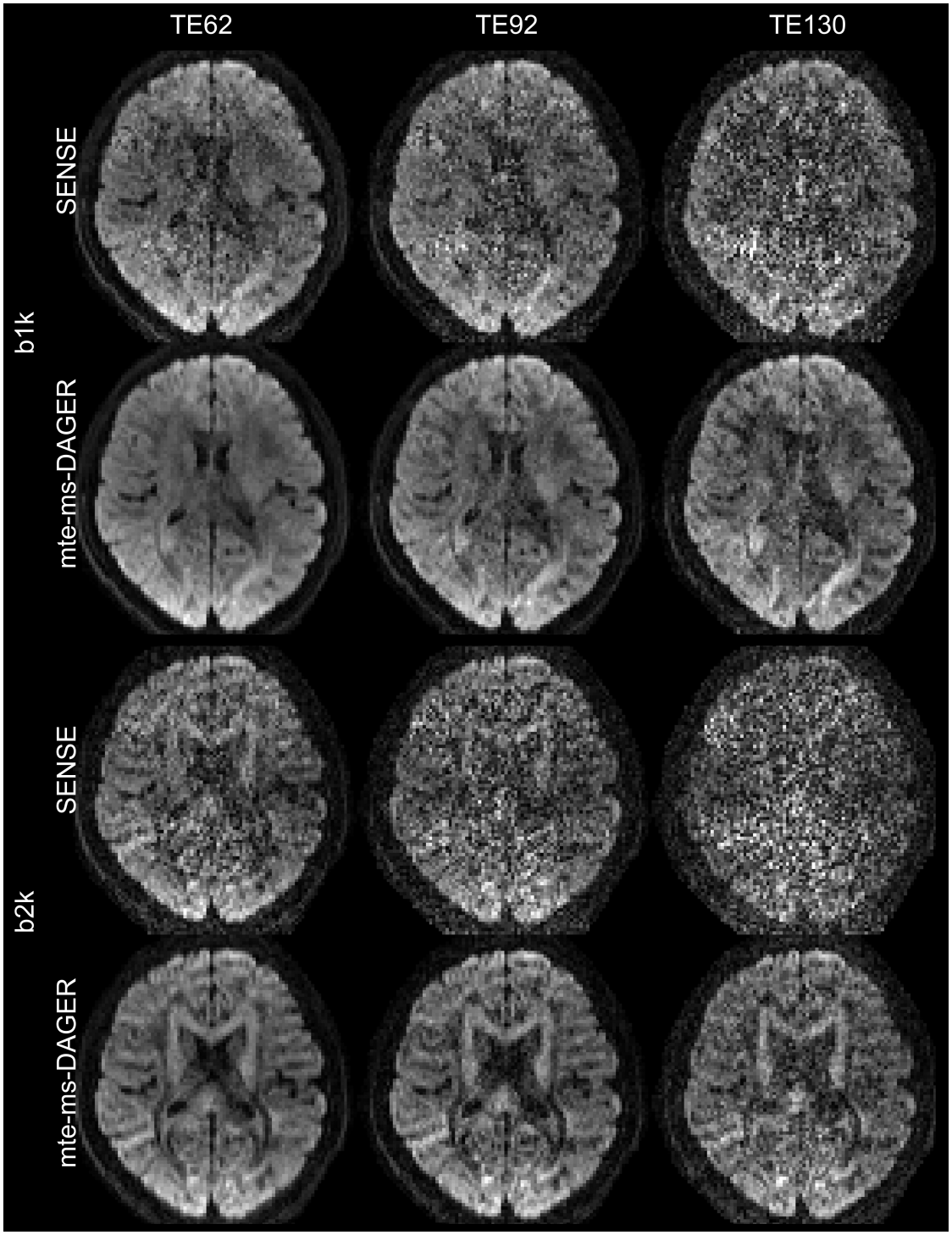

Figure 5.13: Comparison of DWI reconstruction results from SENSE and mte-ms-DAGER for patient1. b = 1000 s/mm^2('b1k') and b = 2000 s/mm^2('b2k') data at different echo times are shown. SENSE results are dominated by noise especially for the b2k data at TE = 92 and 130 ms. mte-ms-DAGER substantially improves image SNR, showing more clear structure information.

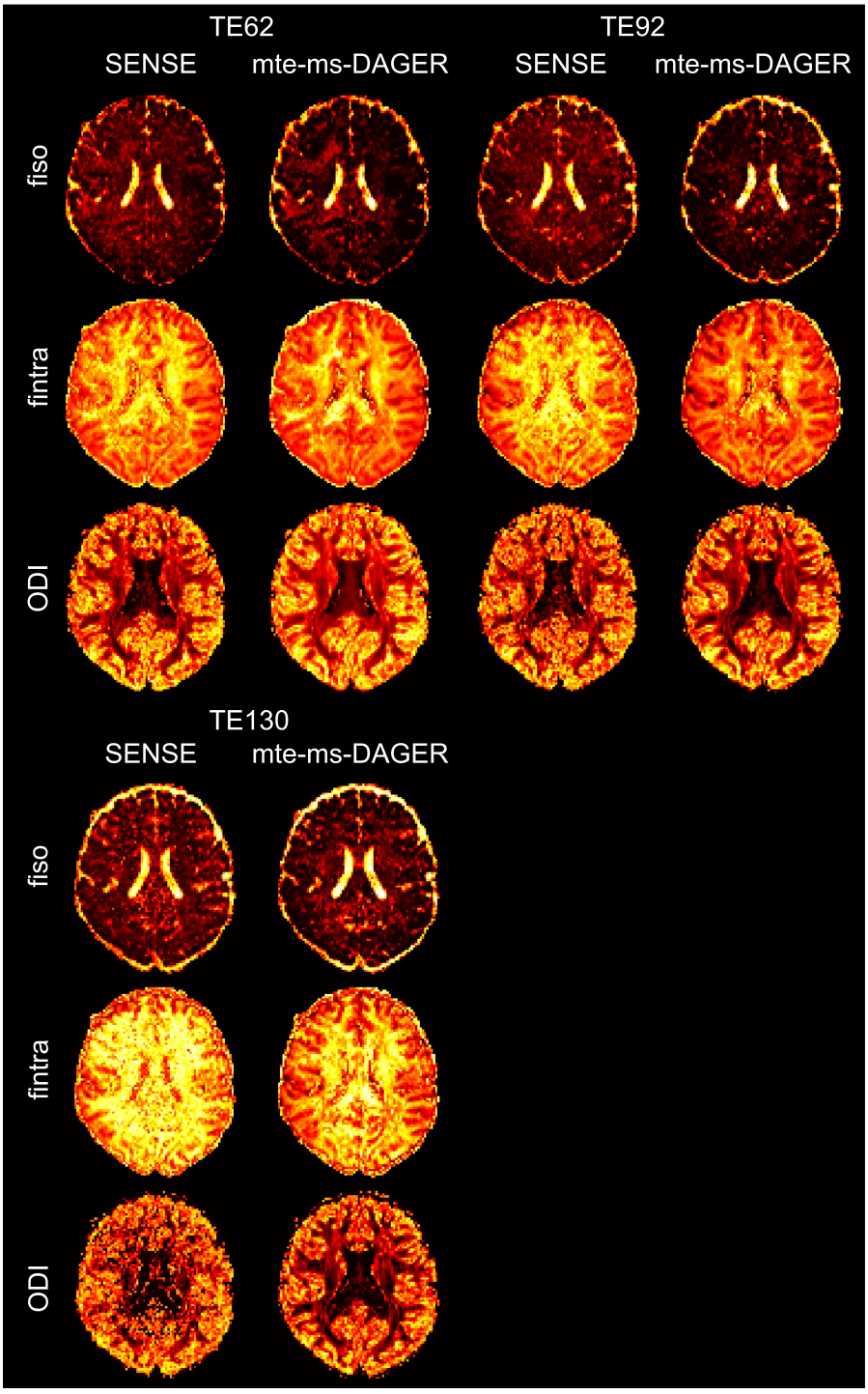

Figure 5.14: Comparison of NODDI fitting results from different reconstruction methods for patient 1. Isotropic fraction (fiso), intra-cellular fraction (fintra), and orientation dispersion index (ODI) maps are shown. Due to the high noise levels in SENSE reconstruction results, bias can be found in fintra and ODI maps at TE 92 and 130 ms. Meanwhile, mte-ms-DAGER shows reduced bias in fitting results owing to improved image quality.

Figure 5.15 shows the parameters from the multi-TE standard model fitting for patient 1 using DWI data from three TEs. Consistent with healthy dataset as in Figures 5.8 and 5.12, T2 values and diffusivity in the centre part of the brain from SENSE results appear to be higher, which might suggest higher level of g factor-related noise. mte-ms-DAGER, however, appear to produce more consistent results compared to the reference SMS = 2 data in healthy subject.

Reconstruction results from SENSE and mte-ms-DAGER for TBI patient 2 are show in Figure 5.16. mte-ms-DAGER robustly improve the image SNR and recover structure details compared to SENSE at different shells and TEs.

Figure 5.17 shows the parameters from NODDI fitting for patient 2 at each TE. Fitting results from SENSE appear to show more bias and errors especially in maps at TE = 92 and 130 ms due to the high noise levels, while mte-ms-DAGER substantially corrects for these bias.

Figure 5.18 shows the parameters from the multi-TE standard model fitting for patient 2 using DWI data from three TEs. Consistent with previous findings, mte-ms-DAGER increases SNR and reduces aliasing artifacts, appearing to produce more robust fitting results compared to SENSE.

5.5 Discussion

In this work, we proposed a joint k-q-TE reconstruction method to accelerate multi-TE dMRI acquisition. By using Gaussian Process to exploit the sharing information in the q-TE space, we achieved a high acceleration factor of 12× (in plane R = 2, SMS = 6) on a 3T clinical scanner. We also designed a clinically feasible multi-TE dMRI in vivo acquisition protocol (in total 6 minutes including b=0 and all calibration scans) and tested the robustness and performance of the proposed techniques on healthy volunteers and TBI patients in practical applications.

One potential concern for the joint reconstruction method is that smoothing effects beyond what is intrinsic to the data may be introduced when borrowing information from other volumes. In previous works [27, 90], we have evaluated the

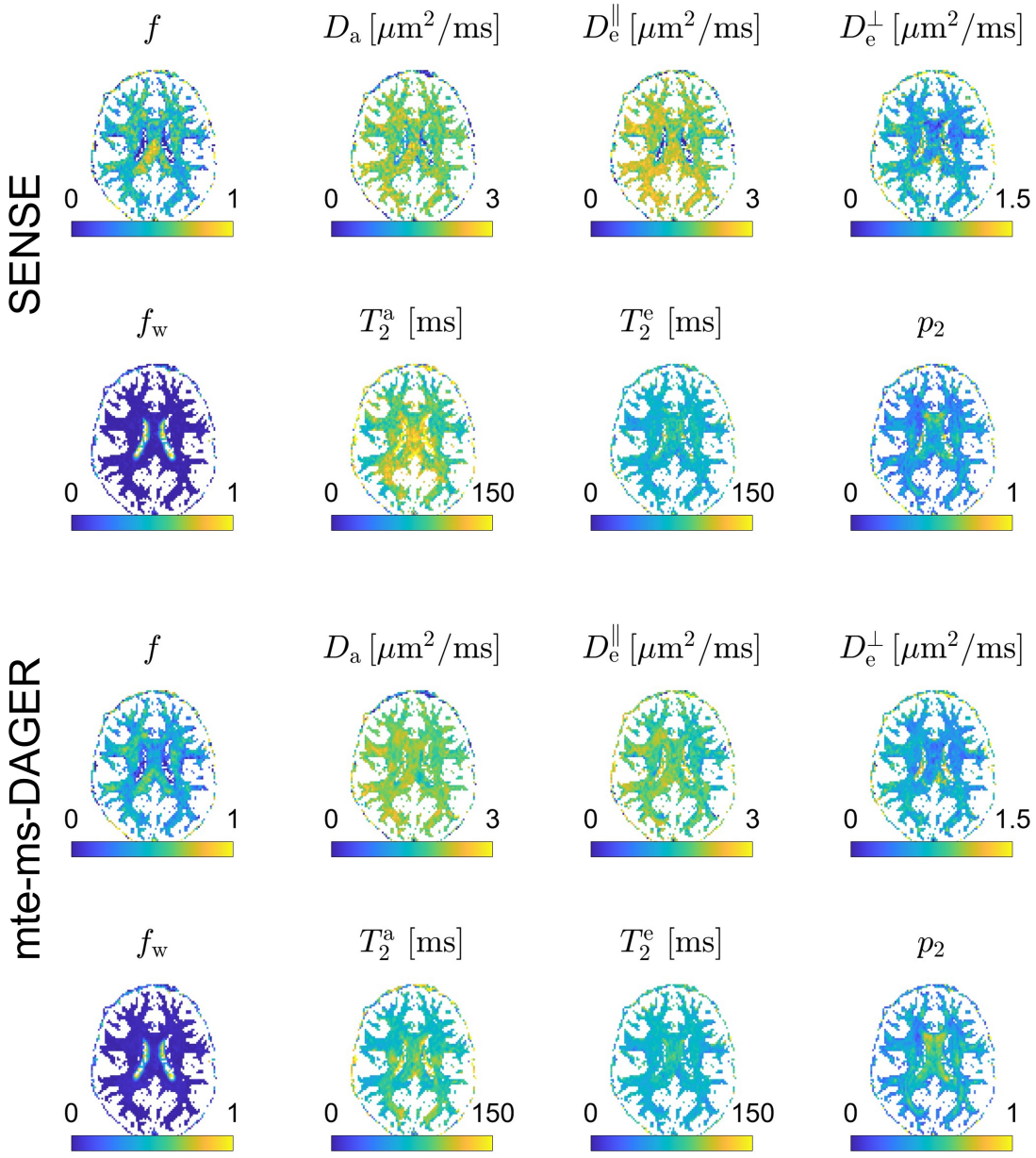

Figure 5.15: Comparison of multi TE Standard model fitting results from different reconstruction methods for patient 1.Fractions for axons and free water (f, f_w,anisotropy(p_2), diffusivity($D_a, D_e^{\parallel}, D_e^{\perp}$) and compartmental T_2 values($T_{2a}, T_{2e}^{\parallel}, T_{2e}^{\perp}$) are shown. SENSE results are corrupted by noise while mte-ms-DAGER improves the fitting results.A white matter mask is applied.

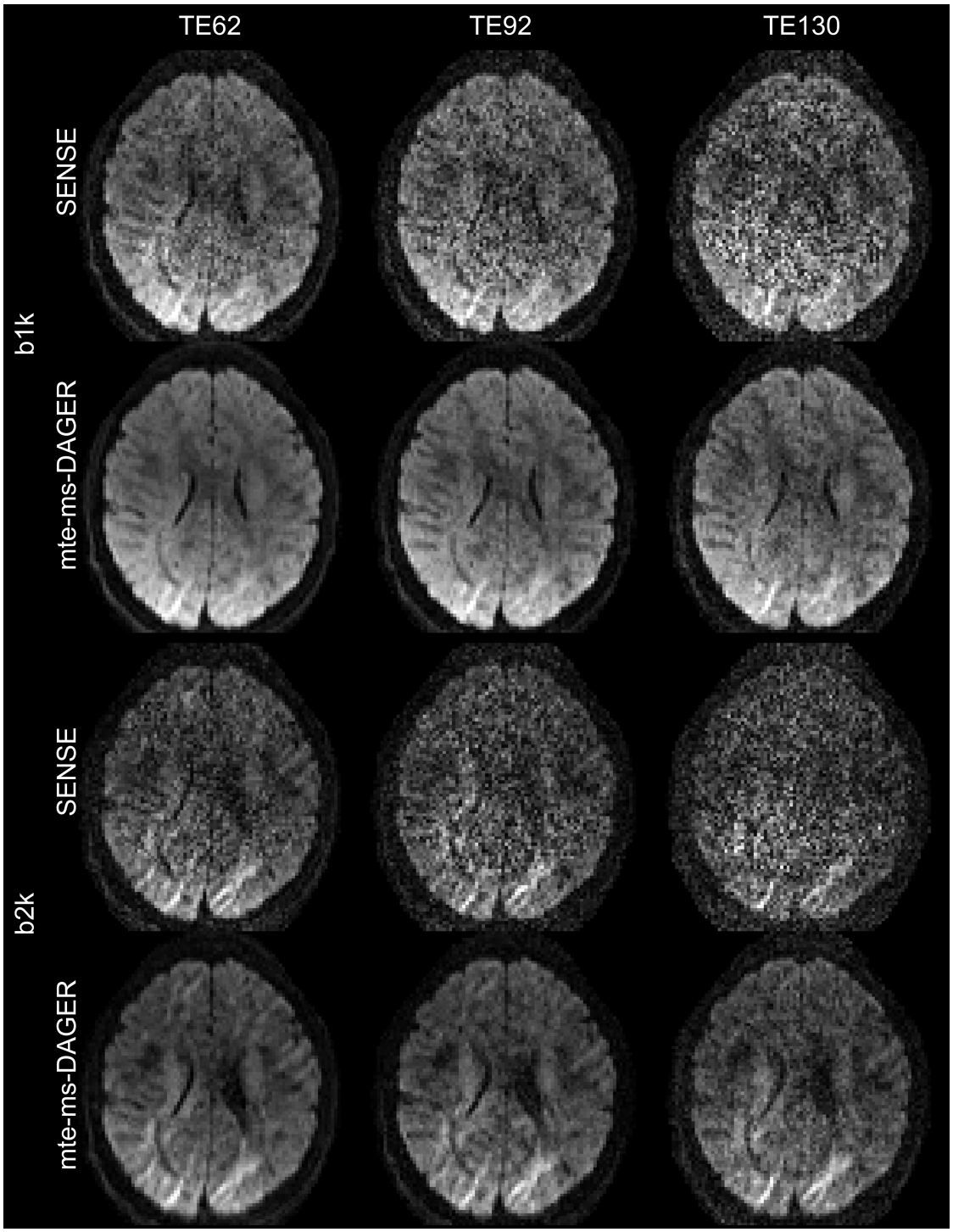

Figure 5.16: Comparison of DWI reconstruction results from SENSE and mte-ms-DAGER for patient 2. b = 1000 s/mm^2('b1k') and b = 2000 s/mm^2('b2k') data at different echo times are shown. SENSE results show high noise levels for the data at TE = 92 and 130 ms while mte-ms-DAGER robustly improves image SNR, providing higher quality data for analysis.

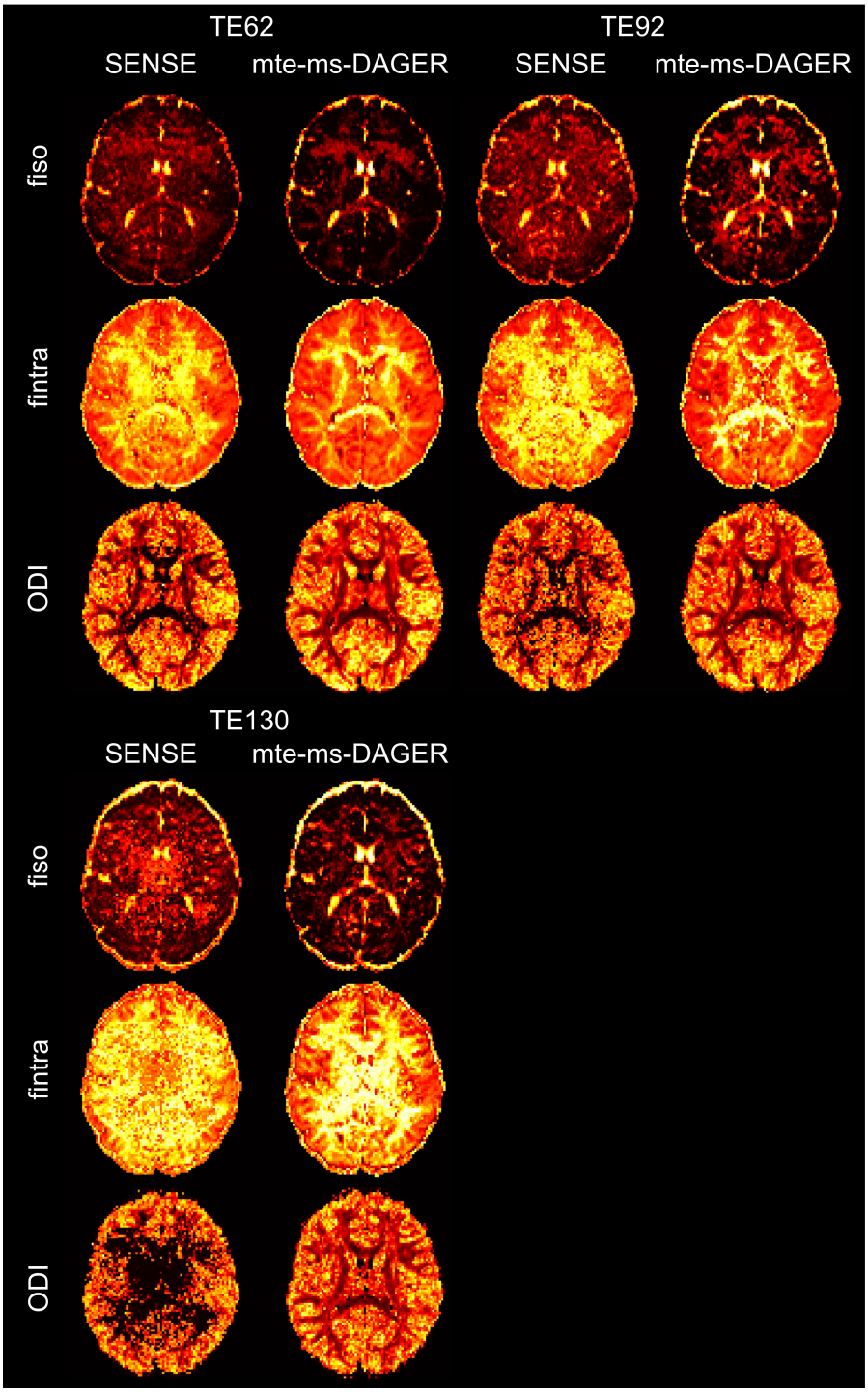

Figure 5.17: Comparison of NODDI fitting results from different reconstruction methods for patient 2. Isotropic fraction (fiso), intra-cellular fraction (fintra), and orientation dispersion index (ODI) maps are shown. Overestimation in fintra maps and bias in ODI maps can found in SENSE results at higher TES. Meanwhile, mte-ms-DAGER shows less bias compared to SENSE.

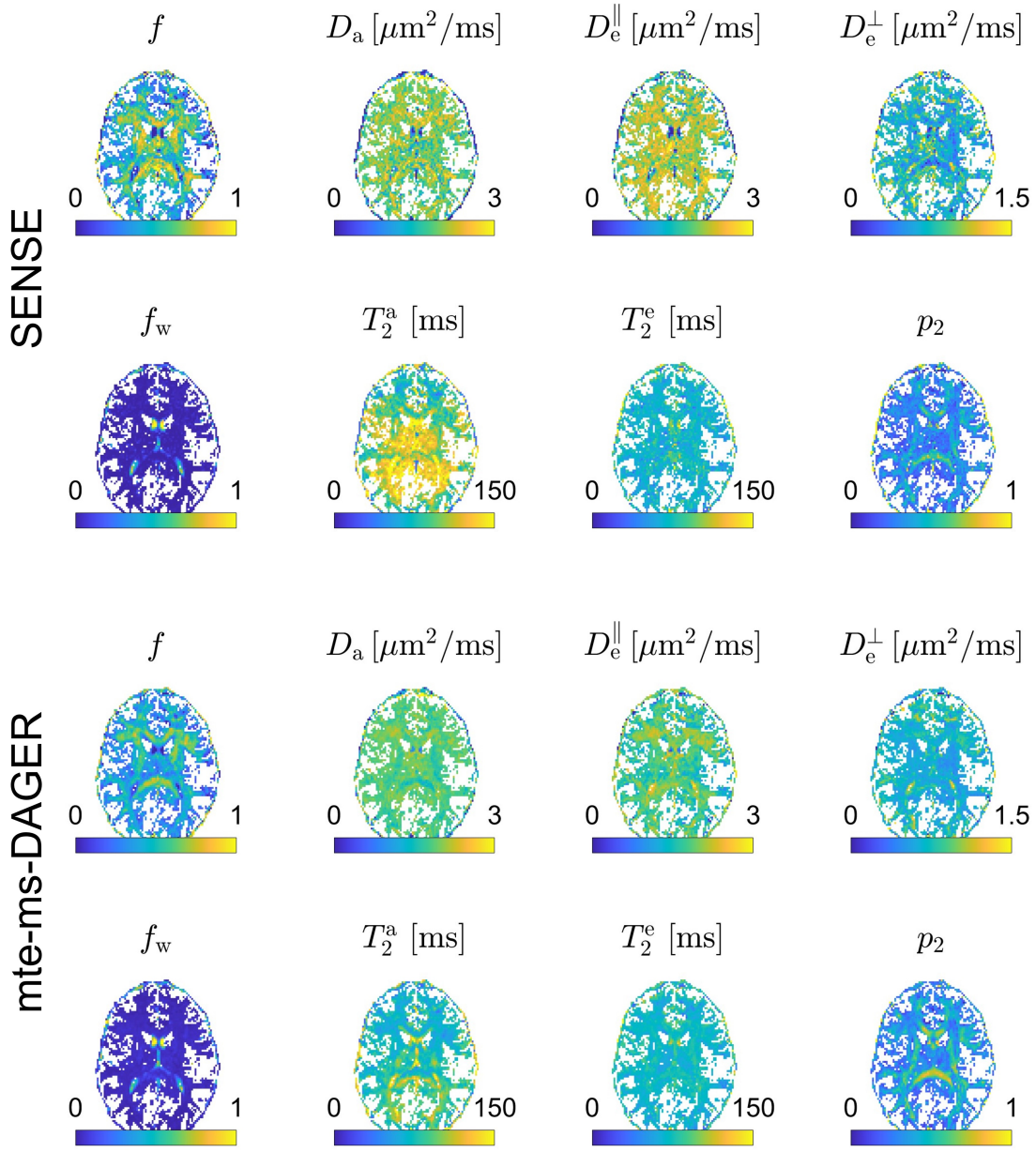

Figure 5.18: Comparison of multi TE Standard model fitting results from different reconstruction methods for patient 2.Fractions for axons and free water (f, f_w,anisotropy(p_2), diffusivity($D_a, D_e^{\parallel}, D_e^{\perp}$) and compartmental T_2 values($T_{2a}, T_{2e}^{\parallel}, T_{2e}^{\perp}$) are shown. SENSE results in the centre brain are dominated by noise due to the high g factor, while mte-ms-DAGER reduces the noise level and artifacts, appearing to show more robust fitting results.A white matter mask is applied.

angular smoothing and cross-shell smoothing effects of the proposed reconstruction method. Based on angular covariance and cross-shell ratio calculation, we demonstrated that the smoothing effect is small. In this work, we used a high SNR public multi-TE dataset to test the cross-TE covariance as shown in Figure 5.1. The GP prediction results show similar cross-TE covariance compared to reference, indicating that the introduced cross-TE smoothing is small.

Apart from the covariance function, the mean function design can also affect the GP modelling performance. One common way for GP modelling is to assume zero mean for the data after subtracting an estimation of the mean values. In previous works[27, 90], we used averaged values for all diffusion volumes as an estimation of the mean value. The covariance function is capable of capturing the diffusion contrast variation across different shells and diffusion directions. However, in multi-TE condition, data acquired with different TEs have global signal intensity changes due to the T2 decay. If directly using the averaging of all volumes across all TEs as the mean function estimation, large global intensity difference will remain between different TEs after subtracting the mean value from the data, which may lead to unstable hyperparameter fitting. Additionally, magnitude averaging and complex averaging may also affect the estimation accurate of the mean function, as radian noise in the magnitude images can introduce bias. In Figure 5.19, we compare different mean function designs with simulation data as used in Figure 5.3. We choose four different methods for calculating the mean values: magnitude direct averaging of all volumes (direct avg), magnitude averaging of volumes from each TE(TE mag avg), complex averaging of volumes from each TE(TE cpx avg) and complex averaging of volumes from each TE and each shell(TE-shell cpx avg). We calculate the nRMSE values between reconstruction results using different mean functions and the reference. Complex averaging of volumes from each TE and each shell (TE-shell cpx avg), i.e., generating a separate mean functions for each TE and each b shell, shows the least error, which indicates that it's more accurate to exploit the intrinsic data smoothness by separately capturing intensity difference and contrast difference with mean function and covariance function. Another way

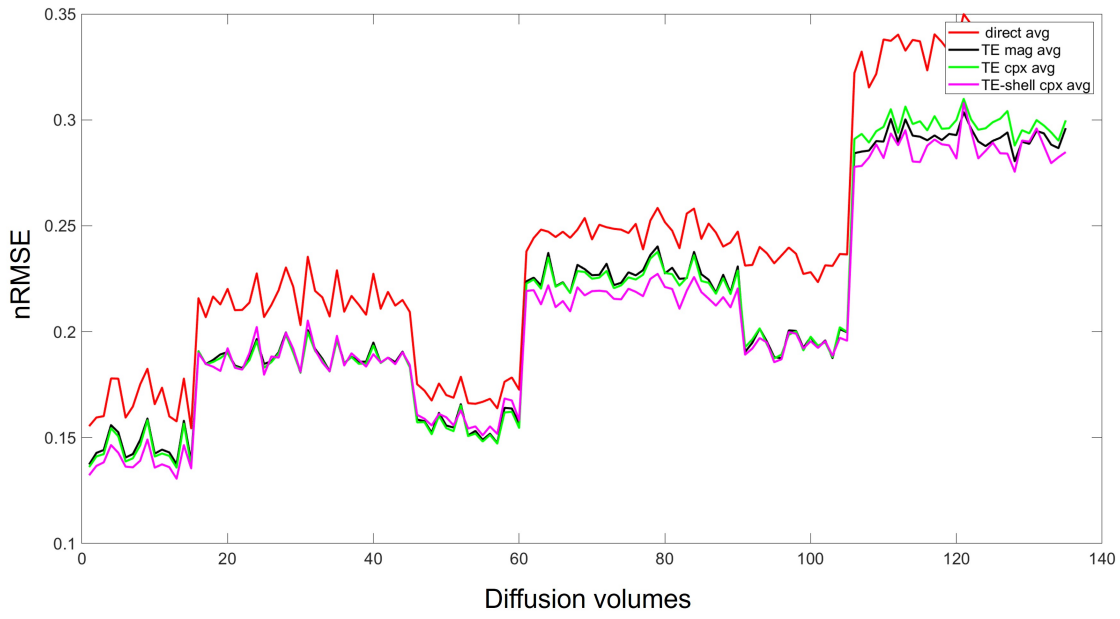

Figure 5.19: Comparison on different mean functions using simulation data. Different designs of mean functions are tested using simulation data. nRMSE values calculated from reconstruction results using different mean functions (direct magnitude averaging of all volumes(direct avg), magnitude averaging of volumes from each TE(TE mag avg), complex averaging of volumes from each TE(TE cpx avg) and complex averaging of volumes from each TE and each shell(TE-shell cpx avg)) with the ground truth are shown.

to model the cross-TE mean signal intensity changes is to use an exponential decay function based on the physical principles of T2 signal decay. However, when strong noise exists in higher TE data points, the exponential decay fitting may not be robust and accurate. Future research will explore how this physics-informed mean function may affect the GP modelling accuracy.

In Figure 5.20, we tested the robustness of the hyperparameter fitting against noise. We added different levels of noise to the high SNR public multi-TE dataset [194] used in q-TE GP covariance validation experiments and then fitted the GP model with the noise-corrupted data (SNR 24.7 dB, 17.8 dB, 13.7 dB, 10.9 dB and 8.6 dB respectively). Then we generated predictions for the original multi-TE data using GP model inference with fitted parameters under different noise levels. Finally, we calculated the nRMSE values between the GP prediction and the reference. We found that with the increase of noise levels, the nRMSE values still remain relatively low, indicating that the GP hyperparameter fitting is robust even at high

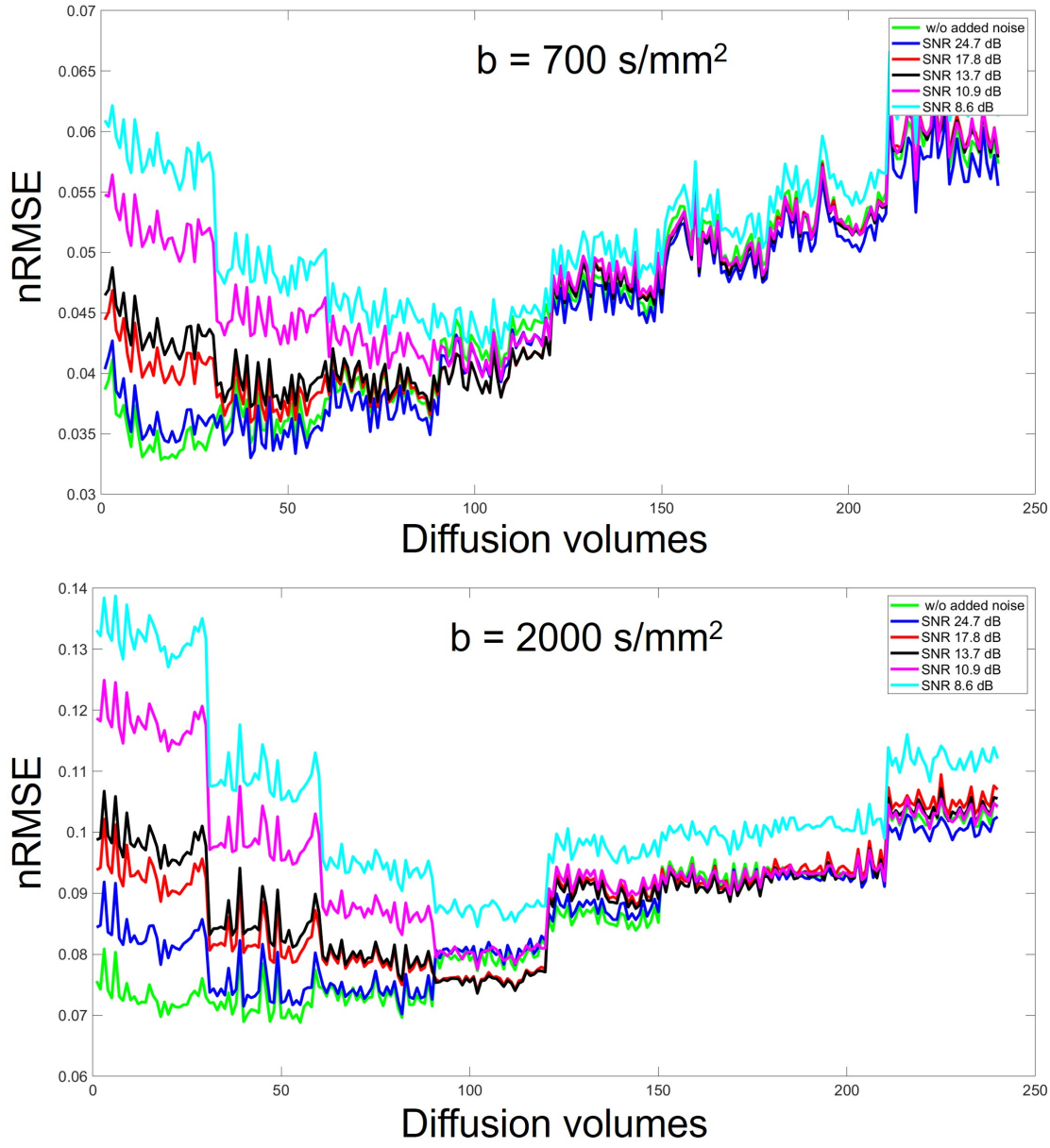

Figure 5.20: Testing hyperparameter fitting robustness against noise. GP models are fitted with data with different SNRs by adding different levels of noise are added to the reference data. Then the fitted GP models are used to predict the original reference data.The nRMSE values between GP prediction and reference data are shown.

noise levels, proving the GP model's robustness against noise.

One challenge for the GP-based joint reconstruction is that with the increased number of hyperparameters and more complex covariance function structures, the computing time and complexity is increased. Thus, the hyperparameter optimisation may take a long time, and the optimisation may become less robust and easier to

fall into local minima. One way to improve fitting efficiency is to use more advanced optimisation algorithms. Currently, conjugate gradient based optimisation was used. Other gradient-based or gradient-free based methods may be used to improve the fitting performance. Besides, deep learning based methods can also be used to estimate the covariance values, as they show promising results dealing with nonlinear high-dimension data[198–200]. These advanced hyperparameter fitting methods will be investigated in the future.

Another major challenge for the joint reconstruction method is the inter-volume misalignment due to subject motion especially when scanning patients. The geometric mismatches between volumes lead to blurring artifacts if not corrected. In this preliminary investigation, no significant motion was observed in the subject data shown in this chapter, thus we haven't included motion correction in the reconstruction. However, for the larger patient cohort data, motion may exist. In a previous work shown in chapter 4 of this thesis, we proposed mr-ms-DAGER which jointly corrects for motion and eddy current effects, and reconstruct the images, showing robust performance against large movements. Thus, the proposed joint k-q-TE method can be incorporated into the mr-ms-DAGER framework which improves the robustness of the method .

Multi-TE dMRI provides improved specificity for tissue microstructure modelling, which may provide a more sensitive biomarker for lesions like micro bleeding by detecting free water fraction[201]. For the ongoing study, about 30 TBI patients have been scanned with the accelerated multi-TE dMRI sequence. An investigation into the correlation between microstructure model parameters derived from our multi-TE dMRI data and pathology will be carried out in the future on this larger cohort of data together with our clinical collaborators. Diffusion analysis models beyond what we've evaluated so far will also be tested.

This current work also has some limitations. Firstly, we assume that q space relations and cross-TE relations are orthogonal in covariance function design, yet q-TE dimensions may have coupling effects. Future work will explore designing of a better mean function and a covariance function to capture such relation, potentially

with deep learning based methods, and explore extension to multi-dimensional dMRI with more encoding contrasts. Secondly, we used multi-TE standard model to analyse the multi-TE dMRI data, which requires an accurate noise estimation as an input along with the imaging data. However, current noise estimation method based on random theory [108] might not be accurate, which may explain some remaining differences between the fitting results of mte-ms-DAGER and SMS = 2 reference data as in Figure 5.8. We plan to further investigate the noise estimation method and further improve the fitting accuracy and robustness.

5.6 Conclusion

In this work, we proposed a joint k-q-TE reconstruction method for accelerating multi-TE multi-shell dMRI acquisition. Based on simulation and in vivo data test for both healthy volunteers and TBI patients, our proposed method robustly improves image quality for the multi-shell dMRI data at different echo times in shorter scan times compared to conventional methods and produces robust microstructure fitting results. This technique can facilitate the wider application of advanced microstructure signal models using combined diffusion-relaxometry information.

6 Summary and Future Work

Contents

6.1 Summary of the thesis

The trade-off between spatial resolution, model specificity and scan time has long been a major challenge for microstructural imaging with diffusion MRI, limiting its wider applications. Joint reconstruction uses intrinsic data redundancy and exploits the data smoothness along contrast encoding dimensions, enabling high acceleration factors and offering a potential solution to achieving high dMRI scan efficiency while preserving the image quality. This thesis presents advanced acquisition and reconstruction methods based on joint reconstruction to achieve fast and robust microstructural imaging with dMRI.

Joint k-q reconstruction methods use the shared information in q space to assist reconstruction of undersampled k space data. However, if not designed correctly, these methods may introduce extra smoothing effects beyond the intrinsic smoothness which leads to bias when fitting diffusion analysis models. Besides,

current k-q reconstruction methods mainly focus on exploiting shared information between diffusion directions within single shell, which is suboptimal for high b values where all directions have very low SNR. In Chapter 3, we propose a multi-shell diffusion MRI with Gaussian process estimated reconstruction of multi-band imaging by extending the previous DAGER method to multi-shell condition to reduce the demand of diffusion volume numbers in each shell and improve the performance of higher b value shells. A diverse q space sampling pattern is designed to better utilize complementary information across both diffusion directions and b shells. We also adapt our method to be robust under the Rician noise conditions in lower SNR data. The computing time for each iteration is 20 minutes per slice group and the 1.5 mm isotropic whole-brain data takes about 10 hours for 6 iterations on our cluster. This work achieves highly accelerated (TR = 3.5 s) multi-shell diffusion MRI acquisition with high image quality on a 7T scanner.

Motion and eddy current lead to misalignment between different imaging volumes. If not corrected, the geometric mismatches can lead to blurring and artifacts in joint reconstruction that pulls information from all volumes simultaneously. In Chapter 4, we introduce an eddy current and motion robust joint k-q reconstruction by incorporating the motion and eddy current correction into the joint reconstruction framework. A computationally efficient algorithm which splits the optimisation problem into two sub-problems substantially reduces the memory burden. The computing time for each iteration is 2 hours and the 1.5 mm isotropic whole-brain data takes about 12 hours for 6 iterations on our cluster. With the proposed iterative joint motion/eddy current correction and image reconstruction, we achieve robust SMS = 6 accelerated (TR = 1.8 s) multi-shell diffusion MRI acquisition for microstructural imaging at 3T.

Combined relaxometry-diffusion techniques provide higher specificity for microstructure mapping, yet the acquisition of higher-dimensional data significantly increases scan time. Chapter 5 investigates extending joint reconstruction method to accelerate combined relaxometry-diffusion using multi-TE dMRI as an example. We design the GP modelling for multi-TE dMRI signal and validate it using a

public multi-TE dataset. Then we extend the previous joint k-q reconstruction method to multi-TE q space condition using the proposed GP modelling. An in vivo acquisition protocol was designed and the preliminary results on both healthy volunteers and patients demonstrate that the proposed method can achieve robust microstructural fitting within much shorter scan time (TR = 2.2 s) compared to conventional methods at 3T. The computing time for each iteration is 15 minutes per slice group and the 2 mm isotropic whole-brain data takes about 6 hours for 6 iterations on our cluster.

In conclusion, this thesis presents the acquisition and reconstruction methods we developed for faster dMRI scans, which improves scan efficiency and preserves the image quality, showing robust microstructural fitting results. GP offers a model-free data-driven way to provide prior for the reconstruction. By incorporating multi-shell GP modelling, ms-DAGER method improves reconstruction performance for multi-shell dMRI data especially higher b value shells where the image SNR is low. By incorporating q-TE GP modelling, mte-ms-DAGER method further improves image quality for multi-TE multi-shell dMRI data especially at higher TEs with intrinsically low SNR due to signal decay. By adding motion correction and eddy current correction, mr-ms-DAGER method improves the robustness of previously proposed joint k-q reconstruction techniques and corrects for the blurring and artifacts led by the inter-volume inconsistency in practical scans. With different components, our proposed methods can be extended to different applications, achieving a more robust acceleration method for dMRI. These techniques have the potential to facilitate the translation of microstructural imaging with dMRI to practical applications.

6.2 Future work

On-scanner deployment

To apply our proposed fast dMRI techniques to practical applications, we'll further optimise our proposed framework for on-scanner deployment. We plan to combine the proposed multi-shell and multi-TE GP estimated reconstruction in chapters 3 and 5 with motion and eddy current correction in chapter 4 into a single package.

Specially, we plan to develop a software package containing the algorithms we developed which offers options for different kinds of reconstructed data including single shell dMRI data, multi-shell dMRI data and multi-TE dMRI data. By selecting different options, different mean and covariance functions will be selected which provide GP prior for reconstruction respectively. The motion robust and eddy current corrected reconstruction algorithm can also be activated when motion or strong eddy current distortions exist during the scans.

Our sequence is based on a product sequence which can be compiled as WIP (work in progress) packages and deployed on other scanners via C2P. For the reconstruction methods, we'll investigate converting the current MATLAB based packages to python or c++ based packages and developing faster optimisation algorithms to further accelerate the reconstruction and achieve near real-time workflow.A user-friendly interface will also be developed to enable other researchers or clinicians to easily use the method.

Fast high resolution dMRI scans using 3D acquisition techniques

Our proposed joint reconstruction methods enable fast 2D SMS dMRI acquisition with a high SMS acceleration factor. However, the achievable resolution is limited due to the intrinsic low SNR efficiency of 2D SMS technique. Meanwhile, 3D dMRI acquisition techniques have shown promising results for acquiring submillimeter diffusion data using 3D multi-slab technique which optimises the SNR efficiency [84, 85, 202, 203], yet it's time consuming to acquire a lot of thin slabs for high spatial and angular resolution diffusion data. Thus, to achieve rapid high resolution dMRI for microstructural imaging with improved image quality, the joint reconstruction methods can be applied to accelerate 3D multi-slab acquisition and a complementary 3D sampling patterns in a local q space local neighbourhood (e.g. acquiring different undersampled CAIPI shots in the multi-shot 3D acquisition) can be designed.

Deep learning-based methods may be also combined to further improve image SNR[204–208]. For example, deep priors can be trained with deep learning networks to exploit the spatial smoothness[209, 210] and then used in the constrained

reconstruction combing with the data consistency term. By adding deep priors as another constraint term into the current reconstruction framework to improve image quality, we can acquire higher resolution dMRI data within shorter scan times compared to conventional 3D acquisition techniques.

Simultaneous k space and q space acceleration based on Gaussian Process estimated reconstruction

In the current work, we only undersample the data in k space for acceleration. To accelerate dMRI scans, q space acceleration can also be explored. Missing q space points can be estimated from other local q space points using Gaussian Process models, so that it's possible to recover a densely sampled q space from a more sparsely sampled q space with Gaussian Process estimated reconstruction. However, it may pose extra smoothing effects in q space and affects the k space reconstruction performance as the useable sharing information is reduced. Thus, we will investigate how to design an optimized under sampling pattern in both k and q space, which achieves a global optimal in terms of scan time and microstructural fitting accuracy.

Improved covariance function design

In Gaussian Process estimated joint reconstruction, we need to design a covariance function with hyperparameters to describe the underlying data relations. For simpler regime, it's practical to use conventional covariance functions and validate the design using ground truth data without noise. For example, in [90], the covariance function for multi-shell q space data is explored where the angular covariance function and cross-shell covariance function are considered orthogonal. This assumption is valid when the acquired b values are relatively small (i.e. $1000 s/mm^2$<b<$3000 s/mm^2$), where angular contrast is similar across shells. However, when the b value is high, the strong diffusion contrasts make the angular covariance more shell-dependent (i.e. data at higher b shell has lower angular smoothing). In addition, signal variations across shells are different between higher b value shells (e.g. b = 5000 and 6000 s/mm^2) compared to between lower b value shells with the same b value difference (e.g. b = 1000 and 2000 s/mm^2). Thus, a more complicated covariance function

considering shell-dependent diffusion contrast is needed to better describe the data relations. However, there are some challenges for designing such new function. Firstly, it's difficult to design a function satisfying positive-definite property required for GP covariance, while being capable of capturing the complicated q space relation. Secondly, it might be computationally demanding and prone to degeneracy to fit the covariance function with an increasing number of hyperparameters. Future work will attempt to design better covariance functions including using mathematical analysis and deep learning based methods [199, 200], and incorporate them into the current reconstruction framework to improve the information sharing when q space sampling covers a wide range of b-values. On one hand, deep learning networks can be used to learn the covariance function between higher dimensional data using a self-supervised loss function by minimising the difference between GP estimation and data. In this way, the complicated non-linear relations between high-dimensional data points can be captured. On the other hand, deep learning networks can be used for the GP hyperparameters optimisation of more complicated covariance functions by setting the marginal likelihood of the Bayesian inference framework as the loss function. In this way, the hyperparameters can be updated in a faster and more efficient way.

Accelerating multi-dimensional dMRI with more contrasts

In chapter 5, we demonstrate the potential of using joint reconstruction for multi-dimensional dMRI using multi-TE dMRI as an example. Future work will explore fast multi-dimensional dMRI with more contrasts like T1, T2* ,magnetic transfer, time-dependent diffusion [211] or b-tensor imaging[212]. On the one hand, a more efficient contrast encoding and acquisition strategy can be investigated such as using shared contrast preparation modules [173] and using complementary sampling patterns for contrast encodings to facilitate reconstruction[213, 214]. On the other hand, we will extend our joint reconstruction method to exploit the sharing information in high-dimensional space using novel GP mean and covariance function design to enable acquiring fewer sampling points in the multi-dimensional space

and achieving higher k space acceleration factors. In this way, we aim to improve multi-dimensional dMRI scan efficiency, facilitating more accurate and robust microstructural imaging within clinically feasible time.

References

[1] D. Le Bihan and H. Johansen-Berg. "Diffusion MRI at 25: exploring brain tissue structure and function". In: *Neuroimage* 61.2 (2012), pp. 324–41. URL: https://www.ncbi.nlm.nih.gov/pubmed/22120012.

[2] Y. Assaf, H. Johansen-Berg, and M. Thiebaut de Schotten. "The role of diffusion MRI in neuroscience". In: *NMR Biomed* 32.4 (2019), e3762. URL: https://www.ncbi.nlm.nih.gov/pubmed/28696013.

[3] P. J. Basser and D. K. Jones. "Diffusion-tensor MRI: theory, experimental design and data analysis - a technical review". In: *NMR Biomed* 15.7-8 (2002), pp. 456–67. URL: https://www.ncbi.nlm.nih.gov/pubmed/12489095.

[4] J. D. Tournier, S. Mori, and A. Leemans. "Diffusion tensor imaging and beyond". In: *Magn Reson Med* 65.6 (2011), pp. 1532–56. URL: https://www.ncbi.nlm.nih.gov/pubmed/21469191.

[5] E. Kaden et al. "Multi-compartment microscopic diffusion imaging". In: *Neuroimage* 139 (2016), pp. 346–359. URL: https://www.ncbi.nlm.nih.gov/pubmed/27282476.

[6] D. C. Alexander et al. "Imaging brain microstructure with diffusion MRI: practicality and applications". In: *NMR Biomed* 32.4 (2019), e3841. URL: https://www.ncbi.nlm.nih.gov/pubmed/29193413.

[7] H. Zhang et al. "NODDI: practical in vivo neurite orientation dispersion and density imaging of the human brain". In: *Neuroimage* 61.4 (2012), pp. 1000–16. URL: https://www.ncbi.nlm.nih.gov/pubmed/22484410.

[8] J. H. Jensen et al. "Diffusional kurtosis imaging: the quantification of non-gaussian water diffusion by means of magnetic resonance imaging". In: *Magn Reson Med* 53.6 (2005), pp. 1432–40. URL: https://www.ncbi.nlm.nih.gov/pubmed/15906300.

[9] Ileana O Jelescu and Matthew D Budde. "Design and validation of diffusion MRI models of white matter". In: *Frontiers in physics* 5 (2017), p. 61.

[10] W. Wu and K. L. Miller. "Image formation in diffusion MRI: A review of recent technical developments". In: *J Magn Reson Imaging* 46.3 (2017), pp. 646–662. URL: https://www.ncbi.nlm.nih.gov/pubmed/28194821.

[11] K. P. Pruessmann et al. "SENSE: sensitivity encoding for fast MRI". In: *Magn Reson Med* 42.5 (1999), pp. 952–62. URL: https://www.ncbi.nlm.nih.gov/pubmed/10542355.

[12] M. A. Griswold et al. "Generalized autocalibrating partially parallel acquisitions (GRAPPA)". In: *Magn Reson Med* 47.6 (2002), pp. 1202–10. URL: https://www.ncbi.nlm.nih.gov/pubmed/12111967.

[13] D. A. Feinberg et al. “Multiplexed echo planar imaging for sub-second whole brain FMRI and fast diffusion imaging”. In: *PLoS One* 5.12 (2010), e15710. URL: https://www.ncbi.nlm.nih.gov/pubmed/21187930.

[14] K. Setsompop et al. “Blipped-controlled aliasing in parallel imaging for simultaneous multislice echo planar imaging with reduced g-factor penalty”. In: *Magn Reson Med* 67.5 (2012), pp. 1210–24. URL: https://www.ncbi.nlm.nih.gov/pubmed/21858868.

[15] Markus Barth et al. “Simultaneous multislice (SMS) imaging techniques”. In: *Magnetic resonance in medicine* 75.1 (2016), pp. 63–81.

[16] K. L. Miller et al. “Multimodal population brain imaging in the UK Biobank prospective epidemiological study”. In: *Nat Neurosci* 19.11 (2016), pp. 1523–1536. URL: https://www.ncbi.nlm.nih.gov/pubmed/27643430.

[17] A. T. Vu et al. “High resolution whole brain diffusion imaging at 7 T for the Human Connectome Project”. In: *Neuroimage* 122 (2015), pp. 318–331.

[18] T. H. Kim, K. Setsompop, and J. P. Haldar. “LORAKS makes better SENSE: Phase-constrained partial fourier SENSE reconstruction without phase calibration”. In: *Magn Reson Med* 77.3 (2017), pp. 1021–1035. URL: https://www.ncbi.nlm.nih.gov/pubmed/27037836.

[19] S. Rosenzweig et al. “Simultaneous multi-slice MRI using cartesian and radial FLASH and regularized nonlinear inversion: SMS-NLINV”. In: *Magn Reson Med* 79.4 (2018), pp. 2057–2066. URL: https://www.ncbi.nlm.nih.gov/pubmed/28840612.

[20] Van J Wedeen et al. “Mapping complex tissue architecture with diffusion spectrum magnetic resonance imaging”. In: *Magnetic resonance in medicine* 54.6 (2005), pp. 1377–1386.

[21] J. P. Haldar et al. “Fast submillimeter diffusion MRI using gSlider-SMS and SNR-enhancing joint reconstruction”. In: *Magn Reson Med* 84.2 (2020), pp. 762–776. URL: https://www.ncbi.nlm.nih.gov/pubmed/31919908.

[22] M. Mani et al. “Multi-band- and in-plane-accelerated diffusion MRI enabled by model-based deep learning in q-space and its extension to learning in the spherical harmonic domain”. In: *Magn Reson Med* 87.4 (2022), pp. 1799–1815. URL: https://www.ncbi.nlm.nih.gov/pubmed/34825729.

[23] M. Mani, V. A. Magnotta, and M. Jacob. “qModeL: A plug-and-play model-based reconstruction for highly accelerated multi-shot diffusion MRI using learned priors”. In: *Magn Reson Med* 86.2 (2021), pp. 835–851. URL: https://www.ncbi.nlm.nih.gov/pubmed/33759240.

[24] C. Y. Lee and M. Mani. “2D CAIPI accelerated 3D multi-slab diffusion weighted EPI combined with qModeL reconstruction for fast high resolution microstructure imaging”. In: *Magn Reson Imaging* 111 (2024), pp. 57–66. URL: https://www.ncbi.nlm.nih.gov/pubmed/38599504.

[25] X. Shi et al. “Parallel imaging and compressed sensing combined framework for accelerating high-resolution diffusion tensor imaging using inter-image correlation”. In: *Magn Reson Med* 73.5 (2015), pp. 1775–85. URL: https://www.ncbi.nlm.nih.gov/pubmed/24824404.

[26] M. Mani et al. "Acceleration of high angular and spatial resolution diffusion imaging using compressed sensing with multichannel spiral data". In: *Magn Reson Med* 73.1 (2015), pp. 126–38. URL: https://www.ncbi.nlm.nih.gov/pubmed/24443248.

[27] W. Wu et al. "Diffusion Acceleration with Gaussian process Estimated Reconstruction (DAGER)". In: *Magn Reson Med* 82.1 (2019), pp. 107–125. URL: https://www.ncbi.nlm.nih.gov/pubmed/30825243.

[28] Lucilio Cordero-Grande et al. "Sensitivity encoding for aligned multishot magnetic resonance reconstruction". In: *IEEE Transactions on Computational Imaging* 2.3 (2016), pp. 266–280.

[29] Freddy Odille et al. "Generalized reconstruction by inversion of coupled systems (GRICS) applied to free-breathing MRI". In: *Magnetic Resonance in Medicine: An Official Journal of the International Society for Magnetic Resonance in Medicine* 60.1 (2008), pp. 146–157.

[30] B. Lampinen et al. "Probing brain tissue microstructure with MRI: principles, challenges, and the role of multidimensional diffusion-relaxation encoding". In: *Neuroimage* 282 (2023), p. 120338. URL: https://www.ncbi.nlm.nih.gov/pubmed/37598814.

[31] P. J. Slator et al. "Combined diffusion-relaxometry microstructure imaging: Current status and future prospects". In: *Magn Reson Med* 86.6 (2021), pp. 2987–3011. URL: https://www.ncbi.nlm.nih.gov/pubmed/34411331.

[32] Jelle Veraart, Dmitry S Novikov, and Els Fieremans. "TE dependent Diffusion Imaging (TEdDI) distinguishes between compartmental T2 relaxation times". In: *NeuroImage* 182 (2018), pp. 360–369.

[33] Paddy J Slator et al. "Combined diffusion-relaxometry MRI to identify dysfunction in the human placenta". In: *Magnetic resonance in medicine* 82.1 (2019), pp. 95–106.

[34] Zhi-Pei Liang et al. *Principles of magnetic resonance imaging : a signal processing perspective*. IEEE Press series in biomedical engineering. Bellingham, Wash. New York: SPIE Optical Engineering Press ; IEEE Press, 2000, xv, 416 p.

[35] E. Mark Haacke. *Magnetic resonance imaging : physical principles and sequence design*. New York: Wiley, 1999, xxvii, 914 p.

[36] Matt A. Bernstein, Kevin Franklin King, and Ziaohong Joe Zhou. *Handbook of MRI pulse sequences*. Amsterdam ; Boston: Academic Press, 2004, xxii, 1017 p.

[37] In-Young Choi and Peter Jezzard. *Advances neuro MR techniques and applications*. eng. Advances in Magnetic Resonance Technology and Applications ; Volume 4. London, England: Academic Press, 2021.

[38] Lars G Hanson. "Is quantum mechanics necessary for understanding magnetic resonance?" In: *Concepts in Magnetic Resonance Part A: An Educational Journal* 32.5 (2008), pp. 329–340.

[39] G. J. Stanisz et al. "T1, T2 relaxation and magnetization transfer in tissue at 3T". In: *Magn Reson Med* 54.3 (2005), pp. 507–12. URL: https://www.ncbi.nlm.nih.gov/pubmed/16086319.

[40] F. A. Breuer et al. “Controlled aliasing in parallel imaging results in higher acceleration (CAIPIRINHA) for multi-slice imaging”. In: *Magn Reson Med* 53.3 (2005), pp. 684–91. URL: https://www.ncbi.nlm.nih.gov/pubmed/15723404.

[41] Mark A Griswold et al. “Autocalibrated coil sensitivity estimation for parallel imaging”. In: *NMR in Biomedicine: An International Journal Devoted to the Development and Application of Magnetic Resonance In vivo* 19.3 (2006), pp. 316–324.

[42] David O Walsh, Arthur F Gmitro, and Michael W Marcellin. “Adaptive reconstruction of phased array MR imagery”. In: *Magnetic Resonance in Medicine: An Official Journal of the International Society for Magnetic Resonance in Medicine* 43.5 (2000), pp. 682–690.

[43] ZP Liang et al. “Making better SENSE: wavelet denoising, Tikhonov regularization, and total least squares”. In: *Proc. ISMRM*. Vol. 2388. 2002.

[44] FH Lin et al. “Reconstruction of sensitivity encoded images using regularization and discrete time wavelet transform estimates of the coil maps”. In: *Proceedings of the 10th Annual Meeting of ISMRM, Honolulu, HI, USA*. 2002, p. 2389.

[45] M. Uecker et al. “ESPIRiT–an eigenvalue approach to autocalibrating parallel MRI: where SENSE meets GRAPPA”. In: *Magn Reson Med* 71.3 (2014), pp. 990–1001. URL: https://www.ncbi.nlm.nih.gov/pubmed/23649942.

[46] M. Lustig, D. Donoho, and J. M. Pauly. “Sparse MRI: The application of compressed sensing for rapid MR imaging”. In: *Magn Reson Med* 58.6 (2007), pp. 1182–95. URL: https://www.ncbi.nlm.nih.gov/pubmed/17969013.

[47] M. Lustig and J. M. Pauly. “SPIRiT: Iterative self-consistent parallel imaging reconstruction from arbitrary k-space”. In: *Magn Reson Med* 64.2 (2010), pp. 457–71. URL: https://www.ncbi.nlm.nih.gov/pubmed/20665790.

[48] Felix A Breuer et al. “General formulation for quantitative G-factor calculation in GRAPPA reconstructions”. In: *Magnetic Resonance in Medicine: An Official Journal of the International Society for Magnetic Resonance in Medicine* 62.3 (2009), pp. 739–746.

[49] Heidi Johansen-Berg and Timothy E. J. Behrens. *Diffusion MRI : from quantitative measurement to in-vivo neuroanatomy*. 2nd. London, UK ; Waltham, MA: Elsevier/Academic Press, 2014, xii, 614 p.

[50] A. Einstein. “Über die von der molekularkinetischen Theorie der Wärme geforderte Bewegung von in ruhenden Flüssigkeiten suspendierten Teilchen”. In: *Annalen der Physik* 322.8 (1905), pp. 549–560.

[51] V. G. Kiselev. “Fundamentals of diffusion MRI physics”. In: *NMR Biomed* 30.3 (2017). URL: https://www.ncbi.nlm.nih.gov/pubmed/28230327.

[52] Erwin L Hahn. “Spin echoes”. In: *Physical review* 80.4 (1950), p. 580.

[53] Herman Y Carr and Edward M Purcell. “Effects of diffusion on free precession in nuclear magnetic resonance experiments”. In: *Physical review* 94.3 (1954), p. 630.

[54] Henry C Torrey. “Bloch equations with diffusion terms”. In: *Physical review* 104.3 (1956), p. 563.

[55] Edward O Stejskal and John E Tanner. "Spin diffusion measurements: spin echoes in the presence of a time-dependent field gradient". In: *The journal of chemical physics* 42.1 (1965), pp. 288–292.

[56] P. J. Basser, J. Mattiello, and D. LeBihan. "MR diffusion tensor spectroscopy and imaging". In: *Biophys J* 66.1 (1994), pp. 259–67. URL: https://www.ncbi.nlm.nih.gov/pubmed/8130344.

[57] Norman J Beauchamp Jr et al. "MR diffusion imaging in stroke: review and controversies." In: *Radiographics* 18.5 (1998), pp. 1269–1283.

[58] Yu Zhang et al. "White matter damage in frontotemporal dementia and Alzheimer's disease measured by diffusion MRI". In: *Brain* 132.9 (2009), pp. 2579–2592.

[59] J Renoux et al. "MR diffusion tensor imaging and fiber tracking in inflammatory diseases of the spinal cord". In: *American Journal of Neuroradiology* 27.9 (2006), pp. 1947–1951.

[60] Dmitry S Novikov et al. "Rotationally-invariant mapping of scalar and orientational metrics of neuronal microstructure with diffusion MRI". In: *NeuroImage* 174 (2018), pp. 518–538.

[61] Marco Palombo et al. "SANDI: A compartment-based model for non-invasive apparent soma and neurite imaging by diffusion MRI". In: *Neuroimage* 215 (2020), p. 116835.

[62] Kim Butts et al. "Diffusion-weighted interleaved echo-planar imaging with a pair of orthogonal navigator echoes". In: *Magnetic resonance in medicine* 35.5 (1996), pp. 763–770.

[63] Samantha J Holdsworth et al. "Readout-segmented EPI for rapid high resolution diffusion imaging at 3T". In: *European journal of radiology* 65.1 (2008), pp. 36–46.

[64] David A Porter and Robin M Heidemann. "High resolution diffusion-weighted imaging using readout-segmented echo-planar imaging, parallel imaging and a two-dimensional navigator-based reacquisition". In: *Magnetic Resonance in Medicine: An Official Journal of the International Society for Magnetic Resonance in Medicine* 62.2 (2009), pp. 468–475.

[65] Karla L Miller and John M Pauly. "Nonlinear phase correction for navigated diffusion imaging". In: *Magnetic Resonance in Medicine: An Official Journal of the International Society for Magnetic Resonance in Medicine* 50.2 (2003), pp. 343–353.

[66] D Porter and E Mueller. "Multi-shot diffusion-weighted EPI with readout mosaic segmentation and 2D navigator correction". In: *Proceedings of the 12th annual meeting of ISMRM, Kyoto, Japan.* Vol. 442. 2004.

[67] James G Pipe, Victoria G Farthing, and Kirsten P Forbes. "Multishot diffusion-weighted FSE using PROPELLER MRI". In: *Magnetic Resonance in Medicine: An Official Journal of the International Society for Magnetic Resonance in Medicine* 47.1 (2002), pp. 42–52.

[68] Chunlei Liu, Michael E Moseley, and Roland Bammer. “Simultaneous phase correction and SENSE reconstruction for navigated multi-shot DWI with non-cartesian k-space sampling”. In: *Magnetic resonance in medicine* 54.6 (2005), pp. 1412–1422.

[69] Chunlei Liu et al. “Self-navigated interleaved spiral (SNAILS): application to high-resolution diffusion tensor imaging”. In: *Magnetic Resonance in Medicine: An Official Journal of the International Society for Magnetic Resonance in Medicine* 52.6 (2004), pp. 1388–1396.

[70] N. K. Chen et al. “A robust multi-shot scan strategy for high-resolution diffusion weighted MRI enabled by multiplexed sensitivity-encoding (MUSE)”. In: *Neuroimage* 72 (2013), pp. 41–7. URL: https://www.ncbi.nlm.nih.gov/pubmed/23370063.

[71] Merry Mani et al. “Multi-shot sensitivity-encoded diffusion data recovery using structured low-rank matrix completion (MUSSELS)”. In: *Magnetic resonance in medicine* 78.2 (2017), pp. 494–507.

[72] Hemant K Aggarwal, Merry P Mani, and Mathews Jacob. “MoDL-MUSSELS: model-based deep learning for multishot sensitivity-encoded diffusion MRI”. In: *IEEE transactions on medical imaging* 39.4 (2019), pp. 1268–1277.

[73] G. Ramos-Llorden et al. “High-fidelity, accelerated whole-brain submillimeter in vivo diffusion MRI using gSlider-spherical ridgelets (gSlider-SR)”. In: *Magn Reson Med* 84.4 (2020), pp. 1781–1795. URL: https://www.ncbi.nlm.nih.gov/pubmed/32125020.

[74] Bertram J Wilm et al. “Single-shot spiral imaging enabled by an expanded encoding model: D emonstration in diffusion MRI”. In: *Magnetic resonance in medicine* 77.1 (2017), pp. 83–91.

[75] Yoojin Lee et al. “On the signal-to-noise ratio benefit of spiral acquisition in diffusion MRI”. In: *Magnetic resonance in medicine* 85.4 (2021), pp. 1924–1937.

[76] Bertram Jakob Wilm et al. “Minimizing the echo time in diffusion imaging using spiral readouts and a head gradient system”. In: *Magnetic resonance in medicine* 84.6 (2020), pp. 3117–3127.

[77] Trong-Kha Truong, Nan-kuei Chen, and Allen W Song. “Inherent correction of motion-induced phase errors in multishot spiral diffusion-weighted imaging”. In: *Magnetic Resonance in Medicine* 68.4 (2012), pp. 1255–1261.

[78] Trong-Kha Truong and Arnaud Guidon. “High-resolution multishot spiral diffusion tensor imaging with inherent correction of motion-induced phase errors”. In: *Magnetic resonance in medicine* 71.2 (2014), pp. 790–796.

[79] Tie-Qiang Li, Dong-Hyun Kim, and Michael E Moseley. “High-resolution diffusion-weighted imaging with interleaved variable-density spiral acquisitions”. In: *Journal of Magnetic Resonance Imaging: An Official Journal of the International Society for Magnetic Resonance in Medicine* 21.4 (2005), pp. 468–475.

[80] Hua Guo et al. “POCS-enhanced inherent correction of motion-induced phase errors (POCS-ICE) for high-resolution multishot diffusion MRI”. In: *Magnetic resonance in medicine* 75.1 (2016), pp. 169–180.

[81] Dinghui Wang, Nicholas R Zwart, and James G Pipe. "Joint water–fat separation and deblurring for spiral imaging". In: *Magnetic Resonance in Medicine* 79.6 (2018), pp. 3218–3228.

[82] Guangqi Li et al. "Comparison of uniform-density, variable-density, and dual-density spiral samplings for multi-shot DWI". In: *Magnetic Resonance in Medicine* 90.1 (2023), pp. 133–149.

[83] Mathias Engström and Stefan Skare. "Diffusion-weighted 3D multislab echo planar imaging for high signal-to-noise ratio efficiency and isotropic image resolution". In: *Magnetic resonance in medicine* 70.6 (2013), pp. 1507–1514.

[84] Robert Frost et al. "3D multi-slab diffusion-weighted readout-segmented EPI with real-time cardiac-reordered k-space acquisition". In: *Magnetic resonance in medicine* 72.6 (2014), pp. 1565–1579.

[85] Wenchuan Wu et al. "High-resolution diffusion MRI at 7T using a three-dimensional multi-slab acquisition". In: *NeuroImage* 143 (2016), pp. 1–14.

[86] Erpeng Dai, Simin Liu, and Hua Guo. "High-resolution whole-brain diffusion MRI at 3T using simultaneous multi-slab (SMSlab) acquisition". In: *Neuroimage* 237 (2021), p. 118099.

[87] Simin Liu et al. "Three-dimensional diffusion MRI using simultaneous multislab with blipped-CAIPI in a 4D k-space framework". In: *Magnetic Resonance in Medicine* 90.3 (2023), pp. 978–994.

[88] Kawin Setsompop et al. "High-resolution in vivo diffusion imaging of the human brain with generalized slice dithered enhanced resolution: Simultaneous multislice (g S lider-SMS)". In: *Magnetic resonance in medicine* 79.1 (2018), pp. 141–151.

[89] M. Seeger. "Gaussian processes for machine learning". In: *Int J Neural Syst* 14.2 (2004), pp. 69–106. URL: https://www.ncbi.nlm.nih.gov/pubmed/15112367.

[90] X. Ye, K. L. Miller, and W. Wu. "Accelerated multi-shell diffusion MRI with Gaussian process estimated reconstruction of multi-band imaging". In: *Magn Reson Med* 94.2 (2025), pp. 694–712. URL: https://www.ncbi.nlm.nih.gov/pubmed/40189808.

[91] J. D. Tournier. "Diffusion MRI in the brain - Theory and concepts". In: *Prog Nucl Magn Reson Spectrosc* 112-113 (2019), pp. 1–16. URL: https://www.ncbi.nlm.nih.gov/pubmed/31481155.

[92] Y. Assaf and P. J. Basser. "Composite hindered and restricted model of diffusion (CHARMED) MR imaging of the human brain". In: *Neuroimage* 27.1 (2005), pp. 48–58. URL: https://www.ncbi.nlm.nih.gov/pubmed/15979342.

[93] D. S. Novikov et al. "Quantifying brain microstructure with diffusion MRI: Theory and parameter estimation". In: *NMR Biomed* 32.4 (2019), e3998. URL: https://www.ncbi.nlm.nih.gov/pubmed/30321478.

[94] C. Liao et al. "High-fidelity mesoscale in-vivo diffusion MRI through gSlider-BUDA and circular EPI with S-LORAKS reconstruction". In: *Neuroimage* 275 (2023), p. 120168. URL: https://www.ncbi.nlm.nih.gov/pubmed/37187364.

[95] S. K. HashemizadehKolowri et al. “Simultaneous multi-slice image reconstruction using regularized image domain split slice-GRAPPA for diffusion MRI”. In: *Med Image Anal* 70 (2021), p. 102000. URL: https://www.ncbi.nlm.nih.gov/pubmed/33676098.

[96] L. Ying et al. “A statistical approach to SENSE regularization with arbitrary k-space trajectories”. In: *Magn Reson Med* 60.2 (2008), pp. 414–21. URL: https://www.ncbi.nlm.nih.gov/pubmed/18666100.

[97] Yang Ji et al. “Accelerated diffusion and relaxation-diffusion MRI using time-division multiplexing EPI”. In: *Magnetic resonance in medicine* 86.5 (2021), pp. 2528–2541.

[98] Yang Ji et al. “Accelerating joint relaxation-diffusion MRI by integrating time division multiplexing and simultaneous multi-slice (TDM-SMS) strategies”. In: *Magnetic resonance in medicine* 87.6 (2022), pp. 2697–2709.

[99] B. Bilgic et al. “Accelerated diffusion spectrum imaging with compressed sensing using adaptive dictionaries”. In: *Magn Reson Med* 68.6 (2012), pp. 1747–54. URL: https://www.ncbi.nlm.nih.gov/pubmed/23008145.

[100] M. I. Menzel et al. “Accelerated diffusion spectrum imaging in the human brain using compressed sensing”. In: *Magn Reson Med* 66.5 (2011), pp. 1226–33. URL: https://www.ncbi.nlm.nih.gov/pubmed/22012686.

[101] L. Ning et al. “A joint compressed-sensing and super-resolution approach for very high-resolution diffusion imaging”. In: *Neuroimage* 125 (2016), pp. 386–400. URL: https://www.ncbi.nlm.nih.gov/pubmed/26505296.

[102] Q. Tian et al. “DeepDTI: High-fidelity six-direction diffusion tensor imaging using deep learning”. In: *Neuroimage* 219 (2020), p. 117017. URL: https://www.ncbi.nlm.nih.gov/pubmed/32504817.

[103] E. Aliotta, H. Nourzadeh, and S. H. Patel. “Extracting diffusion tensor fractional anisotropy and mean diffusivity from 3-direction DWI scans using deep learning”. In: *Magn Reson Med* 85.2 (2021), pp. 845–854. URL: https://www.ncbi.nlm.nih.gov/pubmed/32810351.

[104] V. Golkov et al. “q-Space Deep Learning: Twelve-Fold Shorter and Model-Free Diffusion MRI Scans”. In: *IEEE Trans Med Imaging* 35.5 (2016), pp. 1344–1351. URL: https://www.ncbi.nlm.nih.gov/pubmed/27071165.

[105] Z. Li et al. “DIMOND: DIffusion Model OptimizatioN with Deep Learning”. In: *Adv Sci (Weinh)* (2024), e2307965. URL: https://www.ncbi.nlm.nih.gov/pubmed/38634608.

[106] J. L. Andersson and S. N. Sotiropoulos. “Non-parametric representation and prediction of single- and multi-shell diffusion-weighted MRI data using Gaussian processes”. In: *Neuroimage* 122 (2015), pp. 166–76. URL: https://www.ncbi.nlm.nih.gov/pubmed/26236030.

[107] A. Foi. “Noise Estimation and Removal in Mr Imaging: The Variance-Stabilization Approach”. In: *2011 8th Ieee International Symposium on Biomedical Imaging: From Nano to Macro* (2011), pp. 1809–1814. URL: %3CGo%20to%20ISI%3E://WOS:000298849400413.

[108] X. D. Ma, K. Ugurbil, and X. P. Wu. "Denoise magnitude diffusion magnetic resonance images via variance -stabilizing transformation and optimal singular -value manipulation". In: *Neuroimage* 215 (2020). URL: %3CGo%20to%20ISI%3E://WOS:000539990200022.

[109] Chunfeng Huang, Haimeng Zhang, and Scott M Robeson. "On the validity of commonly used covariance and variogram functions on the sphere". In: *Mathematical Geosciences* 43.6 (2011), pp. 721–733.

[110] Christopher M Bishop and Nasser M Nasrabadi. *Pattern recognition and machine learning*. Vol. 4. 4. Springer, 2006.

[111] S. N. Sotiropoulos et al. "Advances in diffusion MRI acquisition and processing in the Human Connectome Project". In: *Neuroimage* 80 (2013), pp. 125–43. URL: https://www.ncbi.nlm.nih.gov/pubmed/23702418.

[112] T. E. Behrens et al. "Probabilistic diffusion tractography with multiple fibre orientations: What can we gain?" In: *Neuroimage* 34.1 (2007), pp. 144–55. URL: https://www.ncbi.nlm.nih.gov/pubmed/17070705.

[113] Dominic JA Welsh and Martin B Powell. "An upper bound for the chromatic number of a graph and its application to timetabling problems". In: *The Computer Journal* 10.1 (1967), pp. 85–86.

[114] F. A. Breuer et al. "Controlled aliasing in parallel imaging results in higher acceleration (CAIPIRINHA) for multi-slice imaging". In: *Magn Reson Med* 53.3 (2005), pp. 684–91. URL: https://www.ncbi.nlm.nih.gov/pubmed/15723404.

[115] Benjamin Zahneisen et al. "Three-dimensional Fourier encoding of simultaneously excited slices: generalized acquisition and reconstruction framework". In: *Magnetic resonance in medicine* 71.6 (2014), pp. 2071–2081.

[116] Kawin Setsompop, David A Feinberg, and Jonathan R Polimeni. "Rapid brain MRI acquisition techniques at ultra-high fields". In: *NMR in Biomedicine* 29.9 (2016), pp. 1198–1221.

[117] J. L. Andersson, S. Skare, and J. Ashburner. "How to correct susceptibility distortions in spin-echo echo-planar images: application to diffusion tensor imaging". In: *Neuroimage* 20.2 (2003), pp. 870–88. URL: https://www.ncbi.nlm.nih.gov/pubmed/14568458.

[118] M. Jenkinson et al. "Fsl". In: *Neuroimage* 62.2 (2012), pp. 782–90. URL: https://www.ncbi.nlm.nih.gov/pubmed/21979382.

[119] M. Hernandez-Fernandez et al. "Using GPUs to accelerate computational diffusion MRI: From microstructure estimation to tractography and connectomes". In: *Neuroimage* 188 (2019), pp. 598–615. URL: https://www.ncbi.nlm.nih.gov/pubmed/30537563.

[120] Elizabeth B Hutchinson et al. "Analysis of the effects of noise, DWI sampling, and value of assumed parameters in diffusion MRI models". In: *Magnetic resonance in medicine* 78.5 (2017), pp. 1767–1780.

[121] M. de Groot et al. "Improving alignment in Tract-based spatial statistics: evaluation and optimization of image registration". In: *Neuroimage* 76 (2013), pp. 400–11. URL: https://www.ncbi.nlm.nih.gov/pubmed/23523807.

[122] Martin Cousineau et al. “A test-retest study on Parkinson’s PPMI dataset yields statistically significant white matter fascicles”. In: *NeuroImage: Clinical* 16 (2017), pp. 222–233.

[123] Derek K Jones and Peter J Basser. ““Squashing peanuts and smashing pumpkins”: how noise distorts diffusion-weighted MR data”. In: *Magnetic Resonance in Medicine: An Official Journal of the International Society for Magnetic Resonance in Medicine* 52.5 (2004), pp. 979–993.

[124] M. Zaitsev, J. Maclaren, and M. Herbst. “Motion artifacts in MRI: A complex problem with many partial solutions”. In: *J Magn Reson Imaging* 42.4 (2015), pp. 887–901. URL: https://www.ncbi.nlm.nih.gov/pubmed/25630632.

[125] Frank Godenschweger et al. “Motion correction in MRI of the brain”. In: *Physics in medicine & biology* 61.5 (2016), R32.

[126] Rachel W Chan et al. “Characterization and correction of eddy-current artifacts in unipolar and bipolar diffusion sequences using magnetic field monitoring”. In: *Journal of Magnetic Resonance* 244 (2014), pp. 74–84.

[127] J. Maclaren et al. “Prospective motion correction in brain imaging: a review”. In: *Magn Reson Med* 69.3 (2013), pp. 621–36. URL: https://www.ncbi.nlm.nih.gov/pubmed/22570274.

[128] Maxim Zaitsev et al. “Magnetic resonance imaging of freely moving objects: prospective real-time motion correction using an external optical motion tracking system”. In: *Neuroimage* 31.3 (2006), pp. 1038–1050.

[129] Juliane Ludwig et al. “Pilot tone–based motion correction for prospective respiratory compensated cardiac cine MRI”. In: *Magnetic Resonance in Medicine* 85.5 (2021), pp. 2403–2416.

[130] Eric Seth Michael, Franciszek Hennel, and Klaas Paul Pruessmann. “Motion-compensated diffusion encoding in multi-shot human brain acquisitions: insights using high-performance gradients”. In: *Magnetic Resonance in Medicine* 92.2 (2024), pp. 556–572.

[131] Hao Chen et al. “High-resolution multi-shot diffusion-weighted MRI combining markerless prospective motion correction and locally low-rank constrained reconstruction”. In: *Magnetic resonance in medicine* 89.2 (2023), pp. 605–619.

[132] M Dylan Tisdall et al. “Volumetric navigators for prospective motion correction and selective reacquisition in neuroanatomical MRI”. In: *Magnetic resonance in medicine* 68.2 (2012), pp. 389–399.

[133] Aaron T Hess et al. “Real-time motion and B0 corrected single voxel spectroscopy using volumetric navigators”. In: *Magnetic resonance in medicine* 66.2 (2011), pp. 314–323.

[134] Veronika Spieker et al. “Deep learning for retrospective motion correction in MRI: a comprehensive review”. In: *IEEE Transactions on Medical Imaging* 43.2 (2023), pp. 846–859.

[135] Zijing Dong et al. “Motion-corrected k-space reconstruction for interleaved EPI diffusion imaging”. In: *Magnetic resonance in medicine* 79.4 (2018), pp. 1992–2002.

[136] David Atkinson et al. "Automatic correction of motion artifacts in magnetic resonance images using an entropy focus criterion". In: *IEEE Transactions on Medical imaging* 16.6 (1997), pp. 903–910.

[137] Michael S Hansen et al. "Retrospective reconstruction of high temporal resolution cine images from real-time MRI using iterative motion correction". In: *Magnetic Resonance in Medicine* 68.3 (2012), pp. 741–750.

[138] Xi Chen, Wenchuan Wu, and Mark Chiew. "Motion compensated structured low-rank reconstruction for 3D multi-shot EPI". In: *Magnetic Resonance in Medicine* 91.6 (2024), pp. 2443–2458.

[139] Thomas Küstner et al. "Automated reference-free detection of motion artifacts in magnetic resonance images". In: *Magnetic Resonance Materials in Physics, Biology and Medicine* 31.2 (2018), pp. 243–256.

[140] Thomas Küstner et al. "Retrospective correction of motion-affected MR images using deep learning frameworks". In: *Magnetic resonance in medicine* 82.4 (2019), pp. 1527–1540.

[141] Mark Jenkinson et al. "Improved optimization for the robust and accurate linear registration and motion correction of brain images". In: *Neuroimage* 17.2 (2002), pp. 825–841.

[142] Mark Jenkinson and Stephen Smith. "A global optimisation method for robust affine registration of brain images". In: *Medical image analysis* 5.2 (2001), pp. 143–156.

[143] Brett Levac et al. "Accelerated motion correction with deep generative diffusion models". In: *Magnetic Resonance in Medicine* 92.2 (2024), pp. 853–868.

[144] Peter Jezzard, Alan S Barnett, and Carlo Pierpaoli. "Characterization of and correction for eddy current artifacts in echo planar diffusion imaging". In: *Magnetic resonance in medicine* 39.5 (1998), pp. 801–812.

[145] J. L. R. Andersson and S. N. Sotiropoulos. "An integrated approach to correction for off-resonance effects and subject movement in diffusion MR imaging". In: *Neuroimage* 125 (2016), pp. 1063–1078. URL: `https://www.ncbi.nlm.nih.gov/pubmed/26481672`.

[146] Gabriel Ramos-Llordén et al. "Eddy current-induced artifact correction in high B-value ex vivo human brain diffusion MRI with dynamic field monitoring". In: *Magnetic resonance in medicine* 91.2 (2024), pp. 541–557.

[147] Antoine Legouhy et al. "Eddeep: Fast eddy-current distortion correction for diffusion MRI with deep learning". In: *International Conference on Medical Image Computing and Computer-Assisted Intervention*. Springer. 2024, pp. 152–161.

[148] Jelle Veraart et al. "Denoising of diffusion MRI using random matrix theory". In: *Neuroimage* 142 (2016), pp. 394–406.

[149] Matteo Maggioni et al. "Nonlocal transform-domain filter for volumetric data denoising and reconstruction". In: *IEEE transactions on image processing* 22.1 (2012), pp. 119–133.

[150] Gabrio Rizzuti, Alessandro Sbrizzi, and Tristan Van Leeuwen. "Joint retrospective motion correction and reconstruction for brain MRI with a reference contrast". In: *IEEE Transactions on Computational Imaging* 8 (2022), pp. 490–504.

[151] Congyu Liao et al. “Distortion-free, high-isotropic-resolution diffusion MRI with gSlider BUDA-EPI and multicoil dynamic B0 shimming”. In: *Magnetic resonance in medicine* 86.2 (2021), pp. 791–803.

[152] Ziyu Li et al. “Sampling strategies and integrated reconstruction for reducing distortion and boundary slice aliasing in high-resolution 3D diffusion MRI”. In: *Magnetic resonance in medicine* 90.4 (2023), pp. 1484–1501.

[153] Y. Liao et al. “Mapping tissue microstructure of brain white matter in vivo in health and disease using diffusion MRI”. In: *Imaging Neurosci (Camb)* 2 (2024). URL: https://www.ncbi.nlm.nih.gov/pubmed/40800319.

[154] Daniel C Alexander et al. “Imaging brain microstructure with diffusion MRI: practicality and applications”. In: *NMR in Biomedicine* 32.4 (2019), e3841.

[155] T. Mitchell et al. “Neurite orientation dispersion and density imaging (NODDI) and free-water imaging in Parkinsonism”. In: *Hum Brain Mapp* 40.17 (2019), pp. 5094–5107. URL: https://www.ncbi.nlm.nih.gov/pubmed/31403737.

[156] N. Colgan et al. “Application of neurite orientation dispersion and density imaging (NODDI) to a tau pathology model of Alzheimer’s disease”. In: *Neuroimage* 125 (2016), pp. 739–744. URL: https://www.ncbi.nlm.nih.gov/pubmed/26505297.

[157] X. Fu et al. “Microstructural White Matter Alterations in Mild Cognitive Impairment and Alzheimer’s Disease : Study Based on Neurite Orientation Dispersion and Density Imaging (NODDI)”. In: *Clin Neuroradiol* 30.3 (2020), pp. 569–579. URL: https://www.ncbi.nlm.nih.gov/pubmed/31175374.

[158] T. Schneider et al. “Sensitivity of multi-shell NODDI to multiple sclerosis white matter changes: a pilot study”. In: *Funct Neurol* 32.2 (2017), pp. 97–101. URL: https://www.ncbi.nlm.nih.gov/pubmed/28676143.

[159] S. By et al. “Application and evaluation of NODDI in the cervical spinal cord of multiple sclerosis patients”. In: *Neuroimage Clin* 15 (2017), pp. 333–342. URL: https://www.ncbi.nlm.nih.gov/pubmed/28560158.

[160] M. Caranova et al. “A systematic review of microstructural abnormalities in multiple sclerosis detected with NODDI and DTI models of diffusion-weighted magnetic resonance imaging”. In: *Magn Reson Imaging* 104 (2023), pp. 61–71. URL: https://www.ncbi.nlm.nih.gov/pubmed/37775062.

[161] M. D. Does. “Inferring brain tissue composition and microstructure via MR relaxometry”. In: *Neuroimage* 182 (2018), pp. 136–148. URL: https://www.ncbi.nlm.nih.gov/pubmed/29305163.

[162] M. Palombo et al. “Joint estimation of relaxation and diffusion tissue parameters for prostate cancer with relaxation-VERDICT MRI”. In: *Sci Rep* 13.1 (2023), p. 2999. URL: https://www.ncbi.nlm.nih.gov/pubmed/36810476.

[163] R. V. Mulkern et al. “Multi-component apparent diffusion coefficients in human brain: relationship to spin-lattice relaxation”. In: *Magn Reson Med* 44.2 (2000), pp. 292–300. URL: https://www.ncbi.nlm.nih.gov/pubmed/10918329.

[164] B. Lampinen et al. “Towards unconstrained compartment modeling in white matter using diffusion-relaxation MRI with tensor-valued diffusion encoding”. In: *Magn Reson Med* 84.3 (2020), pp. 1605–1623. URL: https://www.ncbi.nlm.nih.gov/pubmed/32141131.

[165] I. R. Leppert et al. "Efficient whole-brain tract-specific T(1) mapping at 3T with slice-shuffled inversion-recovery diffusion-weighted imaging". In: *Magn Reson Med* 86.2 (2021), pp. 738–753. URL: https://www.ncbi.nlm.nih.gov/pubmed/33749017.

[166] S. De Santis et al. "Resolving relaxometry and diffusion properties within the same voxel in the presence of crossing fibres by combining inversion recovery and diffusion-weighted acquisitions". In: *Magn Reson Med* 75.1 (2016), pp. 372–80. URL: https://www.ncbi.nlm.nih.gov/pubmed/25735538.

[167] J. Veraart, D. S. Novikov, and E. Fieremans. "TE dependent Diffusion Imaging (TEdDI) distinguishes between compartmental T(2) relaxation times". In: *Neuroimage* 182 (2018), pp. 360–369. URL: https://www.ncbi.nlm.nih.gov/pubmed/28935239.

[168] J. T. E. Johnson et al. "In vivo disentanglement of diffusion frequency-dependence, tensor shape, and relaxation using multidimensional MRI". In: *Hum Brain Mapp* 45.7 (2024), e26697. URL: https://www.ncbi.nlm.nih.gov/pubmed/38726888.

[169] T. Gong et al. "MTE-NODDI: Multi-TE NODDI for disentangling non-T2-weighted signal fractions from compartment-specific T2 relaxation times". In: *Neuroimage* 217 (2020), p. 116906. URL: https://www.ncbi.nlm.nih.gov/pubmed/32387626.

[170] S. Coelho et al. "Assessment of Precision and Accuracy of Brain White Matter Microstructure using Combined Diffusion MRI and Relaxometry". In: *ArXiv* (2024). URL: https://www.ncbi.nlm.nih.gov/pubmed/38463511.

[171] J. S. Duncan, P. Bartlett, and G. J. Barker. "Technique for measuring hippocampal T2 relaxation time". In: *AJNR Am J Neuroradiol* 17.10 (1996), pp. 1805–10. URL: https://www.ncbi.nlm.nih.gov/pubmed/8933861.

[172] G. B. Chavhan et al. "Principles, techniques, and applications of T2*-based MR imaging and its special applications". In: *Radiographics* 29.5 (2009), pp. 1433–49. URL: https://www.ncbi.nlm.nih.gov/pubmed/19755604.

[173] J. Hutter et al. "Integrated and efficient diffusion-relaxometry using ZEBRA". In: *Sci Rep* 8.1 (2018), p. 15138. URL: https://www.ncbi.nlm.nih.gov/pubmed/30310108.

[174] F. Wang et al. "Echo planar time-resolved imaging (EPTI)". In: *Magn Reson Med* 81.6 (2019), pp. 3599–3615. URL: https://www.ncbi.nlm.nih.gov/pubmed/30714198.

[175] Z. Dong et al. "SNR-efficient distortion-free diffusion relaxometry imaging using accelerated echo-train shifted echo-planar time-resolving imaging (ACE-EPTI)". In: *Magn Reson Med* 88.1 (2022), pp. 164–179. URL: https://www.ncbi.nlm.nih.gov/pubmed/35225368.

[176] Z. Dong et al. "Romer-EPTI: Rotating-view motion-robust super-resolution EPTI for SNR-efficient distortion-free in-vivo mesoscale diffusion MRI and microstructure imaging". In: *Magn Reson Med* 93.4 (2025), pp. 1535–1555. URL: https://www.ncbi.nlm.nih.gov/pubmed/39552568.

[177] Z. Dong et al. "Single-shot Echo Planar Time-resolved Imaging for multi-echo functional MRI and distortion-free diffusion imaging". In: *bioRxiv* (2024). URL: https://www.ncbi.nlm.nih.gov/pubmed/38328081.

[178] D. Ma et al. “Magnetic resonance fingerprinting”. In: *Nature* 495.7440 (2013), pp. 187–92. URL: https://www.ncbi.nlm.nih.gov/pubmed/23486058.

[179] M. Afzali et al. “MR Fingerprinting with b-Tensor Encoding for Simultaneous Quantification of Relaxation and Diffusion in a Single Scan”. In: *Magn Reson Med* 88.5 (2022), pp. 2043–2057. URL: https://www.ncbi.nlm.nih.gov/pubmed/35713357.

[180] X. Cao et al. “DTI-MR fingerprinting for rapid high-resolution whole-brain T(1) , T(2) , proton density, ADC, and fractional anisotropy mapping”. In: *Magn Reson Med* 91.3 (2024), pp. 987–1001. URL: https://www.ncbi.nlm.nih.gov/pubmed/37936313.

[181] H. Fan et al. “Simultaneous perfusion, diffusion, T(2) *, and T(1) mapping with MR fingerprinting”. In: *Magn Reson Med* 91.2 (2024), pp. 558–569. URL: https://www.ncbi.nlm.nih.gov/pubmed/37749847.

[182] Carolin M Pirk et al. “Deep learning-based parameter mapping for joint relaxation and diffusion tensor MR fingerprinting”. In: *Medical Imaging with Deep Learning*. PMLR. 2020, pp. 638–654.

[183] D. Benjamini and P. J. Basser. “Use of marginal distributions constrained optimization (MADCO) for accelerated 2D MRI relaxometry and diffusometry”. In: *J Magn Reson* 271 (2016), pp. 40–5. URL: https://www.ncbi.nlm.nih.gov/pubmed/27543810.

[184] A. Planchuelo-Gomez et al. “Optimisation of quantitative brain diffusion-relaxation MRI acquisition protocols with physics-informed machine learning”. In: *Med Image Anal* 94 (2024), p. 103134. URL: https://www.ncbi.nlm.nih.gov/pubmed/38471339.

[185] S. Kundu et al. “Mapping the individual human cortex using multidimensional MRI and unsupervised learning”. In: *Brain Commun* 5.6 (2023), fcad258. URL: https://www.ncbi.nlm.nih.gov/pubmed/37953850.

[186] Y. Ji et al. “Accelerating joint relaxation-diffusion MRI by integrating time division multiplexing and simultaneous multi-slice (TDM-SMS) strategies”. In: *Magn Reson Med* 87.6 (2022), pp. 2697–2709. URL: https://www.ncbi.nlm.nih.gov/pubmed/35092081.

[187] Berkin Bilgic, Vivek K Goyal, and Elfar Adalsteinsson. “Multi-contrast reconstruction with Bayesian compressed sensing”. In: *Magnetic resonance in medicine* 66.6 (2011), pp. 1601–1615.

[188] Angshul Majumdar and Rabab K Ward. “Accelerating multi-echo T2 weighted MR imaging: analysis prior group-sparse optimization”. In: *journal of Magnetic Resonance* 210.1 (2011), pp. 90–97.

[189] Angshul Majumdar and Rabab K Ward. “Joint reconstruction of multiecho MR images using correlated sparsity”. In: *Magnetic resonance imaging* 29.7 (2011), pp. 899–906.

[190] Berkin Bilgic et al. “Highly accelerated multishot echo planar imaging through synergistic machine learning and joint reconstruction”. In: *Magnetic resonance in medicine* 82.4 (2019), pp. 1343–1358.

[191] Felix Lugauer et al. “Accelerating multi-echo water-fat MRI with a joint locally low-rank and spatial sparsity-promoting reconstruction”. In: *Magnetic Resonance Materials in Physics, Biology and Medicine* 30.2 (2017), pp. 189–202.

[192] Wenchuan Wu. “Dynamic field mapping and distortion correction using single-shot blip-rewound EPI and joint multi-echo reconstruction”. In: *Magnetic Resonance in Medicine* 92.1 (2024), pp. 82–97.

[193] Junzhou Huang, Chen Chen, and Leon Axel. “Fast multi-contrast MRI reconstruction”. In: *Magnetic resonance imaging* 32.10 (2014), pp. 1344–1352.

[194] P. Wongkornchaovalit et al. “Multi-TE Diffusion MRI Dataset for Exploring Combined Diffusion-Relaxometry Methods in Microstructure Imaging”. In: *Sci Data* 12.1 (2025), p. 1191. URL: `https://www.ncbi.nlm.nih.gov/pubmed/40640197`.

[195] Jonathan R Polimeni et al. “Reducing sensitivity losses due to respiration and motion in accelerated echo planar imaging by reordering the autocalibration data acquisition”. In: *Magnetic resonance in medicine* 75.2 (2016), pp. 665–679.

[196] M. Reisert et al. “Disentangling micro from mesostructure by diffusion MRI: A Bayesian approach”. In: *Neuroimage* 147 (2017), pp. 964–975. URL: `https://www.ncbi.nlm.nih.gov/pubmed/27746388`.

[197] D. S. Novikov et al. “Rotationally-invariant mapping of scalar and orientational metrics of neuronal microstructure with diffusion MRI”. In: *Neuroimage* 174 (2018), pp. 518–538. URL: `https://www.ncbi.nlm.nih.gov/pubmed/29544816`.

[198] Florian Gerber and Douglas Nychka. “Fast covariance parameter estimation of spatial Gaussian process models using neural networks”. In: *Stat* 10.1 (2021), e382.

[199] Kevin Cremanns and Dirk Roos. “Deep Gaussian covariance network”. In: *arXiv preprint arXiv:1710.06202* (2017).

[200] Geoffrey E Hinton and Russ R Salakhutdinov. “Using deep belief nets to learn covariance kernels for Gaussian processes”. In: *Advances in neural information processing systems* 20 (2007).

[201] Peiyu Huang et al. “White matter free water is a composite marker of cerebral small vessel degeneration”. In: *Translational stroke research* 13.1 (2022), pp. 56–64.

[202] Ziyu Li et al. “Submillimeter diffusion MRI using an in-plane segmented 3D multi-slab acquisition and denoiser-regularized reconstruction”. In: *bioRxiv* (2024), pp. 2024–10.

[203] Ziyu Li et al. “Submillimeter diffusion MRI using an in-plane segmented 3D multi-slab acquisition and denoiser-regularized reconstruction”. In: *Medical Image Analysis* (2025), p. 103834.

[204] Kerstin Hammernik et al. “Learning a variational network for reconstruction of accelerated MRI data”. In: *Magnetic resonance in medicine* 79.6 (2018), pp. 3055–3071.

[205] Florian Knoll et al. “Deep-learning methods for parallel magnetic resonance imaging reconstruction: A survey of the current approaches, trends, and issues”. In: *IEEE signal processing magazine* 37.1 (2020), pp. 128–140.

[206] Thomas Küstner et al. “CINENet: deep learning-based 3D cardiac CINE MRI reconstruction with multi-coil complex-valued 4D spatio-temporal convolutions”. In: *Scientific reports* 10.1 (2020), p. 13710.

[207] Kerstin Hammernik et al. “Physics-driven deep learning for computational magnetic resonance imaging: Combining physics and machine learning for improved medical imaging”. In: *IEEE signal processing magazine* 40.1 (2023), pp. 98–114.

[208] Sebastian Gassenmaier et al. “Deep learning applications in magnetic resonance imaging: has the future become present?” In: *Diagnostics* 11.12 (2021), p. 2181.

[209] Kerem C Tezcan et al. “MR image reconstruction using deep density priors”. In: *IEEE transactions on medical imaging* 38.7 (2018), pp. 1633–1642.

[210] Jiaming Liu et al. “RARE: Image reconstruction using deep priors learned without groundtruth”. In: *IEEE Journal of Selected Topics in Signal Processing* 14.6 (2020), pp. 1088–1099.

[211] Olivier Reynaud. “Time-dependent diffusion MRI in cancer: tissue modeling and applications”. In: *Frontiers in Physics* 5 (2017), p. 58.

[212] Carl-Fredrik Westin et al. “Q-space trajectory imaging for multidimensional diffusion MRI of the human brain”. In: *Neuroimage* 135 (2016), pp. 345–362.

[213] Junwei Yang et al. “Fast multi-contrast MRI acquisition by optimal sampling of information complementary to pre-acquired MRI contrast”. In: *IEEE Transactions on Medical Imaging* 42.5 (2022), pp. 1363–1373.

[214] Zepeng Wang et al. “Multi-parametric molecular imaging of the brain using optimized multi-TE subspace MRSI”. In: *IEEE Transactions on Biomedical Engineering* 71.6 (2024), pp. 1732–1744.